MEASUREMENTS OF THE 2001 APRIL 15 AND 2005 JANUARY 20 GROUND-LEVEL ENHANCEMENTS BY THE MILAGRO WATER ČERENKOV DETECTOR

BY

Trevor Morgan

B.S., University of New Hampshire (2004)

DISSERTATION

Submitted to the University of New Hampshire
in Partial Fulfillment of
the Requirements for the Degree of

Doctor of Philosophy
in
Physics

September, 2010

This dissertation has been examined and approved.

_____

Dissertation Director, James M. Ryan, Professor, Physics

_____

Martin A. Lee, Professor, Physics

_____

Clifford Lopate, Professor, Physics

_____

Mark L. McConnell, Professor, Physics

_____

Per Berglund, Professor, Physics

_____

Date

For my mother and father.

ACKNOWLEDGEMENTS

First of all, I would like to thank my advisor, Jim Ryan, for all his guidance during my graduate career. I'd also like to thank my committee of Mark McConnell, Marty Lee, Clifford Lopate, and Per Berglund. For all their helpful discussions and assistance I'd like to recognize the following people: Bruce McKibben, Terry Forbes, Ed Chupp, Jack Lockwood, Christian Seymour, Jim Connell, Joe Hollweg, Eberhard Mobius, Amitava Bhattacharjee, Jason Legere, John Macri, Allan Tylka, Richard Mewaldt, Harm Moraal, Don Smart, Peggy Shea, Ed Cliver, Erwin Flückiger, Abe Flacone, James Ledoux, Gerry Share, Aaron Torok, Lorenzo Zana, Jing Lao, Trevor Leonard, Andrew Vandenberg, Camden Ertley, Guoqin Ren, and Mark Maciolek.

For unpublished data I'd like to thank Clifford Lopate, Charles Farrugia, Eino Valtonen, Paul Evenson and Gerry Share.

I would also like to thank many of those who helped advance my work with the Milagro observatory, including Brenda Dingus, Andrew Smith, David Williams, Owen Marshall, Vlasios Vasiliou, Gary Walker, Aous Abdo, Gus Sinnis, Scott Delay, Gaurang Yodh, Tony Shoup and the entire Milagro collaboration.

Also a special thanks to Robbin Williams, Katie Makem, Michelle Walker, and Lindsay Belaidi for travel plans and organization.

Much of this work resulted from two Coordinated Data Analysis Workshops (CDAW) on ground-level enhancements, held in January 2009 in Palo Alto, California, and in November 2009, Huntsville, Alabama, organized by Nariaki Nitta and Nat Gopalswamy.

This work has been supported by the National Science Foundation (under grants PHY-0075326, PHY-0096256, PHY-0097315, PHY-0206656, PHY-0245143, PHY-0245234, PHY-0302000, and ATM-0002744, ATM-0411651, ATM-0339527) the US Department of Energy (Office of High-Energy Physics and Office of Nuclear Physics), Los Alamos National Laboratory, the University of California, and the Institute of Geophysics and Planetary Physics.

TABLE OF CONTENTS

DEDICATION.....iii

ACKNOWLEDGEMENTS.....iv

LIST OF TABLES.....x

LIST OF FIGURES.....xi

ABSTRACT.....xviii

CHAPTER PAGE

INTRODUCTION.....1

1 SOLAR PHYSICS OVERVIEW.....4

1.1 PHYSICAL CHARACTERISTICS.....4

1.2 SURFACE MAGNETIC FIELD AND THE SOLAR CYCLE.....7

1.3 SOLAR WIND AND INTERPLANETARY MAGNETIC FIELD.....10

1.4 SOLAR FLARES AND CORONAL MASS EJECTIONS.....14

1.4.1 SOLAR FLARES.....14

1.4.2 CORONAL MASS EJECTIONS.....16

1.5 SOLAR ENERGETIC PARTICLES.....20

1.5.1 IMPULSIVE VS. GRADUAL EVENTS.....22

1.5.2 SHOCK ACCELERATION.....26

1.5.3 A BRIEF SUMMARY OF SOLAR ENERGETIC PARTICLES.....29

2 COSMIC RAYS AND AIR SHOWERS....32
2.1 COSMIC RAYS....32
2.1.1 COMPOSITION AND SPECTRUM....33
2.1.2 SOURCES AND DISTRIBUTION....35
2.1.3 SOLAR MODULATION OF COSMIC RAYS....37
2.2 AIR SHOWERS....39
2.2.1 DEVELOPMENT IN ATMOSPHERE....40
2.2.2 GROUND-LEVEL STRUCTURE....44
2.3 AIR SHOWER DETECTION INSTRUMENTS....46
2.3.1 AIR ČERENKOV TELESCOPES....46
2.3.2 AIR FLUORESCENCE....48
2.3.3 EXTENDED AIR SHOWER ARRAYS....49
3 NEUTRON MONITORS....51
3.1 THE EARTH AS A DETECTOR FOR COSMIC RAYS....51
3.2 DEVELOPMENT OF THE WORLD WIDE NEUTRON MONITOR NETWORK....56
3.2.1 DESIGN....57
3.2.2 GROUND-LEVEL ENHANCEMENT OBSERVATIONS AND RESULTS....60
4 THE MILAGRO DETECTOR....69
4.1 ČERENKOV EMISSION....69
4.2 PHYSICAL DESCRIPTION....70

4.2.1 LOCATION....70
4.2.2 DETECTOR LAYOUT....72
4.3 ELECTRONICS AND DATA ACQUISITION SYSTEM....75
4.4 DATA TYPES....78
4.5 SIMULATING THE MILAGRO DETECTOR....79
4.5.1 MONTE CARLO SIMULATIONS....79
4.5.2 SIMULATING THE COSMIC RAY BACKGROUND....81
4.5.3 SENSITIVITY TO PITCH-ANGLE DISTRIBUTIONS....83
4.5.4 SIMULATING GROUND-LEVEL ENHANCEMENTS....85
4.6 COMPARISON TO OTHER INSTRUMENTS....89
5 THE 2001 APRIL 15 AND 2005 JANUARY 20 EVENTS....91
5.1 THE 2001 APRIL 15 EVENT....91
5.1.1 OBSERVATIONS WITH OTHER INSTRUMENTS....91
5.1.2 GROUND-LEVEL ENHANCEMENT....94
5.2 THE 2005 JANUARY 20 EVENT....99
5.2.1 OBSERVATIONS WITH OTHER INSTRUMENTS....99
5.2.2 GROUND-LEVEL ENHANCEMENT....102
6 DATA ANALYSIS AND PROCEDURE....107
6.1 BACKGROUND CORRECTION USING A PRINCIPAL COMPONENT ANALYSIS....107
6.2 SPECTRAL ANALYSIS....111
6.2.1 CHI-SQUARED ANALYSIS....113

6.2.2 RESPONSE FUNCTIONS....114
6.2.3 EXTENDING THE SPECTRUM USING SPACECRAFT DATA....116
6.3 EXAMPLE ANALYSIS: 2005 JANUARY 20 0656-0701 UT....118
7 RESULTS AND CONCLUSIONS....122
7.1 2001 APRIL 15 GROUND-LEVEL ENHANCEMENT....122
7.1.1 PITCH-ANGLE DISTRIBUTION....122
7.1.2 EVENT TIMING....126
7.1.3 PROTON SPECTRA....127
7.2 2005 JANUARY 20 GROUND-LEVEL ENHANCEMENT....130
7.2.1 PITCH-ANGLE DISTRIBUTION....130
7.2.2 EVENT TIMING....134
7.2.3 PROTON SPECTRA....139
7.3 DISCUSSION....145
7.4 CONCLUSIONS....152
APPENDIX A SIMULATION PLOTS....153
APPENDIX B TIME-RESOLVED SPECTRA PLOTS....163
REFERENCES....169

LIST OF TABLES

1.1 Severity of radio blackouts from increases in X-ray intensity due to solar flares....15

1.2 Severity of geomagnetic storms due to passing coronal mass ejections....19

1.3 Different features and compositions observed in impulsive and gradual events...24

1.4 Effects of solar radiation storms near the Earth....25

2.1 Properties of elementary particles discovered in air showers....42

3.1 Design improvements to the original IGY neutron monitor....60

3.2 Properties of neutron monitors still in operation (part 1 of 2)....67

Properties of neutron monitors still in operation (part 2 of 2)....68

4.1 Simulated vs. measured cosmic ray background rates in Milagro....83

6.1 Explanation of variables contained within equation 6.5....111

7.1 Evolution of spectral parameters during the 2001 April 15 GLE....128

7.2 Evolution of spectral parameters during the 2005 January 20 GLE....142

7.3 Various characteristics and timing information on both the 2001 April 15 and 2005 January 20 events....146

LIST OF FIGURES

1.1 (Left) The different layers that compose the Sun. (Right) A coronagraph image taken by the LASCO instrument aboard SOHO.....5

1.2 The Sun's differential rotation caused by plasma motions in the convective zone results in the twisting of magnetic field lines.....7

1.3 An active region on the Sun's surface as seen by the TRACE spacecraft.....8

1.4 (Top) The range of solar latitudes at which sunspots appear creates a butterfly diagram. (Bottom) Sunspot coverage relative to the visible surface reveals the 11-year cycle of solar activity.....9

1.5 Solar wind speeds during solar minimum and solar maximum observed by the Ulysses spacecraft.....11

1.6 (Top) Magnetic field lines from the Sun carried by the solar wind create an Archimedean spiral. (Bottom) The interplanetary magnetic field creates a region in the interstellar medium known as the heliosphere.....13

1.7 (Top) The first images of a coronal mass ejection by Tousey (1973). (Bottom) Modern images of a coronal mass ejection taken from SOHO/LASCO.....18

1.8 Intensity-time profiles of electrons and protons in (a) gradual and (b) impulsive events.....23

1.9 Proton intensity vs. time profiles for observers viewing a coronal mass ejection from the western solar limb (left), central meridian (middle), and eastern solar limb (right).....30

2.1 Comparison of observed cosmic ray and Solar System abundances.....33

2.2 (Left) The cosmic ray spectrum. (Right) Kepler's supernova is viewed in multiple bands of the electromagnetic spectrum.....34

2.3 Fractional differences of the cosmic ray rates as viewed by Milagro.....37

2.4 (Top) The 11-year cycle of solar activity is seen from the anti-correlation between sunspot number and cosmic ray intensity. (Bottom) A short-term drop in cosmic ray intensity known as a Forbush decrease.....39

2.5 (Top) Development of an air shower. (Bottom) Total number of shower particles for proton and iron primaries at different initial energies as a function of atmospheric depth.....43

2.6 The lateral density distribution in air showers.....45

2.7 The VERITAS array of air Čerenkov telescopes.....47

2.8 Google Earth map of the Pierre Auger Observatory.....50

3.1 SOHO composite image depicting the solar wind incident upon the Earth's magnetic field.....52

3.2 The dynamics of a charged particle in a uniform magnetic field.....53

3.3 (Top) Map of cutoff rigidities for all locations on the globe. (Bottom) Simulated trajectories through the Earth's magnetic field for cosmic rays of different rigidities.....55

3.4 (Top) Cross-sectional view of the IGY neutron monitor pile. (Bottom) The NM64 supermonitor configuration.....58

3.5 (Left) The 1956 February 23 GLE. (Right) The 1978 May 7 GLE observed by the

Durham, NH station.....62

3.6 (Left) Rigidity spectra for multiple episodes of the 1956 February 23 GLE. (Right) Rigidity spectra during the 1978 May 7 GLE for both a worldwide neutron monitor network analysis and the ratio between the Mt. Washington and Durham stations.....64

3.7 Locations and asymptotic viewing directions for the 11 neutron monitors that make up Spaceship Earth.....66

4.1 Aerial view of the Milagro detector.....71

4.2 (Top) Inside view of the Milagro detector before it was filled with water. (Bottom) Cross sectional schematic of the PMT layout of the Milagro pond.....74

4.3 The signal pulse in Milagro's front end boards is used to classify events.....76

4.4 (Left) A cosmic-ray proton’s simulated interactions in the atmosphere. (Right) Simulated light in one of Milagro’s Hamamatsu PMTs.....80

4.5 Map of shower cores thrown 1-3 km from the center of Milagro.....86

4.6 The effective area ratios for the 16-PMT and 25-PMT channels as a function of inverse energy.....87

4.7 Milagro scaler channel specific yield functions for an isotropic (bottom) and an anisotropic (top) pitch-angle distribution.....88

5.1 (Top) GOES X-ray intensity around the time of the 2001 April 15 event. (Bottom) SOHO/LASCO images of the associated coronal mass ejection.....92

5.2 IMP-8 proton data during the 2001 April 15 event.....93

5.3 Cosmic ray intensities at the Climax neutron monitor around the time of the 2001

April 15 event.....95

5.4 (Top) The PCA corrected background rate around the time of the 2001 April 15 GLE. (Bottom) A quadratic fit to the cosmic ray background was used to isolate the GLE in Milagro channels.....96

5.5 Ground-level enhancements during the 2001 April 15 event for the Mt. Washington, Durham, and Climax neutron monitors.....97

5.6 Ground-level enhancements during the 2001 April 15 event for the Milagro low and high threshold channels.....98

5.7 (Top) GOES X-ray intensity around the time of the 2005 January 20 event. (Bottom) SOHO/LASCO and SOHO/EIT images of the associated coronal mass ejection.....100

5.8 Proton intensities measured by the ERNE instrument aboard SOHO during the 2005 January 20 event.....101

5.9 (Top) Cosmic ray intensities at Milagro and the Haleakala neutron monitor around the time of the 2005 January 20 event. (Bottom) Linear background subtraction to isolate the 2005 January 20 GLE from the cosmic ray background in the Milagro high threshold channel.....103

5.10 Ground-level enhancements during the 2005 January 20 event for Mt. Washington, Durham, and Climax neutron monitors, as well as the Milagro low threshold channel.....104

5.11 Ground-level enhancements during the 2005 January 20 event for Milagro high threshold, 6-PMT, 8-PMT, and 12-PMT channels.....105

5.12 Ground-level enhancements during the 2005 January 20 event for Milagro 16- PMT, 25-PMT, and 32-PMT channels.....106

6.1 (Top) The raw Climax count rate is anti-correlated with barometric pressure. (Bottom) The PCA correction for Climax is nearly identical to the standard pressure correction.....108

6.2 Environmental parameters (top) are used to correct the Milagro low threshold channel for a period of time surrounding the 2005 January 20 GLE (bottom)....110

6.3 Selected response functions during the 2005 January 20 GLE.....115

6.4 Flux vs. rigidity for ground-level data channels during 2005 January 20 0656-0701 UT.....119

6.5 SOHO/ERNE and ground-level data for 2005 January 20 0656-0701 UT (left) and the resulting χ-squared fit yielding equation 6.16 (right).....121

7.1 GLE profiles for Milagro and Climax (top), and Spaceship Earth (bottom) during the 2001 April 15 event.....123

7.2 Pitch angle excesses and deficits measured by a network of muon detectors during the 2001 April 15 event.....125

7.3 Evolution of the proton spectra during the 2001 April 15 GLE.....129

7.4 Comparison of the 2001 April 15 and 2005 January 20 GLE profiles.....130

7.5 (Left) Increases over background for selected Milagro multiplicity channels during the 2005 January 20 event. (Right) Simulated increases over background in selected Milagro multiplicity channels for different pitch-angle distributions.....131

7.6 GLE profiles for Milagro 6-PMT and Climax (top), and Spaceship Earth (bottom) during the 2005 January 20 event.....133

7.7 Inverse velocity vs. onset time for ground-level detectors and the SOHO/ERNE instrument during the 2005 January 20 event.....136

7.8 CORONAS-F/SONG gamma ray profiles during the 2005 January 20 event....138

7.9 GLE profiles for the Milagro 6-PMT channel and the Mt. Washington and Climax neutron monitors.....140

7.10 Evolution of the proton spectra during the 2005 January 20 GLE.....141

7.11 Evolution of the break energy during the 2001 April 15 and January 20 GLEs..143

7.12 GLE profiles for the 1989 October 22 event in the McMurdo, South Pole and Thule neutron monitors.....151

A.1 Simulated proton effective area vs. throw distance for a zenith pitch-angle distribution from 3.13-9 GeV.....154

A.2 Simulated proton effective area vs. throw distance for a zenith pitch-angle distribution from 12.5-35 GeV.....155

A.3 Simulated proton effective area vs. throw distance for an isotropic pitch-angle distribution from 3.13-9 GeV.....156

A.4 Simulated proton effective area vs. throw distance for an isotropic pitch-angle distribution from 12.5-35 GeV.....157

A.5 Isotropic vs. zenith proton specific yield functions for Mt. Washington, Durham, and Climax neutron monitors, as well as the Milagro low threshold channel.....158

A.6 Isotropic vs. zenith proton specific yield functions for Milagro high threshold,

6-PMT, 8-PMT, and 12-PMT channels.....159

A.7 Isotropic vs. zenith proton specific yield functions for Milagro 16-PMT and 25-PMT channels.....160

A.8 Zenith proton specific yield functions for Climax, Mt. Washington, and Durham neutron monitors, as well as all available Milagro channels.....161

A.9 Isotropic proton specific yield functions for Climax, Mt. Washington, and Durham neutron monitors, as well as all available Milagro channels.....162

B.1 Proton spectra for multiple time intervals in the 2001 April 15 GLE.....165

B.2 Proton spectra for multiple time intervals in the 2001 April 15 GLE.....166

B.3 Proton spectra for the final time interval in the 2001 April 15 GLE and multiple time intervals of the 2005 January 20 GLE.....167

B.4 Proton spectra for multiple time intervals in the 2005 January 20 GLE.....168

ABSTRACT

MEASUREMENTS OF THE 2001 APRIL 15 AND 2005 JANUARY 20 GROUND-LEVEL ENHANCEMENTS BY THE MILAGRO WATER ČERENKOV DETECTOR

by

Trevor Morgan

University of New Hampshire, September, 2010

The Sun is capable of accelerating particles up to high energies, the highest of which (>1 GeV) are detectable at the Earth's surface. Although the accelerating source is tied to the solar magnetic field, the physical process responsible continues to be debated. Essential information about the location and nature of the acceleration mechanism can be obtained from measurements of the highest-energy particles.

The Milagro instrument was originally designed as a very-high-energy gamma-ray detector, but was also sensitive to cosmic rays and high-energy solar particles. Milagro registered ground-level enhancements for the 2001 April 15 and 2005 January 20 solar events during its operation from January 2000 to March 2008, the latter of which was the most intense in 50 years. The multiple data channels in Milagro, combined with complementary neutron monitor data, enabled for a detailed analysis of the energetic proton spectra even during the brief anisotropic phase of the 2005 January 20 event.

For both events the results for the proton spectra are consistent with a coronal shock origin. A timing analysis for the controversial 2005 January 20 event reveals that the prompt arrival of the relativistic protons and rapid evolution of the observed profiles measured at ground-level stations can be attributed to a coronal shock origin and do not require an additional or different process, *i.e.*, direct solar-flare acceleration.

Introduction

Energetic particle acceleration is a process common to many astrophysical sources, including the Sun. Due to its proximity, the Sun can be studied in far more detail than sources outside our own Solar System such as supernova remnants and active galactic nuclei. Therefore, the Sun is an excellent laboratory for studying many of the processes of particle acceleration that take place throughout the universe.

Most of our knowledge on solar energetic particles, and their acceleration processes, is from research at energies below ~1 giga-electron volt (one electron volt is the energy gained when an electron is accelerated through a potential difference of one volt). This is because there are very few particles to detect at higher energies due to the power-law spectra, which drops rapidly with increasing energy. Furthermore, it is difficult to design spacecraft instruments with enough sensitivity to detect particles at these higher energies.

Ground-based instruments, such as the Milagro water Čerenkov detector, indirectly measure the high-energy solar energetic particles by observing their secondary products resulting from collisions in the atmosphere. Measurements of solar energetic particles at GeV energies is important because it provides information on the acceleration mechanism(s) taking place at the Sun. The Milagro instrument possessed several advantages over a standard neutron monitor, enabling it to study particles at these energies in great detail.

This dissertation begins with an overview of the Sun and relevant solar processes (*e.g.*, solar flares and coronal mass ejections). Determining the source of solar particles accelerated to cosmic-ray energies (>1 GeV) is difficult because coronal mass ejections and flares often occur together (and always do for ground-level enhancements), however one does not necessarily cause the other. Research on solar particles at these energies requires an understanding of cosmic rays and their interactions in the atmosphere, discussed in chapter 2.

Neutron monitors have continually studied cosmic rays and ground-level enhancements since the 1950s, their design and relevant contributions are covered in chapter 3. The Milagro instrument was sensitive to cosmic rays in the same energy regime as neutron monitors, and thus sensitive to high-energy solar particles. Chapter 4 describes the Milagro instrument, which detected two ground-level enhancements during its operation, the 2001 April 15 and 2005 January 20 events (Chapter 5).

The multiple data channels in Milagro allowed for a measurement of the proton spectrum (analysis procedure described in chapter 6) even during the brief initial phase of the 2005 January 20 ground-level enhancement, which could not be measured using neutron monitors. The evolution of the proton spectra during both events is discussed in chapter 7, along with its implications on the accelerating source. In addition to the proton spectra, the various timing characteristics of charged particles and electromagnetic emissions in these events provide insight to the acceleration mechanism(s) responsible for the highest-energy protons. These characteristics are particularly important for the 2005 January 20 event, in which ground-level intensity reached extraordinary levels

within a few minutes. The observed ground-level profile during the 2005 January 20 event has generated controversy regarding whether existing theories can explain how solar particles can be accelerated to GeV energies in such a short amount of time or if some other process in the associated flare itself is responsible for the particles.

Chapter 1

Solar Physics Overview

Beginning with an overview of the Sun, this chapter introduces the dynamics of the solar magnetic field. Processes arising from the ever-changing and complex nature of this field close to the solar surface can accelerate particles to cosmic-ray energies.

1.1 Physical Characteristics

About 5 billion years ago a region of dense gas (>a millionth of an ounce per cubic mile) spanning trillions of miles across began to collapse due to its own gravitational attraction. Over millions of years it condensed, all the while with the material in the center growing hotter. Fusion of hydrogen into helium began once temperatures reached about ten million degrees Kelvin, providing the constant energy and required pressure to support the 1.989×10^{30} kg mass that we know as the Sun. The fusion process converts nearly 7×10^{8} tons of hydrogen into 6.95×10^{8} tons of helium every second, with an energy release of 3.86×10^{33} ergs. The Sun is currently in the prime of its life, its mass consisting of 70% hydrogen, 28% helium, and ~2% heavier elements.

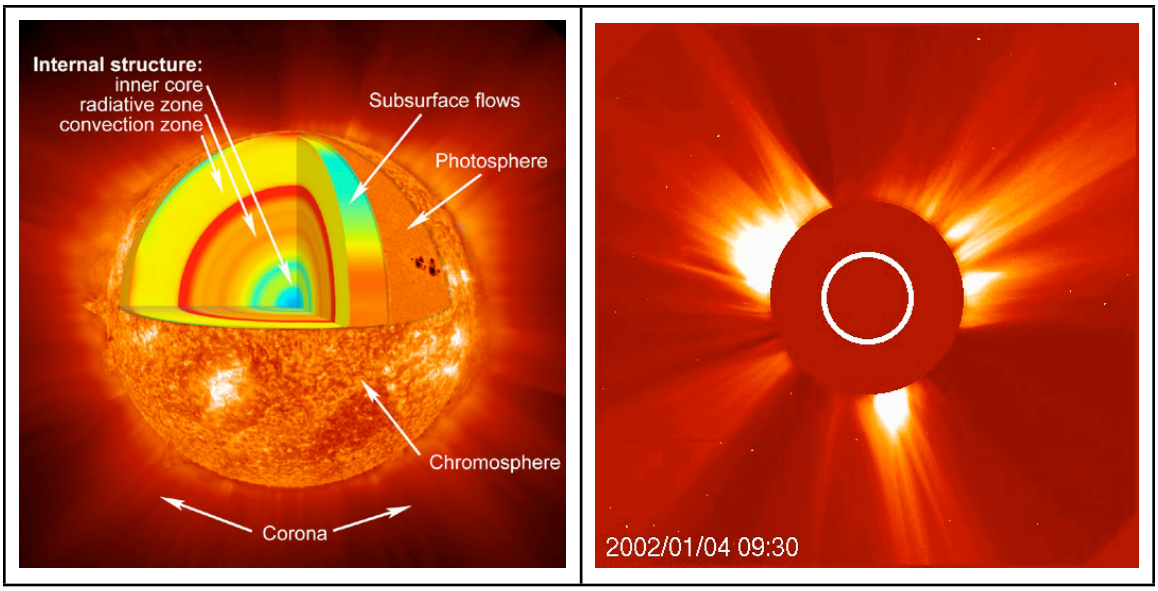

Figure 1.1: (Left) The different layers that compose the Sun. (Right) A coronagraph image taken by the LASCO instrument aboard the SOHO spacecraft shows plasma at millions of degrees Kelvin continually streaming outward. The edge of the photosphere is indicated by the white ring.

The Sun's core extends from its center to ~0.25 $R_\odot$ ($R_\odot$ = 695,000 km = 109 $R_\oplus$) with an average temperature of ~1.5 × 10^7 K and average density of ~1.6 × 10^5 kg/m^3, sufficient conditions for nuclear burning of hydrogen via the proton-proton chain. From the outer edge of the core to the boundary with the convective zone at ~0.75 $R_\odot$ lies a cooler region known as the radiative zone. In this region hydrogen and helium ions absorb and re-emit photons from the core, the photons diffuse outwards to regions of lower density and temperature. Gamma rays from hydrogen burning take an average of 1.7 × 10^5 years (Mitalas and Sills, 1992) to be transported out to the convective zone, losing most of their energy in the process.

Energy from the radiative zone is transferred to the outermost layers of the Sun through the convection zone. Bulk quantities of plasma rise to the surface of the convection zone at several km/s, surrender their heat, and then fall back down toward the

radiative zone to be reheated. This heat is transferred to the opaque outermost layer of the Sun known as the photosphere. This region has a thickness of ~500 km and a temperature of ~6,000 K. By the time the gamma rays that began their journey in the core reach this layer they have lost enough energy to place them in the visible range of the electromagnetic spectrum. The photosphere has a mottled appearance, a result of the columns of plasma that rise through the convective zone. Typical diameters of these columns (called granulation cells) are ~1,000 km. The photosphere defines the radius of the Sun at its visible edge.

Above the photosphere is the chromosphere, a ~2000 km thick layer with temperature ranging from ~4,000-20,000 K. Spike-like jets of plasma (spicules) with diameters comparable to the granulation cells give the chromosphere a jagged appearance. This region participates in much of the solar activity such as flares and prominences. Between the chromosphere and corona is the transition region. In this thin region the temperature rapidly rises to above a million K, while the density decreases appropriately to maintain hydrostatic equilibrium. The mechanism for this heating is not well understood, however it is believed to be from the dissipation of wave motions, specifically magnetohydrodynamic waves (Cranmer et al., 2007).

Above the transition region the temperature profile flattens and remains on the order of 10^6 K. This hot atmosphere is called the corona. Its brightness is one millionth that of the photosphere, so it may only be viewed during a total solar eclipse or by using a coronagraph such as in Figure 1.1.

1.2 Surface Magnetic Field and the Solar Cycle

The interior layers of the Sun are believed to rotate as a rigid body. The outer layers, beginning with the convective zone, rotate differentially with latitude (~25 days at the equator, ~33 days at the poles). The faster rotation near the equator twists the Sun's dipole magnetic field (Figure 1.2). Plasma motions in the convection zone are not simply vertical, the Coriolis force due to the Sun's rotation results in a swirling effect. These turbulent plasma motions coupled with the Sun's differential rotation leads to the generation of electric currents and magnetic fields through the dynamo mechanism.

Streams of plasma carrying concentrated magnetic field ropes can break through the photosphere. These regions can have multiple sections of opposing magnetic polarities oriented inward and outward from the surface with magnetic field strengths ranging from ~1,000-4,000 Gauss (regions without any activity are ~1 Gauss, twice as strong as the Earth's surface magnetic field) and are known as active regions. Areas of opposing magnetic polarities inhibit the mixing of surrounding hot plasma, causing them

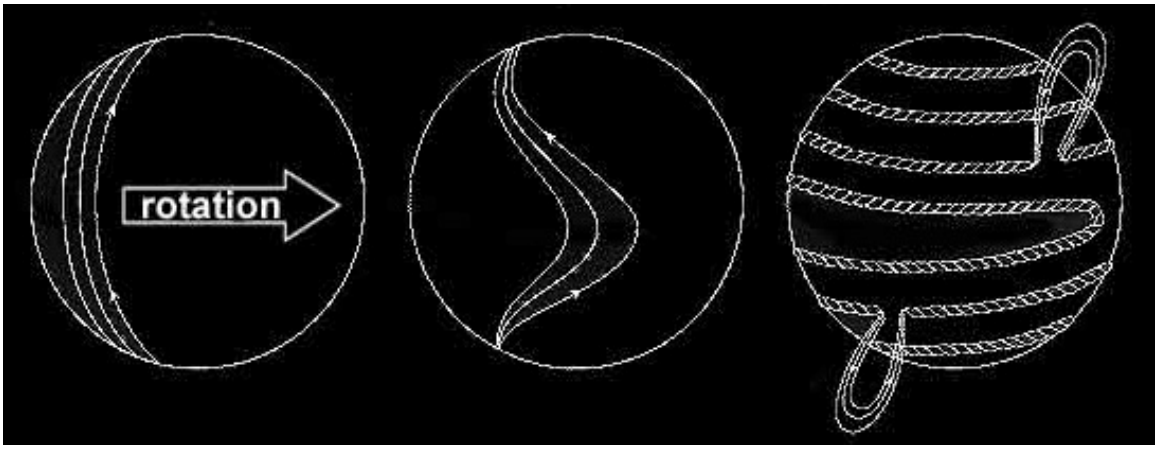

Figure 1.2: The Sun's differential rotation caused by plasma motions in the convective zone results in the twisting of magnetic field lines.

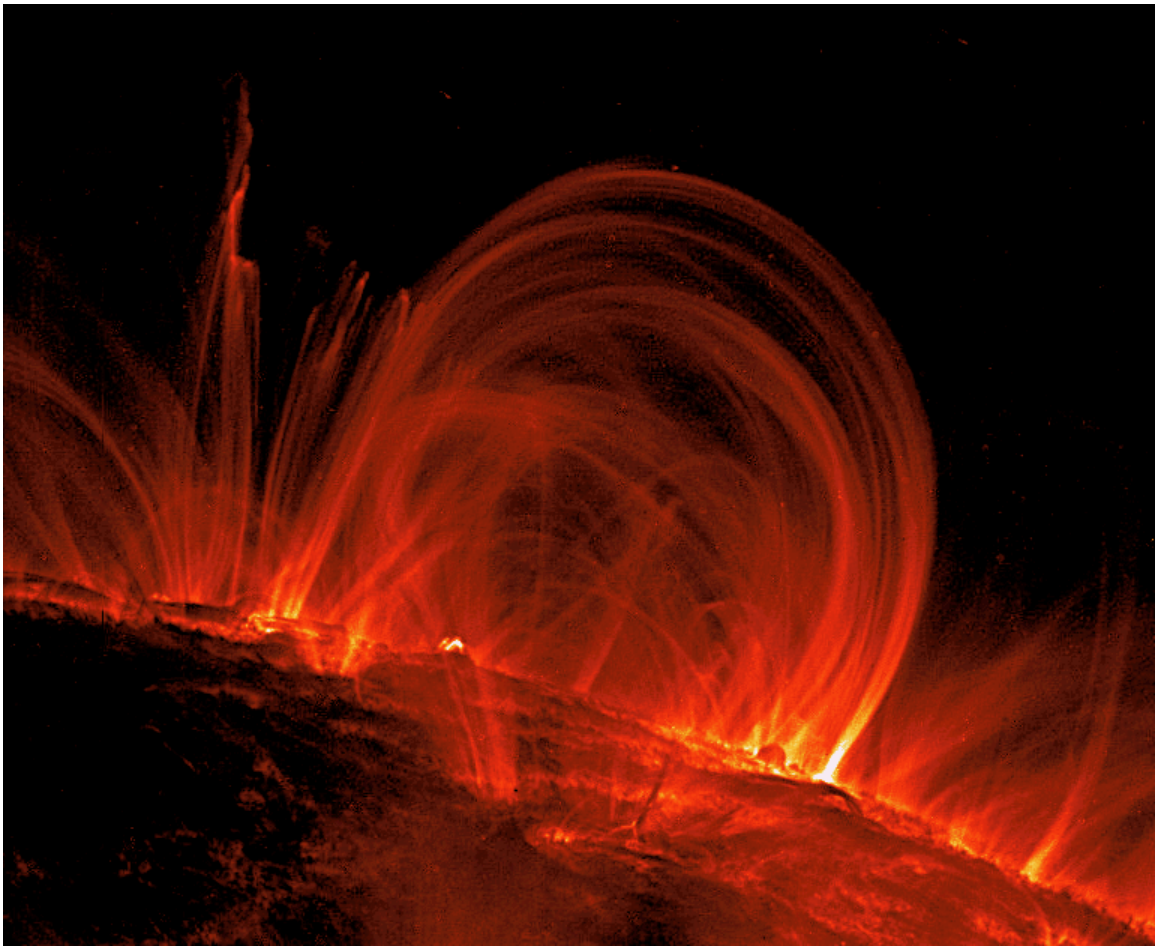

Figure 1.3: An active region on the Sun's surface as seen by the TRACE spacecraft. Photons emitted from plasma that is frozen into the magnetic field reveal its loop structure.

to be cooler (darker) than the remainder of the photosphere. These visible phenomenon (typically the size of the earth) can become as large as Jupiter and are called sunspots, and can often form in groups within an active region. The high magnetic field intensity within active regions can produce large explosions in the Sun's atmosphere (solar flares) and eject large amounts of plasma, the process of which is called a coronal mass ejection (CME).

As the solar dipole field continues to wind-up, solar activity increases due to more active regions and sunspots. Over time increasing fluxes of opposite magnetic field

polarity build up in the two solar hemispheres, which distorts the overall dipole structure. Eventually this causes the Sun's magnetic poles to flip. Solar activity then gradually decreases to a minimum before the differential rotation and swirling convective flows begin to produce increasing active regions and sunspots, causing the magnetic poles to flip again. The oscillating solar activity resulting from the Sun's polarity flips has an 11-year period known as the solar cycle.

Because the existence of sunspots are well correlated with solar activity, their number or frequency follows the solar cycle. Although some historical observations of sunspots date back thousands of years, their cyclic nature wasn't recognized until the early 1800s. Rudolf Wolf began systematic observations of sunspots in 1848, and to this

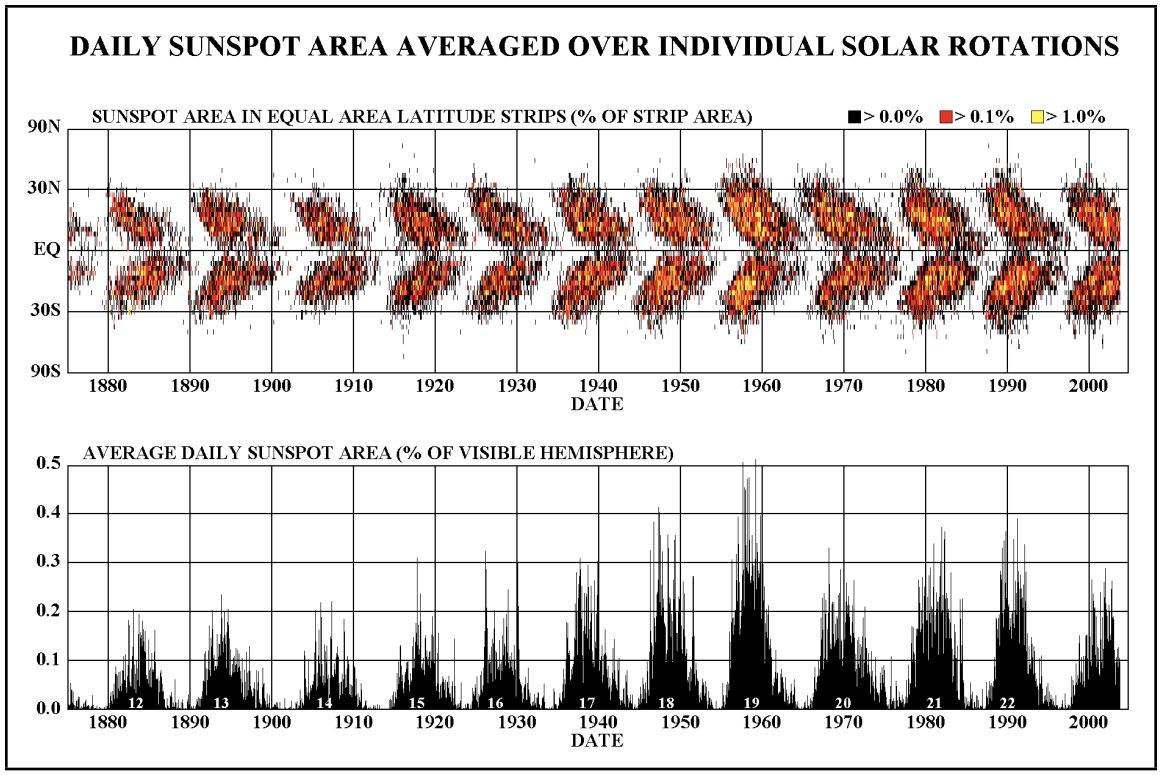

Figure 1.4: (Top) The range of solar latitudes at which sunspots appear creates a plot known as a butterfly diagram. (Bottom) In addition to the Wolf sunspot number, sunspot coverage relative to the visible surface also reveals the 11-year cycle of solar activity. (Graph courtesy of Hathaway at NASA-MSFC)

day the most traditional method of tracking the solar cycle is by recording the Wolf sunspot number (another method is the long-term variation of cosmic rays as discussed in section 2.1.3). Peaks in sunspot number occur during the solar maximum phase, and likewise, valleys occur during the solar minimum phase.

1.3 Solar Wind and Interplanetary Magnetic Field

George Fitzgerald was the first to suggest that matter could be regularly accelerated away from the Sun (Fitzgerald, 1892). His ideas of were further developed by Kristian Birkeland, who made geomagnetic surveys of auroral activity and concluded that the Sun emits a continuous flux of charged particles filling up interplanetary space (Birkeland, 1908, 1913), however these conclusions were not supported by any other evidence.

In the early 1950s, Ludwig Biermann re-introduced Birkeland's theories by developing a model attempting to explain how the gaseous tails of comets were always oriented away from the Sun (Biermann, 1953). At the same time a competing model from Sydney Chapman explained the Sun's corona as a static atmosphere that extended well past earth's orbit (Chapman, 1957). It was Eugene Parker who suggested that Biermann's continuous flux of solar particles was Chapman's extended solar atmosphere expanding away in space as a supersonic flow (Parker, 1958). The solar atmosphere is so hot, even at large distances, that neither gravitational attraction or pressure can confine it, the resulting supersonic flow is known as the solar wind.

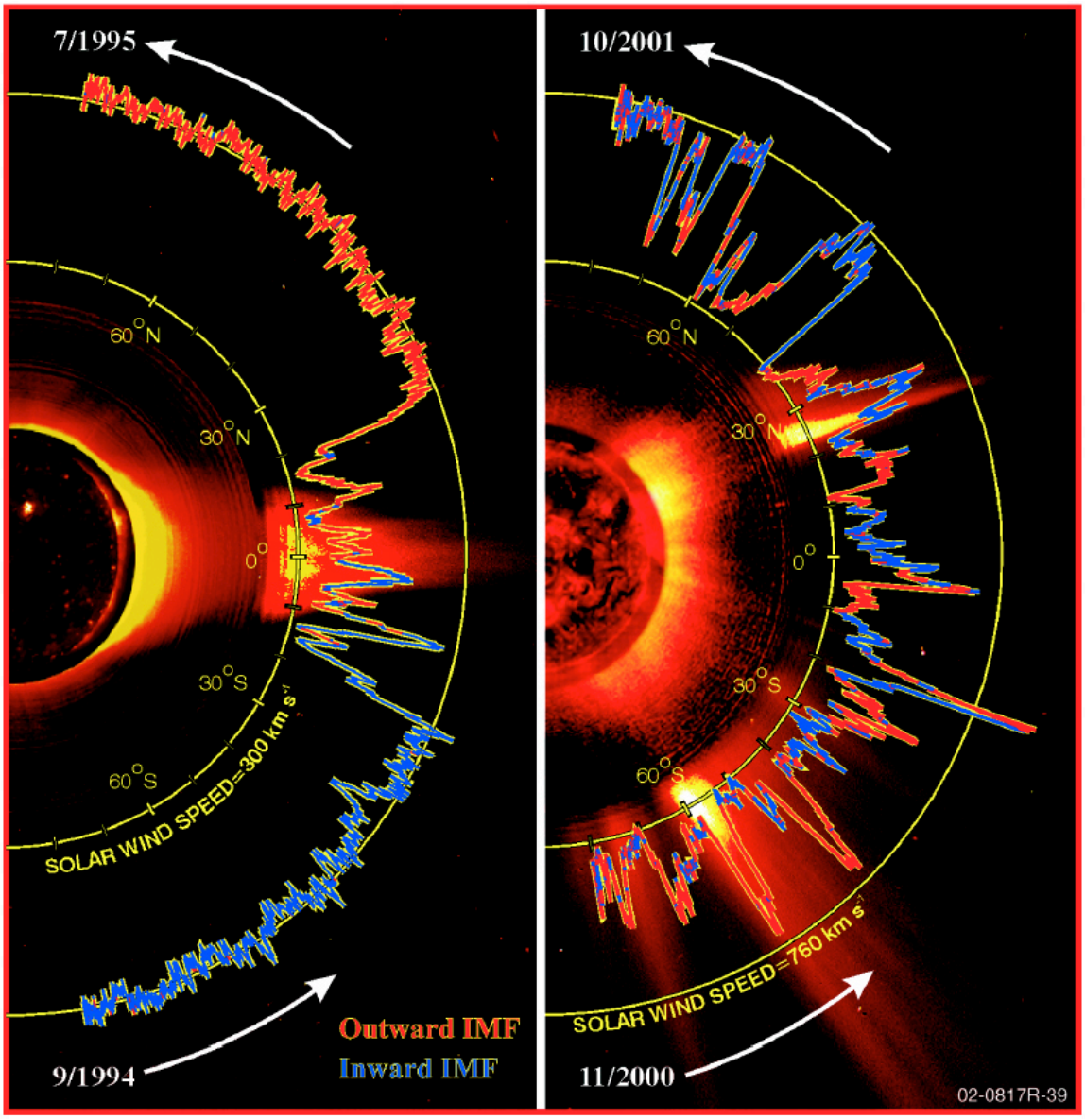

Figure 1.5: The Ulysses spacecraft orbited the Sun at high polar latitudes and tracked the variations of the solar wind speed and magnetic field during a period of solar minimum (left) and solar maximum (right). The active regions during solar maximum cause complex variations in the magnetic field and solar wind.

The solar wind blows approximately radially at an average velocity of ~450 km/s (Figure 1.5). Comprised of plasma, this wind is composed mostly of electrons and hydrogen ions below 1 keV, as well as contributions from ionized helium (~4%) and trace amounts of heavier elements. It has two typical behaviors termed the slow solar wind

and the fast solar wind. The slow solar wind has a composition similar to that of the corona and an average velocity of about 400 km/s. It has a complex structure and is more variable in intensity than the fast solar wind. The fast solar wind has less structure with a typical velocity of 750 km/s, and it nearly matches the composition of the photosphere. The fast solar wind is thought to originate from coronal holes, which are funnel-like regions of open field lines typically at high latitudes.

The rotation of the Sun and the flow of the solar wind combine to make the geometry of the interplanetary magnetic field (IMF). As the solar wind transports plasma radially outward, the magnetic field is also transported due to the fact that it is frozen into the highly conductive plasma. The energy density of the solar wind is much greater than that of the magnetic field, therefore the magnetic field geometry is greatly altered because it is governed by the state of the solar wind. The magnetic field lines attached to the Sun's surface are thus curved to form an Archimedean spiral, referred to as the Parker spiral (Figure 1.6).

The solar wind continues radially outward in the heliosphere at supersonic velocities until reaching distances at which ram pressure from the interstellar medium slows it down. The resulting shock wave that compresses and strengthens the IMF is known as the termination shock. Recently, the voyager missions passed through the shock between ~75 AU and ~100 AU (Stone et al., 2005), and found its radius to vary with solar activity. The theoretical boundary where the solar wind is stopped by the interstellar medium (heliopause) as well as a turbulent region where the interstellar wind hits the heliosphere (bow shock) are both being investigated by missions such as

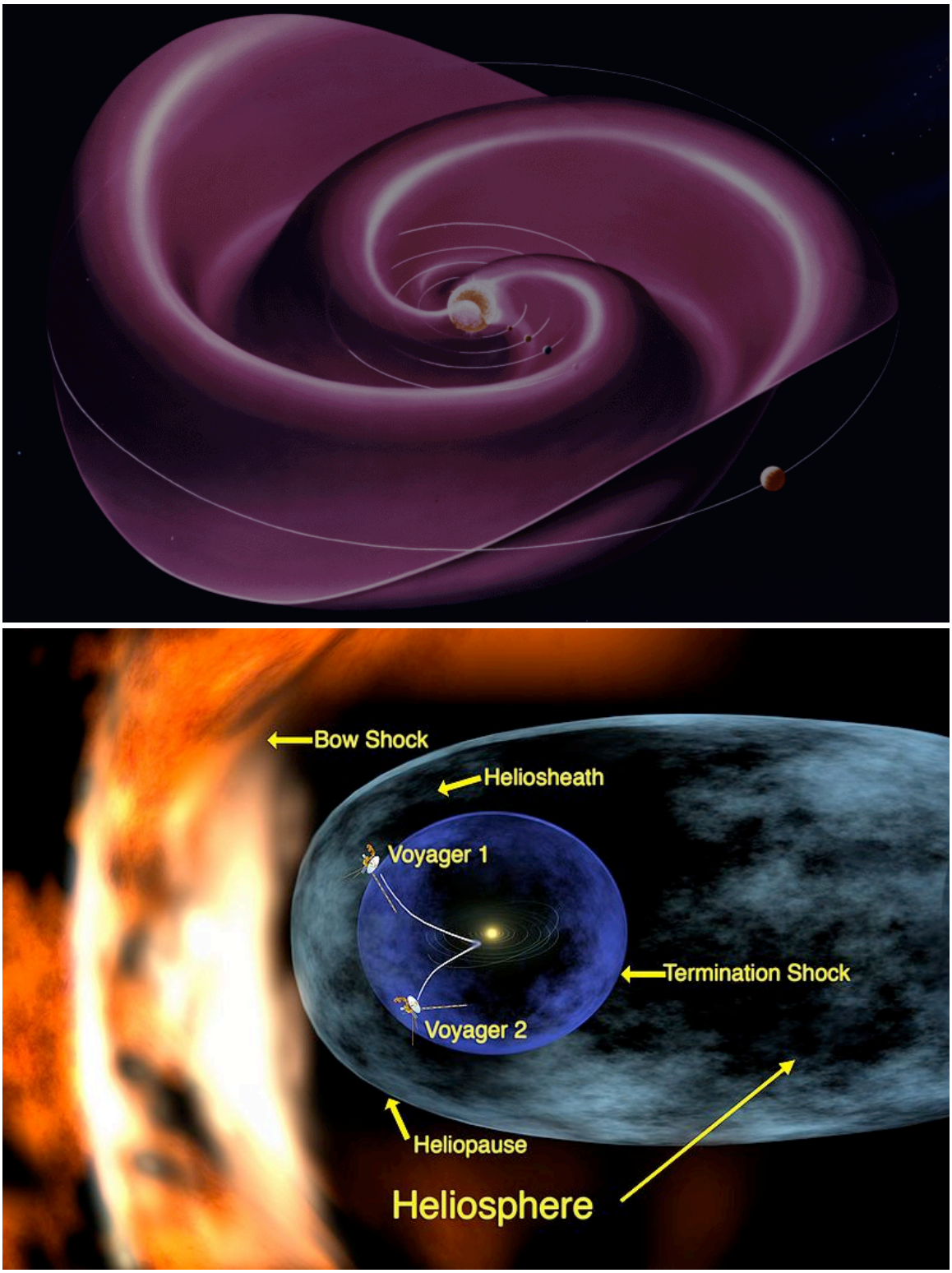

Figure 1.6: (Top) Magnetic field lines from the Sun carried by the solar wind create an Archimedean spiral. The wavy "ballerina skirt" plane defines the neutral current sheet that separates northward and southward solar magnetic field polarities (artist's rendition courtesy of NASA's Werner Heil). (Bottom) The interplanetary magnetic field generated by the Sun's rotation and the solar wind create a region in the interstellar medium known as the heliosphere (artist's rendition courtesy of NASA's Walt Felmer).

Voyager I and II. The NASA Interstellar Boundary Explorer (IBEX) was launched in 2008 to make the first map of the heliosphere and interstellar medium interface (Figure 1.6).

1.4 Solar Flares and Coronal Mass Ejections

1.4.1 Solar Flares

Explosions in the Sun's lower atmosphere that release large amounts of energy are called solar flares. The first observation came in September of 1859 by Richard Carrington. While drawing sunspots he noticed two patches of intense light that appeared and faded within 5 minutes (Carrington, 1860). The Earth's geomagnetic field was disturbed 17 hours later with aurora seen as far south as Cuba. Carrington suggested a possible relationship with the preceding solar activity, an idea first put forth by Sabine (1852). A recent study of ice in Greenland revealed that Carrington's flare was the most powerful of the past 500 years (Battersby, 2005).

In 1908, George Hale observed spectral lines known to change when produced in strong magnetic fields, and concluded that sunspots were intensely magnetic (Hale 1908). That fit nicely with earlier observations of equatorial extensions resembling magnetic field lines (Bigelow 1890), and prominence motion appearing to be influenced by a magnetic field (Deslandres 1894).

Radio Blackouts		
Scale	**GOES Flux (# per cycle)**	**Effects seen at Earth**
R5 (Extreme)	X20 (<1)	Complete HF radio blackout for hours on sunlit side. LF maritime and aviation navigation signals experience outages causing loss in positioning for many hours on sunlit side. Increased satellite navigation errors for several hours on sunlit side and possibly night side.
R4 (Severe)	X10 (~8)	HF radio communication blackout on most of sunlit side for 1-2 hours. LF maritime and aviation navigation signals experience outages for 1-2 hours, minor disruptions in satellite navigation possible.
R3 (Strong)	X1 (~175)	Wide area blackout of HF radio communication for ~hours, LF navigation signals degraded for ~hours.
R2 (Moderate	M5 (~350)	Limited blackout of HF on sunlit side, LF navigation signals degraded for ~tens of minutes.
R1 (Minor)	M1 (~2000)	Weak degradation of HF radio, LF navigation signals degraded for brief intervals.

Table 1.1: Severity of radio blackouts from increases in X-ray intensity due to solar flares. Thousands of M1 flares occur on the Sun during each 11-year cycle, causing negligible effects. Extreme events occur much less often, but the effects greatly impact communication on the Earth. (Courtesy of NOAA Space Weather Prediction Center)

The connection between solar flares and intense magnetic fields found in active regions has been established for roughly a century. However, an understanding of what may be taking place in these events is just evolving. The basic picture consists of restructuring the local magnetic field in the active region. As the magnetic field lines reconnect the energy is deposited into the solar flare (Forbes, 2000).

Solar flares are classified optically in terms of the maximum brightness in H-alpha as well as their coverage on the solar disk. The brightness is assigned a

designation of F, N, or B corresponding to faint, normal or brilliant, while a numerical value from 0-4 (a value of 4 indicates >24.8 square degrees of coverage) indicates the area of coverage. Solar flares are also ranked logarithmically in X-rays according to the peak flux of 1-8 Angstrom (10^{-10} m) photons in units of W/m^2 aboard the Geostationary Operational Environmental Satellite (GOES). The magnitude of intensity is assigned one of the following classes, in ascending order, of A, B, C, M or X. Each class represents a decade in peak intensity, within which is a linear scale from 1-9 (X1 corresponds to 10^{-4} W/m^2). The more powerful M and X class flares often affect conditions in the Earth's magnetosphere (Table 1.1).

There is no certain indication that an active region on the Sun will produce a flare, however there are properties of sunspots and active regions that correlate with flares. Thus, predictions of GOES M and X class flares are given in terms of probabilities with 24 or 48 hours notice by the U.S. National Oceanic and Atmospheric Administration (NOAA).

1.4.2 Coronal Mass Ejections

In the 1930s, Chapman and Ferraro proposed an intermittent solar wind that only occurred during active times (Chapman, 1919; Chapman and Ferraro, 1931a, 1931b, 1932, 1933). This quantitative model described the impact of a cloud of ionized gas upon the Earth's geomagnetic field. Additional observations of solar flares were made in the following years (Hale 1931; Newton 1940, 1943), however they were not all associated

with a succeeding geomagnetic disturbance at the earth. Although it was suggested that the geomagnetic storms accompanying solar flares were caused by streams of plasma interacting with the Earth's magnetic field (Hale 1931, Chapman 1950), it would be decades before the phenomenon was seen in Thompson scattered white light.

The transient disturbances that link flares on the Sun to the geomagnetic storms at the earth were first viewed by the Seventh Orbiting Solar Observatory (OSO-7) coronagraph (Tousey et al., 1973; Figure 7). Additional observations aboard the Skylab spacecraft measured the speeds from <100 to >1200 km/s, which strongly indicated that the higher speed "plasma clouds", or CMEs, could produce the solar wind flows responsible for geomagnetic storms (Gosling et al. 1974, 1976). The achievements of OSO-7 and Skylab would contribute to a new view on how particles are accelerated up to high energies, leading to successive missions such as the Solar Maximum Mission (SMM) launched in 1980, as well as the Yohkoh (Japanese for "Sunbeam") and Solar and Heliospheric Observatory (SOHO) spacecrafts launched in the 1990s.

CMEs are generally believed to originate from the eruption of a prominence or filament, or high speed ejecta from a coronal hole. Initially closed magnetic field lines that are frozen into the ejected plasma are stretched out into the corona. When the magnetic instabilities reach a critical point the field lines reconnect close to the surface, driving the ejected mass outwards via the Lorentz force. CMEs can eject more than 10^{13} kg of mass at speeds in excess of 2000 km/s. These numbers correspond to a kinetic energy release of over 4×10^{32} ergs to simply lift the material out of the Sun's gravitational field. A typical high speed CME will consist of shock front at the leading

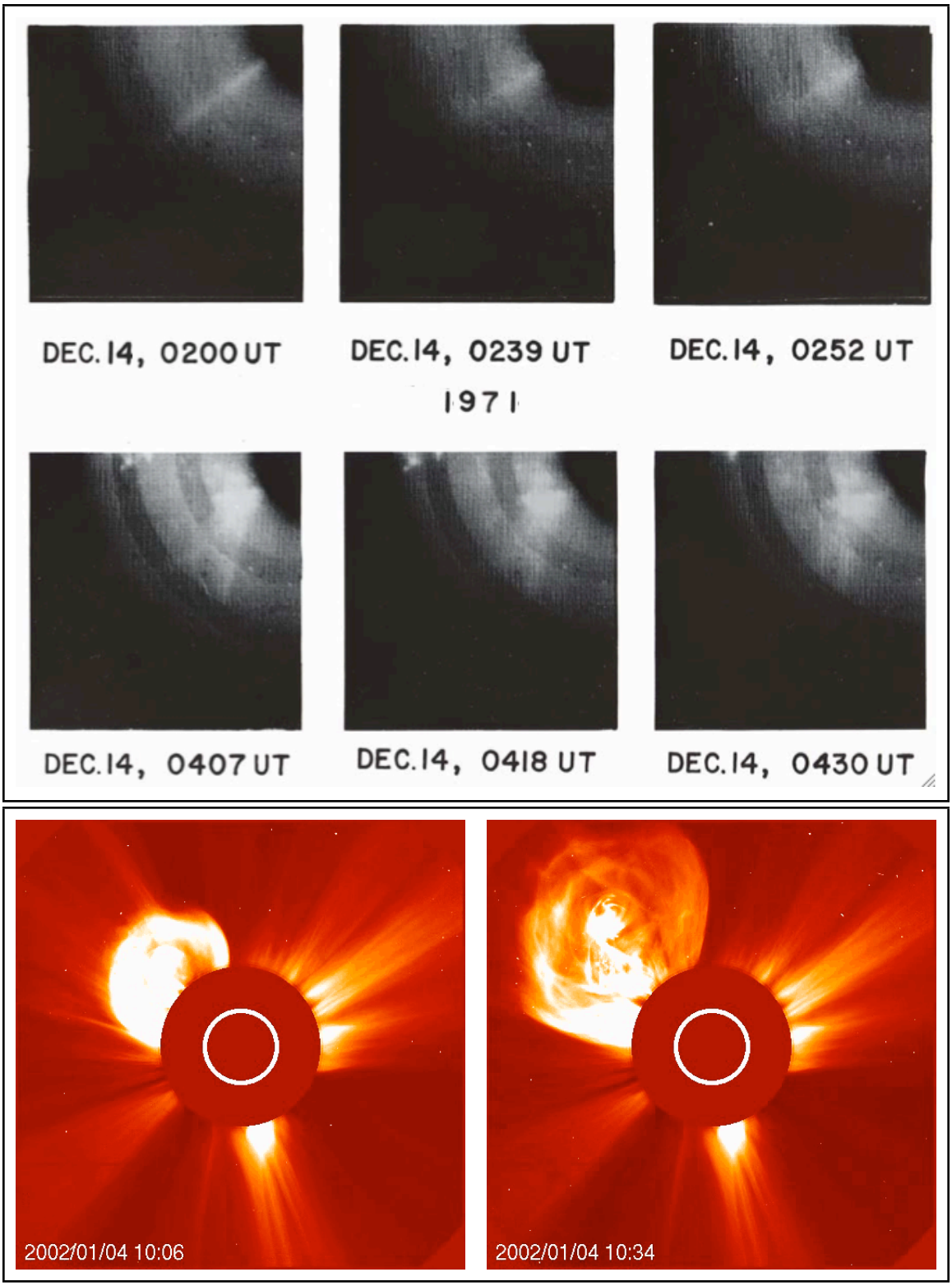

Figure 1.7: (Top) The first images of a coronal mass ejection by Tousey (1973). Images are corrected for a variety of effects including background light from stars, planets, and interplanetary dust. Modern images, such as from SOHO/LASCO (bottom) are vastly improved over those from early experiments.

Geomagnetic Storms		
Scale	**K_p values (# per cycle)**	**Effects seen at Earth**
G5 (Extreme)	9 (~4)	Widespread voltage control problems, some grid systems may experience complete collapse or blackouts, spacecrafts may experience extensive surface charging and problems with orientation, HF radio blackout in many areas for one to two days, satellite navigation degraded for days, LF radio navigation out for hours, aurora can be been seen as low as Florida.
G4 (Severe)	8 (~100)	Voltage control problems, spacecrafts may experience some surface charging, tracking problems, and orientation problems, HF radio sporadic, satellite navigation degraded for hours, aurora can been seen as low as Alabama.
G3 (Strong)	7 (~200)	Voltage and spacecraft corrections may be required, LF radio navigation problems, intermittent satellite navigation problems, aurora can be seen as low as Illinois.
G2 (Moderate	6 (~600)	Voltage outages possible in high-latitude power systems, corrections to spacecraft by ground control, aurora can be seen as low as New York.
G1 (Minor)	5 (~1700)	Minor impacts on power grids and satellite operations, aurora can be seen as low as Maine.

Table 1.2: Severity of geomagnetic storms caused by passing coronal mass ejections. The coronal mass ejection that impacted Earth on March 13, 1989 collapsed the Hydro-Québec power grid in seconds, leaving over 6 million people without power and causing significant economic loss. (Courtesy of NOAA Space Weather Prediction Center)

edge, a cavity behind the shock front, and a core of plasma (bottom-left image in Figure 1.7) . The angular extent of CMEs that produce solar energetic particle events is large (up to ~180°).

The geomagnetic disturbances that often follow large solar flares are caused by CMEs as they impact the Earth's magnetosphere (see section 3.1). As the CME propagates outward it compresses (strengthens) the IMF at its leading edge. As it washes over the Earth, the increased magnetic field intensity rearranges the geometry of the Earth's magnetic field causing geomagnetic storms. The severity of these storms can range from minor disturbances in satellite operation to widespread ground-level electrical failures and power outages (Table 1.2).

1.5 Solar Energetic Particles

Electrons, protons, and ions are accelerated to MeV and GeV energies by solar processes and are called solar energetic particles (SEPs). Although CMEs are the largest processes that take place near the Sun, their existence was unknown until the 1970s, much later than evidence for SEPs. The timeline of these discoveries led to an inaccurate view of the respective roles played by flares and CMEs, a view that is only beginning to realign today.

SEPs above one GeV originating from the Sun were first reported by Scott E. Forbush in 1946. He discovered three "obviously unusual increases" in the Cheltenham, Maryland Compton-Bennett ionization chamber data from 1942-1946, and correctly concluded that they had been caused by charged particles emitted from the Sun (Forbush, 1946). In addition, the charged particles must have had sufficient energy to penetrate the

Earth's magnetic field to be detected at ground-level (~a few GeV, as opposed to ~tens of MeV for geomagnetic storm particles), leading to the term "solar cosmic rays (SCRs)". The computed maximum energy of the protons for the 1946 July 25 event was 7.3 GeV (Forbush et al.,1949).

In the early 1950s, neutron monitors (NMs) were placed at locations throughout the world (Simpson, 2000). One of the goals for these instruments was to measure the relativistic particles, *i.e.*, SCRs, discovered by Forbush. The 1956 February 23 event would be the first ground-level enhancement (GLE) detected by NMs, and is still the largest GLE ever recorded (see section 3.2.2). Using NM data, the Chicago group (Meyer et al., 1956; Lüst and Simpson, 1957) concluded that the 1956 February 23 GLE was due to particles accelerated at or near the Sun. The analysis of the particle flux revealed that only the solar magnetic field was capable of achieving the >15 GeV energies detected (Parker, 1957). Solar flares and CMEs both derive their energy from the same solar magnetic field, however only flares were known to exist before the 1970s.

Over the next decades many large SEP events (>10 MeV) were observed, some of which produced GLEs (>1 GeV). Most of these events were associated with large solar flares, however the prompt arrival of SCRs was generally restricted to flare events occurring in the western solar hemisphere (see section 3.2.2) where the Earth would be magnetically well-connected to the flare site through the Parker spiral (east/west on the Sun are in Earth-based coordinates). Since the flare was the only observable feature that was correlated with these events, it was generally believed to be the origin of the SCRs.

The early picture of SEPs consisted of acceleration directly above the flare site with the energy being derived from the strong magnetic fields in the flaring region (Gosling, 1993). Diffusive transport from the flare site to a field line connected to Earth, as modeled by Gleeson and Axford (1967), accounted for the delays in GLE onset times which were observed when the flare region was not magnetically well-connected. This simple model worked well showing prompt rises-to-maximum for flares originating on the western solar hemisphere, and slow rises-to-maximum for flares originating on the eastern solar hemisphere. Flare acceleration and diffusive transport remained as the accepted source of all SEP events for many years.

1.5.1 Impulsive vs. Gradual Events

In 1977, X-ray events were separated into classes using Skylab measurements (Pallavicini et al., 1977). One class consisted of compact flares of short duration with smaller volume and faster rise/decay times (impulsive), and another comprised of larger volume, longer duration events with longer rise/decay times (gradual), the latter being associated with CMEs (Sheeley et al., 1975). Kahler et al. (1978, 1984, 1987) found a high correlation (96%) between large SEP events and CMEs. Different proton/electron ratios in the SEPs associated with the two classes of X-ray events were found by Cane et al. (1986). Although the classification of SEP events (impulsive vs. gradual) originally came from the X-ray time-scale, they are more accurately determined by the intensity vs. time profiles of the SEPs themselves (Figure 1.8).

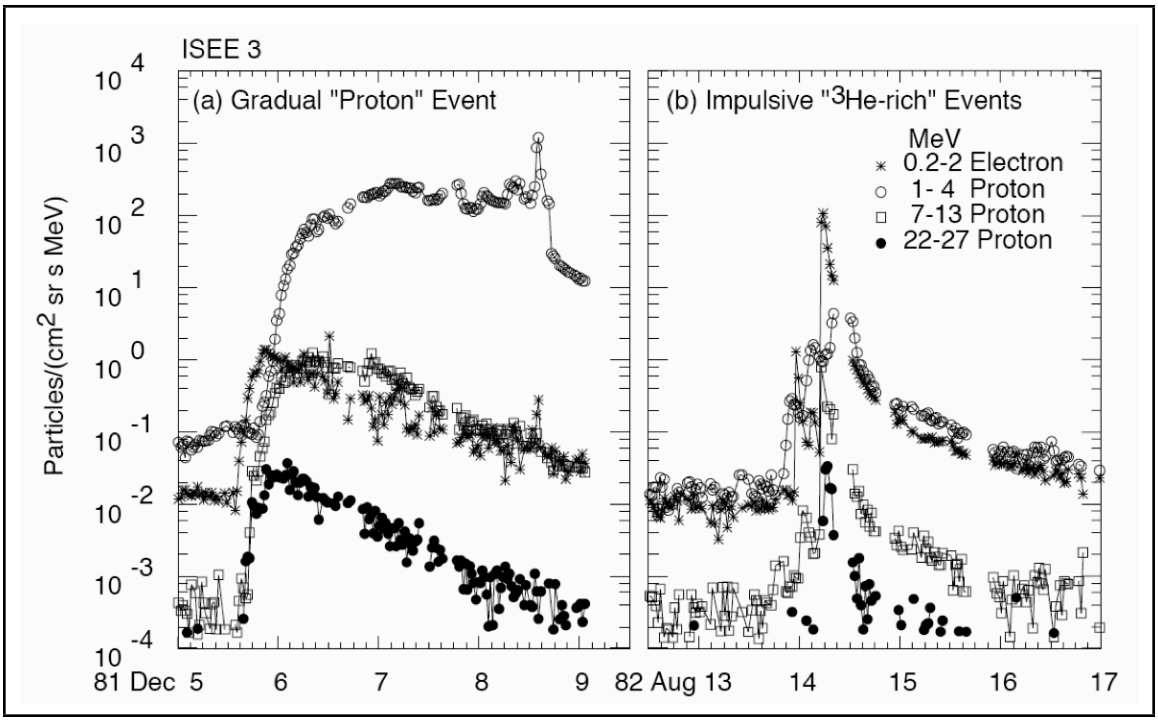

Figure 1.8: Intensity-time profiles of electrons and protons in (a) gradual and (b) impulsive SEP events. Efficient particle acceleration at shock fronts is on the order of days for gradual events, while impulsive events typically have a short-lived burst with a fast decay. (Reames, 1999)

Ionization states of energetic ions in gradual and impulsive events were measured by Luhn et al. (1984, 1987). In gradual events no element above He was fully ionized and the charge state of Fe was 14 ± 1 (in agreement with the results of Tylka et al., 1995), indicating source material with an electron temperature of ~2 × 10^6 K, typical of the corona. In impulsive ^{3}He-rich events all elements through Si were fully ionized and the charge state of Fe was 20.5 ± 1.2, typical of flare-heated material at temperatures of ~10^7 K. Previous work by Hsieh and Simpson (1970) had found some small SEP events with greatly enhanced abundances of the rare isotope ^{3}He. These events were found to have ~1,000-fold enhancements in ^{3}He/^{4}He and ~10-fold enhancements in Fe/O relative to coronal abundances typically found in large SEP events (Mason et al., 1984; Meyer, 1985). Abundance measurements, SEP intensity profiles, and coronagraph images are

some of the modern measurements used to discern if SEP events are impulsive (flare accelerated) or gradual (coronal shock accelerated).

Impulsive events are generally believed to be caused by restructuring magnetic field lines and turbulent wave motions deep in the solar atmosphere where spatial scales and time scales are small, just like flares. Enhancements in electron-to-ion ratios, heavy ions, and ^{3}He relative to coronal values indicate the source material is of a flare origin. They typically exhibit initial sharp peaks in SEP fluxes, but overall fluxes are smaller compared to gradual events and occur over shorter time scales. The SEP intensity vs. time profiles for the "pure" impulsive event on 1982 August 14 are shown in Figure 1.8 (this event is pure because there is no accompanying CME). Impulsive events are dominated by electrons, and the duration of the time profiles is determined by scattering of particles in interplanetary space. The longitudinal distribution of impulsive events is also smaller compared to gradual events. To be observed at Earth, charged particles must

Characteristic	**Impulsive (Flare Acceleration)**	**Gradual (Shock Acceleration)**
Population	electron-rich	proton-rich
Duration	minutes/hours	days
CME	rare	always
Metric Type II	rare	always
^{3}He/^{4}He	~1	~0.0005
H/He	~10	~100
Fe/O	~1	~0.1
Q_{Fe}	~20	~14
Volume	10^{26}-10^{27} cm^3	10^{28}-10^{29} cm^3
Longitudinal Distribution	<60°	~180°
Energy Density	High	Low
Event Frequency (Solar Max)	~1,000 per year	~10 per year

Table 1.3: Different features and compositions observed in impulsive and gradual SEP events.

Solar Radiation Storms		
Scale	**>10 MeV Flux (# per cycle)**	**Effects seen at Earth**
S5 (Extreme)	10^5 (<1)	Unavoidable radiation hazard to astronauts, aircraft passengers exposed to radiation risk, satellites useless with damage possibilities, complete HF blackout, navigation operations difficult.
S4 (Severe)	10^4 (~3)	Unavoidable radiation hazard to astronauts, aircraft passengers may be exposed to radiation risk, satellites experience operational problems, partial HF blackout, increased navigation errors.
S3 (Strong)	10^3 (~10)	Radiation hazard avoidance recommended to astronauts, aircraft passengers may be exposed to radiation risk, satellites may experience noise, HF radio degraded, possible navigation errors.
S2 (Moderate	10^2 (~25)	Aircraft passengers may be exposed to radiation risk, possible navigation errors at polar cap locations.
S1 (Minor)	10 (~50)	Minor impacts on HF radio in polar regions.

Table 1.4: Effects of solar radiation storms near the Earth. In addition to astronaut and aircraft passenger safety hazards, extreme and severe storms can affect and possibly damage satellite operations. (Courtesy of NOAA Space Weather Prediction Center)

be magnetically well-connected and thus originate at western solar longitudes, again implying a point-like origin low in the solar atmosphere such as in a solar flare.

Gradual events are associated with fast CMEs (>500 km/s and sometimes exceeding 2,000 km/s) that accelerate particles for a long time in a coronal shock wave (Mason et al., 1984; Lockwood et al., 1999; Reames, 1999). Most of the major SEP events are gradual and are associated with GLEs observed by instruments such as NMs. Spacecraft measurements by Meyer (1985) revealed that SEP abundance ratios in gradual events were similar to those in the corona and solar wind (Mason et al., 1984). In

addition, SEP ionization states measured by Luhn et al. (1984, 1987) were similar to those at various regions of the corona and the solar wind (Feldman et al. 1981). These findings indicate that the acceleration mechanism was likely taking place at higher solar altitudes removed from the flare site, such as in a CME-driven shock.

Protons are dominant in gradual events, and increases in fluxes generally last for days. Intensity vs. time profiles for the "pure" gradual event on 1981 December 5 are shown in Figure 1.8 (this event is pure because it is associated with an erupting filament (Kahler, 1986), without an accompanying solar flare). Charged particles are efficiently accelerated by the CME-driven shock front as it propagates radially outward to 1 AU, the peak in intensity 3 days later is from the shock passing the earth. The longitudinal distribution for gradual events is nearly uniform across the face of the Sun, suggesting that a shock wave can easily move across field lines while continuing to accelerate particles.

1.5.2 Shock Acceleration

In 1955 Thomas Gold suggested that high speed plasma ejected from the Sun would produce a collisionless shock as it forced its way outward into interplanetary space (Gold, 1955), evidence by spacecraft would come in 1968 by Gosling et al. (1968). CME speeds close to the sun were found to reach >2,000 km/s (Sheeley et al., 1985; Kahler, 1994), well in excess of the ambient solar wind, and capable of driving such shock waves (Cane et al., 1987). Type II radio bursts first observed by Wild et al. (1963),

associated with plasma emission from shock waves, were observed in coincidence with fast CMEs (Stewart et al., 1982; Gary et al., 1984; Gergely et al., 1984). Combined observations by coronagraphs and in-situ measurements made by spacecraft off the limbs of the Sun (Schwenn, 1983; Sheeley et al., 1985; Lindsay et al., 1999) or near the Earth (Webb et al., 2000) show a clear association between CMEs and the subsequent detection of shocks and the related ejected material.

A coronal shock created by the leading-edge of a fast CME will produce magnetic turbulence between regions of upstream and downstream plasma speeds. Particles are accelerated by scattering back and forth across the shock similar to a ping pong ball bouncing between two converging paddles, this process is called diffusive shock acceleration. High energies are achieved when traversing the shock many times, requiring efficient scattering such as in higher density regions with increased turbulence. When the magnetic field is quasi-parallel to the shock normal, the converging flow of scattering centers will cause charged particles to gain velocity each time they traverse the shock. Particles can gain additional energy when the magnetic field is quasi-perpendicular to the shock normal by drifting in the $\mathbf{V_{shock}} \times \mathbf{B}$ electric field at the shock (Decker and Vlahos, 1986a, 1986b), this process is called shock-drift acceleration. A magnetic field configuration that is quasi-perpendicular to the shock normal can increase the maximum attainable energy and decrease the acceleration time because the diffusion coefficient may be much smaller, allowing particles to diffuse fast enough to encounter the shock many more times (Jokipii, 1987).

Coronal shocks will accelerate any charged particle that can be scattered and traverse the shock front, including those from the tail of the thermal distribution of the local plasma (~10 eV), to those from remnants of previous activity at higher energies (~1-100 MeV). The particle population that is swept up and accelerated by the coronal shock is called a seed population. This concept is important because it is easier to accelerate a 10 MeV proton to 1 GeV than to accelerate a 1 keV proton to 1 GeV. A coronal shock model calculated by Lee and Ryan (1986) addresses this relationship and computes the necessary amount of time for particles of different injection energies to reach desired maximum energies (in this model a proton with an injected energy of 10 MeV would reach 1 GeV in ~5 minutes).

The spectrum and timing of the protons accelerated and released by a coronal shock is influenced by several factors. These include the strength of the shock, its speed, the diffusion coefficient up- and downstream of the shock and its radius when it releases the protons into interplanetary space. These factors manifest themselves in a characteristic spectral shape, *i.e.*, a steepening at the highest energies. Arguably, the best measure of these parameters is obtained during the anisotropic phase of a GLE, where the relativistic particles travel to Earth with little or no modification by interplanetary processes.

The proton spectrum is also linked to the duration of the GLE. At lower energies (below a few tens of MeV/nucleon) the protons and ions detected at Earth can be intense for days, whereas relativistic protons (>1 GeV) may only be enhanced for hours or even minutes. Recent modeling of GeV shock acceleration replicates the transient nature of

the GLE (Lee, 2005; Zank et al., 2000). The phenomenon results from (1) the requirements of setting up the shock close to the Sun, (2) maintaining sufficient shock strength to accelerate particles to high energies, (3) maintaining a sufficient level of upstream turbulence to retain the particles for acceleration and (4) a dissipation of the same upstream turbulence that releases the GeV particles to be detected at Earth, if well-connected. Thus, a careful study of the evolution of the intensity, spectrum and pitch-angle distribution is necessary to properly investigate the nature of the accelerating shock and the conditions in the inner heliosphere.

1.5.3 A Brief Summary of Solar Energetic Particles

The strong, complex magnetic fields located in active regions on the Sun lead to solar flares and CMEs. Particles are accelerated by both processes. Impulsive (short-term) events have particle compositions and charge states similar to those of the flaring region. Gradual (long-term) events have particle compositions and charge states that reflect those in the higher corona, and are associated with CMEs.

CMEs can reach speeds in excess of 2,000 km/s, overtaking the existing solar wind speed of ~450 km/s and producing a shock wave. Particles are accelerated by scattering back and forth across the shock and drifting in the $\mathbf{V_{shock}} \times \mathbf{B}$ electric field at the shock. In this model, the physical parameters of the CME determine the maximum energy and injection time of the SEPs. As charged particles escape into interplanetary

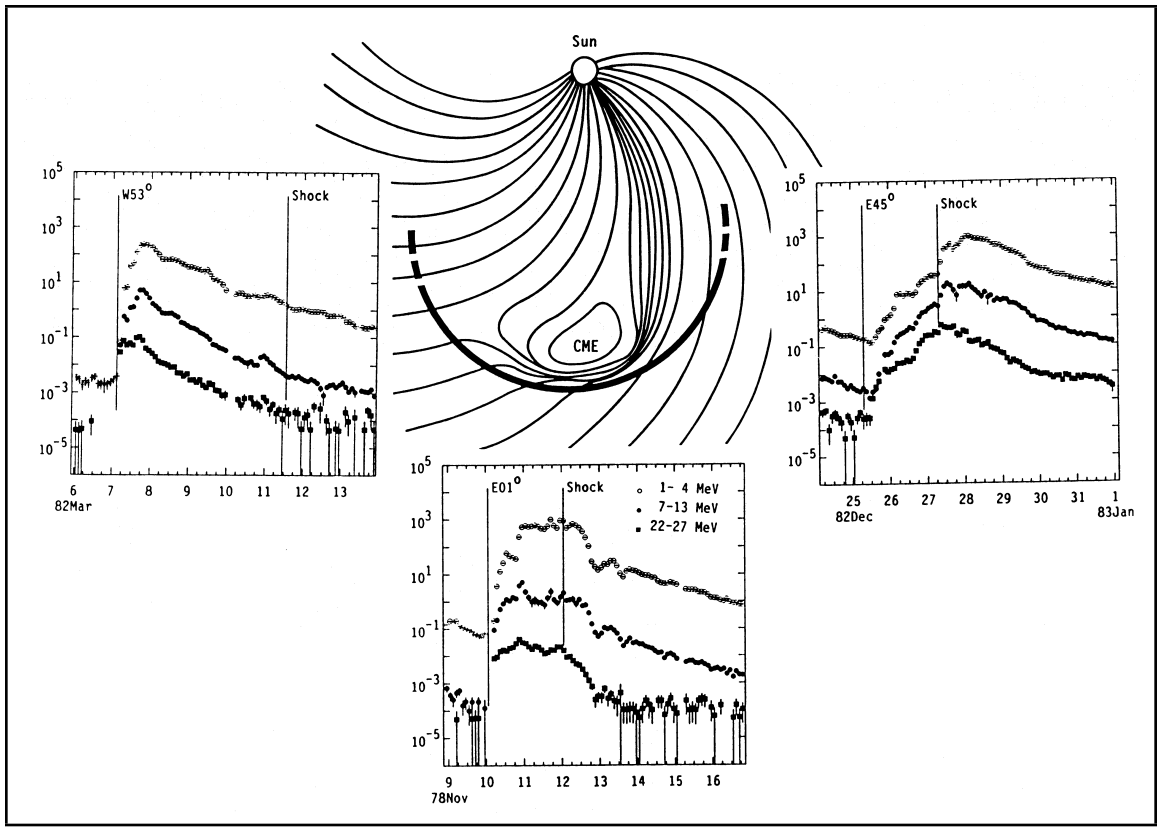

Figure 1.9: Intensity vs. time profiles for protons of different energies for observers viewing a coronal mass ejection from the western solar limb (left), central meridian (middle), and eastern solar limb (right). The charged particles propagating along the Parker spiral will have prompt increases in intensity if initially well-connected to the observer. (Reames, 1999)

space they travel along the magnetic field lines of the Parker spiral resulting from the Sun's rotation and the solar wind (Figure 1.9).

Spacecraft at 1 AU (1 AU is the Sun-Earth distance = 1.495×10^{11} m) detect SEPs up to energies of a few hundred MeV. The largest SEP events can accelerate particles up to relativistic energies (>1 GeV), producing increases in ground-level cosmic ray intensity (GLEs) measured by instruments such as NMs. Traveling at >95% the speed of light, these SCRs arrive at Earth promptly and can provide information on the acceleration region and nature of the coronal shock.

In the chapters ahead, cosmic-ray detectors such as neutron monitors and the Milagro water Čerenkov detector will be described, beginning with a discussion on cosmic rays. Finally, the results and analysis of the 2001 April 15 and 2005 January 20 GLEs using these instruments will be presented.

Chapter 2

Cosmic Rays and Air Showers

Cosmic rays are energetic particles that originate from inside and outside the Solar System. These cosmic rays interact with atmospheric molecules to produce cascades of secondary particles which in turn lead to further cascades, this process is known as an air shower. Multiple components of an air shower penetrate to ground-level where they can be detected.

2.1 Cosmic Rays

On August 7, 1912, Victor Hess measured the ionization of the atmosphere as a function of altitude by carrying three electroscopes in a balloon gondola. He concluded that the ionization was coming from "above" and was possibly of extra-terrestrial origin (Hess, 1912). The term "cosmic radiation" was coined by Millikan in 1925. Experiments at various latitudes by Clay (1927) and longitudes by Johnson (1933) verified that the Earth's magnetic field affected the intensity of the radiation and, thus, that the primary particles are charged. The experiments of Bradt and Peters (1948) revealed that the primary component is comprised not only of protons, but also of a small

fraction of completely stripped nuclei. The current understanding of cosmic rays and their detection followed from these early discoveries.

2.1.1 Composition and Spectrum

Usually the term "cosmic rays" refers to galactic cosmic rays (GCRs). GCRs consist almost entirely of relativistic atomic nuclei stripped of their electrons, the remaining ~1% are electrons and positrons. Of the nuclei, about 90% are protons, ~9% are helium nuclei, and less than 1% are heavier elements. All stable nuclei through uranium (Z=92) are present in GCRs, including some long-lived radioactive nuclei.

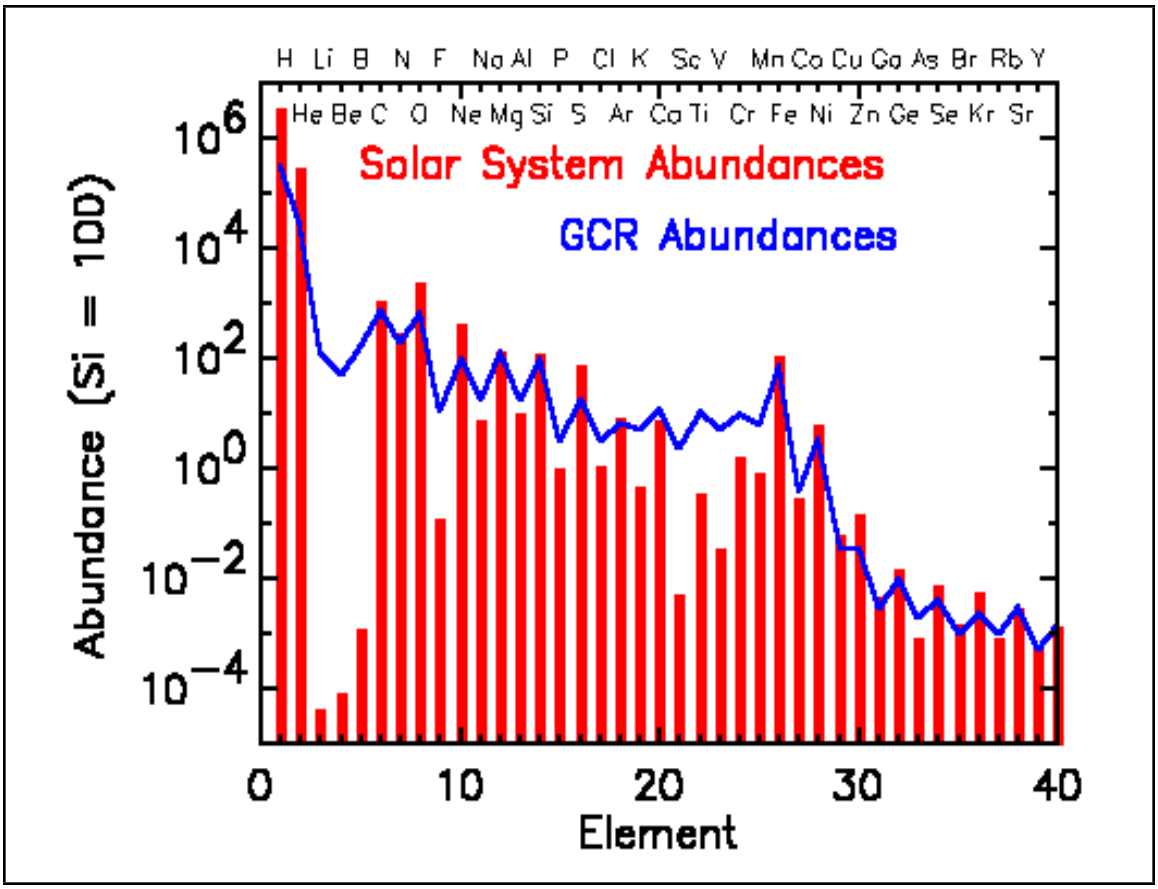

Figure 2.1: Comparison of observed cosmic ray and Solar System abundances, normalized to Silicon.

Chemical abundances of GCR nuclei reveal a strong correlation with Solar System abundances, but with some significant differences (Figure 2.1). The even-odd effect is a universal property of all nuclei that results from nucleosynthesis in dying stars. The most tightly bound nucleus is Fe-56 (Z=26), and marks the endpoint of stellar nucleosynthesis. The abundances of heavier elements decline rapidly thereafter. The abundances of the light elements Li, Be, and B in GCRs are roughly a million times that of their Solar System abundances, and the elements immediately below iron are also elevated by several orders of magnitude.

The energies of GCRs detected at Earth extend from ~100 MeV/nucleon up through $>10^{17}$ eV (the highest manmade energies for protons are $\sim 10^{13}$ eV by the Large Hadron Collider at CERN). The differential cosmic ray spectrum is shown in Figure 2.2.

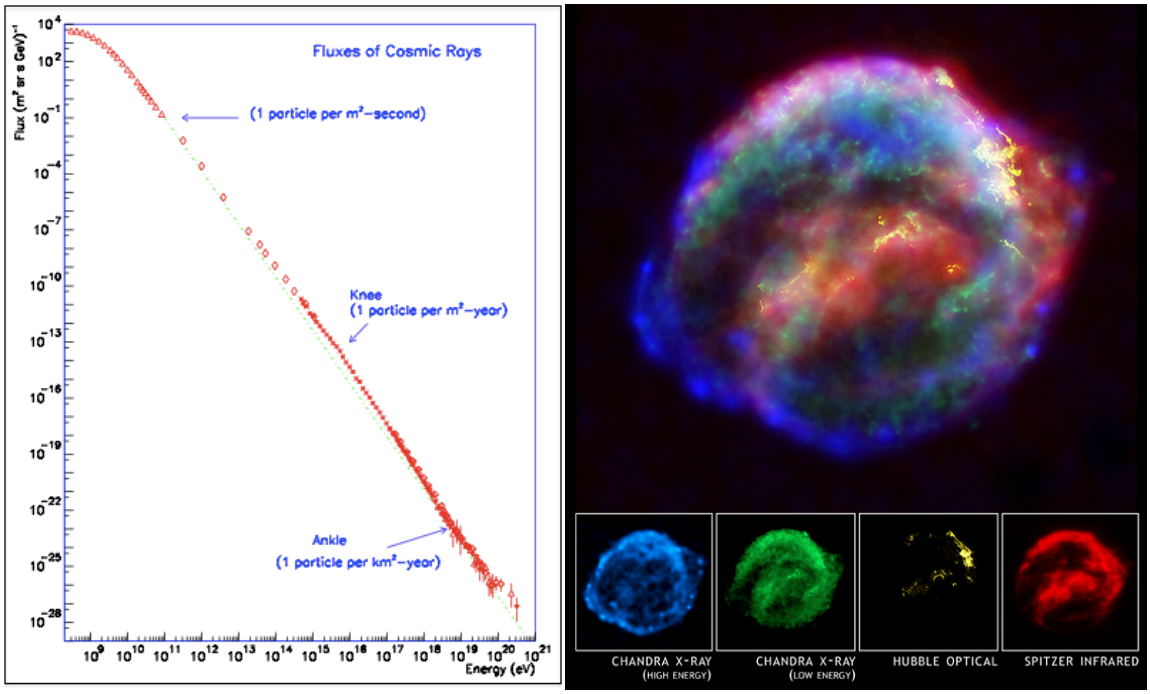

Figure 2.2: The dominant contribution to the cosmic ray spectrum (left) comes from supernova remnants. Kepler's supernova (right) is viewed in multiple bands of the electromagnetic spectrum with three NASA observatories. Expanding shock fronts in supernova remnants can accelerate particles up to energies of $\sim 10^{17}$ GeV.

Between 10^{10} eV and 10^{20} eV the general form of the cosmic ray spectrum is a power law with breaks at approximately 10^{15} eV and $10^{18.5}$ eV. The rollover below a few GeV is an effect of solar modulation, discussed in section 2.1.3. The break at 10^{15} eV is referred to as the knee. This softening of the spectrum is generally attributed to cosmic rays escaping the galaxy due to their gyro-radius becoming comparable to the scale of the galactic disk. At $10^{18.5}$ eV the spectrum appears to harden, this region is referred to as the ankle. At these high energies there are very few particles to detect, given the power-law nature of the spectrum.

2.1.2 Sources and Distribution

The dominant contributor to the cosmic ray spectrum is our own galaxy. Acceleration mechanisms involving fast shocks within supernova remnants can produce GCRs for thousands of years, and are generally used to explain the power law energy spectrum (Figure 2.2). However, this process depends on the strength, speed, and duration of the shock, and therefore has a maximum energy of ~10^{17} eV (Zirakashvili et al., 2007).

Anomalous cosmic rays (ACRs) are interstellar particles that have entered the Solar System unaffected by the magnetic field of the solar wind, been ionized, and then accelerated at the termination shock (a relatively local phenomenon). This component is comprised mainly of elements difficult to ionize, including He, N, O, Ne, and Ar, and are restricted to spacecraft energies (below ~1 GeV). The Sun can also accelerate particles to

GeV energies, however this occurs only a few times per decade, and thus is not a continuous source.

Particles above ~10^{17} eV are referred to as ultra-high-energy cosmic rays (UHECRs). The sources of these particles are unknown, some theories include active galactic nuclei (AGNs), quasars, or gamma-ray bursts (GRBs). UHECRs are thought to originate outside our own galaxy because charged particles above ~10^{15} eV are not trapped by the galactic magnetic field. It is difficult to explain the process of depositing such an extreme amount of energy into a single particle, opening the doors for exotic theories such as dark matter and string theory. An additional complication is that cosmic rays originating further than 50 Mpc from the Earth should interact with the 2.7 K background. This would theoretically lead to an attenuation of the cosmic ray flux above ~5×10^{19} eV known as the GZK cutoff (Greisen, 1966; Zatsepin and Kuzmin, 1966), however observations indicate no such cutoff. Particle detection, and therefore a measurement of the spectrum, above these energies is difficult because cosmic rays above 10^{19} GeV arrive on Earth at a rate of one particle per square kilometer per year.

The angular distribution of GCRs below ~10^{15} eV has a small anisotropy of ~0.1% (Linsley, 1983). This is expected because ions below this energy travel along the magnetic field structure of the galaxy and are subject to multiple scatterings off irregularities in the interstellar field. Extended air shower arrays resolve incident particle directions at higher energies but the small flux does not provide enough statistics for the anisotropy measurements, however the trend does show an increase in anisotropy with increasing energy. A study of the large scale cosmic ray anisotropy by the Milagro

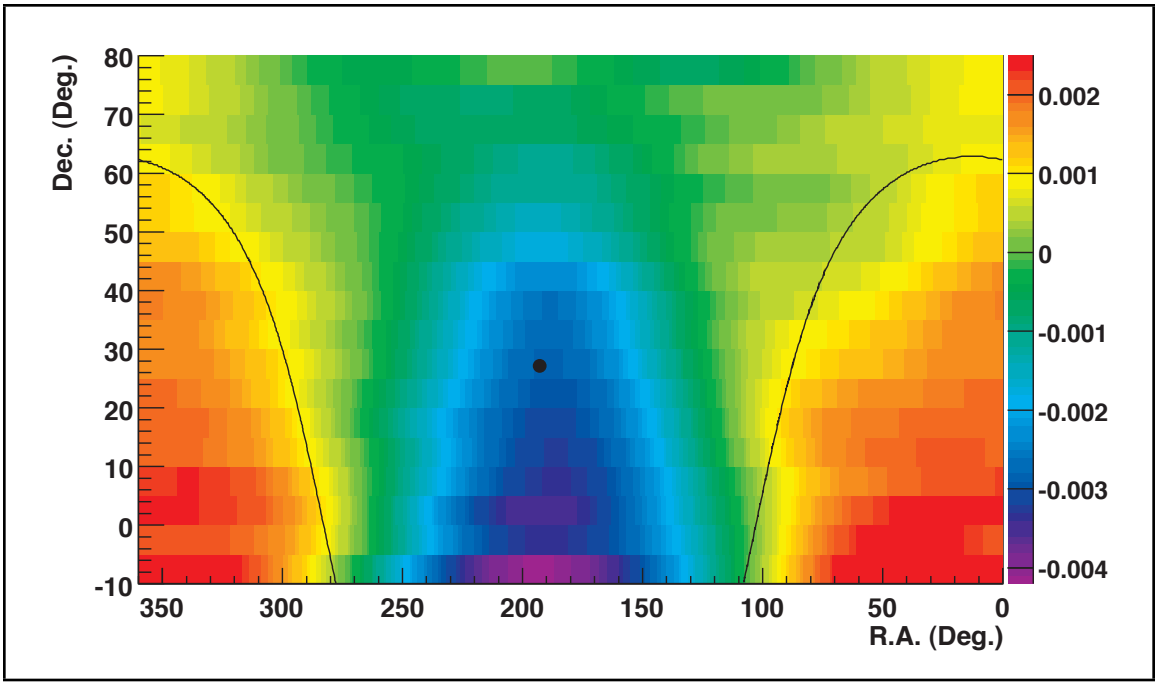

Figure 2.3: Fractional differences of the cosmic ray rates as viewed by Milagro from 2000-2007. The two black lines show the position of the galactic equator and the solid circle shows the position of the galactic north pole. (Abdo et al., 2009)

observatory conducted from 2000-2007 (Figure 2.3) resulted in an anisotropy of 0.1% at a median energy of 6×10^{12} eV (Abdo et al., 2009). A steady increase in the magnitude of the anisotropy was seen over the seven year period.

2.1.3 Solar Modulation of Cosmic Rays

As described in section 1.3, the Sun produces an outward-flowing solar wind carrying a turbulent magnetic field. Lower energy GCRs enter the heliosphere and diffuse inward toward the Sun, gyrating around the IMF and scattering off irregularities. Gradient and curvature drifts convect the GCRs away from the sun (Isenberg and Jokipii,

1979), causing them to suffer energy losses. The combined effect of these processes results in the solar modulation of galactic cosmic rays.

The structure of the IMF varies with solar activity. This, in turn, has an influence on the cosmic ray intensity. When solar activity is at high levels, the IMF structure is highly irregular, further modulating the GCRs and leading to a lower cosmic ray intensity. When solar activity is low the IMF structure is less disrupted and GCRs suffer fewer energy losses in their transport. This leads to a periodic cycle of cosmic ray intensity that is anti-correlated with the 11-year solar cycle (Figure 2.4).

Solar activity can also modulate the cosmic ray intensity on shorter timescales. CMEs are associated with solar activity, and their propagation in the inner heliosphere can distort the magnetic field topology. Dependent on its velocity, a CME typically encounters the Earth anywhere between 18 hours (2,300 km/s) and two days (800 km/s) after liftoff. The magnetic field carried by the plasma within the CME sweeps away some of the low-energy GCRs, resulting in a 3-10% decrease in the cosmic ray intensity over a period of several hours (Figure 2.4). These events are known as Forbush decreases, named after their discoverer Scott E. Forbush (Forbush, 1937). As the CME continues past the Earth a recovery in cosmic ray intensity is observed over several days.

The quickest changes in cosmic ray intensity associated with solar activity are GLEs. The increases over background for these events can be well over 1,000% in some ground-level stations, and can occur within minutes (Figures 5.5, 5.6, 5.10-5.12, 7.1, 7.6, 7.12). More on GLEs will be discussed later.

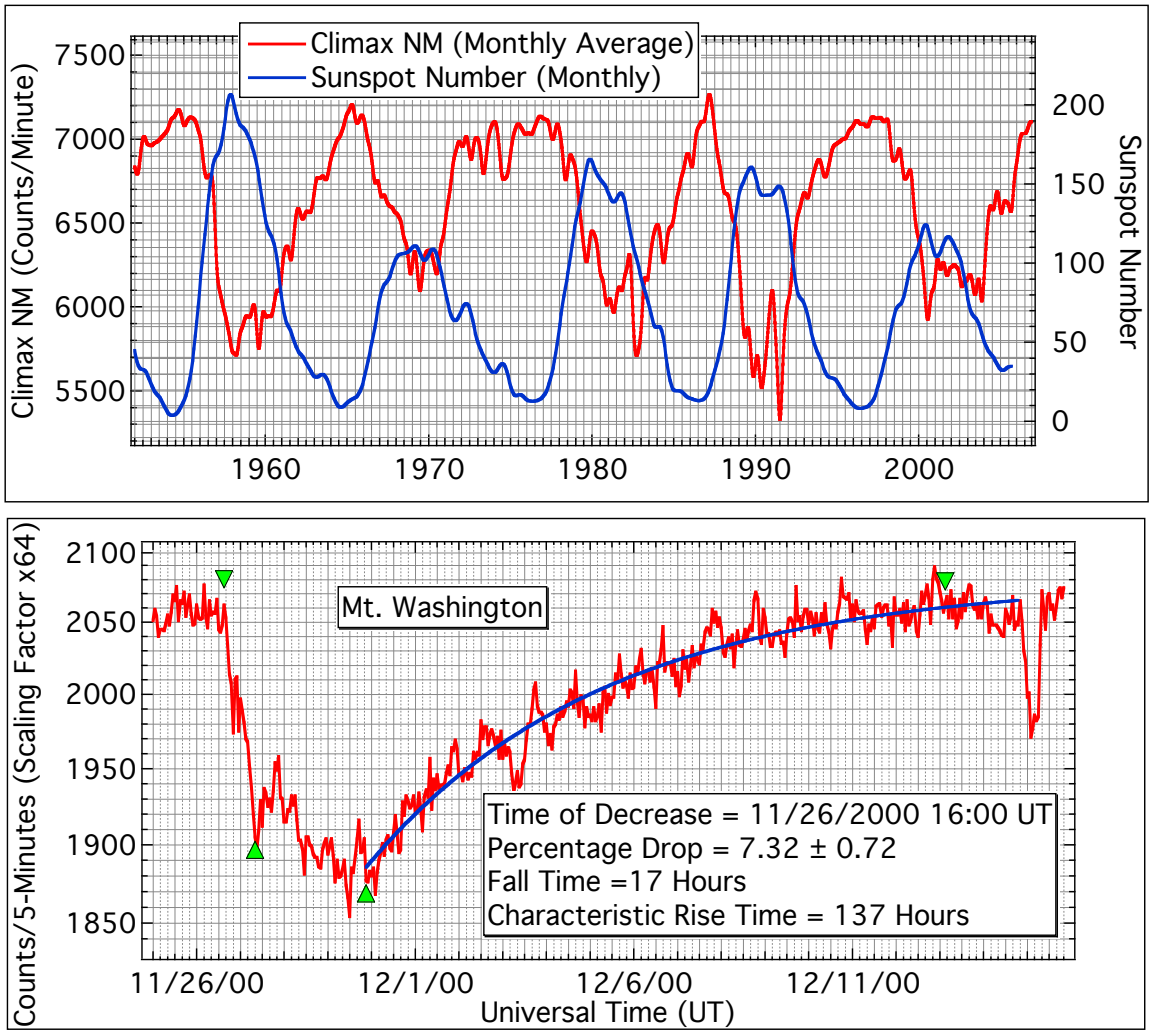

Figure 2.4: Neutron monitors, such as the stations located at Climax, Colorado, and atop Mt. Washington, NH, continuously measure the intensity of the cosmic ray background. (Top) As solar activity increases (visibly observed by the number of sunspots) cosmic rays undergo additional energy losses, the result is a periodic anti-correlation known as the 11-year solar activity cycle. (Bottom) Solar activity can also cause short-term modulation, such as Forbush decreases caused by passing coronal mass ejections.

2.2 Air Showers

Experiments performed at sea-level and mountain altitudes revealed that cosmic rays have a soft component that is easily absorbed in a few mm of lead, and a penetrating component that can pass through several meters of lead and up to great depths underground and in water. Discoveries of new elementary particle species from the

1920s-1940s, notably short-lived pions and muons, solidified the two-component feature of the cosmic radiation.

In 1934, Bruno Rossi found coincidences between multiple counters placed in a horizontal plane and separated by distances too large for these coincidences to be by chance, and noted that "occasionally very extensive groups of particles arrive upon the equipment" (Rossi, 1964). The most systematic early investigation of this phenomenon was by Pierre Auger. His collaboration detected coincidences over a period less than a microsecond in instruments distributed over hundreds of meters at ground-level and correctly concluded that these detected particles were products of high-energy cosmic-ray primaries (Auger et al., 1939).

The overall picture began to develop beginning with a high-energy cosmic ray incident at the top of the atmosphere. Through nuclear collisions, the primary cosmic ray produces multiple secondary components, some of which undergo spontaneous decay, giving rise to other components. This cascade process in the atmosphere is referred to as an air shower. Detection of these air shower particles at ground-level are used to deduce the characteristics of the initiating cosmic ray.

2.2.1 Development in Atmosphere

The atmospheric density decreases exponentially and adiabatically with a scale height of about 7 km. It is useful to define atmospheric depth in units of atmospheric overburden, g/cm^2. When a cosmic ray enters the Earth's atmosphere it interacts strongly

with an air nucleus and produces secondary particles. This takes place at a random atmospheric depth on a statistical basis dependent on the primary particle's mean free path (on average 80 g/cm^2 for a proton with $E_0 \sim 10^{14}$ eV).

This first interaction results in the production of many relativistic particles, the majority of which are pions. Dozens of pions can be produced in a single collision, and depends on the energy of the primary particle. The threshold energy for this process is equivalent to the rest mass of the pion in the center of mass frame. For proton primaries this threshold energy is ~290 MeV. The available energy of the primary particle in the collision is transferred to the production and kinetic energy of the secondary particles, properties of which can be found below in Table 2.1. The production of pions and other particles in nuclear collisions continues to be studied extensively at high-energy colliders such as Jefferson Lab in Virginia and the European Council for Nuclear Research (CERN) in Switzerland.

The primary nucleon initiating the air shower can retain a significant portion of its initial energy and undergo successive nuclear collisions, producing additional high-energy protons and neutrons. The total number of nucleons will reach a maximum at an atmospheric depth dependent on the initial energy of the primary particle (Figure 2.5). The development of these particles constitutes the nucleonic component in air showers.

The neutral pions almost immediately decay into two gamma rays because their mean lifetime is short compared to the intermolecular distance in the upper atmosphere, initiating the electromagnetic or "soft" component of air showers. These photons interact with matter by three processes, the photo-electric effect, Compton scattering, and pair

Particle	Symbol	Mass (MeV)	Mean lifetime (sec)	Decay Modes
Electron	e^-	0.511	stable	
Positron	e^+	0.511	stable	
Muon	μ^-	105.66	2.197×10^{-6}	$e^- + \overline{\nu}_e + \nu_\mu$
	μ^+	105.66	2.197×10^{-6}	$e^- + \nu_e + \overline{\nu}_\mu$
Pion	π^-	139.57	2.603×10^{-8}	$\mu^- + \overline{\nu}_\mu$
	π^+	139.57	2.603×10^{-8}	$\mu^+ + \nu_\mu$
	π^0	134.96	0.83×10^{-16}	$\gamma + \gamma$

Table 2.1: Properties of elementary particles discovered in air showers.

production. The photo-electric effect and Compton scattering can be neglected above a few tens of MeV, where pair production is the dominant process.

Pair production is the process by which a photon interacts with the Coulomb field of the nucleus, creating an electron-positron pair. This occurs at energies higher than the sum of the rest masses of that pair. A high-energy electron emits a photon when it interacts with the electromagnetic field of a nucleus (Bremsstrahlung radiation). These photons, in turn, produce additional electron-positron pairs, and so on. This cycle continues until the initial energy of the neutral pion has been divided up into enough particles for the mean energy of the electron and positron pair to approach a critical energy of ~80 MeV. At this point electrons begin to lose a significant fraction of their energy by ionization, which does not produce additional shower particles. Now, the photo-electric and Compton scattering processes (which also do not produce additional particles) begin to dominate pair production. This is the point in the shower with the greatest number of particles, because the electromagnetic component contains the bulk of air shower particles, and is referred to as shower maximum (Figure 2.5). After shower

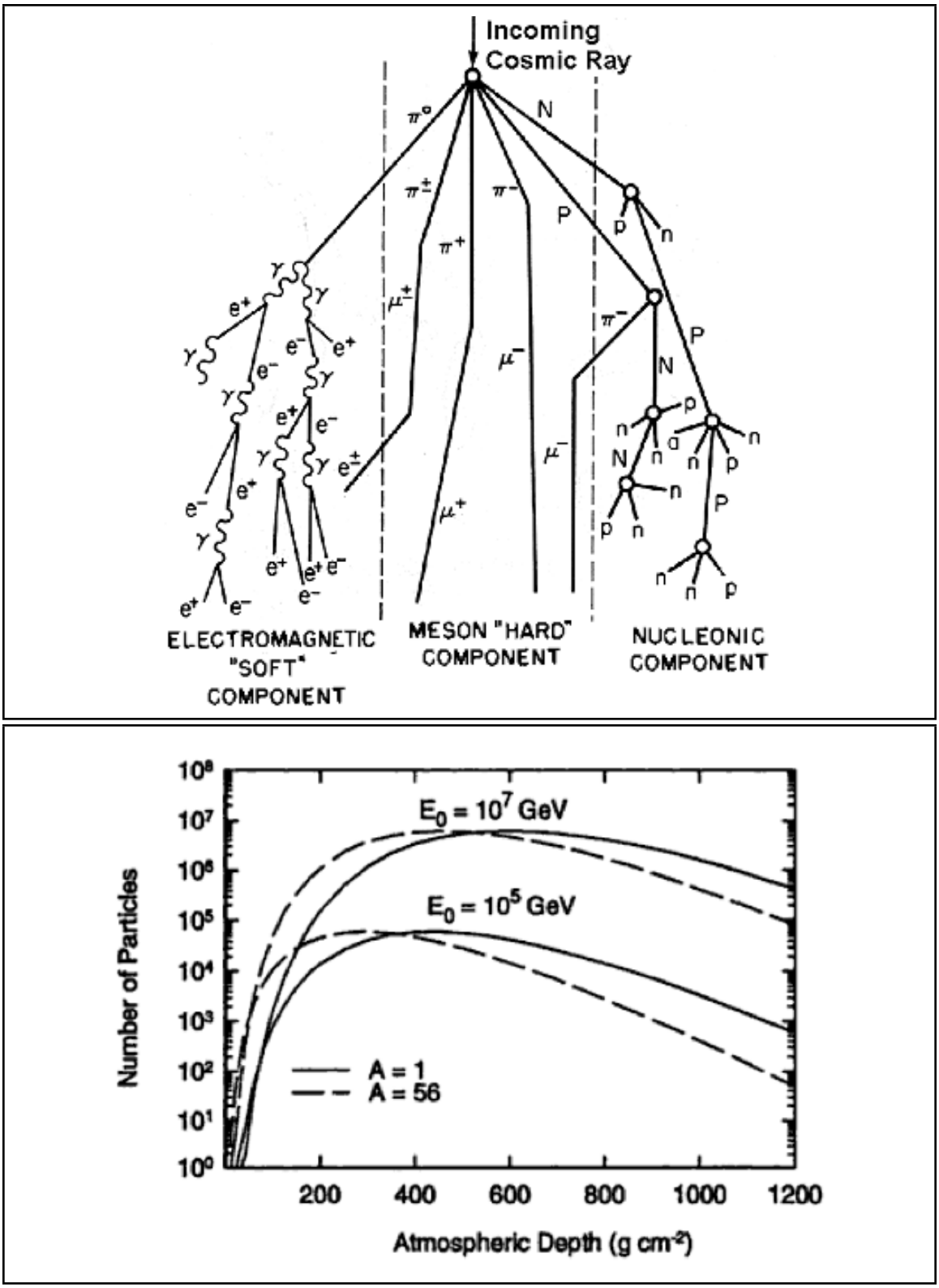

Figure 2.5: (Top) Development of an air shower (Simpson et al., 1953). (Bottom) Total number of shower particles for proton and iron primaries at different initial energies. The position of shower max is at a lower atmospheric overburden (higher altitude) for decreasing primary energy. (Gaisser and Hillas, 1977)

maximum is reached the number of particles decreases as the shower continues to propagate.

In addition to the neutral pions, charged pions are also produced in the first interaction of the primary cosmic ray. The mean lifetime for charged pions are much longer and can therefore collide with molecules in the upper atmosphere, producing charged muons via the decay modes listed in Table 2.1. High-energy muons constitute the "hard" component in air showers, and represent 3-5% of the total number of air shower particles (Treat and Greisen, 1948). Muons are weakly interacting and travel in almost straight lines to ground-level. Their energies are, in general, much greater than their rest mass, thus they are highly relativistic and reach ground-level before they decay. Some charged pions decay and feed back into the electromagnetic component of the air shower.

2.2.2 Ground-Level Structure

The electromagnetic component will experience some lateral "spreading", mostly from Coulomb scattering. Likewise, the nucleonic component will also have some three-dimensional properties due to random interactions while propagating through the atmosphere. However, the dominating contribution to the lateral spread of the air shower is determined by the amount of traverse momentum transferred to the shower particles in the first interaction. Muons may be displaced by a few degrees from the shower core, and when they reach ground-level, the separation can be more than a few kilometers.

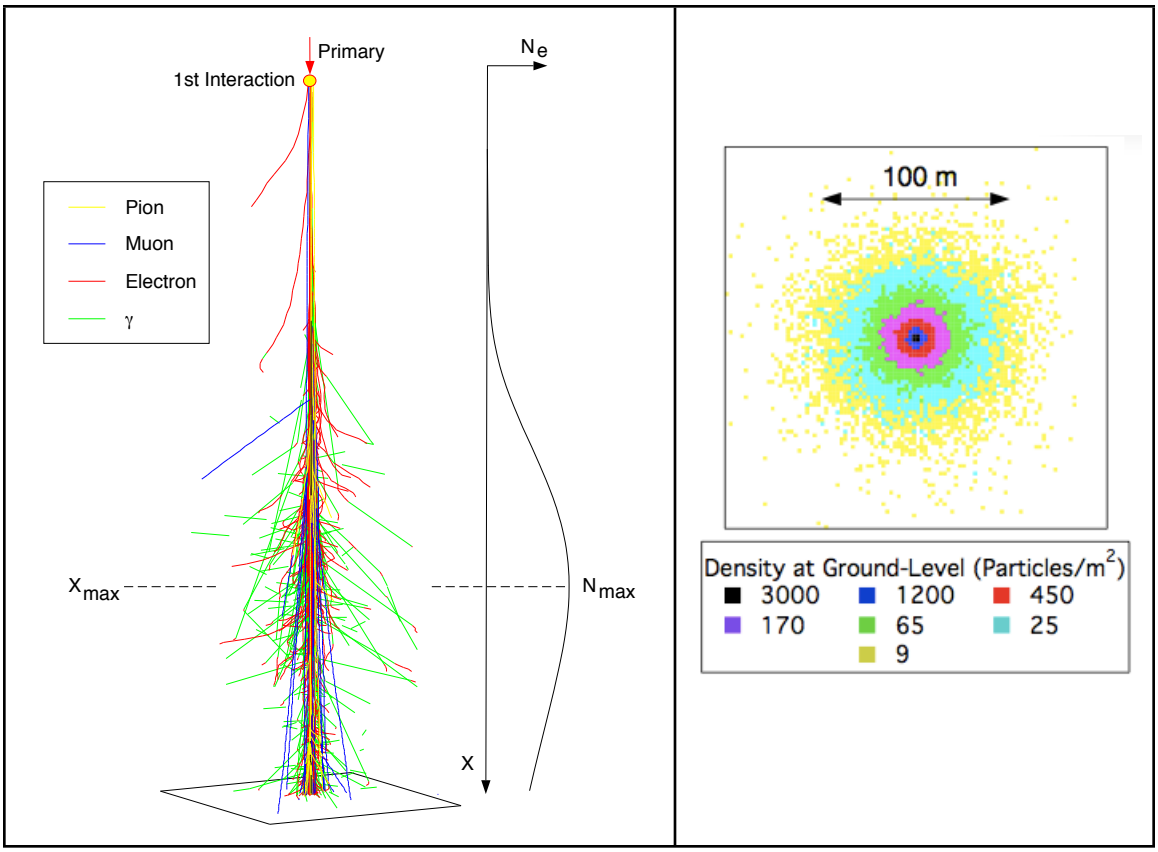

Figure 2.6: The lateral density distribution in air showers, only a small fraction of particles are shown for clarity. (Hinton, 1998)

The resulting distribution at ground-level is a very dense population within ~50 m of the shower core, dominated by photons and electrons (Figure 2.6). As one moves farther outwards the density drops sharply due to the electromagnetic component comprising the bulk of shower particles, and their confinement close to the shower core. Although the muon component represents a small fraction of the total number of air shower particles, they dominate the population at distances far from the shower core (>500 m).

Air showers will also exhibit some thickness features that arise from the different speeds of the particle species. The secondary and higher order particles tend to move through the atmosphere as a thin front (~several meters) referred to as the "pancake"

structure of the shower. Some of the lower energy shower particles may have a longer flight path due to increased scattering, this will produce curvature features on the shower front. Although these particles are traveling near the speed of light, the curvature features cause nanosecond delays, and can be observed in detectors.

2.3 Air Shower Detection Instruments

Although the work discussed in the upcoming chapters relies on atmospheric showers produced by cosmic rays, it is important to acknowledge the contribution of gamma-ray induced air showers. For an instrument such as the Milagro detector (see chapter 4), which is sensitive to cosmic rays although functioning primarily as a gamma-ray telescope, the ability to distinguish between the two types of showers is crucial. The important feature in gamma-ray induced air showers is their lack of muons. Many of the same physical principles and detection techniques are used for both gamma-ray and cosmic-ray shower observations.

In addition to the instruments described in this section, NMs and the Milagro detector (for their contribution to this work) will each be described in the next chapters.

2.3.1 Air Čerenkov Telescopes

When a charged particle is traveling faster than the speed of light in a medium, it radiates in that medium. The photons emitted in this process are known as Čerenkov

light (described in section 4.1). Air Čerenkov telescopes (ACTs) detect the Čerenkov light emitted by an air shower as it travels through air (Weekes, 2003), and are designed to measure TeV gamma rays.

One or more mirrors are used to concentrate the Čerenkov light onto a camera of photomultiplier tubes (PMTs) with fast readout systems. The image on the focal plane of the reflecting mirrors can be used to deduce the shower energy and incident direction. Cosmic rays provide a large source of background for ACTs, shower properties such as lateral spread and muon content are used to deduce the two types of showers. ACTs are limited to operating on dark, moonless nights, and must restrict their field of view in order to minimize background contributions.

The pioneering Whipple 10-m gamma-ray telescope (Weekes et al., 1989) made the first successful detection of a TeV gamma-ray source, the Crab Nebula. The Very Energetic Radiation Imaging Telescope Array System (VERITAS), consisting of four 12-m telescopes, operates in the 50 GeV - 50 TeV energy range. Its design is based on the Whipple telescope, and it is among the present day leaders in ground-based gamma-ray detectors. Each VERITAS telescope has 350 individual mirrors, and a field of view of

Figure 2.7: The VERITAS array of four air Čerenkov telescopes in southern Arizona.

~3.5° with angular resolution ~0.2° (Holder et al., 2006). Other ACTs include the High Energy Stereoscopic System (HESS) telescope in Namibia, and the Major Atmospheric Gamma-ray Imaging Čerenkov (MAGIC) telescope in La Palma.

2.3.2 Air Fluorescence

Air fluorescence was first used as a method of detecting nuclear explosions at Los Alamos National Laboratory in the early 1960s. Relativistic electrons in an air shower excite molecules in the atmosphere, producing ultraviolet light. In the mid 1960's the air fluorescence technique was applied to air showers by a group led by Kenneth Greisen (a former graduate student of Bruno Rossi) at Cornell University. Measuring the energy losses of the relativistic electrons provides an estimate for the energy of the initiating primary particle.

The High Resolution Fly's Eye (HiRes) detector is comprised of 21 spherical 4.2-m mirrors (Bird et al., 1994), in 1999 42 additional mirrors were added ~13 km away to provide stereo measurements. The experiment is located in the deserts of Utah where the atmosphere is very clean and clear, however viewing is still restricted to moonless nights. HiRes is sensitive to the highest-energy cosmic rays (above ~10^{18} eV) and has successfully resolved events with energies greater than 10^{20} eV (Bird et al., 1995), well above the GZK cutoff.

2.3.3 Extended Air Shower Arrays

Due to the power-law nature of the cosmic ray spectrum, instruments covering very large areas are necessary to detect secondary particles from the UHECR primaries. Extended air shower arrays are able to detect these particles by utilizing many small detectors, each with the ability of sampling a small fraction of the total number of air shower particles. Some notable experiments in this field are the High Energy Gamma Ray Astronomy (HEGRA) array in the Canary Islands, the Tibet array, and the Akeno Giant Air Shower Array (AGASA) in Japan.

The largest extended air shower array is the Pierre Auger Observatory (Allekotte et al., 2008) located east of the Andes mountains in Argentina (Figure 2.8). The Auger array consists of 1,600 water Čerenkov tanks, which detect Čerenkov light emitted as a particle travels faster than the speed of light in water (described in section 4.1). Each 3,000 gallon tank detects secondary particles from the air shower, and is separated from its nearest neighbor by 1.5 km, covering an area of 3,000 square kilometers. A clear advantage for the water Čerenkov technique, with respect to that of air Čerenkov, is that they can run uninterrupted regardless of atmospheric conditions.

The Auger array also contains 24 air fluorescence detectors (Pierre Auger Collaboration, 2010a) which resolve ultraviolet light and track the shower's development through the atmosphere. This compliments the water Čerenkov tanks, providing high quality information about the initiating primary particle, however they are restricted to

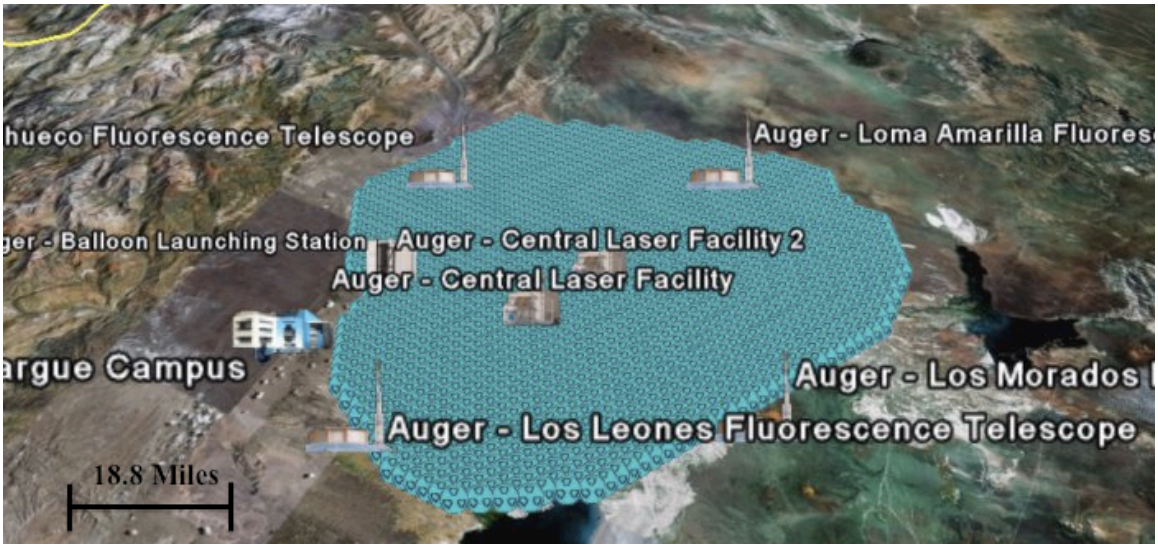

Figure 2.8: Google Earth map of the Pierre Auger Observatory. Covering almost 1200 square miles, the Auger extended air shower array is the largest cosmic ray detector on the Earth.

viewing on clear, moonless nights. The Pierre Auger Observatory has been in operation since 2004, and results for the cosmic ray spectrum above 10^{18} eV have recently been published (Pierre Auger Collaboration, 2010b).

Chapter 3

Neutron Monitors

For a cosmic ray to reach Earth's atmosphere it must possess sufficient momentum to pass through the Earth's geomagnetic field. The structure of the field causes the threshold momentum to be a function of geographic location and direction. Neutron monitors are designed to measure the intensity of the nucleonic component in cosmic-ray showers and are located at many locations around the globe. Even 60 years after its development the neutron monitor continues to play a significant role in the study of cosmic rays and ground-level enhancements.

3.1 The Earth as a Detector for Cosmic Rays

Our planet's spinning outer core of liquid iron and nickel is the foundation for the Earth's dipole magnetic field. This field acts as a shield from the ever-present solar wind. When the wind encounters the Earth's magnetic field it is deflected like water around the bow of a ship. The region of space around the Earth that is traced out by the deflection of the solar wind is called the Earth's magnetosphere (Figure 3.1).

Near the Earth, the magnetic field retains its dipole geometry. At further distances the incident solar wind compresses the Earth's magnetic field in the sunward direction

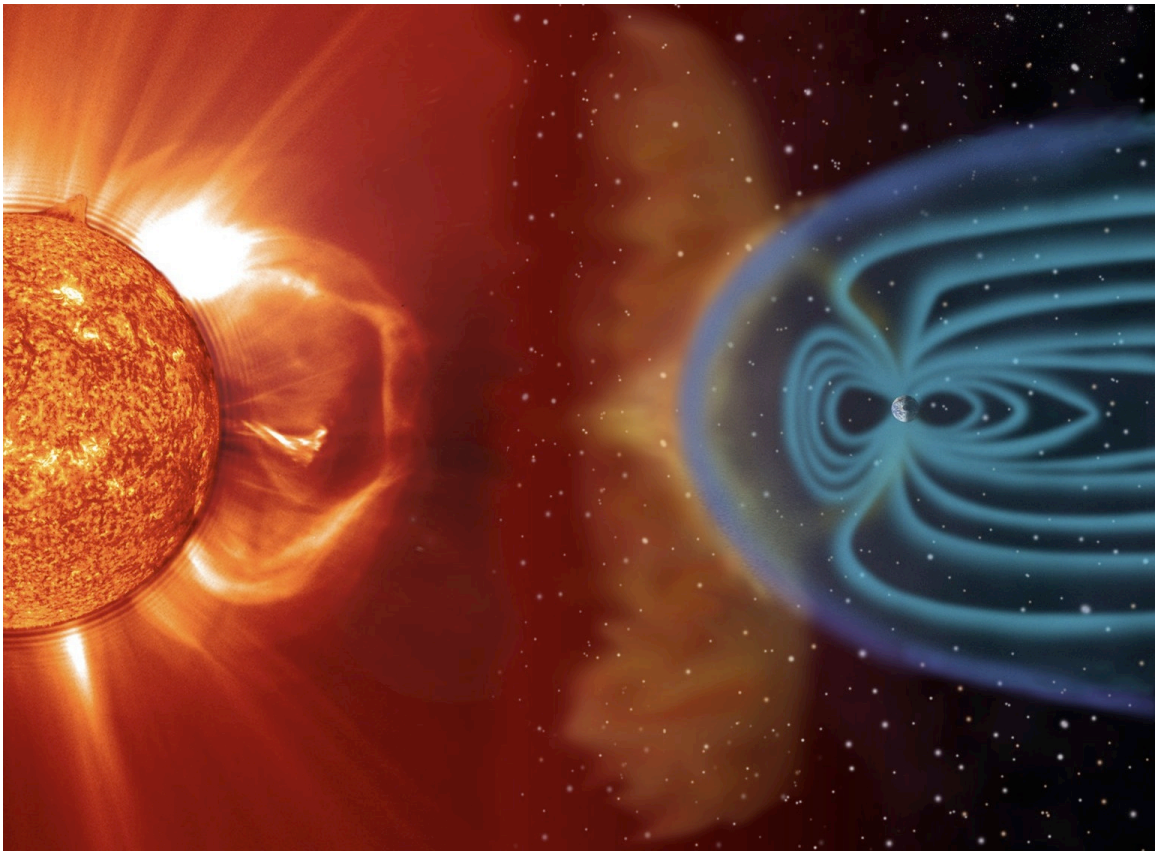

Figure 3.1: SOHO composite image depicting the solar wind incident upon the Earth's magnetic field. The magnetosphere deflects the solar wind, protecting the Earth and tracing out a teardrop shape that extends ~200 Earth radii on the night side. (Figure courtesy of Steele Hill at NASA)

producing a bow shock. The exact distance this compression takes place is determined by a balance between the solar wind ram pressure and the magnetic pressure of the Earth's planetary field (on average it occurs between 10 and 11 Earth radii). Fast CMEs carrying enhancements of charged particles at ~tens of MeV can disrupt this balance and cause geomagnetic storms. The increased solar wind density present in the bow shock at the leading edge of the CME forces some magnetic field lines to restructure by means of magnetic reconnection. Particles accelerated by this process interact with the Earth's upper atmosphere at high latitudes, producing the cascading lights known as the aurora.

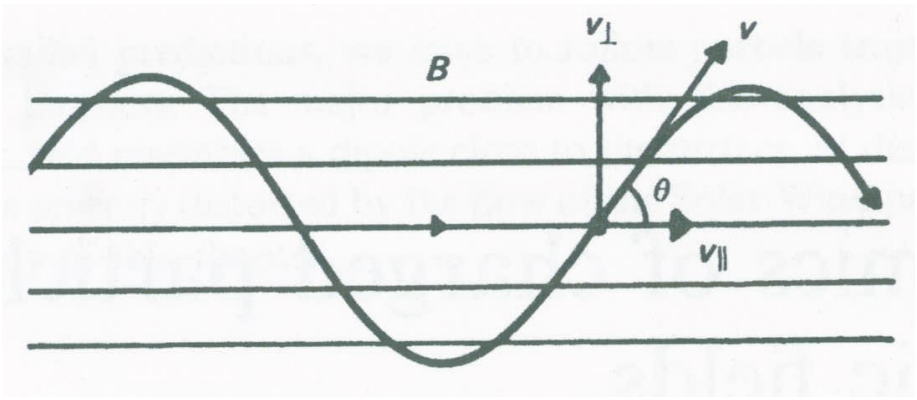

Figure 3.2: The dynamics of a charged particle in a uniform magnetic field. (Longair, 1992)

Beginning with a uniform static magnetic field **B**, the equation of motion for a particle of rest mass m_0, charge ze, and Lorentz factor $\gamma = (1 - v^2 / c^2)^{-1/2}$ is given by

$$\frac{d}{dt}(\gamma m_0 \mathbf{v}) = ze(\mathbf{v} \times \mathbf{B}) \tag{3.1}$$

A charged particle propagating along a magnetic field line has components of velocity parallel and perpendicular to the field line, allowing the result of equation 3.1 to be expressed as

$$r = \gamma m_0 v \sin\theta / zeB \qquad i.e. \qquad v_\perp^2 / r = zevB \sin\theta / \gamma m_0 \tag{3.2}$$

Rewriting equation 3.2 in terms of the momentum p, the gyroradius of the particle can be represented as follows:

$$r = \left(\frac{pc}{ze}\right)\frac{\sin\theta}{Bc} \qquad \text{where } pc / ze \text{ is called the rigidity of the particle} \tag{3.3}$$

This shows that particles with equal rigidities that are injected at the same pitch angle θ, into a magnetic field **B** will trace the same path. Rigidity has the dimensions of electric potential in units typically of GV.

The varying strength of the Earth's magnetic field with geomagnetic position determines particle access to specific locations. At higher latitudes the magnetic field geometry is closely aligned to vertical, meaning that a particle with a smaller gyroradius (lower rigidity) would be able to reach the Earth's atmosphere. The opposite is true as one approaches equatorial latitudes, here the magnetic field has only a small radial component. To reach the atmosphere near the equator a particle's gyroradius must be larger than several Earth radii to overcome the orientation of the magnetic field (higher rigidity). The threshold rigidity required to reach Earth's atmosphere at a certain geographic location is called the cutoff rigidity, and a map illustrating the associated values around the globe is provided in Figure 3.3. Cosmic ray intensities were shown to have a strong relationship with cutoff rigidity (McCracken et al., 1962, 1965, 1968), and observations were well ordered with cutoff rigidity calculations performed by Shea et al. (1965). The Earth's internal magnetic field was also shown to be evolving, requiring consistently updated cutoff rigidity calculations (Shea and Smart, 1970, 1990; Smart et al., 2000; Smart and Shea, 2009).

For particles with rigidities much greater than a given location's cutoff, the gyroradii will be so large that trajectories will be relatively unaltered as the particles travel through the Earth's magnetosphere. However, for lower rigidity particles (approaching the cutoff from above), trajectories become heavily influenced by the magnetic field (Figure 3.3). The directions from which the primary cosmic rays are incident before encountering Earth's magnetosphere are called asymptotic viewing directions.

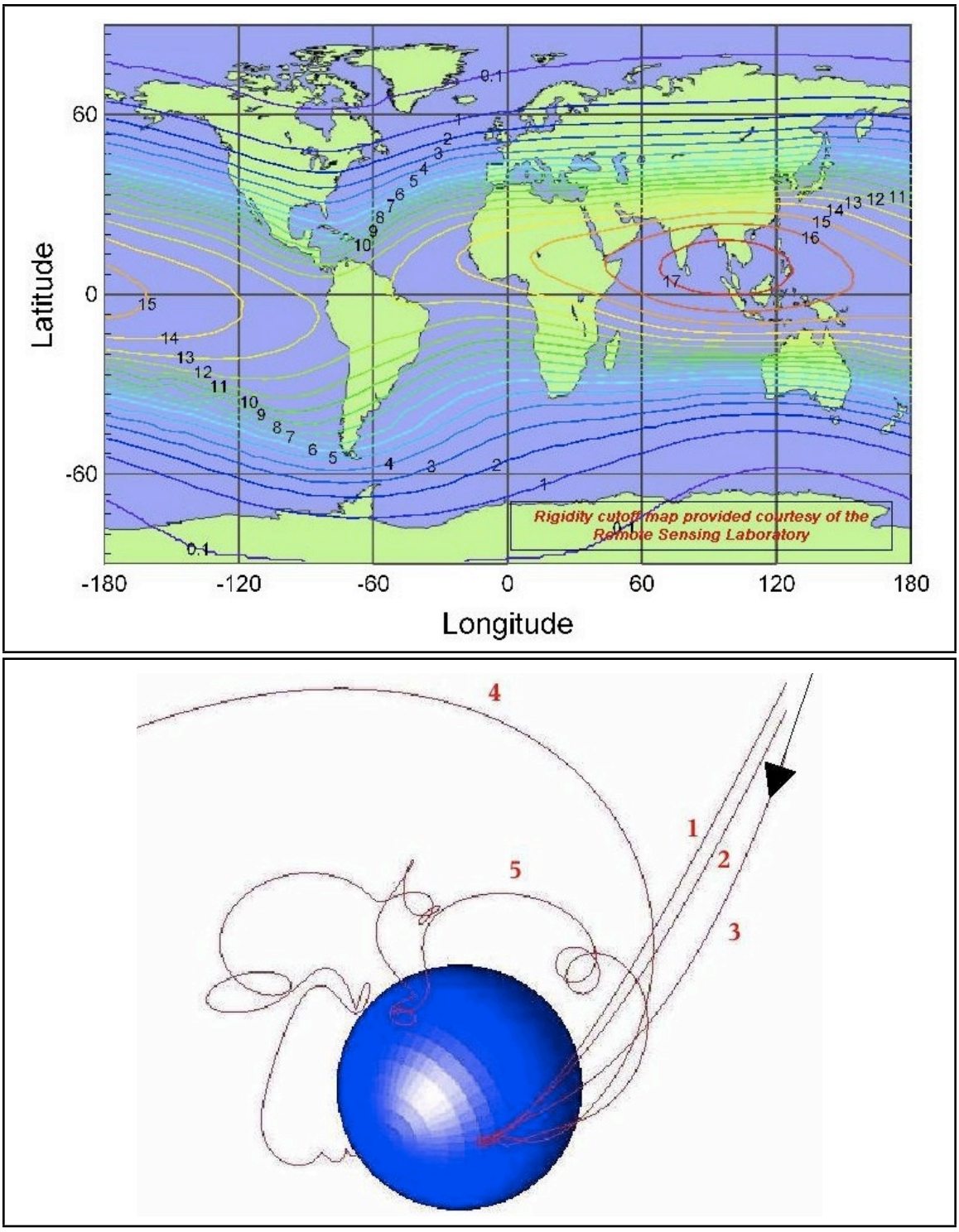

Figure 3.3: (Top) Map of cutoff rigidities (GV) for all locations on the globe (courtesy of the Remote Sensing Laboratory). The dipole nature of the Earth's magnetic field causes a strong latitude dependance, as a result a particle must have a higher minimum rigidity to reach the atmosphere near the equator. (Bottom) Simulated trajectories through the Earth's magnetic field for cosmic rays of different rigidities. Particles labeled 1, 2, 3, 4, and 5 have rigidities of 20, 15, 10, 5, and 4.5 GV respectively. (Desorgher, 2006)

3.2 Development of the Worldwide Neutron Monitor Network

The first instruments to constantly measure cosmic radiation were ionization chambers (Lange and Forbush, 1948, 1957; Beach and Forbush, 1961, 1969). Implemented in the 1930's, the Carnegie network of ionization chambers, operated by Scott E. Forbush, recorded bi-hourly data from five locations: Hafelekar, Austria (1932), Christchurch, New Zealand (1936), Huancayo, Peru (1936), Cheltenham, U.S.A. (1937), and Godhaven, Greenland (1938). The particles detected were muon secondaries from relativistic proton primaries incident on the Earth's atmosphere. For the muons to be detected at ground-level, primary nucleons must have a minimum energy of ~4 GeV. Eventually a detector with a response to lower energy nucleons (producing higher statistics over shorter time intervals) was desired.

In 1946, John A. Simpson began a study on the primary cosmic ray spectrum at the top of the atmosphere through measurements of the nucleonic air shower component. Using Boron-Trifluoride (BF_3) counters leftover from World War II, Simpson conducted a latitude survey of the neutron count rate during high altitude flights (Simpson, 1948, 1951, 2000). The intensity of the nucleonic component was found to vary with latitude by up to 400%. The latitude dependance of the nucleonic component opened a window for studying cosmic rays between ~1-15 GeV, prompting the design for a continually operating nucleonic cascade monitor.

3.2.1 Design

The cylindrical BF_3 tubes used by Simpson had a diameter of 3.8 cm and a length of 87 cm (Simpson et al., 1953). Thermal neutron secondaries at energies of ~tens of MeV resulting from cosmic-ray primaries interact with the BF_3 proportional counters and initiate the reaction

$$ {}^{10}_{5}B + n \rightarrow \left[\begin{array}{cc} {}^{7}_{3}Li^{*} + {}^{4}_{2}He \rightarrow {}^{7}_{3}Li + {}^{4}_{2}He + 0.480\,MeV & 94\% \\ {}^{7}_{3}Li + {}^{4}_{2}He + 2.78\,MeV & 6\% \end{array} \right] \tag{3.4} $$

All electromagnetic components are filtered out by setting the pulse height to a level where only the α particles trigger the instrument.

To be sensitive to high-energy neutrons, the original aircraft experiments rejected slower thermal neutrons by surrounding both the counters and paraffin wax within a cadmium shield. Lead was used in the ground-level design not only for improved thermal neutron shielding, but also to enhance the count rate. The fragmentation or fission of a lead nucleus by an incident high-energy nucleon produces additional multiplicities of fast neutrons, these are then slowed down by the paraffin wax, enabling detection (Simpson, 1953; Simpson and Uretz, 1953).

Multiple tubes were placed close together to increase count rates, typically in groups of 12 (Figure 3.4). The NM "pile" consisted of over 6,500 pounds of lead and more than 3,000 pounds of paraffin wax. This configuration became the standard neutron monitor design and was deployed to Chicago, Illinois and Climax, Colorado

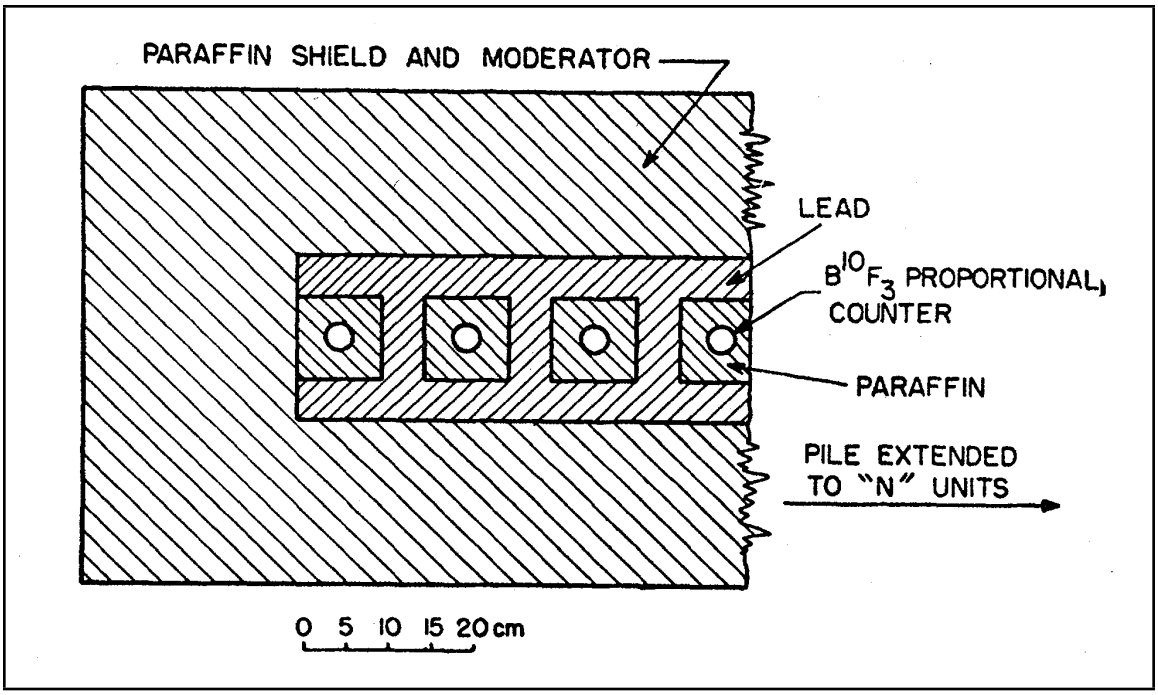

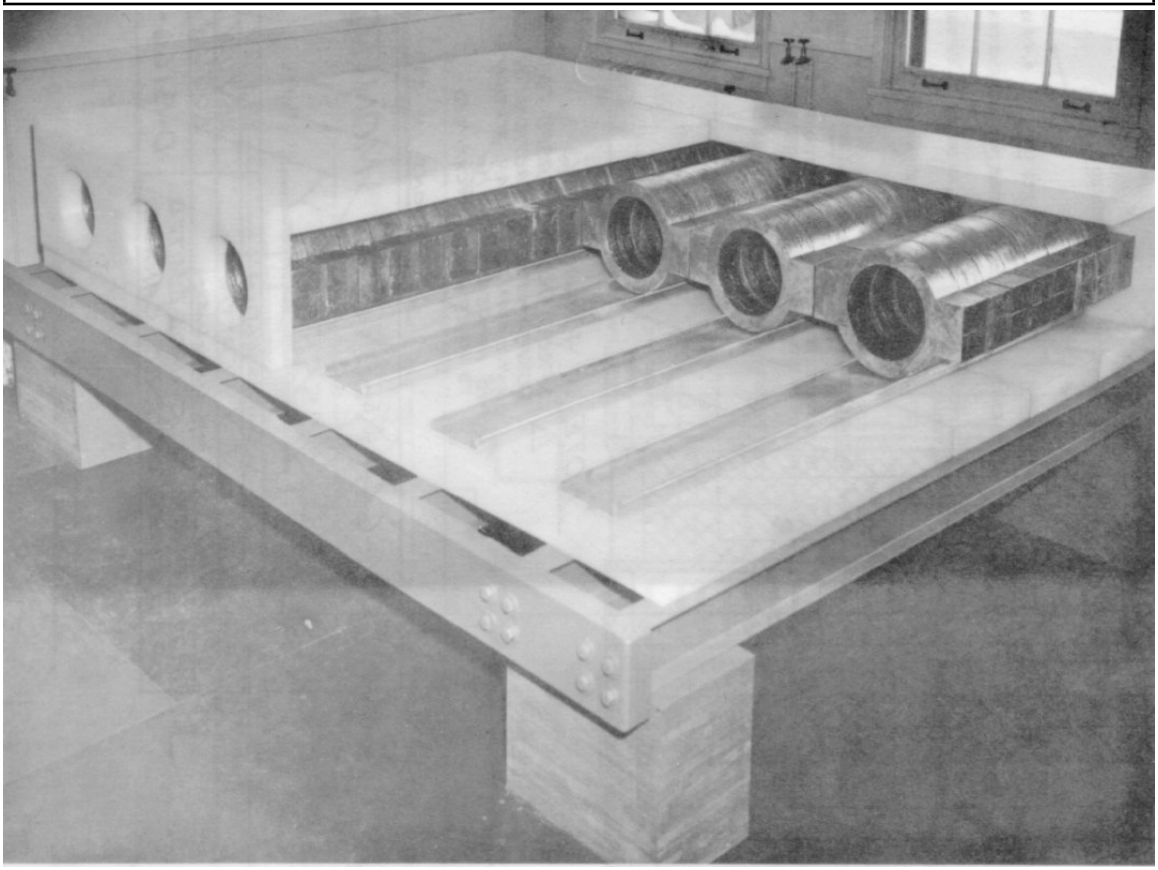

Figure 3.4: (Top) Cross-sectional view of the IGY neutron monitor pile, extended to 12 counters (Simpson, 2000). In this configuration the pile consisted of 6,500 pounds of lead plus approximately 3,000 pounds of paraffin wax. (Bottom) The NM64 supermonitor configuration. The upgraded layout typically groups the larger BP-28 tubes (to be inserted into the lead rings) in groups of six, referred to as "banks". The improved lead ring design is enclosed in polyethylene and mounted on steel beams.

in 1949. In 1951, Climax became the first NM put into operation, and is still operational today.

Muon decay is dependent on local temperature, therefore, intensity measurements for ionization chambers were also dependent on temperature. The "Simpson" NM proved to be a superior cosmic radiation detector. Although the intensity of the nucleonic component has a relationship to barometric pressure, the temperature dependence is negligible (Simpson et al., 1953). The project quickly grew to include twelve stations by 1957. The advances of the NM provided additional scientific momentum to the onset of the 19th solar cycle, marked as the International Geophysical Year (IGY). 39 additional stations were installed in 1957, leading the design to be known as IGY neutron monitors, and bringing the worldwide network to 51 monitors. Although the IGY NM was widely recognized as an excellent detector for studying cosmic ray variations, it soon became clear that improved statistics were required for short-term events such as GLEs.

The Leeds IGY NM reported that only 1.9% of the neutrons produced in the lead were counted (Hughes, 1961, 1966). Larger size BF_3 counters were constructed at the Chalk River Nuclear Laboratories in 1959 (Carmichael, 1968). In 1960, Hatton and Carmichael determined an optimal design for a NM consisting of the larger counters (Hatton and Carmichael, 1964). The new super neutron monitor (NM64) design featured a polyethylene moderator to replace the paraffin wax and a geometrically superior arrangement of lead surrounding the counters (Figure 3.4).

Characteristic	IGY	NM64
Counter type	NW G-15-34A	BP28
Spacing of counters (cm)	15.2	50.0
Moderator material	Paraffin	Polyethylene
Moderator thickness (g/cm^2)	2.95	1.84
Producer material	Lead	Lead
Top area of producer (cm^2)	1.9×10^4	6.21×10^4 (per 6 tubes)
Diameter (cm)	3.8	14.8
Length (cm)	87	191
Pressure (mm Hg)	450	200

Table 3.1: Design improvements to the original IGY neutron monitor by Hatton and Carmichael (1964). The resulting supermonitor design offered a 10-fold increase in count rate.

After the design changes listed in Table 3.1, the efficiency per unit area of the lead producer increased by a factor of ~3. When coupled with the larger area, the overall count rate increased by a factor of ~10. The advantages were evident with the July 1961 GLEs (Steljes and Carmichael, 1961). The majority of NMs still operational today are of the NM64 design (Table 3.2 at the end of this chapter).

3.2.2 Ground-Level Enhancement Observations and Results

In roughly ten years of ionization chamber records, Scott E. Forbush noticed unusual increases for Cheltenham, Maryland on 1942 February 28, 1942 March 7, and 1946 July 25 (Forbush, 1946). The last of three events was not observed by the Huancayo, Peru station due to its high cutoff rigidity (P_c ~13.5 GV), indicating that the increase was due to particles with energies less than that of the Huancayo cutoff. The increases were attributed to charged particles from the Sun (Forbush, 1949), and the occurrence of "impact zones" indicated that the radiation was initially anisotropic (Firor,

1954). The development of the NM, sensitive to a wider range of rigidities, would provide improved measurements of GLEs. Fortunately, the network of NMs was established and operational in the early 1950s enabling detection of the 1956 February 23 event, which remains as the largest GLE ever recorded.

The 1956 February 23 GLE (Figure 3.5) coincided with a strong X-ray flare beginning at 0331 UT and located at N24°, W74° (Smart and Shea, 1990), this was prior to knowledge of CMEs and thus there is no evidence on record. The GLE was resolved in ionization chambers (Forbush, 1956) and all NMs operational at the time, including a ~26% increase in Huancayo, Peru (Meyer et al., 1956; Smart and Shea, 1990), indicating the presence of particles up to energies of ~20 GeV. GLE onset was at ~0350 UT, stations placed around the world varied by ~10 minutes and were originally thought to be the result of velocity dispersion associated with the geomagnetic cutoff rigidities, which were poorly known at the time. In 1957, Lüst and Simpson concluded that the varying onset times were attributed to the initial anisotropy suggested by Firor (Lüst and Simpson, 1957).

Additional GLEs were observed, with widely varying profiles. The decay time constants were noticed to be much shorter when the associated flare was on the western portion of the solar disk (McCracken and Palmeira, 1960). Using asymptotic cones of acceptance, McCracken (1962a, 1962b) showed that several GLEs were strongly anisotropic when the associated flare occurred on the western third of the solar disk. For those events, the rise-time of the GLE was rapid and the initial anisotropic radiation

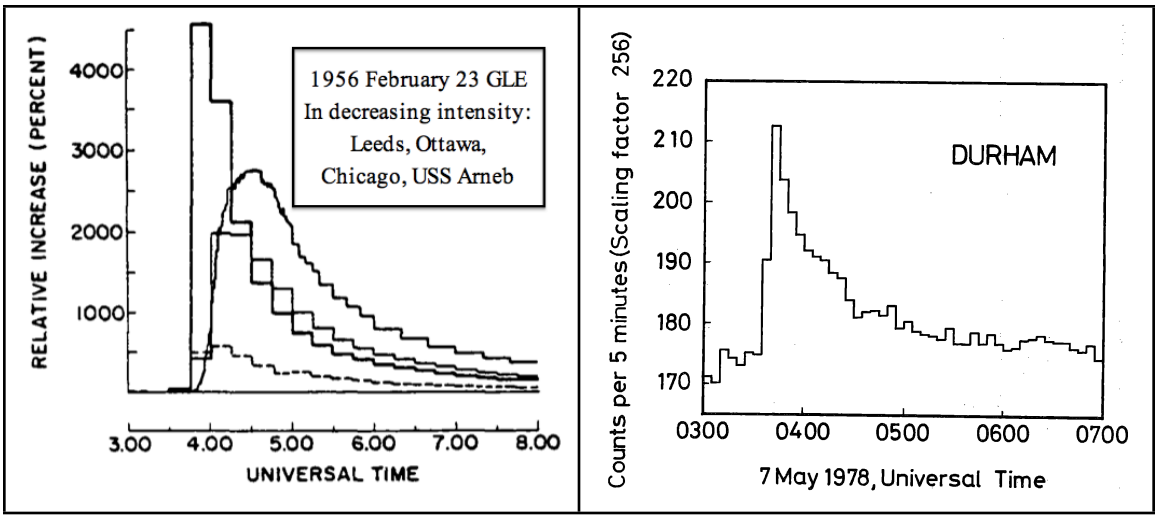

Figure 3.5: (Left) The 1956 February 23 event was the first GLE to be resolved by the neutron monitor network, and to this day remains the largest on record (Smart and Shea, 1990). (Right) The 1978 May 7 GLE observed by the Durham, NH station (Debrunner and Lockwood, 1980). As of this writing there have been 70 GLEs dating back to 1942.

arrived in agreement with the predicted spiral nature of the IMF by Parker (1958). For an event occurring on the eastern two thirds of the solar disk, the rise-time was slower, and the initial radiation was only mildly anisotropic.

As discussed in section 1.5, GLE profiles were initially explained by delays due to diffusive transport of the relativistic particles from the flare site. Although this model worked well, the discovery of CMEs and their high correlation with gradual events and GLEs led to a model involving a CME-driven shock to explain the acceleration and profile of the relativistic particles. In this model, a CME originating from the western third of the solar disk accelerates particles to relativistic energies and releases them low in the corona ($<4\ R_{\odot}$). The relativistic charged particles propagate along the Parker spiral, experience some pitch-angle scattering, and arrive at Earth with an anisotropic distribution in the direction of the IMF. As the CME reaches higher solar altitudes, its angular width (and thus the relativistic particles traversing the shock) can cross multiple

field lines. The resulting pitch-angle distribution decreases in anisotropy after the initial stages of the GLE. Irregularities in the IMF past 1 AU continue to scatter the SCRs roughly an hour after GLE onset, further decreasing the anisotropy. SCRs originating from a CME-driven shock on the eastern two thirds of the solar disk do not initially have access to the Earth via the Parker spiral. As the CME grows in angular width, the relativistic particles cross field lines and eventually have access to the Earth via the Parker spiral. This produces the longer delay in GLE onset, prolonged rise-to-maximum, and decreased anisotropy observed in eastern events (Figure 1.9).

In addition to measuring pitch-angle distributions, placing NMs at strategic locations throughout the globe provides a measurement of the rigidity spectrum from ~1-15 GV (NM locations are provided in Table 3.2). This is possible due to the properties of the Earth's magnetic field discussed in section 3.1. During the isotropic phase of an event, the integral increase in count rate for a station with a particular cutoff rigidity provides a measure of the flux above that rigidity. However, the initial anisotropic distribution that is often associated with well-connected events prohibits this analysis strategy, as the anisotropy modulates count rates depending on the source location.

A study of the 1956 February 23 GLE proton rigidity spectrum using the NM network was performed by Meyer et al. (1956) during multiple episodes of the event (Figure 3.6). At 0500 UT the GLE signal was still above background at the Huancayo and Mexico City stations, indicating the presence of higher rigidity particles. By 0900 UT the flux at higher rigidities had greatly subsided, as a result the rigidity function is

steeper (softer). Similar softening of spectra during a GLE have been observed for other well-connected events (Figure 3.6), such as 1978 May 7 (Debrunner and Lockwood, 1980; Debrunner et al., 1984; Lockwood et al., 2002).

Alternative approaches to measure the proton rigidity spectrum have been attempted, particularly to obtain a result during the initial anisotropic stages. For example, two NMs at the same location but with one excluding the lead producer to yield a different response (Bieber and Evenson, 1991). Many of these approaches failed to find a dependable representation for the sensitivity of the alternate configuration. However, an

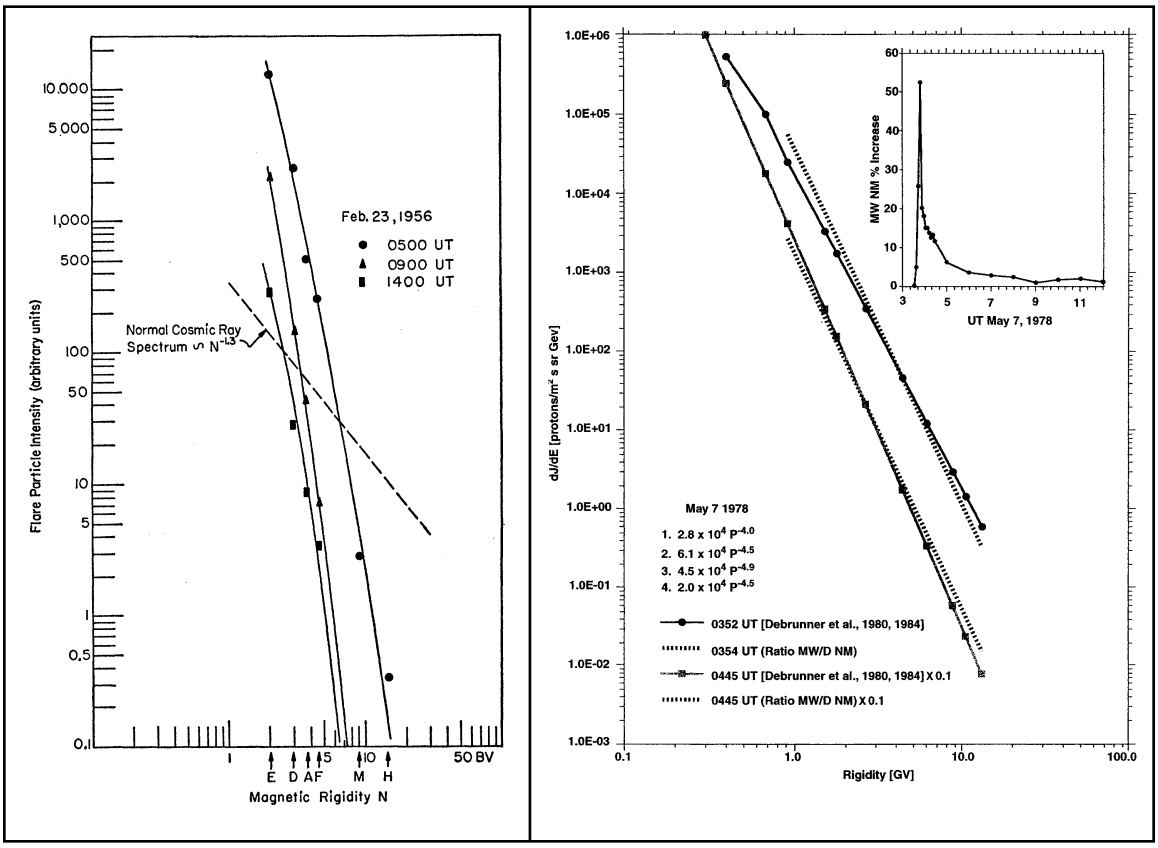

Figure 3.6: (Left) Rigidity spectra for multiple episodes of the 1956 February 23 GLE (Meyer et al., 1956). (Right) Rigidity spectra during the 1978 May 7 GLE for both a worldwide neutron monitor network analysis and the ratio between the Mt. Washington and Durham stations, the later spectra have been scaled down for clarity (Lockwood et al., 2002). In both events the spectra are harder at earlier stages.

approach using two NMs at similar locations, with similar cutoff rigidities, but at different altitudes, was able to yield results in the form of a power-law (Lockwood et al., 2002). The ratio of the enhancements between two stations (*e.g.,* Mt. Washington and Durham, NH) represents a measure of the spectral index in the rigidity range determined by the cutoffs of the NM pair (Figure 3.6).

A measurable upper limit to the GLE proton rigidity spectrum was first suggested in 1971 (Heristchi and Trottet, 1971, 1975; Heristchi et al., 1976). Using the NM network, Heristchi and Trottet calculated the maximum rigidity produced in several events, and concluded that a more detailed spectral form than the standard power-law would be necessary to model the observed proton spectra. The discovery of CMEs and their correlation with large SEP events (Kahler et al., 1978) led to the present theory of coronal shock acceleration (Achterberg and Norman, 1980; Lee and Fisk, 1982; Lee and Ryan, 1986), and Ellison and Ramaty (1985) found an agreement between observed GLE spectra and the spectral form deduced from shock acceleration theory. This new spectral form consisted of the traditional power-law (the spectral index is determined by shock conditions) with an exponential decay, allowing the spectrum to "rollover" at higher energies

$$\frac{dJ}{dE} \propto \left(\frac{dJ}{dE}\right)_0 \exp\left[-\frac{E}{E_0}\right] \tag{3.5}$$

Beginning in 2000 an 11-station network, known as Spaceship Earth, was deployed to four continents to provide three-dimensional measurements of the cosmic ray angular distribution (Bieber and Evenson, 1995; Moraal et al., 2000). The stations are strategically placed at high latitudes and offer two advantages. First, the rigidity cutoffs

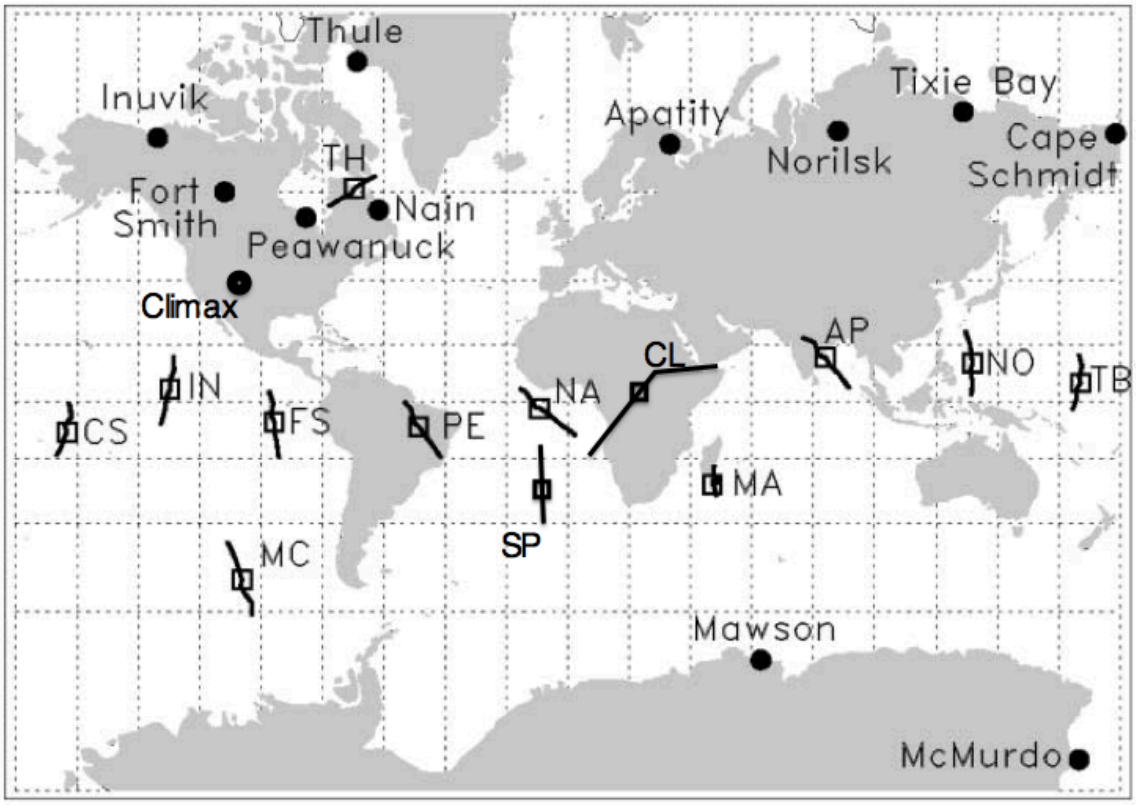

Figure 3.7: Locations and asymptotic viewing directions for the 11 neutron monitors that make up Spaceship Earth (Bieber et al, 2004). The Climax and South Pole (location not pictured) stations have been added to compare viewing direction. The lines show the viewing directions for the central 50% of the detector energy response.

for all stations are essentially zero and thus all stations have the same energy threshold set by the atmospheric cutoff (~0.5 GV). Second, the asymptotic viewing directions (generally well away from the physical location) for the network of stations provide complete coverage of the entire equatorial region, with a three-dimensional perspective from Thule and McMurdo (Figure 3.7). Therefore, Spaceship Earth is an excellent tool for resolving pitch-angle distributions and apparent source directions during the initially anisotropic phases of GLEs.

Even after 60 years of operation, NMs are still heavily relied upon for measurements of cosmic ray intensity in the ~1-15 GV range. The advent of the Space

Age in the late 1950s has furthered our understanding of SEPs and their propagation in the inner heliosphere. However, NMs are still required for measurements of the highest-energy SEPs due to their soft spectra and the small effective areas of spacecrafts.

Station	Coordinates (Lat, Long)	Rigidity Cutoff (GV)	Elevation (m)	Start
Aligarh, India*	27.91, 78.07	14.67	186	1971
Alma-Ata, Kazakhstan	43.25, 76.92	6.61	775, 1670, 3340	1973
Apatity, Russia	67.55, 33.33	0.57	177	1968
Beijing, China	40.08, 116.26	10.06	48	1984
Brisbane, Australia	-27.42, 153.08	6.99	0	1976
Calgary, Canada	51.08, 245.86	1.08	1128	1964
Cape Schmidt, Russia	68.92, 180.53	0.00	0	1981
Chacaltaya, Bolivia	-16.31, 291.85	12.53	5200	1966
Climax, USA*	39.37, 253.82	2.99	3400	1951
Dourbes, Belgium	50.10, 4.60	3.34	225	1969
Durham, USA	43.10, 289.17	1.58	0	1964
Erevan, Armenia	40.17, 44.25	7.58	999, 2000	1988
Fort Smith, Canada	60.02, 248.07	0.33	206	2000
Fukushima, Japan	37.75, 140.48	10.61	66	1971
Gif-sur-Yvette, France	48.68, 2.13	3.60	40	1966
Goose Bay, Canada	53.27, 299.60	0.64	46	1964
Gulmarg, India*	34.07, 74.42	11.58	2743	1968
Hafelekar, Austria	47.32, 11.38	4.38	2290	1968
Haifa, Israel	32.80, 35.00	10.75	2300	1998
Haleakala, USA*	20.72, 203.72	12.91	3052	1963
Haleakala, USA	20.72, 203.72	12.91	3030	1991
Hermanus, S. Africa	-34.42, 19.23	4.58	26	1964
Hobart, Australia	-42.90, 147.33	1.84	18	1978
Inuvik, Canada	68.35, 226.28	0.17	21	1964
Irkutsk, Russia	52.47, 104.03	3.64	433, 2000, 3000	1967
Jungfraujoch, Switzerland*	46.55, 7.98	4.61	3475	1958
Jungfraujoch, Switzerland	46.55, 7.98	4.61	3475	1986
Kerguelen Island	-49.35, 70.27	1.14	33	1964
Kiel, Germany	54.33, 10.13	2.36	54	1964

Table 3.2: Neutron Monitors still in operation (part 1 of 2). Adapted from Smart and Shea (2000). *Note: Many stations may have been rebuilt or upgraded. Stations operating with the original IGY design are denoted by a (*).*

Station	Coordinates (Lat, Long)	Rigidity Cutoff (GV)	Elevation (m)	Start
Kiev, Ukraine	50.72, 30.30	3.57	131	1969
Kingston, Australia	-42.99, 147.29	1.84	65	2000
Leadville, USA	39.75, 255.03	3.03	3098	1968
Lomnicky Stit, Slovakia	49.20, 20.22	3.98	2632	1954
Magadan, Russia	60.12, 151.02	2.09	220	1970
Mawson, Antarctica	-67.60, 62.88	0.20	30	1986
McMurdo, Antarctica	-77.85, 166.72	0.00	50	1964
Mexico City, Mexico	19.33, 260.82	8.61	2274	1970
Morioka, Japan	39.70, 141.13	10.23	131	1977
Moscow, Russia	55.47, 37.32	2.43	200	1966
Mt. Norikura, Japan	36.11, 137.55	11.48	2770	1968
Mt. Washington, USA*	44.30, 288.70	1.46	1909	1954
Mt. Wellington, Australia	-42.92, 147.24	1.84	725	1970
Nain, Canada	56.55, 298.32	0.36	46	1964
Newark, USA	39.68, 284.25	2.09	50	1978
Norilsk, Russia	69.26, 88.05	1.03	0	1971
Novosibirsk, Russia	54.80, 83.00	2.87	163	1971
Oulu, Finland	65.05, 25.47	0.78	15	1964
Peawanuck, Canada	54.98, 274.56	0.47	0	2000
Potchefstroom, S. Africa*	-26.41, 27.06	7.00	1351	1971
Rome, Italy	41.90, 12.52	6.32	0	1966
Sanae, Antarctica	-70.31, 357.59	0.86	856	1964
South Pole, Antarctica	-90.00, 0.00	0.09	2820	1977
Tbilisi, Georgia	41.72, 44.80	6.73	510	1971
Terre Adelie, Antarctica	-66.67, 140.02	0.02	32	1968
Thule, Greenland	76.50, 291.30	0.00	44	1964
Tibet, China	30.11, 90.53	14.10	4300	1998
Tixie Bay, Russia	71.58, 128.92	0.76	0	1966
Tokyo-Itabashi, Japan	35.75, 139.72	11.63	20	1969
Tsumeb, Namibia	-19.12, 17.35	9.21	1240	1976
Turku, Finland	60.40, 22.60	1.36	32	1983
Yakutsk, Russia	62.01, 129.43	1.65	105	1971

Table 3.2: Neutron Monitors still in operation (part 2 of 2). Adapted from Smart and Shea (2000). *Note: Many stations may have been rebuilt or upgraded. Stations operating with the original IGY design are denoted by a (*).*

Chapter 4

The Milagro Detector

Milagro operated in the Jemez Mountains near Los Alamos, New Mexico from January 2000 to March 2008 (Atkins et al. 2000, 2001). The detector was built in a large pond and utilizes the water Čerenkov technique to detect air shower particles. Although Milagro operated primarily as a TeV gamma-ray observatory, it also functions as a cosmic-ray detector. Technical information, in addition to that contained in this chapter, can be found in reviews by McCullough (1999), Falcone (2001), and Abdo (2007).

4.1 Čerenkov Emission

The speed of light depends on the index of refraction of the medium that it is traversing, given by the simple relationship

$$v = \frac{c}{n} \qquad \text{where } n \text{ is the index of refraction} \qquad (4.1)$$

When a charged particle exceeds this velocity it disrupts the electromagnetic field of the medium and radiates, this process is called Čerenkov radiation. Rewriting equation 4.1 in terms of energy gives a threshold energy to this process.

$$E_{th} = \frac{m_o c^2}{\sqrt{1 - \frac{1}{n^2}}} \qquad \text{where } m_0 \text{ is the rest mass of the particle} \qquad (4.2)$$

The Čerenkov radiation is emitted at a characteristic angle in the medium. The radiation propagates in the direction of the **E** × **B** field, leading to an emission angle given by

$$\cos(\theta_c) = \frac{1}{n\beta} \qquad \text{where } \beta \sim 1 \text{ for relativistic particles} \qquad (4.3)$$

The radiation is emitted with axial symmetry about the particle velocity vector in a pattern referred to as the Čerenkov cone, for water (n = 1.33) this angle is ~41°.

4.2 Physical Description

4.2.1 Location

The Milagro detector (Figure 4.1) operated at an elevation of 2650 m above sea level in the Jemez Mountains about 35 miles west of Los Alamos, New Mexico at latitude 35.9° 52′ 45″ N and longitude 106° 40′ 37″ W. This elevation corresponds to an atmospheric overburden of ~750 g/cm^2, roughly 12 free mean paths for protons undergoing nuclear collisions in the atmosphere (~62 g/cm^2). At this elevation the detector was located well below shower maximum for nearly all showers detected. However this situation (observing on the tail of the distribution) is common in the fields of high-energy gamma-ray and cosmic-ray air shower physics. Higher altitude locations closer to shower max can be difficult to maintain, and difficult to access. Rather than placing the instrument closer to shower maximum to detect more shower particles, Milagro attempted to detect a larger fraction of the shower particles incident at ground-

Figure 4.1: Aerial view of the Milagro detector.

level. Traditional extended air shower arrays are composed of small detectors spread over a large area, thus detecting only a small fraction of the shower particles. Milagro operated as a single, large detector, able to sample a large fraction of the shower particles that fell within its active area and thus lowering the energy threshold.

Another factor that contributed to the low threshold energy of Milagro was the geomagnetic field. Particles incident on this field need sufficient rigidity to penetrate down to ground-level (see section 3.1). The threshold rigidity required for this is a function of the location of the detector within the geomagnetic field (Figure 3.3).

Milagro was located at a geomagnetic latitude of 44.5° N, neglecting variations in the geomagnetic field, this places the cutoff rigidity of Milagro at 3.86 GV.

4.2.2 Detector Layout

The core of the Milagro detector is a 6 million gallon pond with a depth of 8 m, and a surface measuring 80 m × 60 m that slopes on all sides yielding bottom dimensions of 50 m × 30 m. The pond is surrounded by 170 individual water Čerenkov detectors, called outriggers, over a 200 m × 200 m area. On the surface of the pond was an inflatable polyethylene cover that provided a light-impermeable environment, allowing the detector to function free of background light 24 hours per day.

To protect the detector from lightning (the Milagro site was among the most lightning prone areas in the United States) a 12,500 m^2 Faraday cage enclosed the entire observatory site. The cage was composed of a mesh of wires suspended by telephone poles, enclosing the pond and the buildings containing the electronics hardware. This structure intercepted and grounded the lightning, protecting the detector from dangerous voltage spikes.

Within the detector, a 2.8 m × 2.8 m (with respect to the surface) grid of sand-filled PVC pipe spanned the floor of the pond, including the sloping sides (Figure 4.2). Photomultiplier tubes (PMTs) were attached to this grid by Kevlar strings before water was added (McCullough et al., 1999). Once the detector was filled with water the PMTs were suspended in two layers within the pond. 450 PMTs submerged under 1.5 m

of water (Air Shower layer or AS layer) detected air shower particles reaching the ground. 273 PMTs under 6 m of water (muon layer) were used to distinguish photon or electron-induced showers from hadron-induced showers. The muon layer PMTs were horizontally offset from the AS layer PMTs by half the grid spacing (Figure 4.2).

The PMTs used in Milagro were 20 cm in diameter (Hamamatsu #R5912SEL). This particular model was chosen because it was found to perform well in the areas important for reconstructing air showers, some of which included good timing resolution at all levels including one photoelectron (2.7 ns for a single photoelectron (PE)), good charge resolution that included a resolved 1 PE peak, good charge linearity (up to ~75 PEs), and high PE collection efficiency (20%, 25% at 325 nm, 450 nm; Atkins et al., 2000)). A waterproof polyvinyl chloride (PVC) casing protected the electronic base of each PMT. A single RG-59 coaxial cable carried the high voltage to the tube and the AC signal from the tube back to the electronic system

The pond densely sampled the air shower particles that reach the detector level. Since the Čerenkov angle in water is ~ 41°, the AS layer PMTs detected the Čerenkov radiation from the relativistic charged particles in the air shower with high efficiency. Roughly 50% of all electromagnetic particles that enter the pond were detected. Gamma rays in an air shower outnumber electrons and positrons by a factor of ~5 at ground-level, and because the AS layer PMTs were placed under 4 radiation lengths of water, gamma rays converted to electrons and positrons before reaching this layer. The electrons and positrons, in turn, Čerenkov radiate in water and were detected. The depth of the muon layer corresponded to 16 radiation lengths of water; thus, all electromagnetic particles

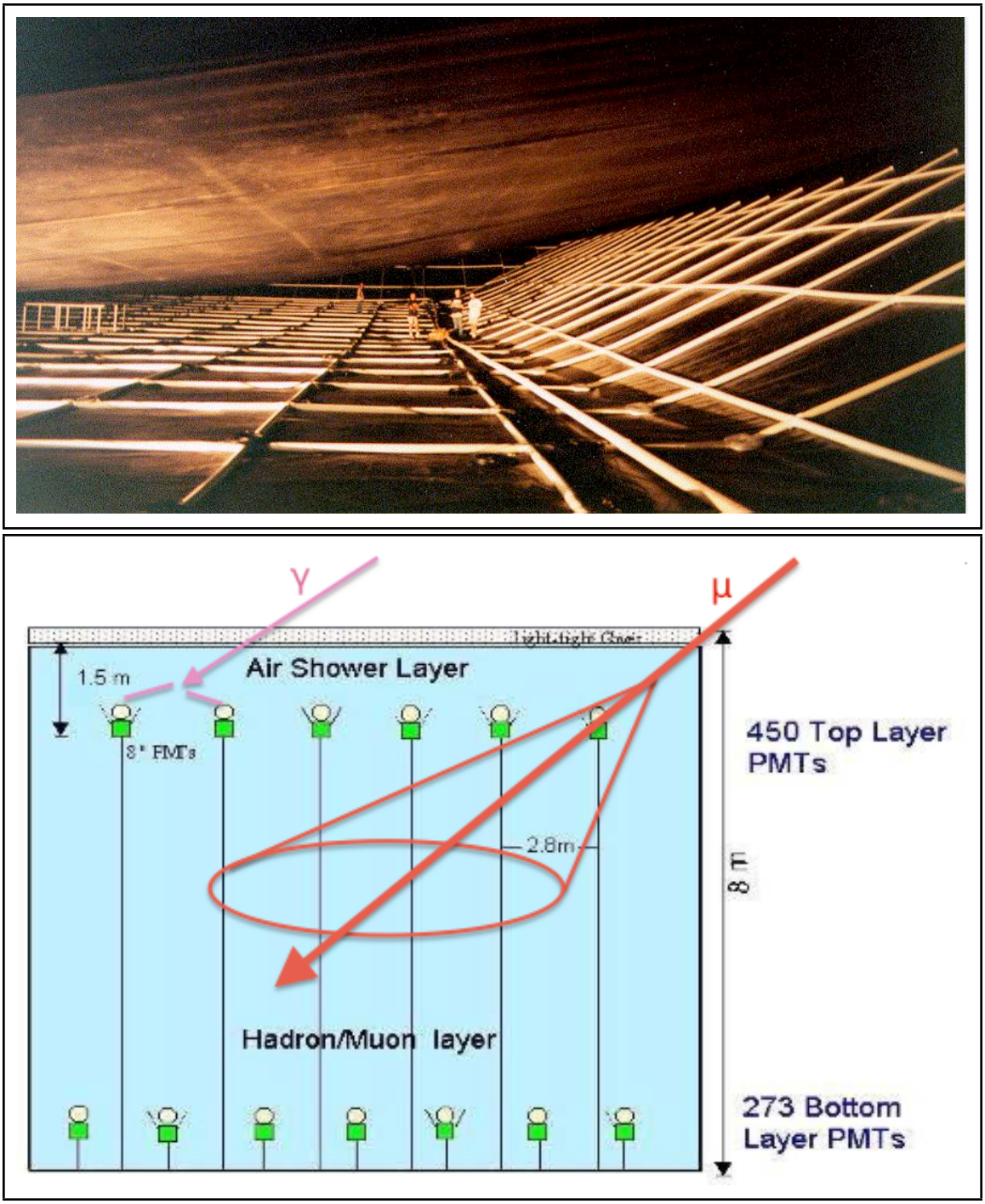

Figure 4.2: (Top) Inside view of the Milagro detector before it was filled with water. The grid of PVC pipe in which the PMTs will be mounted and the light-tight cover can be seen. (Bottom) Cross sectional schematic of the PMT layout of the Milagro pond with an incoming muon's Čerenkov cone and an incoming photon.

in an air shower were absorbed before reaching this layer, only muons and hadrons were able to penetrate and shower near this layer. Muons of energies as low as 1.2 GeV reached the muon layer in Milagro.

The water in Milagro was initially obtained from a fresh water well at the site of the detector and was constantly recirculated at a rate of 200 GPM. During recirculation, the water was filtered through a charcoal filter, a 10 μm filter, a 1 μm filter, a carbon filter, and a 0.2 μm filter to maintain transparency. In addition, the water passed through a UV filter before returning to the pond to prevent any biological growth. To ensure good quality of the water, measurements of the attenuation length were made periodically, the latest had shown an attenuation length of 17 m at 325 nm. The bottom of the pond was lined to keep contaminants out of the filtered water.

4.3 Electronics and Data Acquisition System

The PMT cables were routed out of the pond and subsequently fed through a patch panel (each containing 16 tubes), the signals then traveled to an underground conduit containing the electronics. Each patch was first processed by a custom 16 channel front end board (FEB) that read in the pulse signal from each PMT and distributed the high voltage to each tube. The FEB then processed the signal from each PMT and sent it to the digital boards where timing and pulse height information was prepared for digitization.

To determine the arrival time and charge of a signal in a PMT, the time-over-threshold (TOT) technique was used (Falcone, 2001). The TOT method measures the time a pulse spends above a defined threshold and then relates this time to the size of the signal in the PMT. A more straight-forward way of doing this would have been to pulse height analyze the signals, but due to high cost and the high event rate in Milagro the TOT method was chosen. Pulse height analyzers (PHAs) were not used in Milagro with the exception of calibrating the TOT. The event size and data size were reduced since the time-to-digital (TDCs) contained the pulse height and timing information without the need for a pulse height analysis.

A disadvantage of the TOT technique was that it did not provide as good a measurement of the pulse size as a PHA due to the pulses rising and falling at an exponential rate in time. However this problem was alleviated somewhat by the dynamic range of the TOT being superior to a PHA. Another problem with the TOT technique is that pre-pulses and after-pulses lead to errors in signal durations. To negotiate this

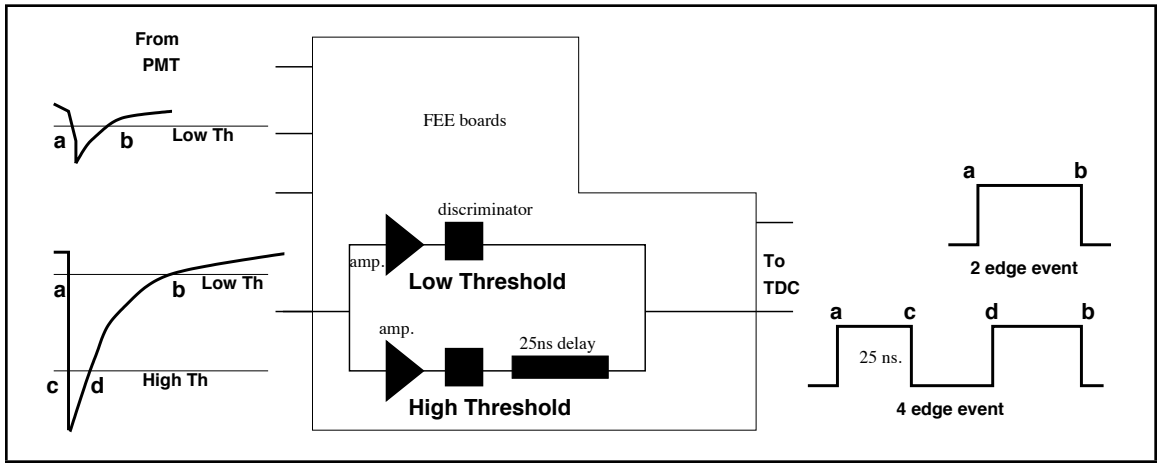

Figure 4.3: Milagro's front end boards measured the time that a signal pulse spent with its voltage in excess of two predetermined thresholds. This time could then be correlated with the amplitude of the pulse by calibrating with an ADC. (Falcone, 2001)

problem, Milagro had two independent thresholds used to differentiate between large events (more likely to have associated pre-pulses) and small events.

In the FEB, the signal from each PMT was split and sent to high gain (~ × 7) and low gain (~ × 1) amplifiers (Atkins et al., 2000). The amplified signals were then sent to a discriminator with preset PE thresholds. The signal from the high gain amplifier was sent to a low threshold discriminator with a ~1/4 PE threshold. The signal from the low gain amplifier was split in two, one part went to a high threshold discriminator with a ~5 PE threshold, and the other went to an output connected to an external PHA for calibration purposes. Whenever the PMT pulse crossed either of the low or high thresholds an edge was generated (Figure 4.3). For a pulse that crossed only the low threshold, two edges were generated. For a pulse that crossed both the low and high thresholds, four edges were generated.

The output of the low and high threshold discriminators were then sent to the digital boards. The digital boards multiplexed the signals from the low and high threshold discriminators, and provided triggering and monitoring information. Each PMT signal crossing a discriminator threshold generated a 300 ns pulse with a 25 mV amplitude (Abdo, 2007). These data were digitized using LeCroy 1887 FASTBUS TDC modules. Each of these modules contained 8 event buffers and 96 channels that could each record up to 16 edges per event with 0.5 ns resolution. The time of each event was recorded by using a latched GPS clock.

After digitization, the data were read out with a FASTBUS smart crate controller (FSCC). The FSCC transferred the data to a pair of dual ported Versa Module Eurocard

(VME) memory modules, which allowed for the simultaneous reading and writing of data. An SGI Challenge L multi-CPU computer was responsible for reading the data from the memory boards over the VMEbus, and controlled the operation of the detector electronics (Abdo, 2007). The system was controlled remotely over the internet, and in cases that required human intervention, the automated system was capable of sending an alert via pager carried by the collaboration member on active shift duty. This system allowed Milagro to operate with less than 0.5% dead time.

4.4 Data Types

The main datasets for the Milagro detector were the triggered rates, used to analyze very-high-energy gamma rays (>100 GeV) and resolve their arrival directions using event reconstruction algorithms based on PMT timing. This required a large number of AS layer PMTs to trigger (50-70) within 200 ns in order to identify the arrival direction and species of the primary particle. However, the energy threshold for protons in this data channel was ~50 GeV, well above the energies produced in an SEP event. For more on Milagro as a gamma-ray observatory see Atkins et al. (2003), and Abdo et al. (2007, 2008).

The scaler datasets in Milagro recorded variations of low and high threshold hits in individual PMTs, and counted these hits similar to a NM. Although these rates were recorded every second, each 16-tube patch would need to be summed over all tubes to give a 16 second count rate. In addition to these low and high threshold scalers were data

channels consisting of discriminations of the analog sum of all AS layer low threshold hits. These multiplicity channels contained 8 levels of discrimination, corresponding to: 6, 8, 10, 12, 16, 25, 32, and 40 pmt multiplicity. The multiplicity channels were recorded every second, and would also need to be summed over all 16 tubes in each patch, providing 16 second rates.

The environment monitoring system (EMS) was used to monitor the status of many aspects of the observatory and its surrounding environment. The EMS recorded meteorological information including temperature, barometric pressure, humidity, wind speed, and precipitation. In addition, pond water characteristics such as depth, recirculation flow rate, pressure within the filtration system, water temperature status of PMTs and their associated high voltage, scaler counter rates from an independent CAMAC system, and trigger rates of the detector were also recorded. All of these data, updated at ~160 second intervals, could be monitored remotely from a web page, and the data were archived.

4.5 Simulating the Milagro Detector

4.5.1 Monte Carlo Simulations

The first stage in determining the Milagro detector's response to cosmic rays is to simulate the production and propagation of cosmic-ray induced air showers through the atmosphere. This is done using the CORSIKA (Cosmic Ray Simulations for Kaskade -

version 6.5021) software package (Heck, 2010). The simulation begins with the first interaction of the primary particle in the atmosphere, followed by the subsequent interactions of the secondary particles in the shower down to ground-level (in this case the Milagro altitude, 2650 m). In order to obtain enough statistics, especially at lower energies near the rigidity cutoff due to the soft proton spectra in GLE events, hundreds of millions of CORSIKA showers were generated. Proton showers were thrown over a zenith angle range of 0-70° to simulate isotropic pitch-angle distributions, and fixed overhead at 0° to simulate an anisotropic pitch-angle distribution. Showers were simulated at logarithmically spaced energies ranging from 3.13-100 GeV for both pitch-angle distributions.

The simulation of air shower particles incident upon the detector was done using the GEANT4 (Geometry and Tracking) software package (Agostinelli et al., 2003). Using the CORSIKA shower results at ground-level, GEANT4 propagated these showers

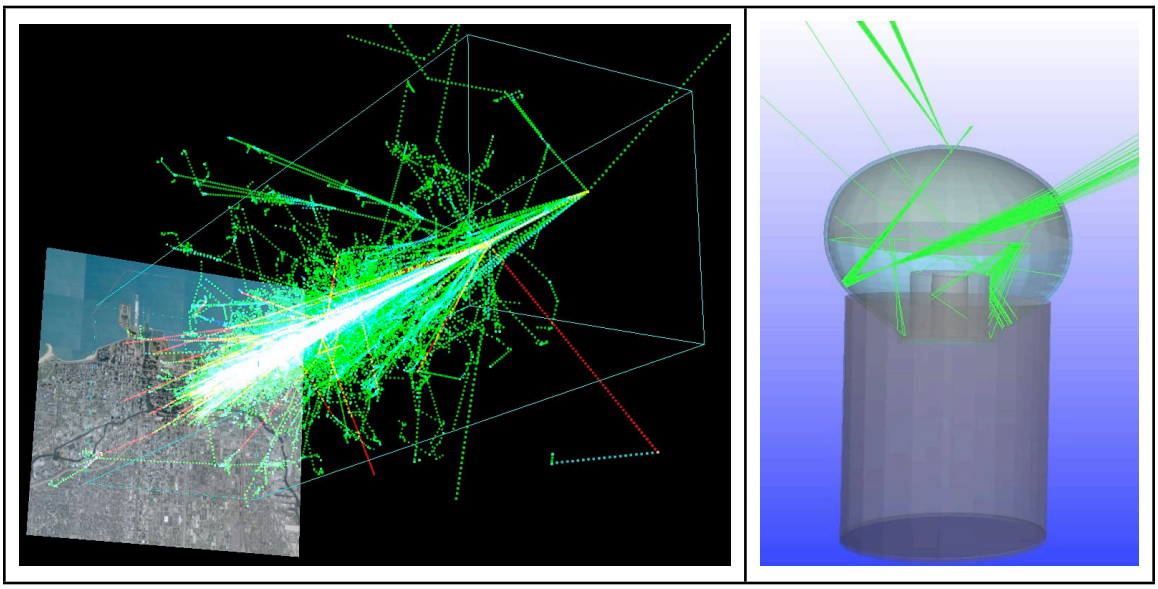

Figure 4.4: (Left) A cosmic-ray proton's simulated interactions in the atmosphere using CORSIKA, an 8 km × 8 km ground map of Chicago is included for reference. (Right) Simulated light in one of Milagro's Hamamatsu PMTs using GEANT4 (figure courtesy of Vlasios Vasiliou).

through a model of the Milagro detector. The interactions of the secondary particles in the shower, such as Čerenkov light production by relativistically charged particles traveling in water, pair production of electron-positron pairs from gamma rays, hadronic interactions, and other interactions were all simulated with GEANT4. The core positions of the CORSIKA showers were thrown randomly over a user defined surface centered on the pond. For each PMT hit, the GEANT4 output included the number of PEs, their arrival times, and the position of detection on the face of the photocathode.

4.5.2 Simulating the Cosmic Ray Background

Milagro's ability to detect air showers was not limited to the physical size of the instrument. Effective area is a measure of the effectiveness an instrument has in detecting particles and is defined as

$$A_{eff} = \frac{N_{Hit}}{N_{Throw}} A_{Throw} \tag{4.4}$$

where A_{Throw} is the area over which the shower cores are distributed, N_{Hit} is the number of hits in the detector, and N_{Throw} is the number of primary particles thrown. Effective area is not to be confused with the efficiency of the detector, although they are related. For example, a detector that is 100% efficient to a radius of 100 m and 0% efficient elsewhere will have an A_{eff} of $1.00 \times \pi(100\text{ m} \times 100\text{ m})$, or 3.14×10^4 m^2. However, a detector that is 2% efficient everywhere out to a 1 km radius will have an A_{eff} of $0.02 \times \pi(1{,}000\text{ m} \times 1{,}000\text{ m})$, or 6.28×10^4 m^2.

To ensure that the Monte Carlo showers were thrown over a large enough area we progressively increased the throw area until the effective area reached an asymptotic value. For the Milagro prototype, Milagrito, this area occurred over a rectangular surface at approximately 7,000 m × 7,000 m (Falcone, 2001). Preliminary simulations in Milagro (referred to as preliminary for reasons described in section 4.5.4) for both isotropic and anisotropic pitch-angle distributions were thrown over circular areas out to a radius of 30,000 m. The asymptotic value was reached at a radius of ~10,000 m, slightly larger than Milagrito.

As discussed in section 2.1.1, the cosmic ray background is dominated by hydrogen (~90%), however there is a significant contribution from helium (~9% by number). For our purposes, helium could be treated as four separate primary particles (the total momentum of the alpha particle is twice that of hydrogen at the same rigidity due to its charge), enabling an estimate of the simulated cosmic ray background to be a factor of 13/9 that of the simulated isotropic proton background.

The scaler effective area curves (also called specific yield functions (SYFs)) were represented as a series of power-laws in rigidity

$$Y(P) = \sum_{i=1}^{n} A_i P^{\alpha_i} \tag{4.5}$$

Equation 4.5 can be rewritten in terms of energy using the relationship in equation 6.12. Using these SYFs and the differential energy spectrum for cosmic-ray protons (Haino et al., 2004), expressed as

$$\frac{dN}{dE} = 0.315\left(\frac{E}{50GeV}\right)^{-2.74} (m^2 \cdot sr \cdot s \cdot GeV)^{-1} \tag{4.6}$$

Data Channel	Simulated Rate (Hz)	Measured Rate* (Hz)	Scale Factor
Low Threshold	$1.8 \times 10^7 \pm 1$ x 10^6	$7.81 \times 10^6 \pm 1.5$ x 10^6	2.3 ± 0.13
High Threshold	$2.4 \times 10^6 \pm 2$ x 10^5	$1.25 \times 10^6 \pm 2.0$ x 10^5	1.9 ± 0.35
6-PMT	$9.7 \times 10^5 \pm 1$ x 10^5	$2.66 \times 10^5 \pm 3.5$ x 10^4	3.7 ± 0.61
8-PMT	$6.7 \times 10^5 \pm 6$ x 10^4	$1.64 \times 10^5 \pm 2.7$ x 10^4	4.1 ± 0.77
12-PMT	$3.3 \times 10^5 \pm 4$ x 10^4	$7.95 \times 10^4 \pm 1.9$ x 10^4	4.2 ± 1.1
16-PMT	$1.9 \times 10^5 \pm 3$ x 10^4	$5.38 \times 10^4 \pm 1.3$ x 10^4	3.55 ± 1.0
25-PMT	$4.9 \times 10^4 \pm 3$ x 10^4	$1.30 \times 10^4 \pm 3.2$ x 10^3	3.8 ± 2.5
Climax NM	$1.3 \times 10^3 \pm$ N/A	$8.50 \times 10^1 \pm 1.9$ x 10^1	15.3 ± 4.6
Durham NM	$1.1 \times 10^3 \pm$ N/A	$1.76 \times 10^2 \pm 2.8$ x 10^1	6.3 ± 2.1
Mt. Washington NM	$1.3 \times 10^3 \pm$ N/A	$4.80 \times 10^2 \pm 9.5$ x 10^1	2.7 ± 0.8

Table 4.1: Simulated vs. measured cosmic ray background rates in Milagro (measured rates were taken before the 2005 January 20 GLE, an analogous set of scale factors was obtained for the 2001 April 15 GLE).

The expected rates in each scaler channel were computed and compared to the measured rates (Table 4.1). The expected rates were given by

$$\int_{\theta=0^\circ}^{\theta=70^\circ} \int_{E_{cut}}^{\infty} E \times Y(E) \frac{dN}{dE} dE \, d\Omega \tag{4.7}$$

4.5.3 Sensitivity to Pitch-Angle Distributions

Preliminary simulations were distributed randomly over a circular area extending out to a 10 km radius. Showers from primary particles at lower energies (below ~10 GeV) were necessary to complete the SYFs for the Milagro scaler channels, but producing hits in the higher multiplicity channels (*e.g.,* 16-PMT and 25-PMT) from these lower energy protons was difficult. Roughly 100 billion showers for each pitch-angle distribution were needed to complete the 16-PMT yield function, and the 25-PMT yield function could not be extended below ~6 GeV. This was not a problem for the 2001 April 15 event, the GLE was only present in the low and high threshold channels. However,

the 2005 January 20 event was the most intense at ground-level in 50 years, and increases over background were recorded in all multiplicity channels up to and including 25-PMT. To utilize the full capability of the Milagro detector to analyze GLEs, the 25-PMT channel yield function would be needed down to the cutoff rigidity. Continuing along the path of the preliminary simulations would require a 10-fold, if not 100-fold, increase in showers produced, thus being an unreasonable approach. A solution to this problem would be provided by the simulations already completed.

Showers produced by primary particles with high zenith angles (closer to the horizon) that reach ground-level are more likely to trigger multiple PMTs (Figure 4.2). This is because a single muon can go through more radiation lengths in the pond before reaching the AS layer depth, thus the Čerenkov cone will illuminate more PMTs. For low (near vertical) zenith angles a single muon is more likely to penetrate below the AS layer before its Čerenkov cone can spread out to hit multiple PMTs. Multiple muons at low zenith angles are needed to reach ground-level and interact with the pond, requiring the shower core to be relatively close to the detector. Multiple PMT hits for low zenith angles would then be dominated by shower cores in close proximity to the pond, with less contribution from shower cores at radial distances >1 km. For high zenith angles, higher multiplicity events could come from either scenario. To investigate this quantitatively, cuts on the preliminary simulations were made, separating the shower cores into two throw distance regions: 0 m - 1 km, and 1-10 km.

The ratio between the effective area of the >1 km thrown cores to the total effective area from all cores was calculated as a function of energy for both pitch-angle

distributions. As predicted, the isotropic simulation set had a much larger contribution from >1 km cores than the zenith simulation set. In addition and perhaps most importantly, we used this relationship for differing PMT multiplicities and compared them to data from the 2005 January 20 event. Using the ratios at GLE energies (<10 GeV), we normalized these ratios to that of the 6-PMT channel. For zenith distributions the ratio trends smaller for increased multiplicity. (Figure 7.5).

Since the cosmic ray background is isotropic, an anisotropic event produces a larger signal above background for lower multiplicity channels with respect to the higher multiplicity channels. Therefore, the count rate increases over background for different Milagro multiplicity channels reveal the pitch-angle distribution present at the time of an event.

4.5.4 Simulating Milagro for Ground-Level Enhancements

To effectively study GLE events, which characteristically have soft spectra at ground-level rigidities, the sensitivity of Milagro to SCRs at rigidities near the cutoff were crucial. Preliminary simulations were unable to produce enough statistics for the 25-PMT scaler below 6 GeV, a major problem for analyzing the largest event detected by Milagro, the 2005 January 20 GLE, which produced an increase over background in this channel. However, these preliminary simulations did reveal trends in the effective area as functions of energy and throw distance.

By taking advantage of Milagro's higher efficiency to shower cores in close proximity to the pond, an extrapolation procedure for the SYFs of the higher multiplicity channels was developed. Showers at logarithmically spaced energies from 3.13-35 GeV were thrown in progressively larger annuli out to a maximum throw distance of 10 km. The total effective area was then a sum of the effective areas from each annulus. The relationships between the effective area from 0-100 m with respect to other annuli such as 100-300 m, 300 m - 1 km, 1-3 km, and 3-10 km as a function of energy were all documented.

To extrapolate the 25-PMT channel for events out to 10 km at rigidities comparable to the cutoff, our simulations were focused close to the detector (0-100 m) where the efficiency was highest. We then compared the result in this region to other

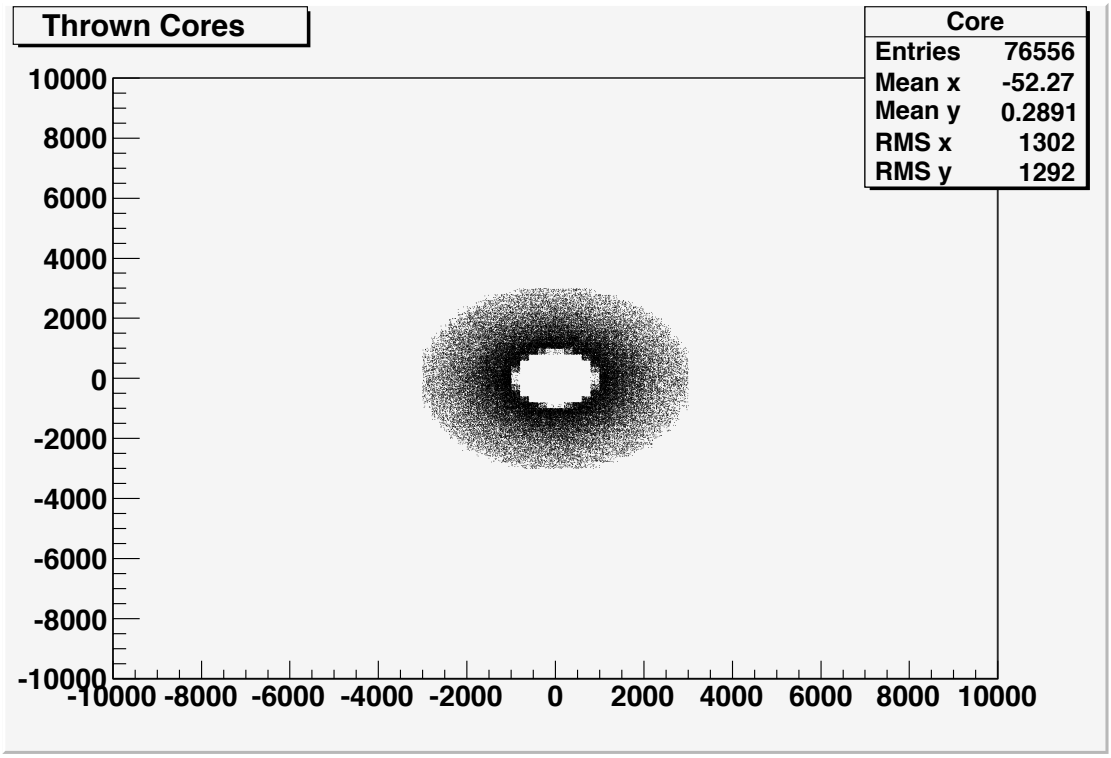

Figure 4.5: 2-D map of shower cores thrown in an annulus 1-3 km from the center of the pond. This particular map is for 25 GeV primary particles.

multiplicity channels. For example, the ratio of the 16-PMT A_{eff} to the 25-PMT A_{eff} as a function of inverse energy is given in Figure 4.6. The data fit nicely to an exponential. Although the 300 m - 1 km region does not have a final data point corresponding to 3.13 GeV, the exponential fit estimates what the value of the ratio will be with respect to the completed 16-PMT result. The results of this extrapolation procedure can be seen in Figure 4.7, and are given in more detail in Figures A.1-A.4.

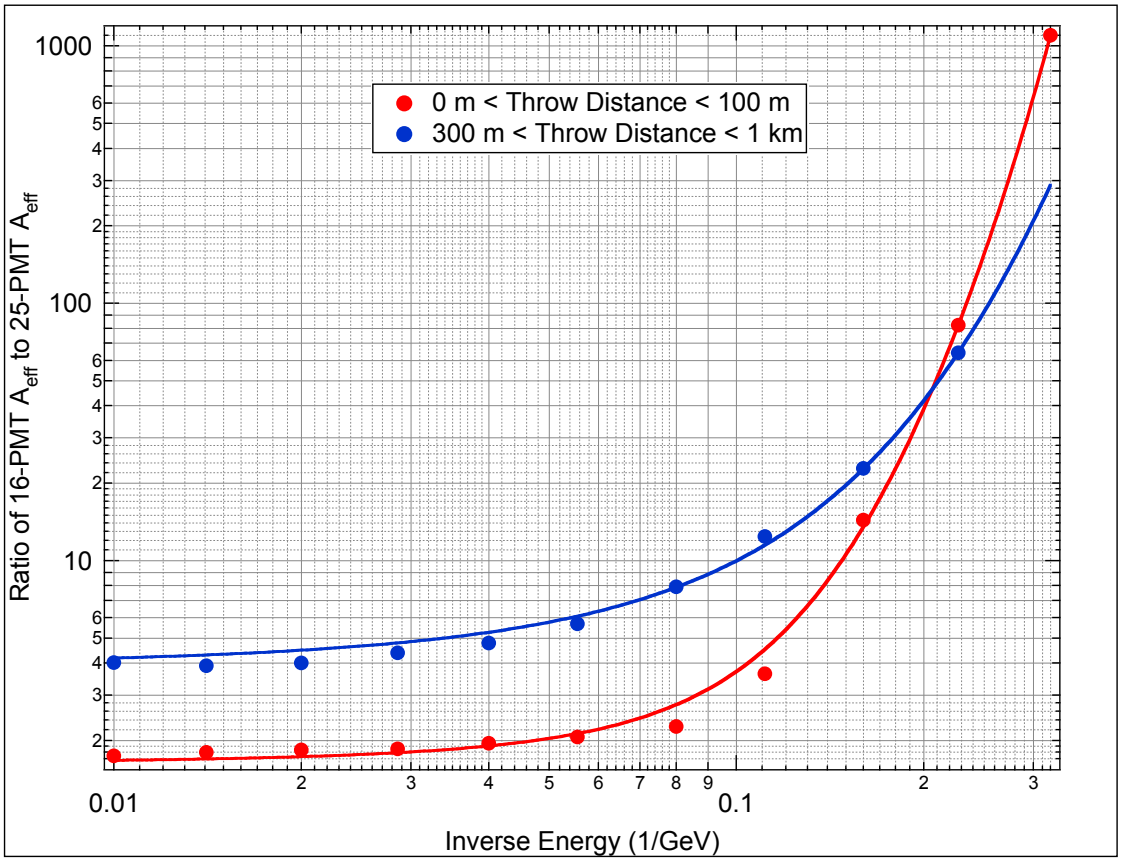

Figure 4.6: The effective area ratios for the 16-PMT and 25-PMT channels as a function of inverse energy. The exponential relationship is used to extrapolate the specific yield function for the 25-PMT channel.

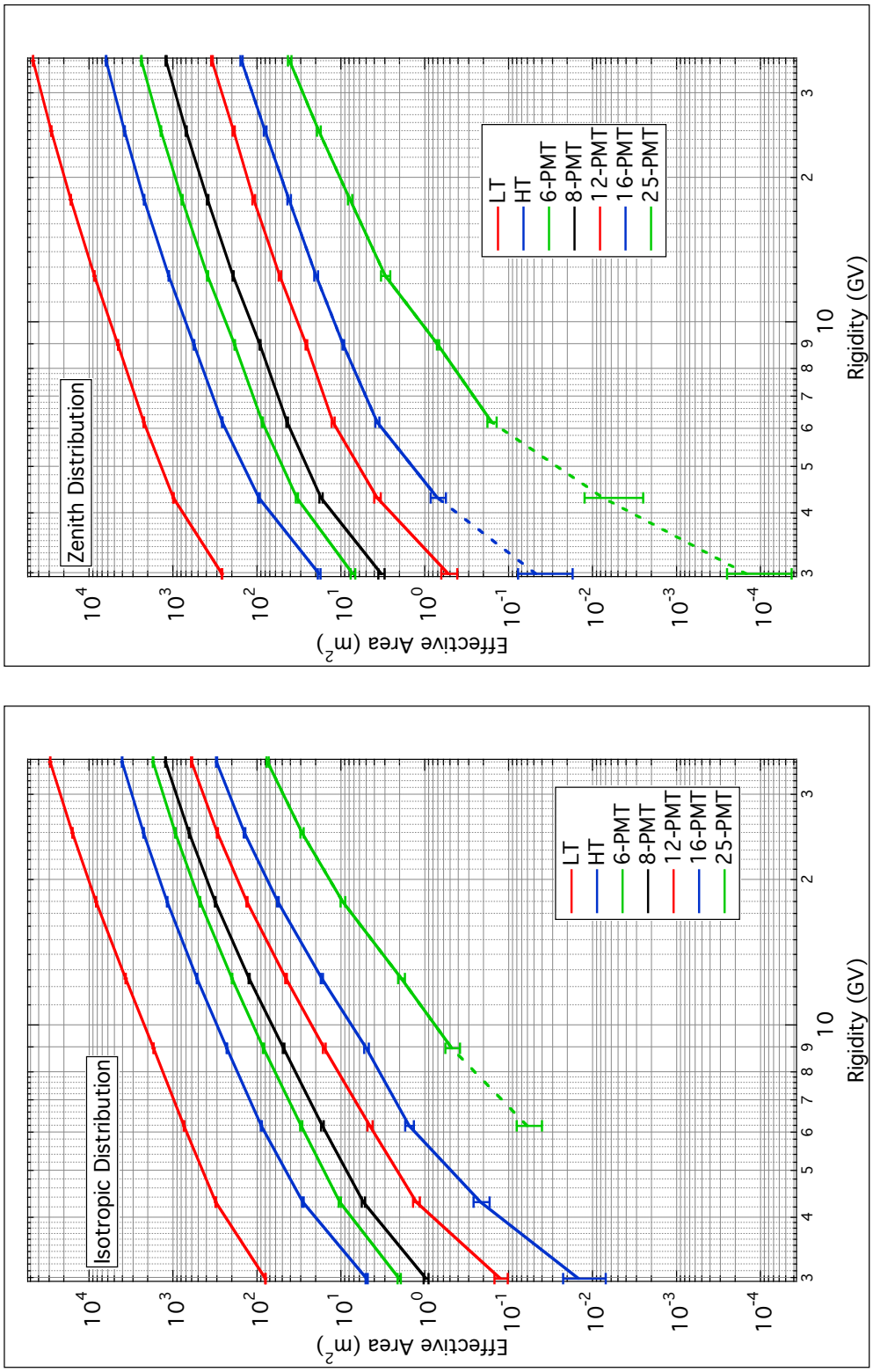

Figure 4.7: Milagro scaler channel specific yield functions for an isotropic (bottom) and an anisotropic (top) pitch-angle distribution. By throwing the shower cores in apertures progressively farther from the center of the detector, we could extrapolate the higher multiplicity specific yield functions to lower rigidities.

4.6 Comparison to Other Instruments

Using the Čerenkov emission of charged particles in water, Milagro was able to detect nearly all particles that crossed the surface of the pond. In contrast, typical extended air shower array detectors cover <1% of the total area over which they are distributed (see section 2.3.3). This feature greatly lowered the energy threshold for Milagro while still retaining the abilities of an extended air shower array. Milagro operated with all-sky coverage and a very high duty cycle (>90%).

Imaging ACTs (see section 2.3.1) are more sensitive to sources than Milagro was, thus, ACTs can observe over shorter timescales with higher significance. However, ACT's duty cycles are severely limited because they must minimize background light by observing on clear moonless nights. ACTs also have a relatively small field of view, making detections of transient unknown sources difficult. Milagro was well suited for these types of studies due to its very high duty cycle and all-sky coverage (Abdo et al., 2007a, 2007b, 2008).

When functioning as a cosmic ray and GLE observatory, Milagro was closely related to NMs (see chapter 3). Like Milagro, NMs operate above thresholds restricted by the cutoff rigidity, however Milagro possessed multiple channels with effective areas several orders of magnitude larger than that of a NM (Figures A.8, A.9). NMs are located around the globe (Table 3.2) with different rigidity cutoffs and atmospheric overburdens, the relative signals in this worldwide network of NMs can be used to determine the anisotropy of GLEs. As described in section 4.5.3, Milagro had this ability independently by utilizing the enhancement ratios between various multiplicity channels.

There are a wide array of spacecraft detectors for cosmic rays and SEPs, but the sensitivity of these instruments is limited by the size of detector capable of being launched into space. This size constraint requires long integration times to be even remotely sensitive to GeV particles. Thus, ground-based detectors such as Milagro and NMs are required to measure the spectra at GeV energies, whereas spacecraft measurements measure the spectra below GeV energies.

Chapter 5

The 2001 April 15 and 2005 January 20 Events

During its eight years of operation the Milagro detector registered strong ground-level enhancements for the 2001 April 15 and 2005 January 20 events, the latter of which was the most intense in 50 years. We will discuss spacecraft and ground-level observations for each event.

5.1 The 2001 April 15 Event

The 2001 April 15 event is associated with an X-class flare and a fast CME. The SEP intensity was among the highest in solar cycle 23 and observed by a variety of spacecrafts. Charged particles were accelerated up to several GeV, producing a GLE detected in many ground-based detectors.

5.1.1 Observations with other Instruments

The X14.4 flare associated with the 2001 April 15 event was detected by GOES-8; it began at 1336 UT and reached a maximum by 1349 UT (Figure 5.1). The

flare, located at S20°, W85°, was the largest in a group of M- and X-class flares from active region 9415 .

The Large Angle and Spectrometric Coronagraph (LASCO) instrument aboard the SOHO spacecraft detected the launch of a CME associated with the X14.4 flare (Figure

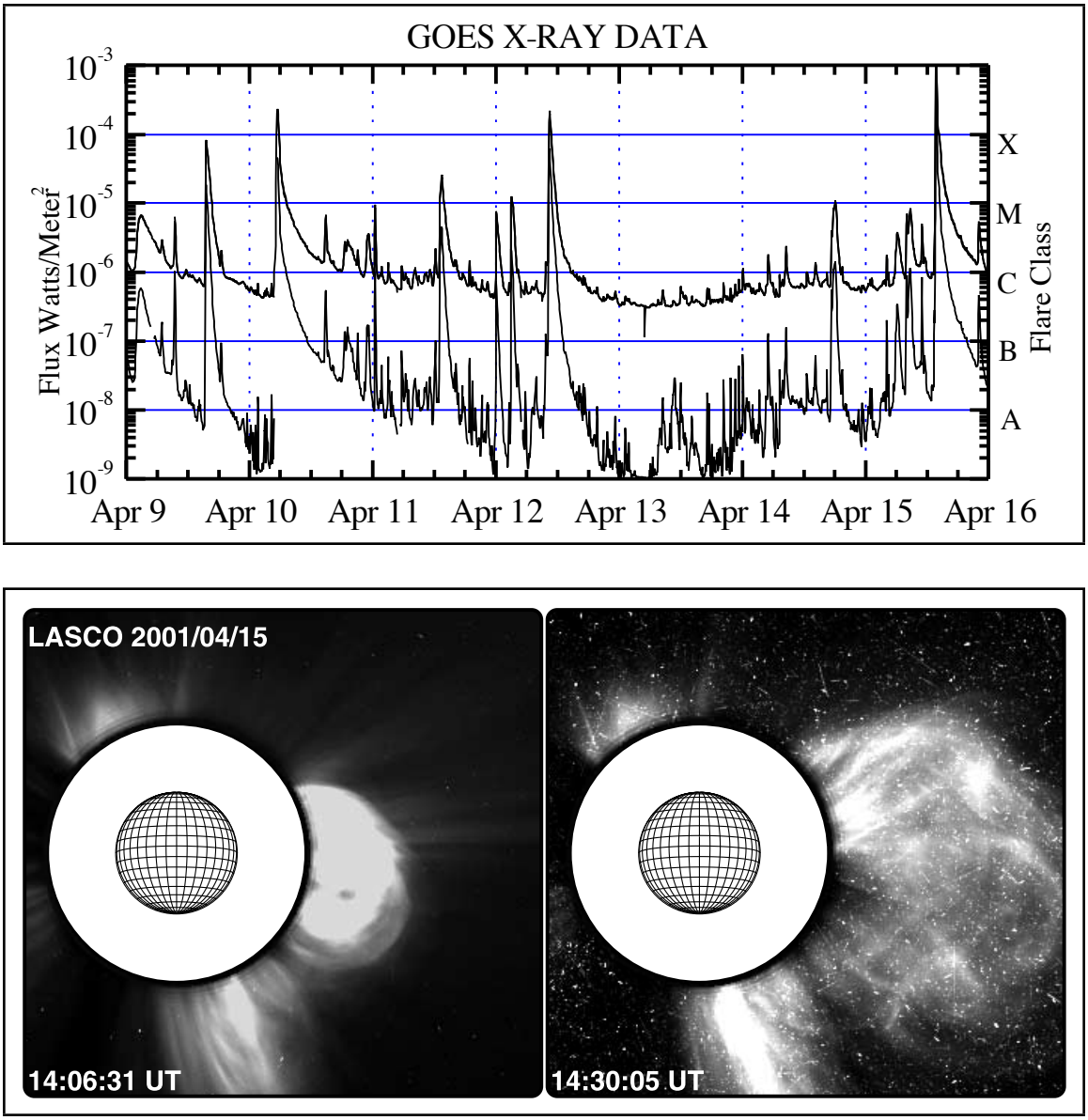

Figure 5.1 (Top) Active region 9415 produced numerous flares from April 9, 2001 to April 16, 2001, the largest being the X14.4 flare on April 15, 2001 (courtesy of NOAA). (Bottom) SOHO/LASCO images during the 2001 April 15 event (Maia et al., 2007). The CME can be seen to propagate outward from the western limb. The "snow" in the second frame is due to charged particles striking the camera.

5.1). Using LASCO's C2 coronagraph (2-6 $R_{\odot}$ field of view), a height vs. time profile resulted in a CME speed of 1200 km-s^{-1} with an extrapolated onset time of 1332 UT (Gopalswamy et al., 2003). The relatively fast CME speed is far in excess of the ambient solar wind speed, in addition there is type II radio emission during early stages of the event (Gopalswamy et al., 2003), evidence for the presence of a CME-driven shock.

The SEP profiles aboard the Interplanetary Monitoring Platform-8 (IMP-8) for the 2001 April 15 event (Figure 5.2), as well as evidence of type II radio emission associated with the fast CME, strongly indicate that particles were accelerated by a CME-driven shock. The ^{3}He/^{4}He ratio measured by the Ultra Low Energy Isotope Spectrometer (ULEIS) instrument aboard the Advanced Composition Explorer (ACE) was 0.22% at 0.5-2 MeV/nucleon (Tylka et al., 2002), only a factor of five greater than the average solar wind value of 0.041% ± 0.003% (Gloeckler et al., 1999). This ratio is much less

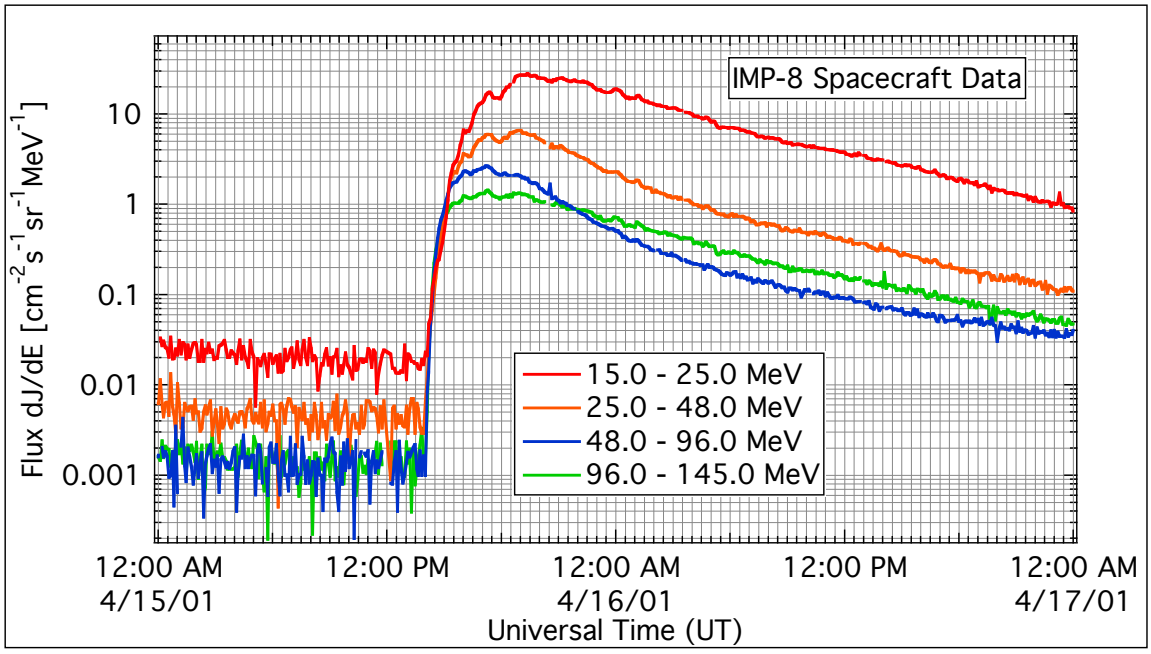

Figure 5.2: IMP-8 spacecraft data (courtesy of Dr. C. Lopate, private communication) for protons from 15-145 MeV during the 2001 April 15 event.

than that of impulsive events (Kallenrode, 2003), suggesting an acceleration region at temperatures comparable to that of the corona such as in a CME-driven shock.

The source location of both the X14.4 flare and the associated CME occurred on the western limb of the Sun, and as a result was magnetically well-connected to the Earth through the Parker spiral. Charged particles accelerated up to GeV energies were injected into interplanetary space, propagating along magnetic field lines. Shortly after the flare and CME onsets, many ground-based detectors registered GLEs due to the associated SCRs.

5.1.2 Ground-Level Enhancement

In 2001 the Sun was the in maximum phase of its cycle, and there was substantial solar activity around the time of the 2001 April 15 GLE (Figure 5.3). Active region 9415 produced numerous M-class flares from April 5-15, including at least three X-class flares with associated halo CMEs. The CME shock passages at Earth caused multiple Forbush decreases, and reduced the cosmic ray background in Climax by ~20%. The 2001 April 15 event occurred when the cosmic ray background was recovering from these decreases. For the Climax, Mt. Washington, and Durham NMs this recovery can be approximated to be linear over the short timeframe of the GLE. Therefore, a linear background subtraction for these NMs satisfactorily isolates the GLE signal from the cosmic ray background (Figure 5.4).

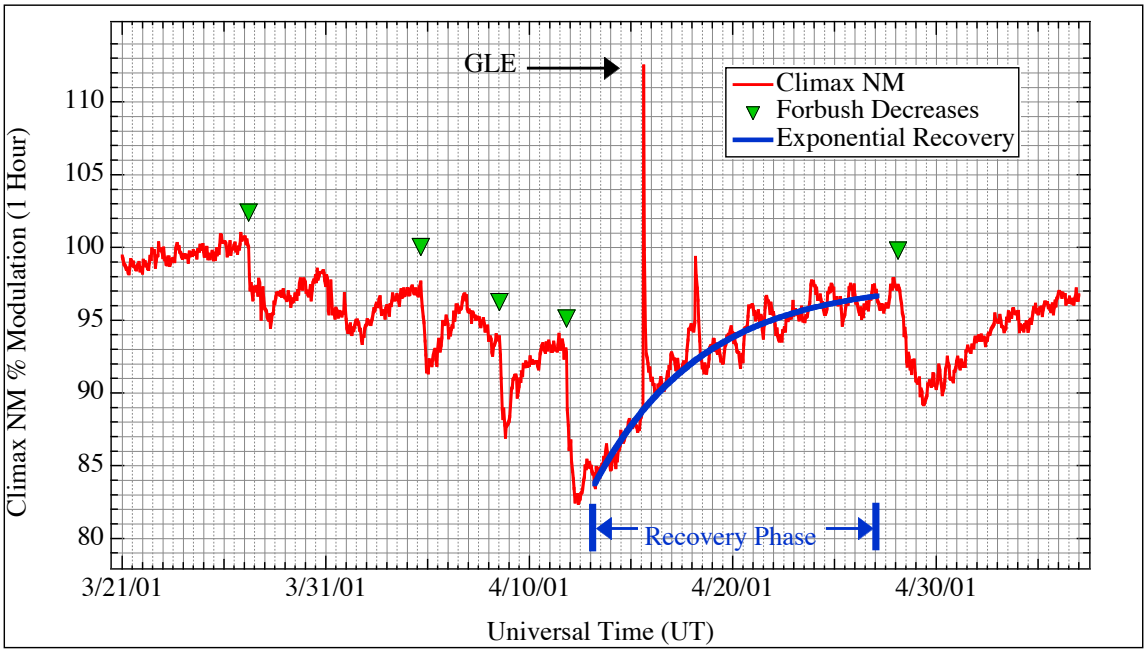

Figure 5.3: Cosmic ray intensities at the Climax neutron monitor around the time of the 2001 April 15 event. Multiple Forbush decreases lower the background rate, and the GLE signal occurs while this background is in an exponential recovery phase.

The largest increase over background in Milagro channels was only ~1.5% (Climax reached 35% in one minute data). Therefore, the background was dominated by small variations in intensity of comparable timescales to that of the GLE, rather than a longer exponential recovery. To isolate the GLE from the PCA corrected channels in Milagro, we fit a quadratic function to the background (with the event removed) for a time period of hours before and after the event (Figure 5.4).

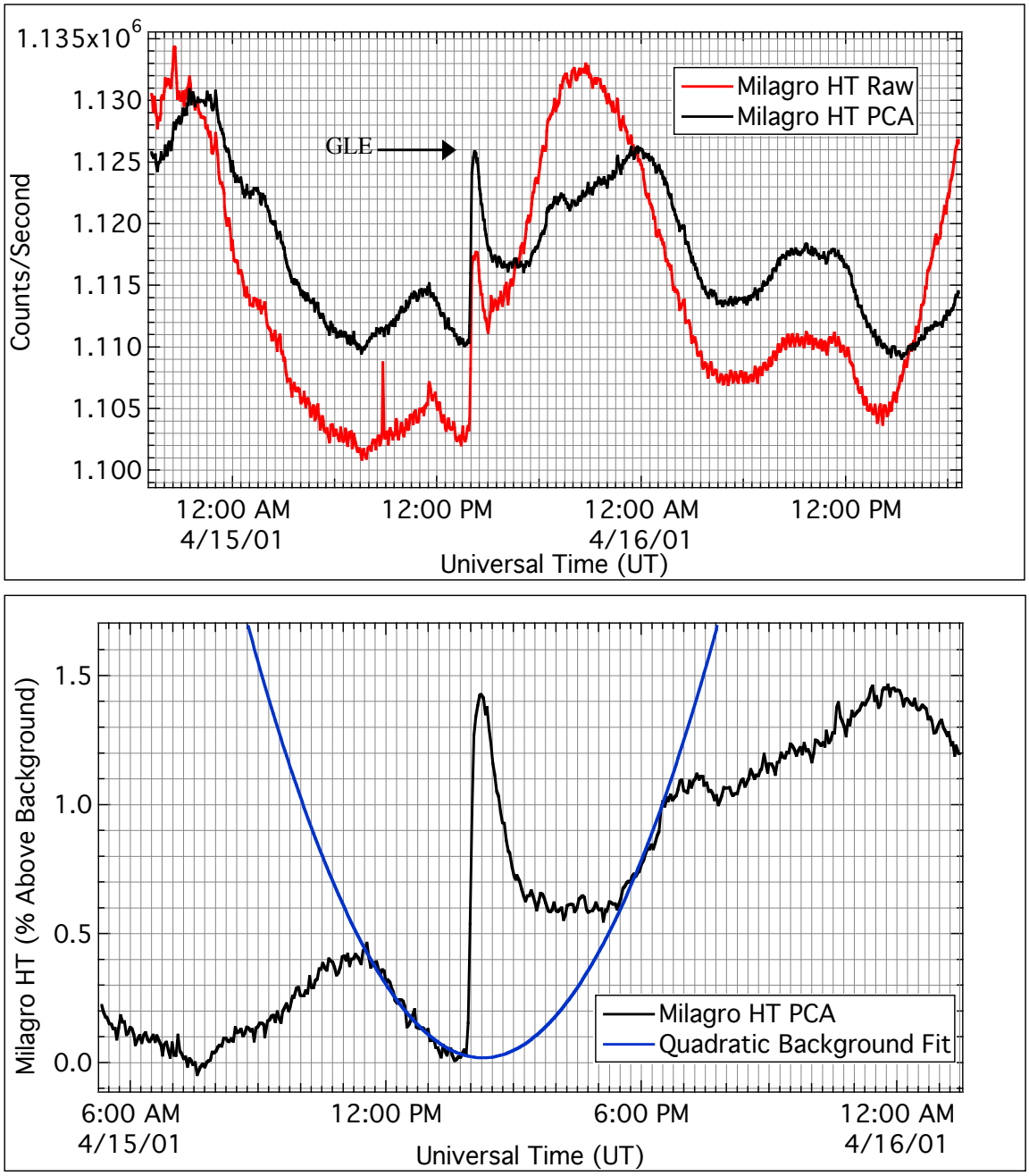

Figure 5.4: The 2001 April 15 GLE was only 1.5% above the PCA corrected background rate (top). To isolate the GLE we performed a quadratic fit to the cosmic ray background in the Milagro channels (bottom).

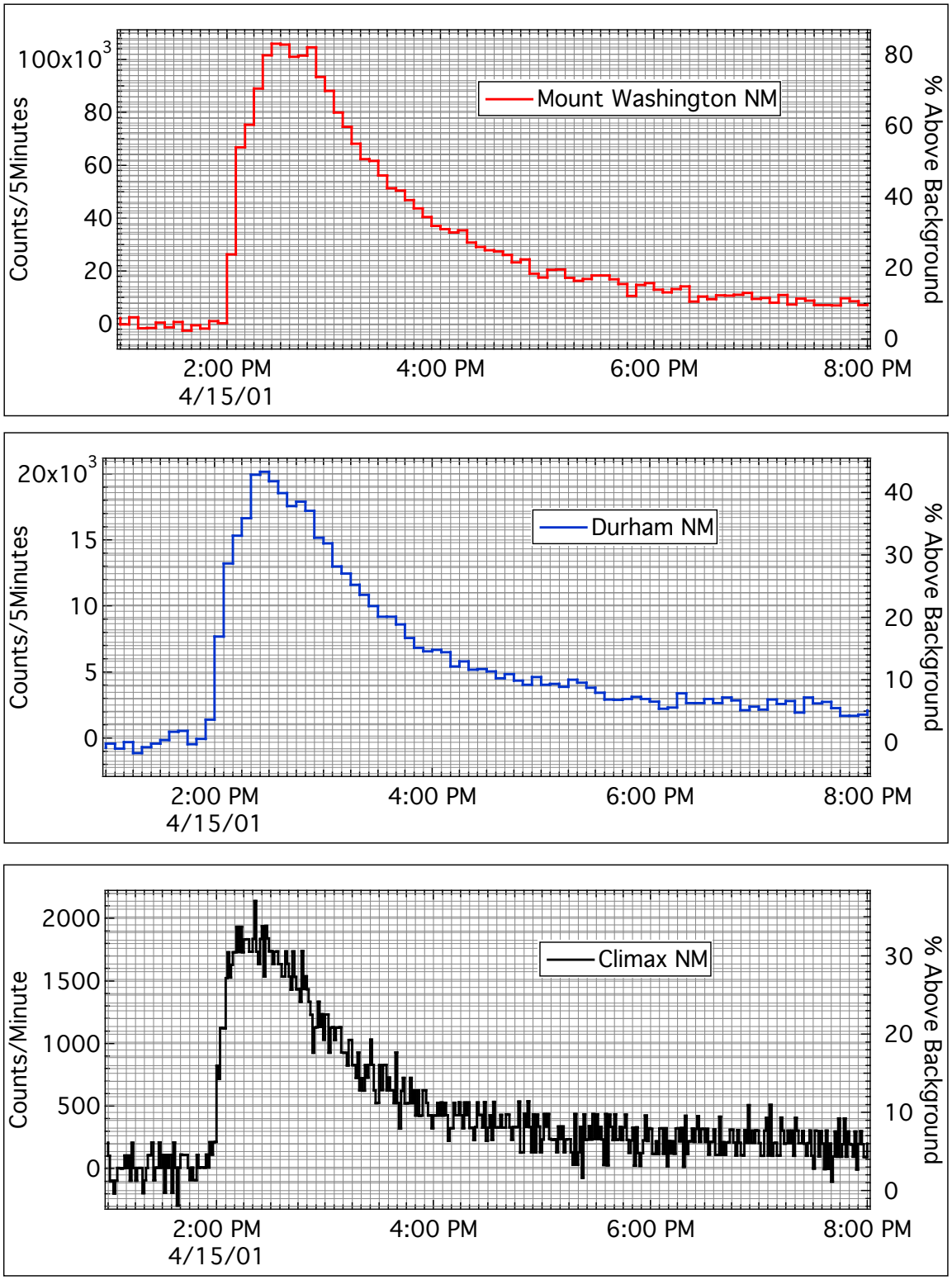

Figure 5.5: Ground-level enhancements during the 2001 April 15 event for the Mt. Washington, Durham, and Climax neutron monitors.

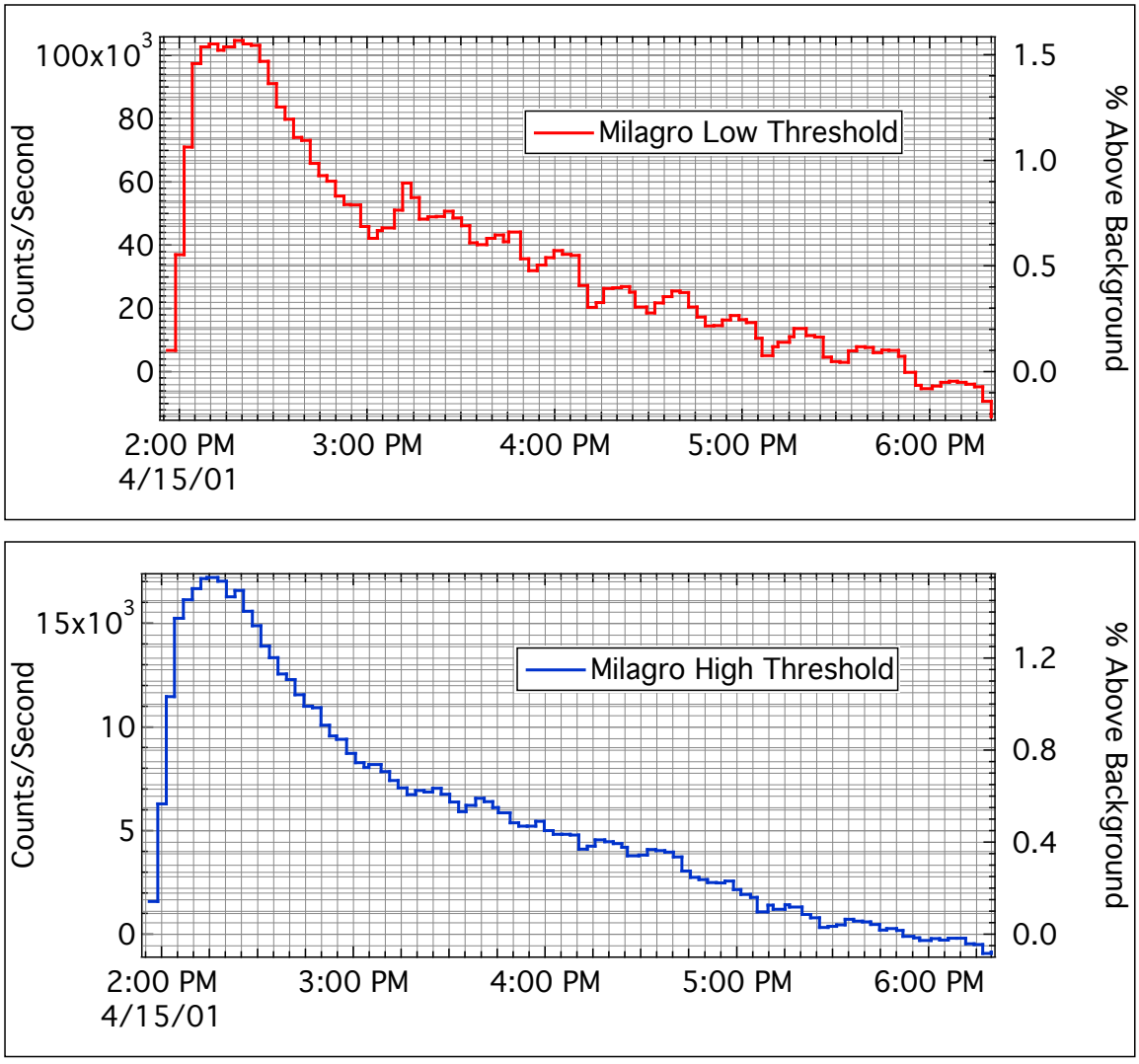

Figure 5.6: Ground-level enhancements during the 2001 April 15 event for the Milagro low and high threshold channels.

5.2 The 2005 January 20 Event

The 2005 January 20 event produced a GLE signal up to ~5,000% above background in some ground-level stations, a level not seen since the 1956 February 23 event. Its rapid evolution and high intensity distinguishes it from other events, making it significant to the field. The event is associated with an X-class flare and a very fast CME (Figure 5.7).

5.2.1 Observations with other Instruments

The X7.1 flare on 2005 January 20 was the largest of multiple M- and X-class flares originating from active region 720. It began at 0636 UT at N12°, W58°, and reached a maximum by 0701 UT. The LACSO and Extreme ultraviolet Imaging Telescope (EIT) instruments aboard SOHO captured images of the associated CME. Gopalswamy et al. (2005) reported a velocity of 3,242 km-s^{-1}, one of the fastest on record.

The event was also observed in hard X-rays by the Reuven Ramaty High Energy Solar Spectroscopic Imager (RHESSI), and in gamma rays by the Solar Neutron and Gamma Ray Spectrometer (SONG) aboard the Russian CORONAS-F spacecraft (Figure 7.8) The high-energy gamma rays (>60 MeV) are a sign of relativistic ion production. The rising edge of this data channel on the SONG instrument occurs at 0645:30 UT (more on event timing will be discussed in section 7.2.2).

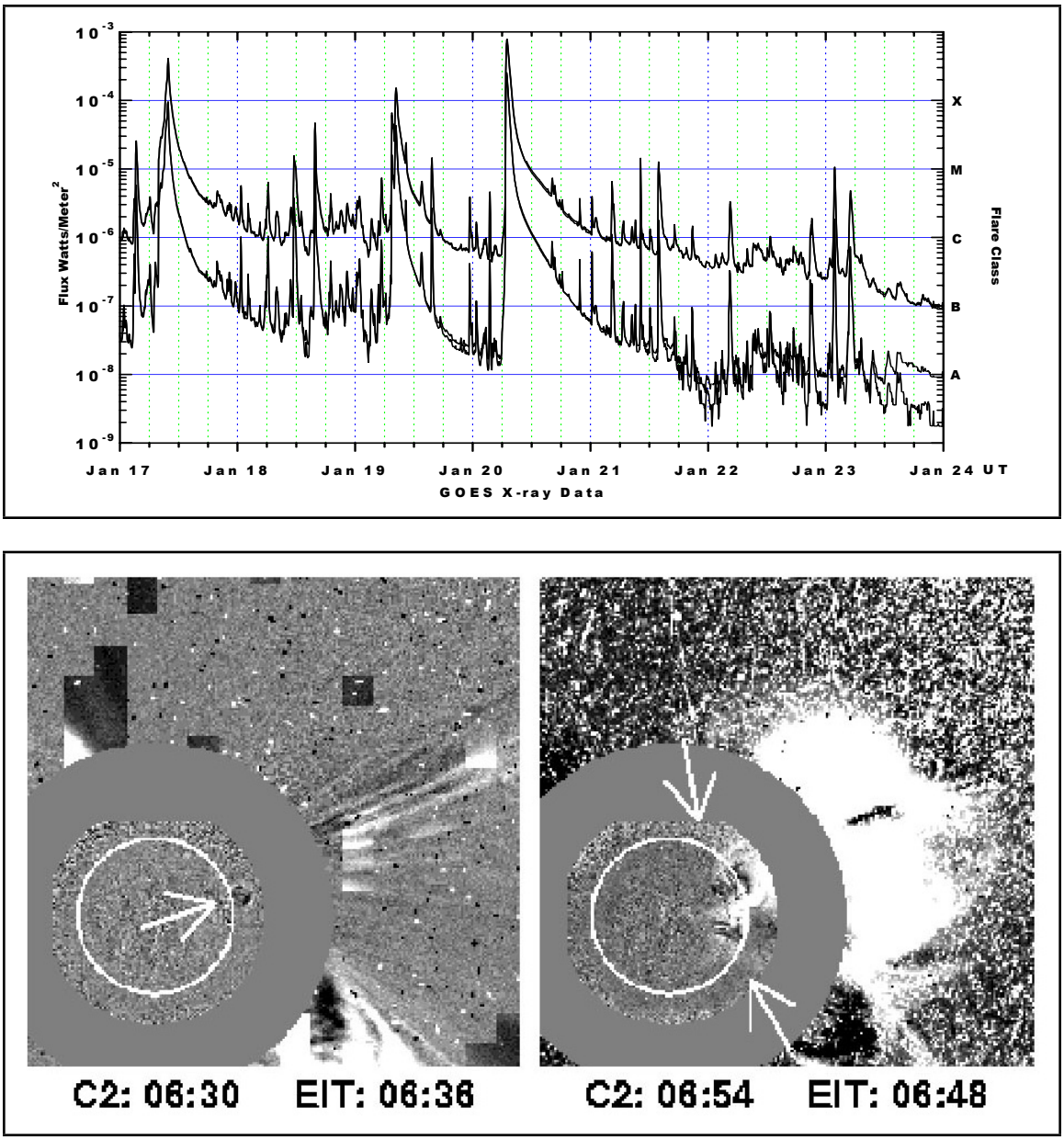

Figure 5.7: (Top) The X7.1 flare detected by GOES-10 and GOES-12 on 2005 January 20 was the largest of a group of M- and X-class flares produced by active region 720 (courtesy of NOAA). (Bottom) SOHO/LASCO images capture the CME propagating outward from the western limb, and superimposed SOHO/EIT images reveal loop structure low in the corona at 0636 UT (Gopalswamy et al, 2005). The "snow" in the second frame is due to charged particles striking the camera.

The SEP profiles for the Energetic and Relativistic Nuclei and Electron experiment (ERNE) aboard SOHO during the 2005 January 20 event (Figure 5.8), as well as evidence of metric type II radio emission coincident with the CME (Gopalswamy

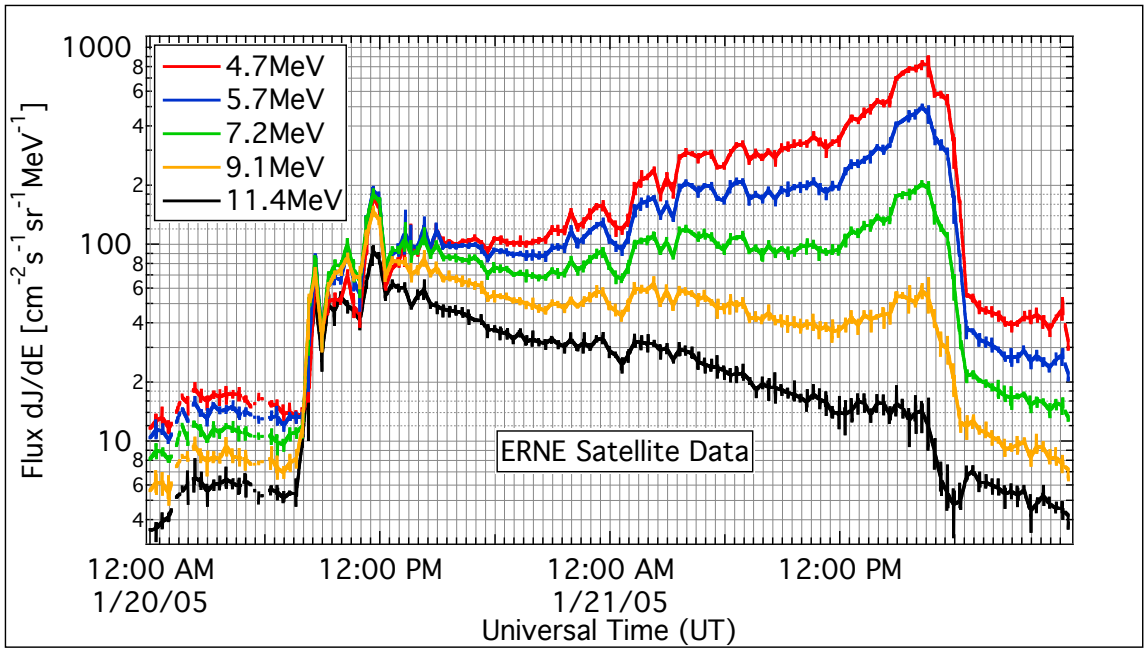

Figure 5.8: Proton intensities from 4.7 MeV to 11.4 MeV measured by the ERNE instrument aboard the SOHO spacecraft during the 2005 January 20 event (courtesy of Dr. E. Valtonen, private communication).

et al., 2005), strongly indicate that particles were accelerated by a CME-driven shock. Charge states aboard the Solar Anomalous and Magnetospheric Particle Explorer (SAMPEX) above ~25 MeV/nucleon were associated with a source temperature of ~1.6 × 10^6 K, typical of solar wind or coronal material, not flare-heated material (see section 1.5.1). In addition, the ^{3}He/^{4}He ratio during the 2005 January 20 event was reported to have an upper limit of 0.077% (Desai et al., 2006). This ratio is only a factor of two greater than a typical solar wind value (Table 1.3) and is further evidence of an acceleration region at temperatures found higher in the corona.

The very prompt arrival and extreme intensity of the highest-energy particles (>1 GeV) make the 2005 January 20 event interesting. Although there is much spacecraft evidence of coronal shock acceleration in various particle species, the anisotropy and fast timing of the >1 GeV particles in ground-level detectors continue to spawn debate on the

accelerating source (*i.e.*, flare accelerated or shock accelerated?). This will be discussed further in chapter 7.

5.2.2 Ground-Level Enhancement

Background levels in Climax were consistent before and after the GLE and the short duration of the event made a background correction for Climax unnecessary, however, background rates in Milagro were rising sharply over this short period. The background rate at the Haleakala NM (courtesy Dr. C. Lopate, private communication) provides insight to how the background in Milagro would be evolving during the GLE (Figure 5.9).

Although the Sun was approaching solar minimum in 2005, there were high levels of solar activity around the time of the 2005 January 20 event. Active region 720 produced multiple large flares from January 15 to January 20, including five X-class flares. The associated CMEs caused multiple Forbush decreases, which modulated the cosmic ray background, and the 2005 January 20 event took place during the recovery phase. The Haleakala NM and Milagro backgrounds track well with each other around the time of the 2005 January 20 GLE, but the Haleakala NM did not register an increase over background because of its high cutoff rigidity (P_c ~13 GV). We can approximate the recovery to be linear in Haleakala over the short duration of the GLE and, due to its well correlated behavior with Milagro, we performed a linear background subtraction on Milagro rates to isolate the 2005 January 20 GLE (Figure 5.9). GLE profiles for Climax,

Mt. Washington, Durham, and all available Milagro channels, are shown in Figures 5.10 to 5.12.

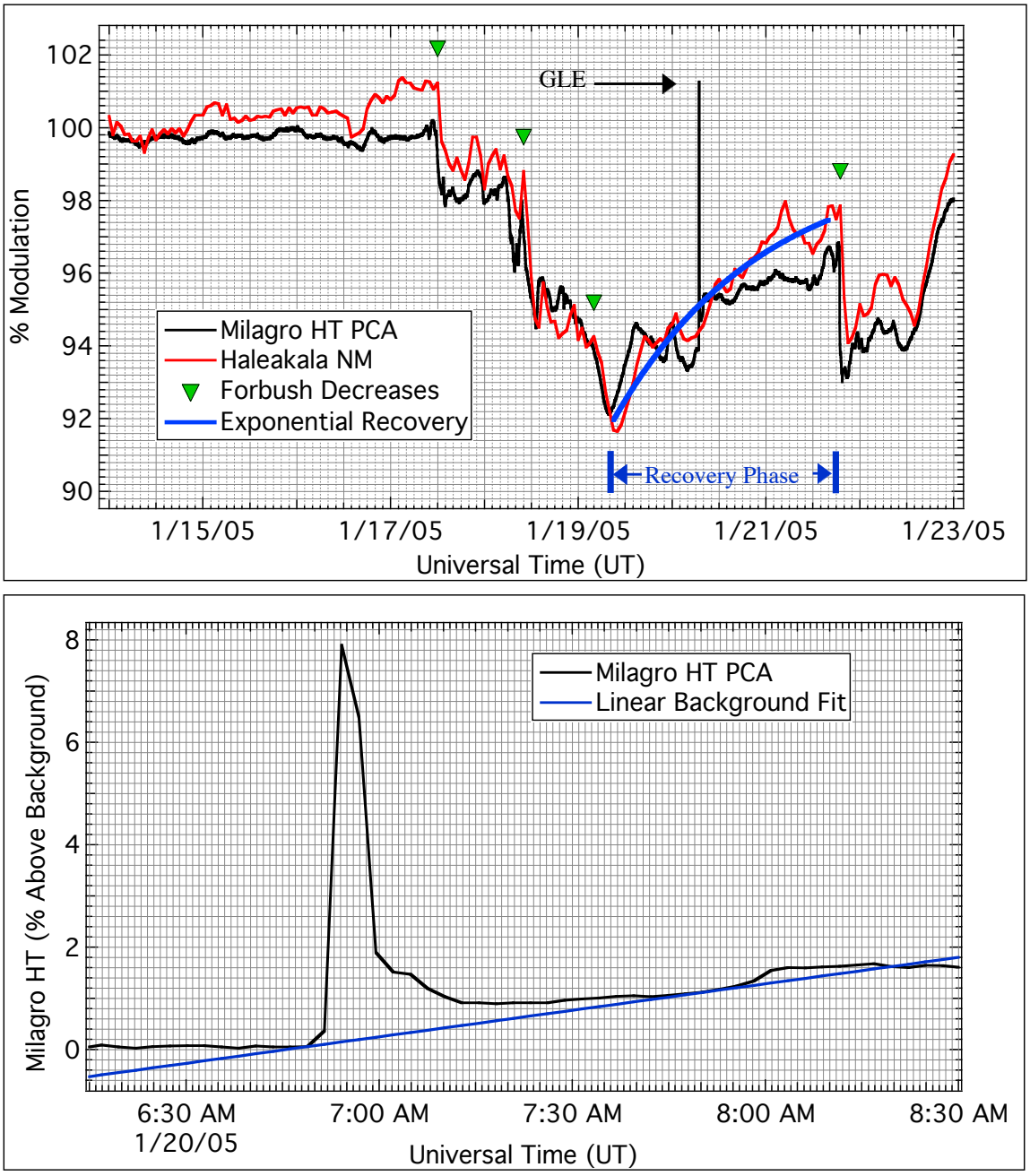

Figure 5.9: (Top) Cosmic ray intensities at Milagro and the Haleakala neutron monitor around the time of the 2005 January 20 event. Multiple Forbush decreases lower the background rate, and the GLE signal occurs while this background is in an exponential recovery phase. (Bottom) Linear background subtraction to isolate the 2005 January 20 GLE from the cosmic ray background in the Milagro high threshold channel, a similar background subtraction was performed for all available Milagro channels.

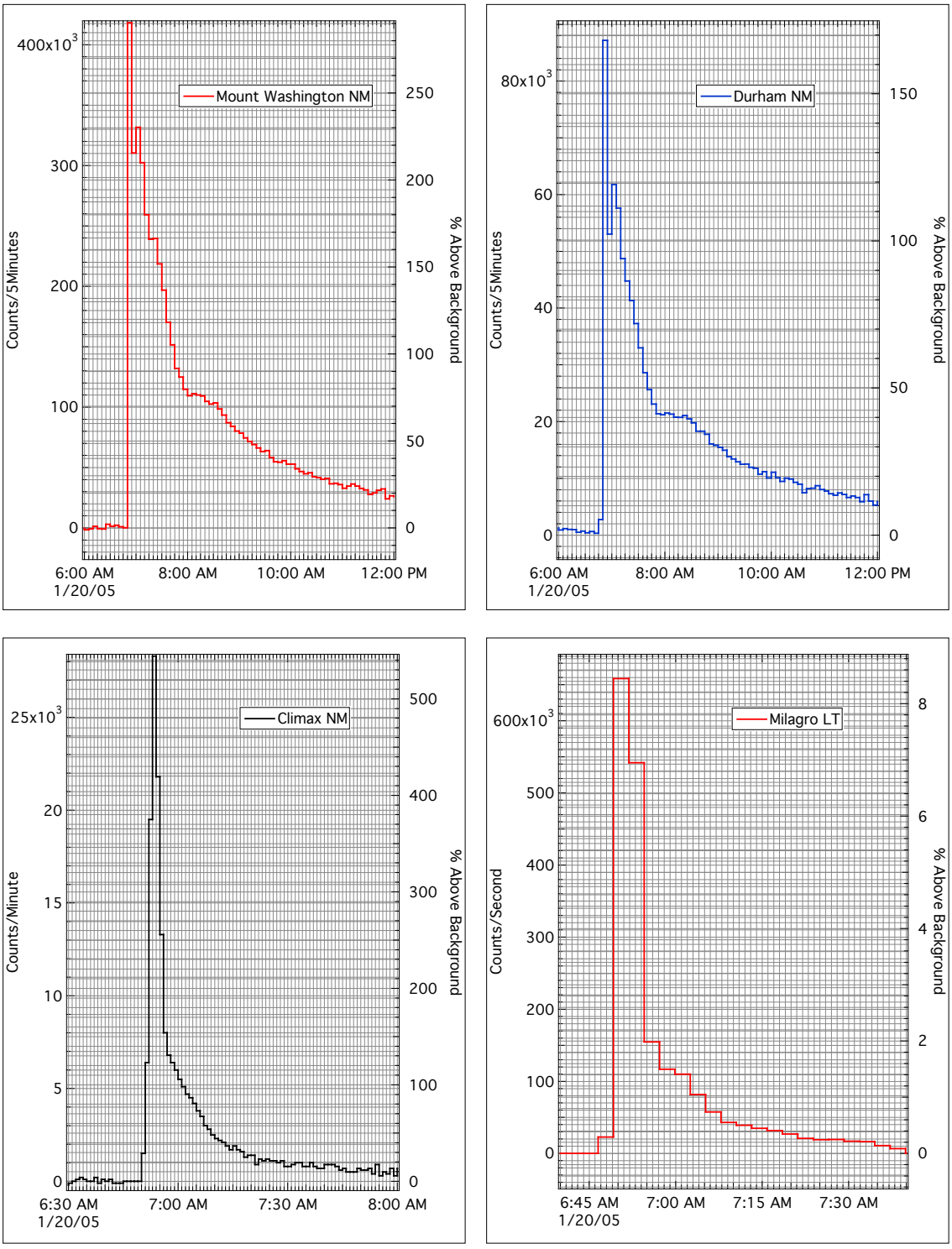

Figure 5.10: Ground-level enhancements during the 2005 January 20 event for Mt. Washington, Durham, and Climax neutron monitors, as well as the Milagro low threshold channel. Note the different time scales.

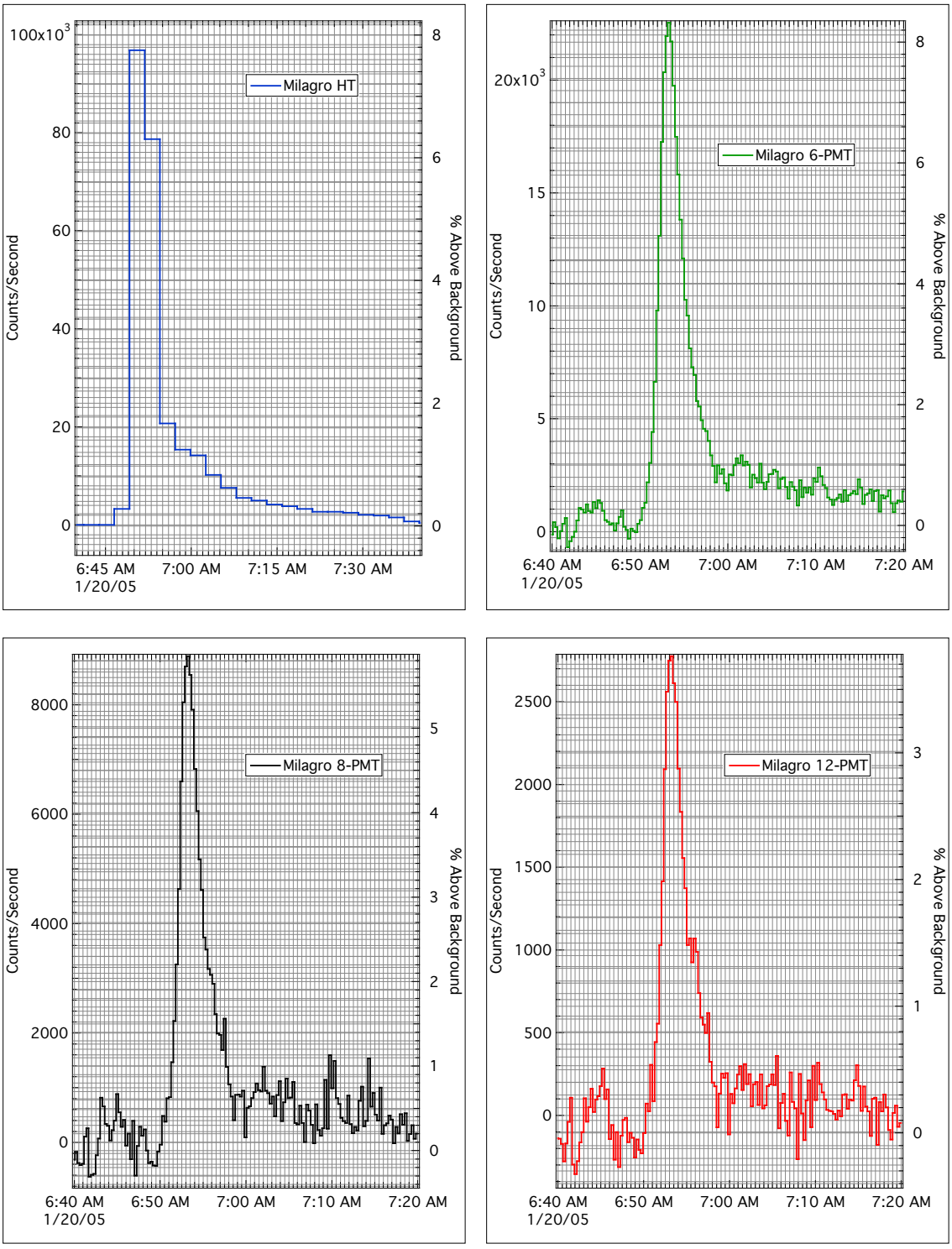

Figure 5.11: Ground-level enhancements during the 2005 January 20 event for Milagro high threshold, 6-PMT, 8-PMT, and 12-PMT channels. Note the different time scales.

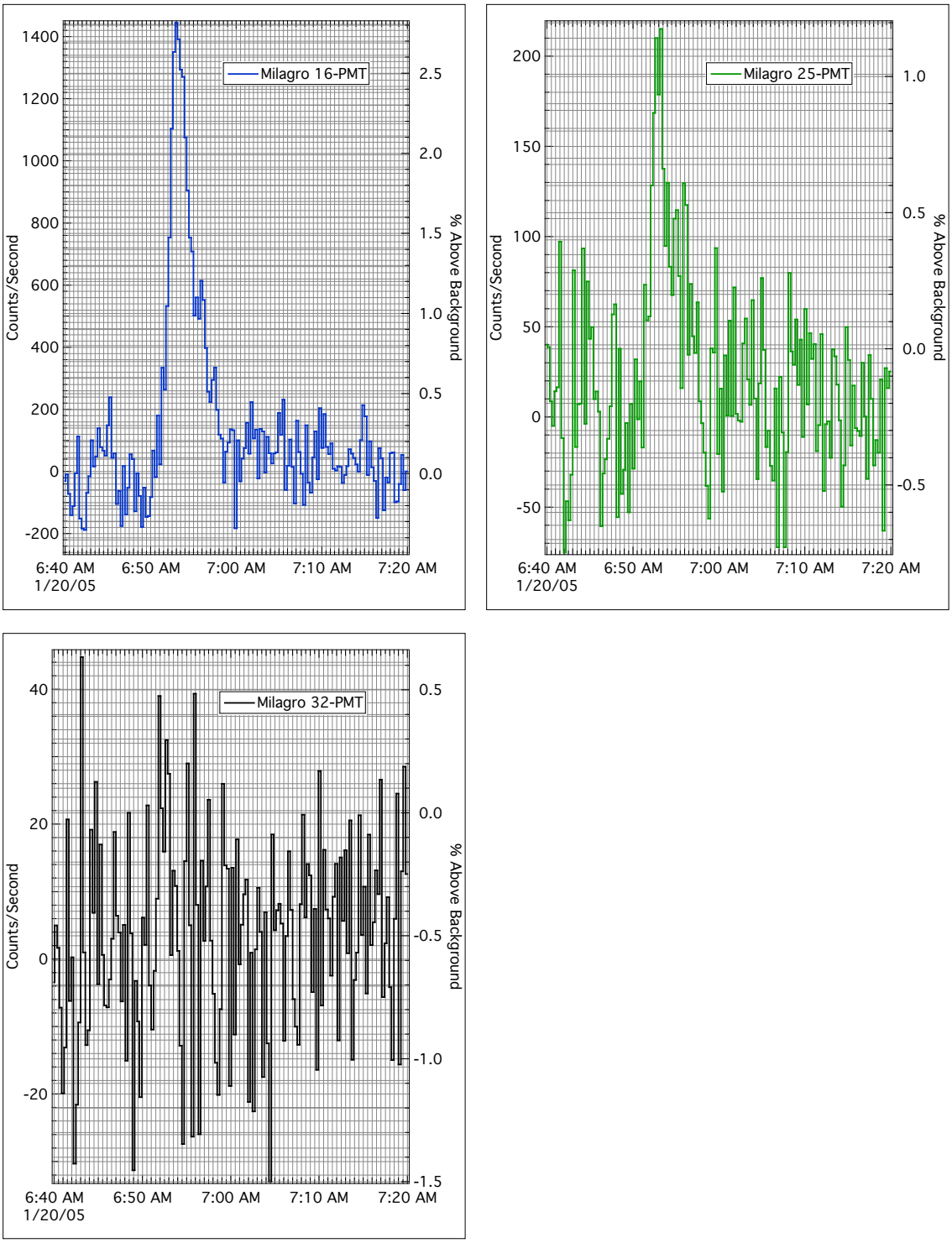

Figure 5.12: Ground-level enhancements during the 2005 January 20 event for Milagro 16-PMT, 25-PMT, and 32-PMT channels.

Chapter 6

Data Analysis and Procedure

6.1 Background Correction using a Principal Component Analysis

To perform an analysis of the events in question we must isolate the signals from the background count rates. The raw data rates from NMs have a known relationship with ground-level barometric pressure, however the Milagro rates have additional effects from several other factors. To relate the Milagro environmental data with background fluctuations we performed a principal component analysis (PCA) of the raw count rate with several environmental indicators. The PCA finds correlations between multiple data sets and defines new dimensions that have a reduced range of fluctuation. To test and illustrate this technique we performed a PCA on the February 2001 Climax NM count rate (Figure 6.1). A PCA can generate its own correction factor for the uncorrected Climax NM count rate and barometric pressure without prior knowledge of the relationship between the two data sets.

Ground-level background rates are inversely related to solar activity, as discussed in section 2.1.3. To keep this modulation factor from affecting the correlations between Milagro background rates and local environmental conditions, datasets were chosen from

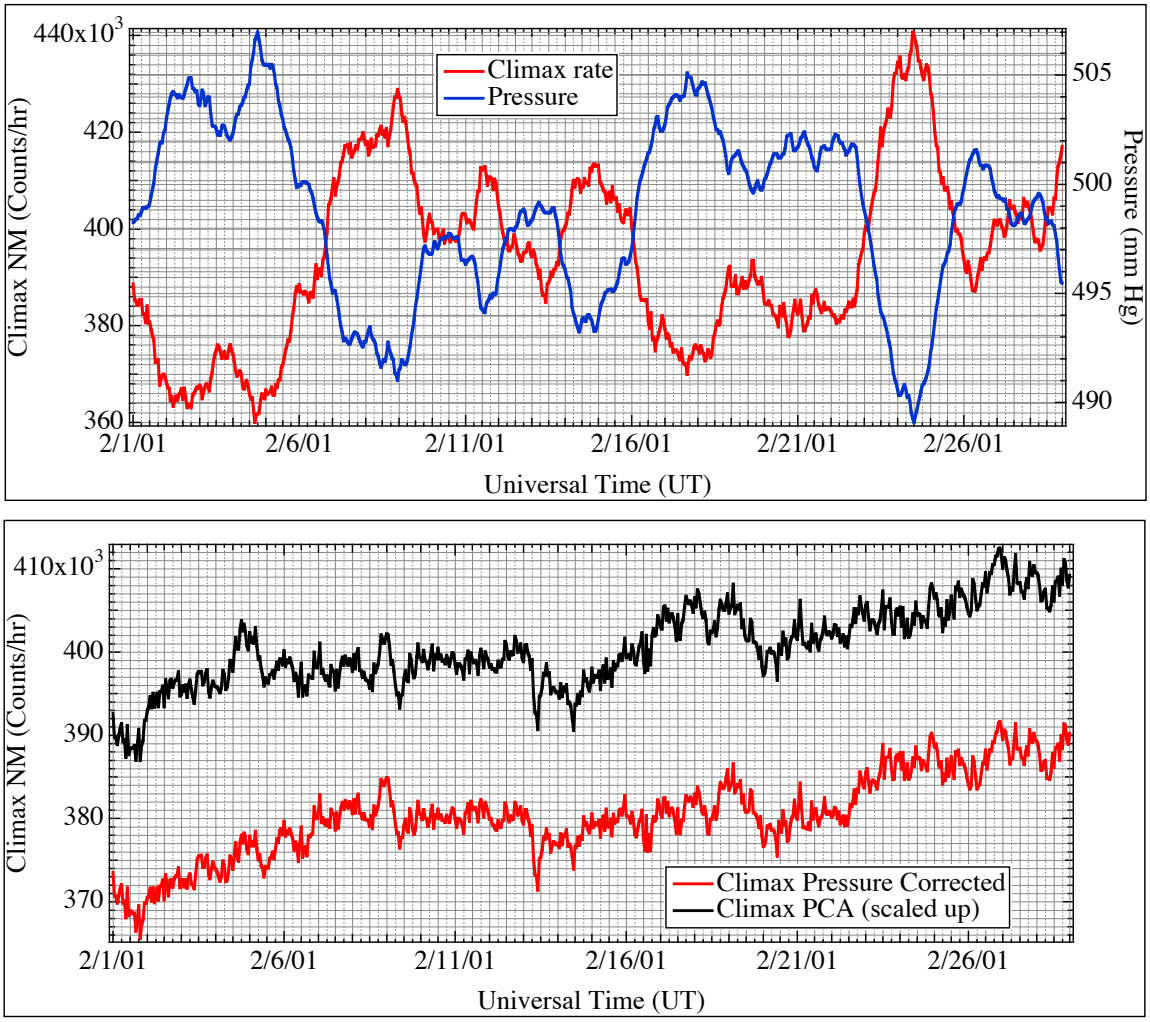

Figure 6.1: February 2001 was a period of low solar activity, providing a good sample for the PCA pressure correction. The raw Climax count rate is anti-correlated with barometric pressure (top). The PCA correction for Climax, scaled up for clarity, is nearly identical to the standard pressure correction (bottom).

a period of low solar activity as indicated by the Climax NM around the time of each GLE.

Background rates in Milagro are affected by at least three environmental parameters: barometric pressure, inside temperature, and outside temperature. Therefore, the PCA must have at least four dimensions—one for the uncorrected count rate and three for the environmental parameters. To perform a PCA, the covariance matrix of the

generated in the form

$$C = \begin{bmatrix} Var(a) & Cov(a,b) & Cov(a,c) & Cov(a,d) \\ Cov(a,b) & Var(b) & Cov(b,c) & Cov(b,d) \\ Cov(a,c) & Cov(b,c) & Var(c) & Cov(c,d) \\ Cov(a,d) & Cov(b,d) & Cov(c,d) & Var(d) \end{bmatrix} \tag{6.1}$$

The variance of a dimension measures the spread of values from the mean of the dimension, defined as

$$Var(a) = \sum_{i=1}^{N} (a_i - \mu_a)^2 \tag{6.2}$$

where a_i is the i^{th} measurement of the dimension a, and μ_a is the mean of the dimension a defined by

$$\mu_a = \frac{1}{N} \sum_{i=1}^{N} a_i \tag{6.3}$$

The covariance between two dimensions is a measure of the correlations between them, expressed as

$$Cov(x,y) = \sum_{i=1}^{N} (x_i - \mu_x)(y_i - \mu_y) = Cov(y,x) \tag{6.4}$$

A positive covariance corresponds to dimensions that are positively correlated with each other, a negative covariance corresponds to dimensions that are anti-correlated (trend in opposite directions), and uncorrelated dimensions have an expectation value covariance of zero.

The principal components are the new dimensions that contain the greatest inter-dimensional correlations, and therefore least correlated with each other. To find the principal components we diagonalize the covariance matrix by rotating the data into the directions of the eigenvectors from the covariance matrix. The principal component with the largest eigenvalue will have the greatest covariance, while the principal component

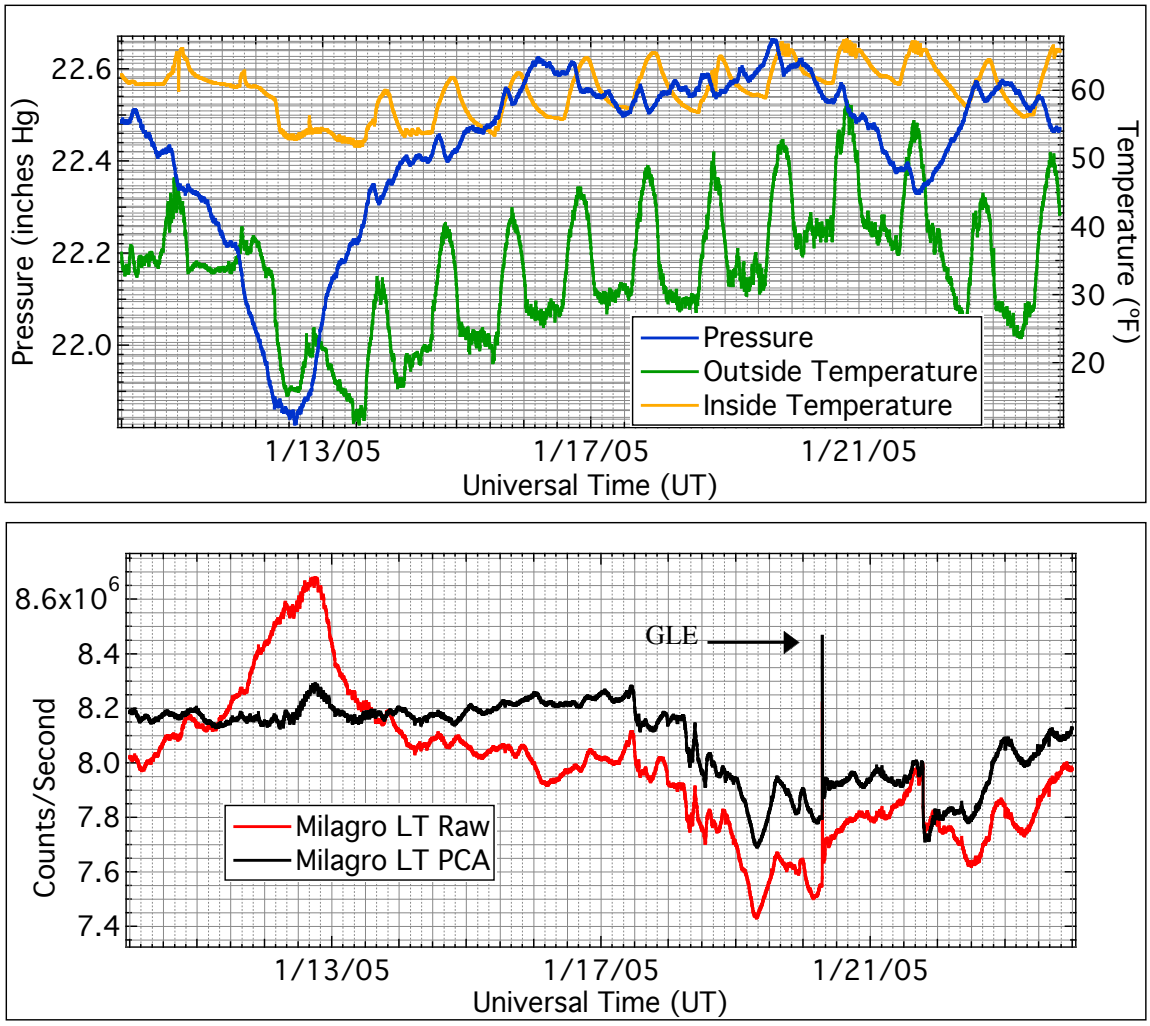

Figure 6.2: Environmental parameters (top) are used to correct the Milagro low threshold channel for a period of time surrounding the 2005 January 20 GLE (bottom).

with the smallest eigenvalue will have the smallest covariance. The component represented by the smallest eigenvalue is then normalized to the raw count rate to obtain the correction factors for each environmental variable. The original datasets are multiplied by their respective correction factors to produce the PCA-corrected count rate (Figure 6.2).

6.2 Spectral Analysis

The increase in count rate for ground-level stations due to SCRs can be expressed as

$$N_{Channel} = \Delta t \Delta\Omega \int_{P_{cutoff}}^{13GV} J(P) Y_{Channel}(P) dP \tag{6.5}$$

$N_{Channel}$	Number of particles detected over the background rate for the given data channel
Δt	Time interval over which the increase in count rate is valid
$\Delta\Omega$	Pitch-angle distribution function (in our case this information is buried within the specific yield functions)
$J(P)$	Proton rigidity function
$Y_{Channel}(P)$	Specific yield function for the given data channel

Table 6.1: Explanation of variables contained within equation 6.5.

The integration is performed in rigidity space from a minimum corresponding to the cutoff rigidity of the detector, and up to a maximum of 13 GV. This upper limit can theoretically be taken to infinity, however the rigidity spectra fall off sharply beyond ~5 GV. For even the hardest spectra (where higher rigidity particles are most pronounced) there is less than a 0.5% contribution above 13 GV, enabling us to set an upper limit to the integration without a significant effect on the results.

As discussed earlier in section 3.2.2, the traditional analysis technique had been to find the count rate increases in a pair of NMs with differing sensitivities in order to compute the proton rigidity spectrum modeled by a power-law.

$$J(P) = BP^{-\gamma} \tag{6.6}$$

Equation 6.5 can now be solved for a family of parameter pairs (B, γ), and curves representing the count rate increases for each NM ($N_{channel}$) can be plotted in these coordinates. The values of B and γ at which two $N_{channel}$ curves intersect gives a result for the flux coefficient and spectral index simultaneously.

However, we expect the power-law solution to be accurate only over a limited range of rigidities. As the acceleration process reaches its upper limits, a steepening of the spectrum at the highest rigidities is expected (see sections 1.5.2, 3.2.2). To account for this characteristic we can represent the proton rigidity function as a power-law with an exponential decay as in equation 3.5 to take into account the limits of the acceleration process (Ellison and Ramatay, 1985).

$$J(P) = BP^{-\gamma} \exp[-P / P_o] \tag{6.7}$$

This representation has three parameters: the flux coefficient, B, spectral index, γ, and break rigidity, P_0. This form reduces to the power-law form of equation 6.6 as P_0 exceeds ground-based rigidities, but does not restrict the result to remain in power-law form, allowing for the spectrum to fall off or steepen at the higher rigidities. Solving for this representation of the rigidity spectrum requires a minimum of three data channels.

Anisotropy effects can be large during the early stages of GLEs; multiple ground-level stations do not sample the same distributions of particles due to these effects. This creates difficulty in obtaining results for proton spectra early in these events. The Milagro detector possesses multiple data channels with differing sensitivities at one location (see section 4.4), and is in close proximity to the Climax NM. An analysis using

the Climax NM and multiple Milagro channels can provide accurate results for the proton spectra early in GLEs despite the large anisotropic effects.

6.2.1 Chi-squared Analysis

Using the power-law representations for the SYFs in equation 4.5, equation 6.5 can now be written as

$$N_{Channel} = \Delta t \int_{P_{cutoff}}^{13GV} \sum_{i=1}^{n} A_i B P^{\alpha_i - \gamma} \exp[-P / P_o] dP \tag{6.8}$$

The integral must be solved numerically. We performed a χ-squared minimization analysis using count rate increases and the statistical error associated for each dataset for Climax, the New Hampshire NMs (excluding 2005 January 20 0651-0656 UT for reasons explained in section 7.2.3), and all available Milagro channels.

The count rate increases were predicted for different rigidity spectra, where all three parameters are varied, densely covering the three-dimensional space spanned by these parameters. An analysis was performed for time slices as short as 5 minutes. The χ-squared technique provides a result for the proton rigidity spectrum that is unique to that particular timeframe. Thus, the evolution of all three parameters in the proton rigidity spectrum could be studied.

It is important to note that the results from this χ-squared procedure have not yet been adjusted for the solid angle viewing area or extended down to spacecraft energies, (these topics are discussed in section 6.2.3) and thus it is NOT the complete solution.

The χ-squared result for the proton rigidity spectrum enables us to find the rigidity ranges each ground-level channel samples based on the detector response at different periods of an event.

6.2.2 Response Functions

The response of a data channel is the product of its SYF and the proton rigidity spectrum.

$$R_{channel}(P) = J(P)Y_{channel}(P) \tag{6.9}$$

The cutoff rigidity combined with the proton rigidity spectrum and SYF curves determine the rigidities a particular data channel is sampling. The lower cutoff rigidities of the NMs compared to that of Milagro naturally cause the NMs to be sensitive at lower rigidities (Figures A.8 and A.9). The relative sensitivity to rigidities near the cutoff for Milagro channels decreases with higher PMT multiplicity (Figure 4.7), therefore the higher multiplicity Milagro channels will be sampling higher rigidities with respect to the low multiplicity channels.

The rigidities each data channel is sampling is greatly influenced by the exponential rollover. The exponential dependance on the break rigidity in the proton rigidity spectrum (equation 6.7) decreases the flux of particles with rigidities above the break value with respect to those below. To illustrate this dependence we look at two separate time intervals during the 2005 January 20 event (Figure 6.3). The χ-squared

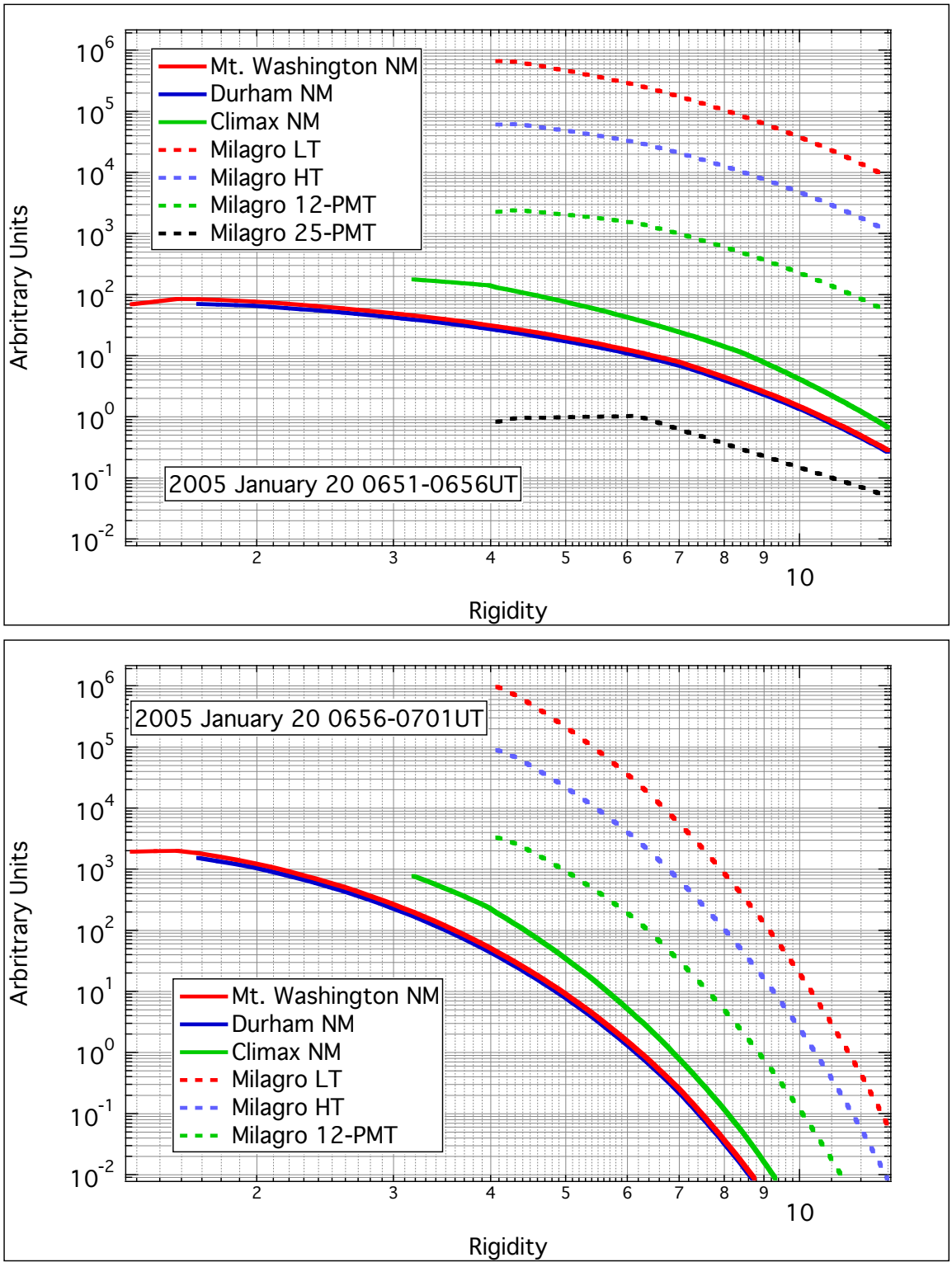

Figure 6.3: Selected response functions during the 2005 January 20 GLE. The χ-squared solution during the anisotropic phase from 0651-0656 UT (top) yielded a higher break rigidity than the isotropic 0656-0701 UT interval (bottom). As a result, there is a greater contribution of high rigidity particles in a given data channel during the 0651-0656 UT time interval. (Milagro 25-PMT was not above background for 0656-0701 UT, and thus its response for this time interval is omitted)

solution for 0651-0656 UT yielded a hard spectrum (break rigidity of ~1.2 GV), however the spectrum obtained for 0656-0701 UT was significantly softer (break rigidity of ~0.5 GV). When we compare these two spectra at 6 GV the exponential factor for the 0651-0656 UT spectrum is $\exp^{-5}$, however for 0656-0701 UT it is $\exp^{-12}$. The exponential characteristic of the break rigidity decreases the flux at 6 GV by several orders of magnitude between the two timeframes, thus the response functions in Figure 6.3 during the latter period fall off much faster.

The mean rigidity each data channel represents must be found separately for each time interval by satisfying the condition

$$\int_{P_{cutoff}}^{P_M} R_{channel}(P)\,dP = \int_{P_M}^{13GV} R_{channel}(P)\,dP \tag{6.10}$$

For error in rigidity we allow for 25% of the total protons to extend either above or below the mean value. For a particular data channel, the rigidity obtained from equation 6.10 is then inserted into a spectrum modeled by equation 6.7 with parameters derived from the χ-squared analysis. This gives a result for the flux at a certain rigidity in differential units of dJ/dP [# / (m^2-s-sr-GV)], with error resulting from the range of sampled rigidities.

6.2.3 Extending the Spectrum Using Spacecraft Data

Although we have a partial solution for the proton rigidity spectrum at GV rigidities, a complete solution for the spectrum is necessary over a broader rigidity range. By adding SEP spacecraft data in the range of ~few MeV to ~tens of MeV we expand our

range of detection to ~3 orders of magnitude in rigidity and as much as ~8 orders of magnitude in flux. These improvements provide better statistical results for spectral parameters such as power-law index and break rigidity than ground-level measurements alone.

A complicating effect in the spacecraft data is velocity dispersion. To be consistent in our analysis of the proton spectrum we must account for the different propagation delays in each energy channel. This delay is determined by the interplanetary path length at the time of the injection (a procedure to solve for this path length is discussed in section 7.2.2), as well as the relativistic velocity of the charged particles detected by a particular energy channel. For each spacecraft energy channel we solve for velocity from the relativistic energy equation

$$E = \gamma mc^2 \tag{6.11}$$

and use the associated interplanetary path length to find the propagation delay.

Intensities for spacecraft data are given in flux units of *dJ/dE* [# / (cm^2-s-sr-MeV)], which we convert to *dJ/dE* [# / (m^2-s-sr-GeV)]. To obtain our ground-level fluxes in the same units we must switch them from dJ/dP to dJ/dE using the relationship between energy and momentum

$$E = \sqrt{(pc)^2 + (mc^2)^2} \tag{6.12}$$

and the chain rule

$$\frac{dJ}{dE} = \frac{dJ}{dP}\frac{dP}{dE} \qquad \text{where} \qquad \frac{dP}{dE} = \frac{\sqrt{(pc)^2 + (mc^2)^2}}{pc} \tag{6.13}$$

SYFs for ground-level detectors are not averaged over the solid angle. For anisotropic distributions this is fine, however for isotropic distributions we must account for this in our results. In Milagro and NM simulations, isotropic distributions extend to a zenith angle of 70° which corresponds to a solid angle of 4.13 steradians. We must divide isotropic fluxes by this factor to keep all results in the same form. Now that we have all fluxes in terms of *dJ/dE* we can represent equation 6.7 in terms of energy.

$$J(E) = BE^{-\gamma} \exp[-E / E_o] \tag{6.14}$$

The broad energy range that the data covers will cause a fitting procedure to neglect some data points to reduce error. To fit our data points with equation 6.14 all data points must have equal weighting. We perform a similar χ-squared analysis as discussed in section 6.2.1 to include the spacecraft results, once again varying all three parameters simultaneously. The analysis predicts the flux at each data channel's rigidity, and finds the best solution by using relative errors from the actual values (Figure 6.5).

6.3 Analysis: 2005 January 20 0656-0701 UT

After the background subtractions have been completed, the resulting count rate increases for each data channel are solely from SCRs. The predicted vs. measured background rate ratios given in Table 4.1 apply to SCRs as well, therefore we scaled the SCR count rates based on the same ratios to obtain the true number of SCRs, represented by $N_{channel}$ in equations 6.5 and 6.8.

The anisotropic phase of the 2005 January 20 GLE concluded at 0656 UT, thus for the 0656 UT-0701 UT time interval we used the isotropic SYFs for Climax, the New Hampshire NMs, and all available Milagro channels (up to 16-PMT for this timeframe). The SYFs and the values for $N_{channel}$ were fed into the χ-squared minimization code, discussed in section 6.2.1. The resulting proton rigidity spectrum is

$$dJ / dP = 2.0 \times 10^{7} P^{-1.2} \exp(-P / 0.51GV) \tag{6.15}$$

The actual data points lie above and below this result. For example, the predicted count increase in the Milagro high threshold channel is 7.50×10^{6}, the actual count increase is 1.21×10^{7}. Note that this corresponds to an error factor of 1.61.

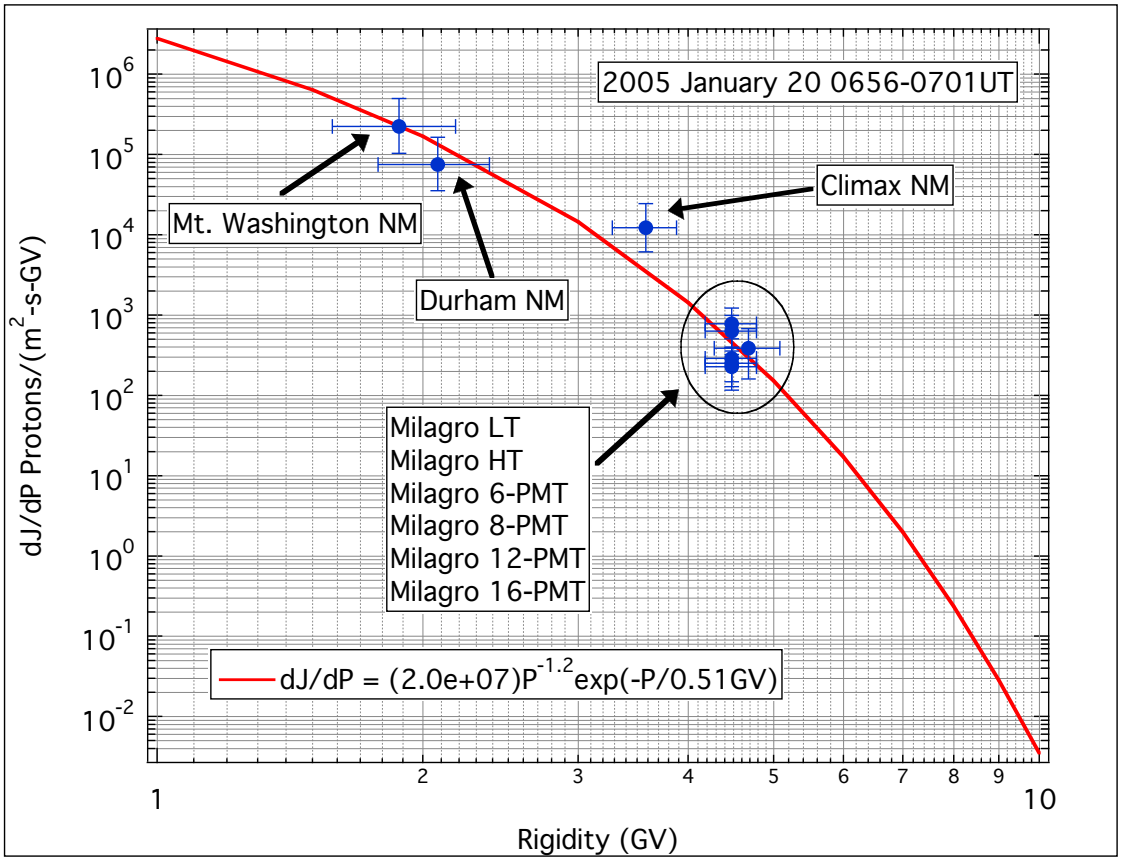

Figure 6.4: Flux vs. rigidity for ground-level data channels during 2005 January 20 0656-0701 UT. The data points lie above and below the χ-squared result of the proton rigidity spectrum for the same timeframe (red curve).

The product of the proton rigidity spectrum and the isotropic SYFs give the response functions of the data channels during this time interval (Figure 6.3, bottom). Using equation 6.10, the mean rigidity for the Milagro high threshold channel is 4.48GV, and inserting this rigidity into equation 6.7 results in a predicted flux of 506 Protons/(m^2-s-GV). This predicted flux is scaled up by the 1.61 factor from the χ-squared technique to give 815 protons/(m^2-s-GV). The low error in rigidity for the Milagro high threshold channel of 0.2 GV corresponds to a positive error in flux of 460 protons/(m^2-s-GV), and the high error in rigidity of 0.3 GV corresponds to a negative error in flux of 396 protons/(m^2-s-GV). We can now plot each data channel's flux for the 2005 January 20 0656-0701 UT timeframe vs. rigidity (Figure 6.4).

A calculation of the interplanetary path length for charged particles at the time of the 2005 January 20 event resulted in a distance of ~1.2 ± 0.1 AU (see section 7.2.2). The Milagro protons have a minimum kinetic energy of 3.2 GeV, corresponding to a velocity of ~0.95c, giving a transit time along a 1.2 AU path length of ~10.5 minutes. The 0651 UT onset in Milagro channels gives the protons an injection time at the Sun of 0640:30 ST (Solar Time). To analyze the proton spectrum during the 2005 January 20 0656-0701 UT time interval we must be consistent in finding the intensity increases due to protons that were injected into interplanetary space from 0645:30-0650:30 ST at all energies. For example, using equation 6.11 for the 4.7 MeV ERNE channel we obtain a velocity of 0.0998c, corresponding to a transit time of ~106 minutes. Therefore, the 0656-0701 UT (0645:30-0650:30 ST) Milagro protons were injected at the same time as the 0831:30-0836:30 UT ((0645:30-0650:30 ST) 4.7 MeV ERNE protons.

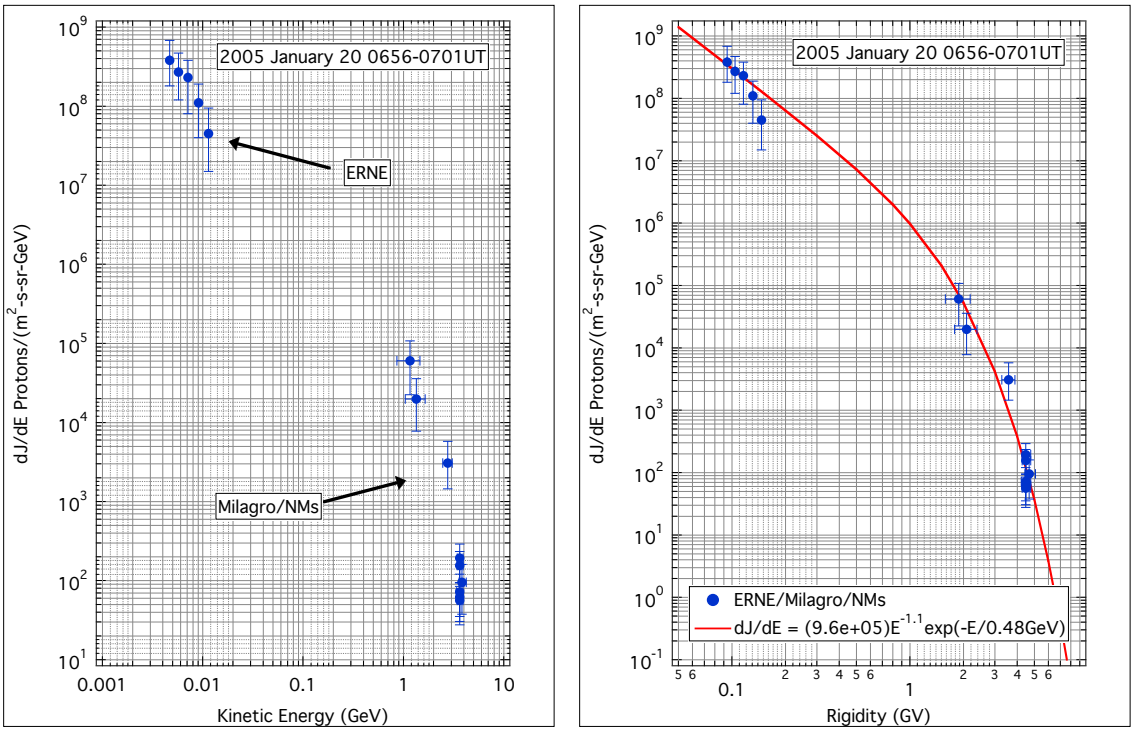

Figure 6.5: ERNE and ground-level data for 2005 January 20 0656-0701 UT (left) and the resulting χ-squared fit yielding equation 6.16 (right).

The ground-level fluxes are scaled by their solid angle factor, and results for all fluxes are converted to units of *dJ/dE* [# / (m^2-s-sr-GeV)] (Figure 6.5, left). A second χ-squared minimization technique (to include the spacecraft data points) finds the best solution for the proton spectrum over all energies (Figure 6.5, right), given by

$$dJ / dE = 9.6 \times 10^5 E^{-1.1} \exp(-E / 0.48 GeV) \qquad (6.16)$$

Chapter 7

Results and Conclusions

Results for the proton spectra during the 2001 April 15 and 2005 January 20 GLEs, based on the analysis procedure described in the previous chapter, are consistent with coronal shock acceleration. A timing analysis for the controversial 2005 January 20 GLE reveals that, although extreme in nature, the entire event can be attributed to a CME-driven shock and not requiring a different process, *i.e.*, direct solar-flare acceleration.

7.1 2001 April 15 Ground-Level Enhancement

7.1.1 Pitch-Angle Distribution

Many of the instruments in the world-wide network of NMs registered a GLE in response to the increase in relativistic protons during the 2001 April 15 event. To interpret the Milagro in the context of those from Spaceship Earth NMs, we added several vertical lines representing crucial stages in the event (Figure 7.1).

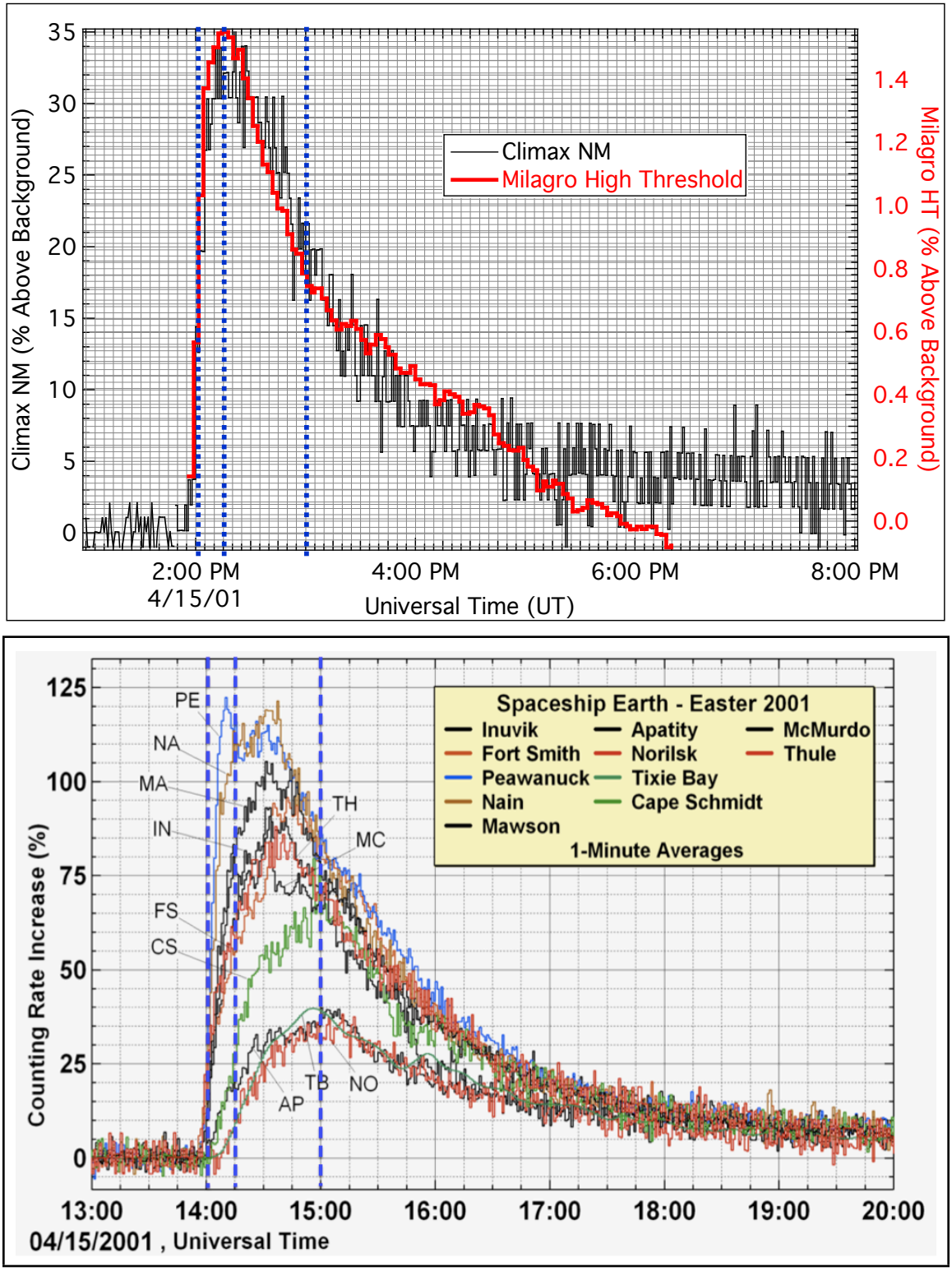

Figure 7.1: GLE profiles for Milagro and Climax (top), and Spaceship Earth (bottom) during the 2001 April 15 event. The vertical blue lines mark the full-width at half-max and peak times for Milagro and Climax profiles and are compared to profiles from Spaceship Earth. (Spaceship Earth neutron monitor rates courtesy of Dr. P. Evenson).

The Spaceship Earth NMs are placed strategically at various locations where the rigidity threshold is governed by the atmospheric cutoff (~0.5 GV), to study the three-dimensional cosmic-ray angular distribution (see section 3.2.2). Of the Spaceship Earth NMs only the Peawanuck and Nain stations (for station characteristics see Table 3.2) resolved the rising edge of the GLE consistent with Milagro and Climax. From Figure 3.7 we see that the viewing directions for particles incident on these stations lie close to that of Climax. This is evidence that Milagro and Climax are detecting the first particles to arrive at 1 AU (streaming directly from the acceleration region). In addition, Milagro and Climax have similar cutoff rigidities, are in close proximity to one another (similar asymptotic directions), and have nearly identical GLE profiles. All of these factors indicate that Milagro and Climax are sampling the same distribution of particles throughout the duration of the event, providing the necessary data to study the proton spectra throughout the entirety of the event (see section 7.1.3).

The onset of the GLE in Milagro and Climax occurred at 1359 UT, with the rising edge lasting roughly ten minutes, and the peak occurring at 1415 UT. Maxima in Spaceship Earth count rates range from 1410 UT at Peawanuck to 1500 UT (*e.g.*, Tixie Bay and Norilsk). Because all Spaceship Earth NMs have the same energy response, the varying rise-to-maximum in GLE profiles indicate that the initial phase is anisotropic, as is typical in well-connected events.

An anisotropy study based on Spaceship Earth NMS (Bieber et al., 2004) shows that the 2001 April 15 GLE was initially anisotropic, gradually evolving into an isotropic event by ~1425 UT. Stations with poorer viewing directions (*e.g.*, Apatity) measured an

attenuated particle intensity most likely seeing only particles that scattered out of the beam by magnetic turbulence (Bieber et al., 2004). An additional survey with a network consisting of four directional muon detectors was performed by Munakata et al. (2001). An excess of particles arriving from zenith directions were measured in coincidence with the onset of the GLE observed at the Thule NM (Figure 7.2). Distribution measurements (taken per hour) subside and replicate the isotropic background later in the event, consistent with the results of Spaceship Earth.

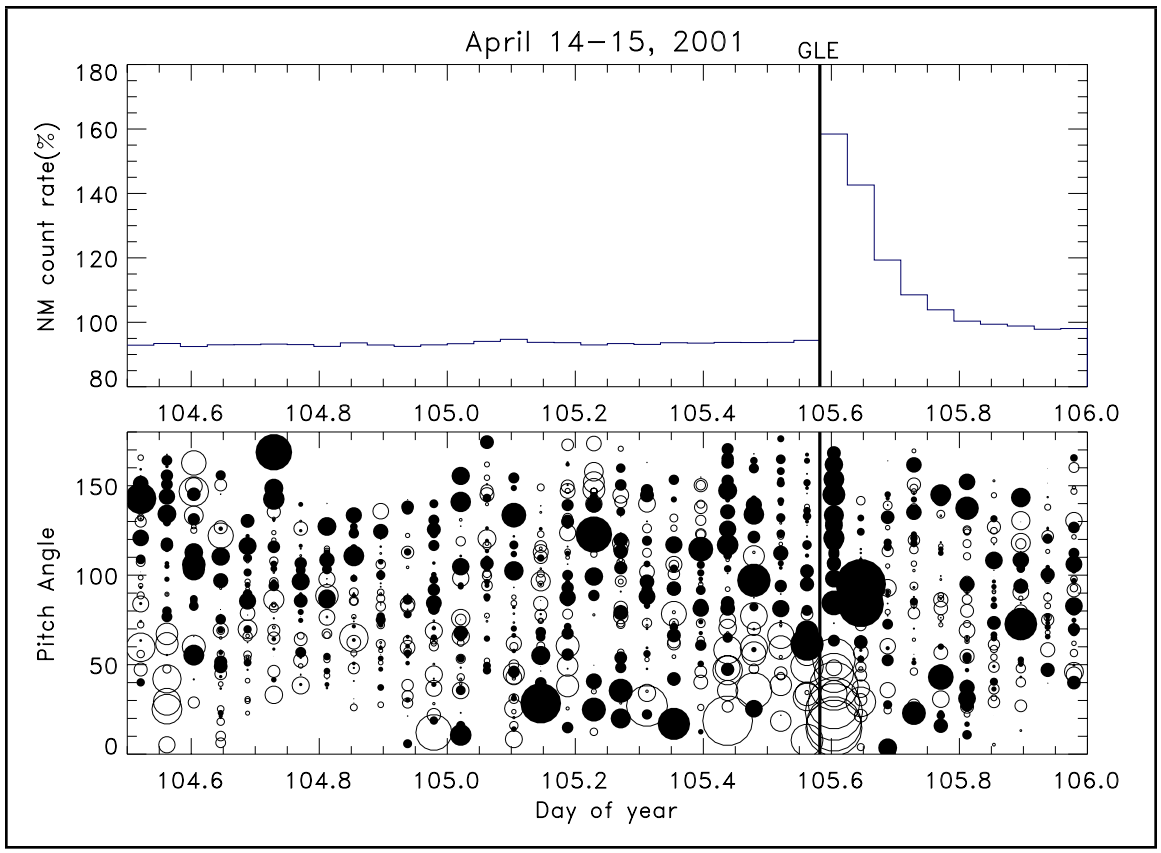

Figure 7.2: Pitch angle excesses and deficits measured by a network of directional muon detectors during the 2001 April 15 event (Munakata et al., 2001). The open circles represent excesses of particles and solid circles represent deficits, the intensity of each measurement is indicated by the size of the circles. A clear excess of particles arriving from the zenith direction is detected during the initial phase of the GLE observed by the Thule neutron monitor.

7.1.2 Event Timing

As described in sections 1.5 and 3.2.2, charged particles often travel along open magnetic field lines in their transit to Earth during well-connected events, the length of this path is determined by the configuration of the Parker spiral at the time of the event. A velocity dispersion analysis of spacecraft particle onsets times by Reames (2009) resulted in a magnetic path length of 1.59 ± 0.01 AU during the 2001 April 15 event, corresponding to a ~13 minute transit time for the highly relativistic particles (a similar analysis for the 2005 January 20 event is described in section 7.2.2). The GLE onset in Milagro was at 1359 UT, requiring the >4 GV protons to have been injected into interplanetary space no later than 1346 ST.

Bieber et al. (2004) and Gopalswamy et al. (2003) estimated that the onset of the associated CME for the 2001 April 15 event (based on CME height-time measurements extrapolated back to the solar surface) occurred at 1332 UT (1324 ST). The onset of the type II radio burst associated with the CME (indicating the presence of shock formation) occurred at 1338:40 ST (Aschwanden, 2010), ~15 minutes after the CME onset and ~7.3 minutes before the injection of the relativistic protons. Using a CME speed of 1200 km/s (Gopalswamy et al, 2003), the onset of the type II radio emission indicates that the shock formed at a height of ~2.5 $R_{\odot}$. The injection of the >4 GV Milagro protons then takes place when the CME is at ~3.3 $R_{\odot}$, consistent with the 2.5-4.0 $R_{\odot}$ result for other CME heights at GLE injection (Kahler, 1994). During the peak stages of the GLE (1410-1425 UT) the CME height ranges from 4.4-6.0 $R_{\odot}$.

7.1.3 Proton Spectra

As discussed in section 7.1.1, the Climax NM and the Milagro detector were among a few ground-level stations to resolve the leading edge of the 2001 April 15 GLE. The similarity of the GLE profiles in both instruments (Figures 5.5, 5.6) indicate that they were sampling the same distribution of particles throughout the entire event (including the leading edge where the anisotropy was greatest). In addition, the Mt. Washington and Durham NMs (Figure 5.5) resolved the rising edge of the GLE consistent with Milagro and Climax. An analysis of the proton spectra in time intervals as short as 5 minutes using these stations was performed following the procedure outlined in chapter 6. Data from IMP-8 (courtesy Dr. C. Lopate, private communication) was added to extend the proton spectra down to MeV energies.

The time interval for each spectral result is expressed in UT based on ground-level observations, however, protons at all energies are consistent with their simultaneous release from the Sun. For example, the results for the proton spectra during the time interval from 1400-1405 UT are from measurements at ground-level from 1400-1405 UT (1347-1352 ST), and in the 96-145 MeV IMP-8 channel from 1413-1418 UT (1347-1352 ST). The UT time intervals in other IMP-8 channels will also differ from the 96-145 MeV channel, but are the same when expressed as solar time. Thus, the results for the proton spectra are given in UT time intervals based on the GLE profile, and represent protons at all energies injected from the acceleration region during the same period and observed at 1 AU.

Time Interval (UT)	Flux, A ($\times 10^5$)	Spectral Index, γ	Break Energy, E_0 (GeV)
1400-1405	0.71 ± 0.2	1.0 ± 0.2	0.69 ± 0.13
1405-1410	2.4 ± 0.4	0.8 ± 0.2	0.56 ± 0.10
1410-1425	3.9 ± 0.9	0.95 ± 0.3	0.54 ± 0.06
1425-1440	4.1 ± 0.5	1.1 ± 0.1	0.51 ± 0.07
1440-1455	16.7 ± 4.9	0.8 ± 0.1	0.41 ± 0.09
1455-1510	23 ± 7.1	0.8 ± 0.2	0.36 ± 0.07
1510-1530	10 ± 3.4	1.15 ± 0.3	0.41 ± 0.05
1530-1550	4.9 ± 1.2	1.4 ± 0.4	0.46 ± 0.08
1550-1610	3.9 ± 1.5	1.55 ± 0.4	0.47 ± 0.09

Table 7.1: Evolution of the spectral parameters from equation 6.7 during the 2001 April 15 GLE. These results are also included graphically in Figures 7.3, B.1, B.2, and B.3.

Results for the proton spectrum analysis are given in Figure 7.3, and in further detail in Figures B.1-B.3. The evolution of the parameters from equation 6.7 are listed in Table 7.1. The results do not replicate a power-law form over all energies at any stage of the event. Instead, for every time interval, the proton spectra break away from a power-law at ground-level energies, indicative of shock acceleration as derived by Ellison and Ramaty (1985).

The break energy is highest during the rising edge of the GLE, producing the hardest spectrum during the event. This is evidence that the conditions for efficient particle acceleration up to the highest energies took place when the CME was low in the corona (~3.6 $R_\odot$ during the rising edge of the GLE in Milagro). The spectra gradually soften through the peak stages of the GLE (Figure 7.11) as the pitch-angle distribution becomes isotropic and the CME reaches higher solar altitudes. We will return to this discussion in section 7.2.2.

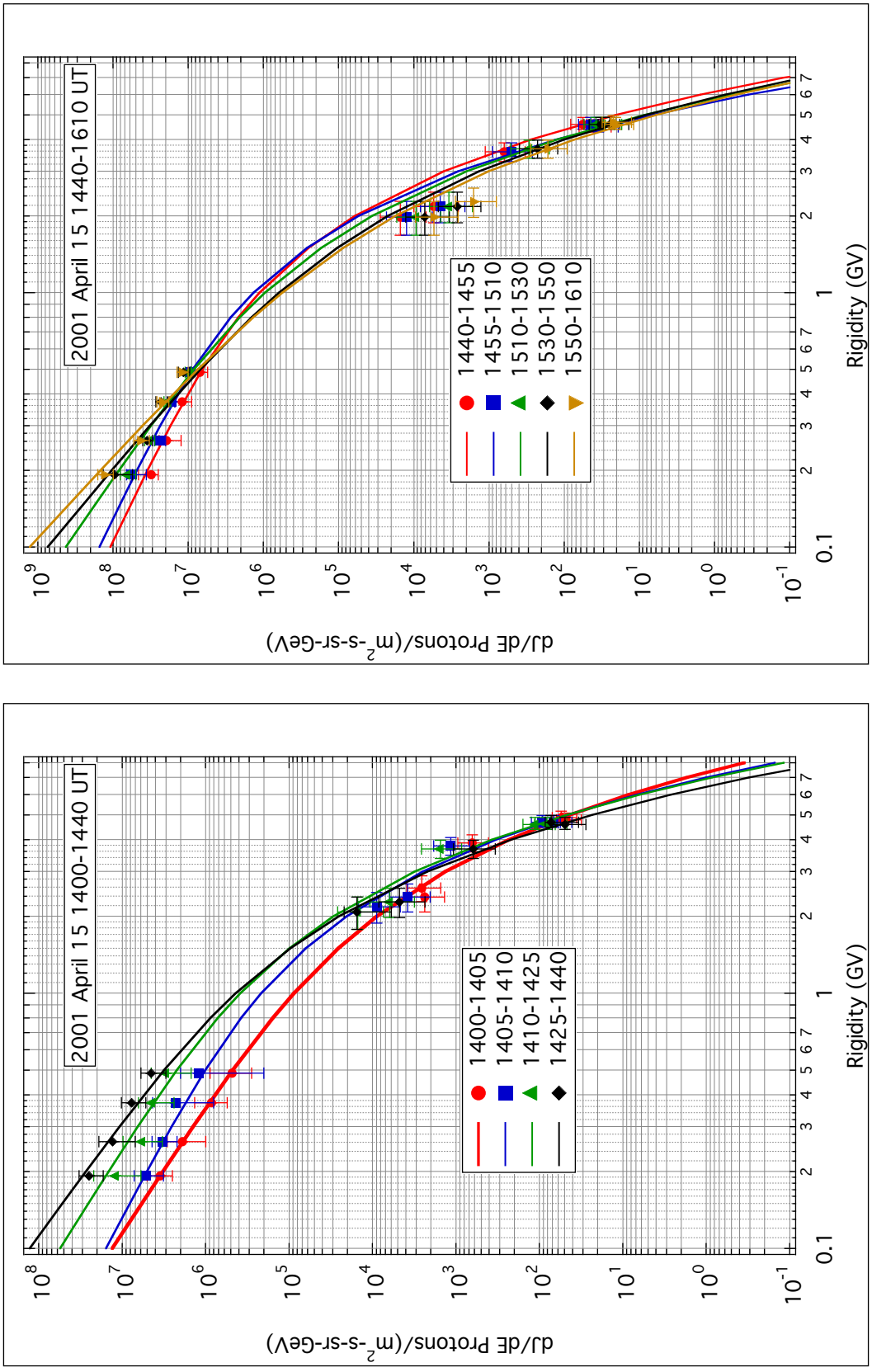

Figure 7.3: Time-resolved proton spectra during the 2001 April 15 GLE.

7.2 2005 January 20 Ground-Level Enhancement

The rapid onset of the 2005 January 20 GLE (Figure 7.4) have led many to conclude that a coronal shock cannot accelerate protons to GeV energies in such a short amount of time. This has made the 2005 January 20 GLE controversial. An investigation of the pitch-angle distribution, event timing, and proton spectra during the event are all crucial in order to determine how and where the highest-energy particles were accelerated.

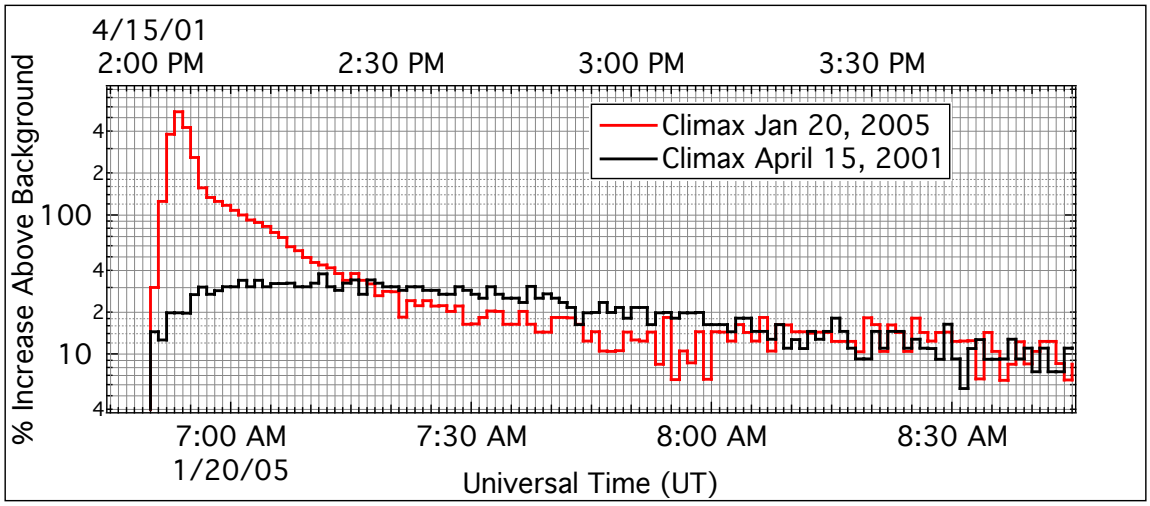

Figure 7.4: Comparison of GLE profiles during the 2001 April 15 and 2005 January 20 events. When viewed on a logarithmic scale, the extreme intensity and rapid evolution of the 2005 January 20 GLE clearly overshadows the 2001 April 15 GLE, which is widely recognized as having a classic GLE profile.

7.2.1 Pitch-Angle Distribution

The notable feature of the 2005 January 20 GLE is the spike-like peak in intensity, even when viewed on a logarithmic scale (Figure 7.4). The full-width at half-max (FWHM) for Milagro and Climax during the 2005 January 20 GLE is only ~3 minutes,

compared to ~1 hour during the 2001 April 15 GLE. In addition, at roughly 0656 UT, the falling edge transitions from a rapid decline (on a timescale similar to the rising edge) to a gradual decay.

The extreme intensity during the initial phase of the 2005 January 20 GLE produced count rate increases in many Milagro multiplicity channels. This provided an opportunity for Milagro to measure the pitch-angle distribution independently (see section 4.5.3). At GLE energies (<10 GeV), shower cores >1 km from the detector contribute more to the isotropic background rate in higher multiplicity channels (e. g. 16-PMT and 25-PMT) than in lower multiplicity channels. In an event with an anisotropic distribution, air shower particles are less likely to reach the detector from shower cores

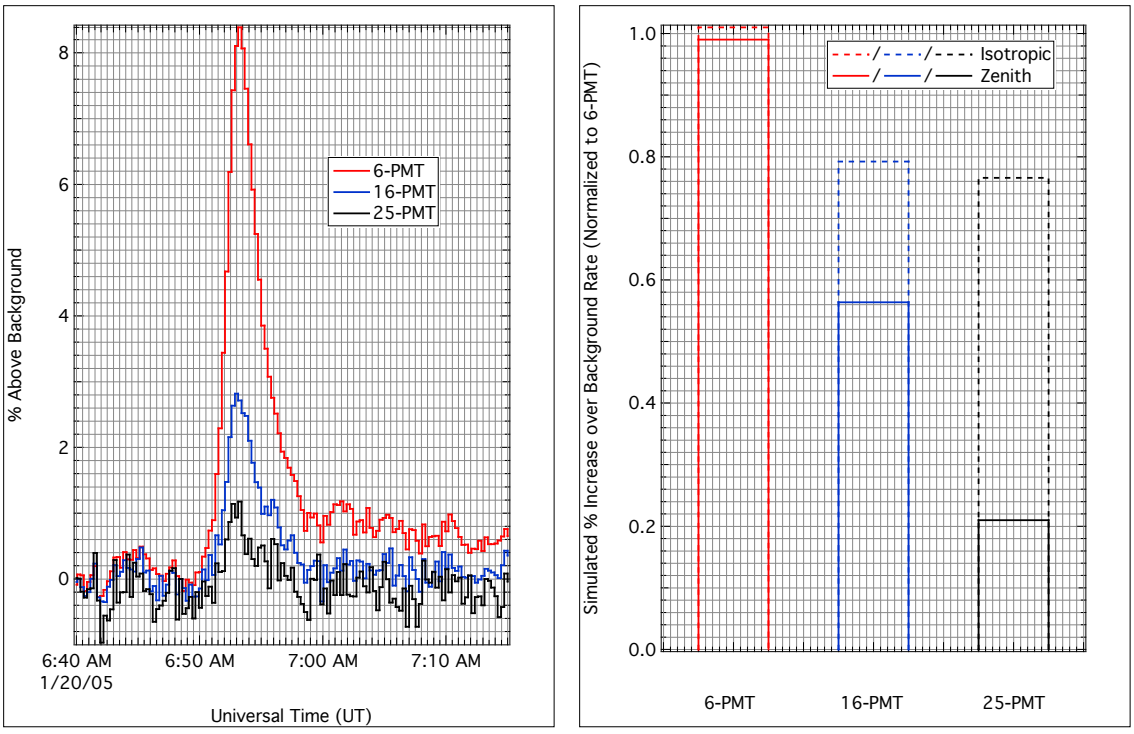

Figure 7.5: (Left) Increases over background for selected Milagro multiplicity channels during the 2005 January 20 event. (Right) The simulated increases over background in selected Milagro multiplicity channels for different pitch-angle distributions (normalized to the 6-PMT channel). The ratios during the initial phase of the 2005 January 20 GLE (0651-0656 UT) conform to an anisotropic pitch-angle distribution.

>1 km away. Using the ratios of the effective area curves as a function of throw distance (Figures A.1-A.4), we found the simulated increases over background in all Milagro multiplicity channels for both an isotropic and anisotropic pitch-angle distribution (Figure 7.5, right). The results show that anisotropic events produce an attenuated signal above background in higher multiplicity channels when compared to the same signal in the lower multiplicity channels. Data during the initial phase of the 2005 January 20 GLE conform to an anisotropic distribution (Figure 7.5, left).

The initial phase of the 2005 January 20 GLE was not resolved by the entire worldwide NM network. This can be seen in the Spaceship Earth NMs, which show large variances in onset time and profile during the initial phase (Figure 7.6). Of the Spaceship Earth NMs, only the South Pole and McMurdo stations yield a profile that resolves the anisotropic peak. From figure 3.7 we can see that, similar to the 2001 April 15 event, Climax's viewing direction is close to that of the stations that can best resolve the initial phase of the GLE. However, the cutoff rigidity at Spaceship Earth stations is essentially zero, therefore the low rigidity threshold is determined by the atmospheric cutoff (~0.5 GV). As a result, velocity dispersion broadens the latter half of the anisotropic peak.

Stations with poor viewing directions, such as Inuvik and Thule (Figure 3.7), did not rise above background levels during the initial phase of the GLE, even though the count rate in some stations were great (>10× over background). Because all Spaceship Earth NMs have the same energy response, this discrepancy suggests that the GeV

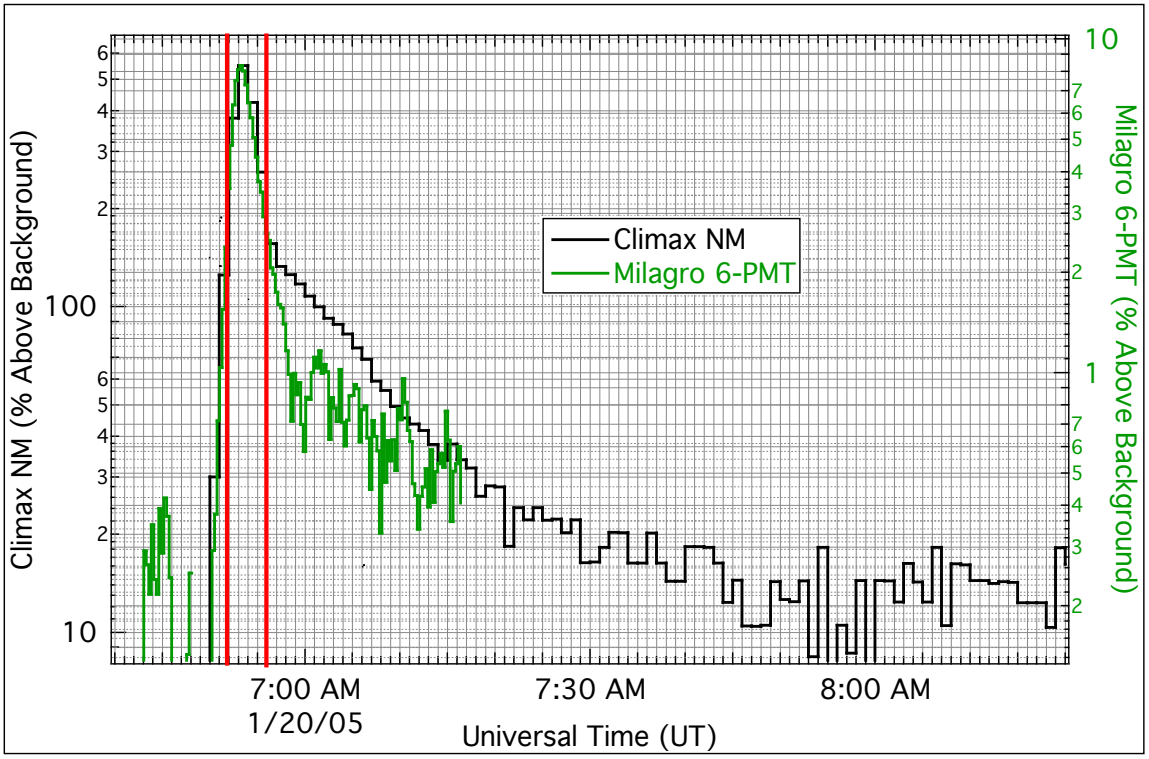

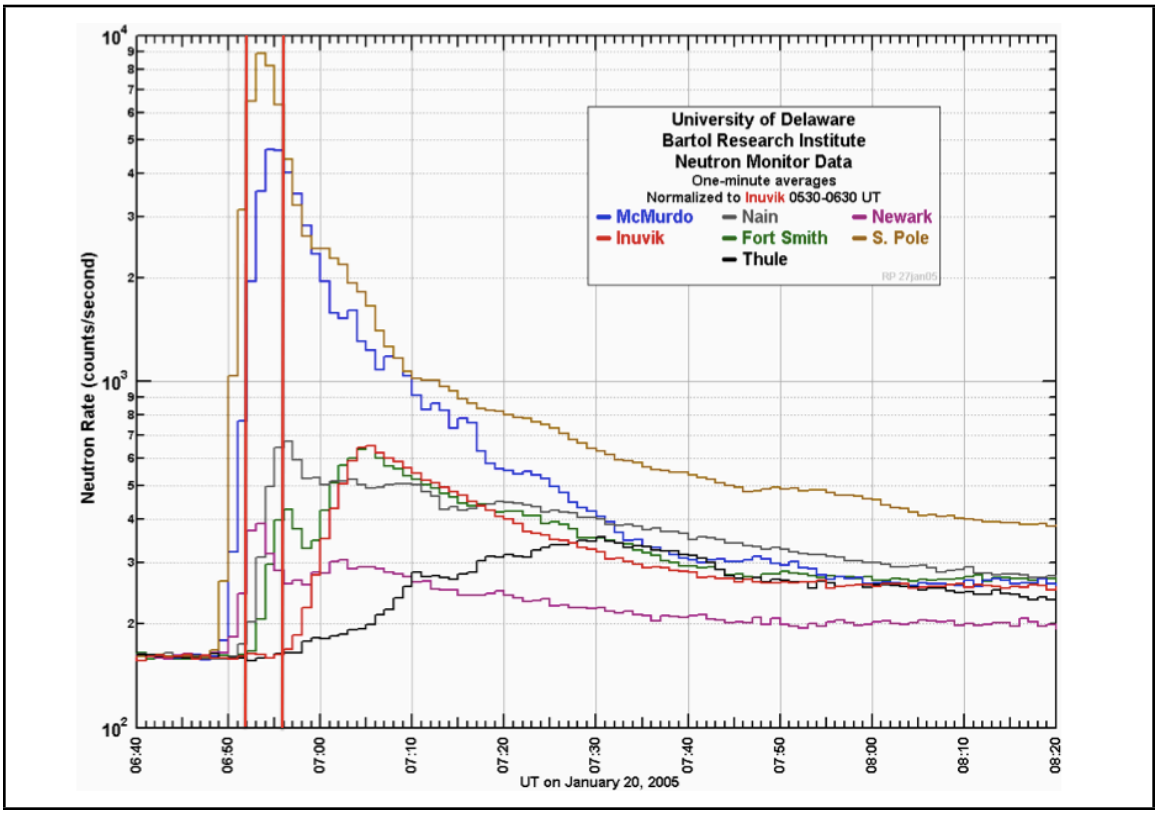

Figure 7.6: GLE profiles for Milagro 6-PMT and Climax (top), and Spaceship Earth (bottom) during the 2005 January 20 event (shown on a logarithmic scale). The vertical red lines represent timestamps for the rising and falling edges of the anisotropic spike resolved by Milagro/Climax and compare them with profiles from Spaceship Earth. (Spaceship Earth neutron monitor rates courtesy of Dr. P. Evenson).

protons in the initial phase of the GLE were confined to a narrow beam with excellent magnetic connection to the acceleration region with minimal scattering along the connecting field line. The rise-to-maximum in Milagro channels (~80 s) is almost an order of magnitude faster than that of the 2001 April 15 GLE (also was a well-connected event), and is further evidence of a very favorable magnetic connection. The preferable conditions for particle transport in the inner heliosphere combined with a favorable magnetic connection could have played a large role in the extreme intensity observed in the early stages of the GLE.

The latest onsets of the Spaceship Earth NMs (*e.g.*, Thule, Inuvik) began at ~0656 UT, well-aligned with the transition to an extended decay phase after the initial spike seen in Milagro and Climax. This is evidence of the pitch-angle distribution decreasing in anisotropy after only ~5 minutes into the event. An analysis by Bütikofer et al. (2009) also shows that the anisotropy present in the initial phase of the event had clearly decreased only a few minutes after the rising edge (between 0653-0703 UT). A separate analysis by Bombardieri et al. (2008) concluded that the GLE was strongly anisotropic at 0650 UT and 0655 UT, followed by rapid decrease in anisotropy after.

7.2.2 Event Timing

As discussed in the previous section, the first protons to arrive at Earth are confined to a narrow beam, and the rapid rise of the GLE signal suggests an excellent magnetic connection to the source region. Therefore, an accurate measurement of the path length traversed by these relativistic protons is necessary to determine when the

particles were released from the acceleration region. We will define this as solar proton release (SPR) time, and will express it in solar time.

Results for the path length at the time of the 2005 January 20 event ranged from less than 1.2 AU (Moraal et al., 2007; Reames, 2009) to 1.76 AU (McCracken et al., 2008). Depending on the path length used, the corresponding result for the SPR time would have an uncertainty of ~4 minutes, not accurate enough for our purposes. To obtain a reliable measurement for the path length we performed an inverse velocity analysis of particle onset times. The velocity dispersion effects for ERNE data channels cause their onset times to be delayed as a function of energy. Combining these onset times with those of relativistic particles in ground-based detectors, yields a measurement of the path length (Figure 7.7).

The path length derived from this analysis is 1.27 ± 0.1 AU, in agreement with the results of a similar analysis performed by Reames (2009), *i.e.,* 1.19 ± 0.02 AU. We further assume an anisotropic pitch-angle distribution width of 20˚ and solar wind speed of 560 km-s^{-1} (courtesy Dr. C. Farrugia, private communication) that was present before the onset and continuing for about one day (the intervening solar wind speed data from SOHO are not available but the magnetic field direction is consistent with a steady wind of this speed). At this speed the quiescent length of the Parker spiral is 1.1 AU. Although shorter, it is roughly consistent with the values from the two independent velocity dispersion analyses described above. We will use a 1.2 ± 0.1 AU path length from here on because it is consistent with the velocity dispersion analyses and solar wind speed measurements.

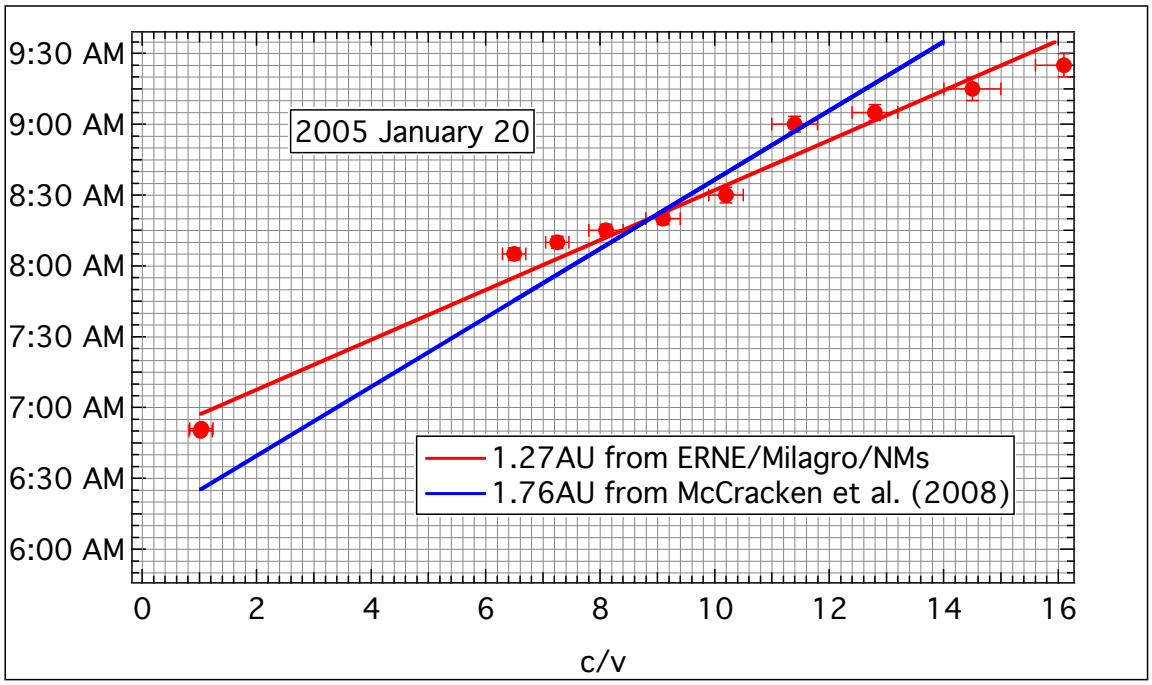

Figure 7.7: Inverse velocity vs. onset time for ground-level detectors and the SOHO/ERNE instrument. The slope of the red fitted line is a measurement of the path length at the time of the 2005 January 20 event. The 1.76 AU result from McCracken et al. (2008) is included to illustrate its incompatibility to the data.

The GLE onset in Milagro data channels occurred at 0650 UT. The 1.2 ± 0.1 AU path length results in a 10.5-minute propagation time for >4 GV protons, corresponding to a SPR time of 0639:30 UT (in agreement with Aschwanden (2010) and Simnett (2006)). The onset of the type II radio emission was at 0635:40 ST (Gopalswamy et al., 2005; Aschwanden, 2010), evidence of shock formation before SPR time. Gopalswamy et al. (2005) fit a kinematic equation based on constant acceleration to the CME associated with the 2005 January 20 GLE using LASCO and EIT images (Figure 5.7),

$$Height = 6.052 - 0.3361t + 0.0057t^2 \qquad (7.1)$$

where t is in minutes from 0600 UT. We note that CME acceleration is known to initially increase sharply before reaching constant speed or even decelerating (Demoulin and Vial, 1992; Uralov et al., 2005). Therefore, results for CME heights based on equation 7.1

should be taken as a lower limit, but it should be a much better approximation than assuming no accelerations.

Using equation 7.1, the CME height at type II onset was 2.3 $R_\odot$ and 2.9 $R_\odot$ at injection (SPR time). At these solar altitudes the CME speed ranged from ~1900-2450 km/s (and perhaps faster), well in excess of the Alfvén speed and thus capable of driving a very strong shock. The peak of the count rate in Milagro and Climax at 0653 UT (0642 ST) places the CME at 3.7 $R_\odot$, low compared to the 5-15 $R_\odot$ heights in other events observed by Kahler (1994).

High-energy gamma rays (>60 MeV) are dominated by π^0-decay emission, a signature of relativistic ion production. Chupp and Ryan (2009) suggested that the high-energy gamma rays and GLE particles may be associated. Therefore, any acceleration model must be able to explain their behavior and transport. The CORONAS-F/SONG 62-310 MeV gamma rays (Kuznetsov et al., 2008) show a clear rise to maximum beginning at 0645:30 UT (0637:10 ST) with a FWHM between 0645:30 UT (0637:10 ST) and 0648:00 UT (0639:40 ST), there is also some preliminary structure from 0644 UT (0635:40 ST) to 0645:30 UT (0637:10 ST).

The time profiles of the relativistic protons and high-energy gamma rays are difficult to explain with a flare-based model in which both populations are released simultaneously. McCracken et al. (2008) attributed the ~7-minute delay at 1 AU between the rising edges of the >60 MeV SONG gamma rays and the Sanae NM (P_c ~0.86 GV) to the path length traversed by the protons, yielding the 1.76 AU result discussed earlier.

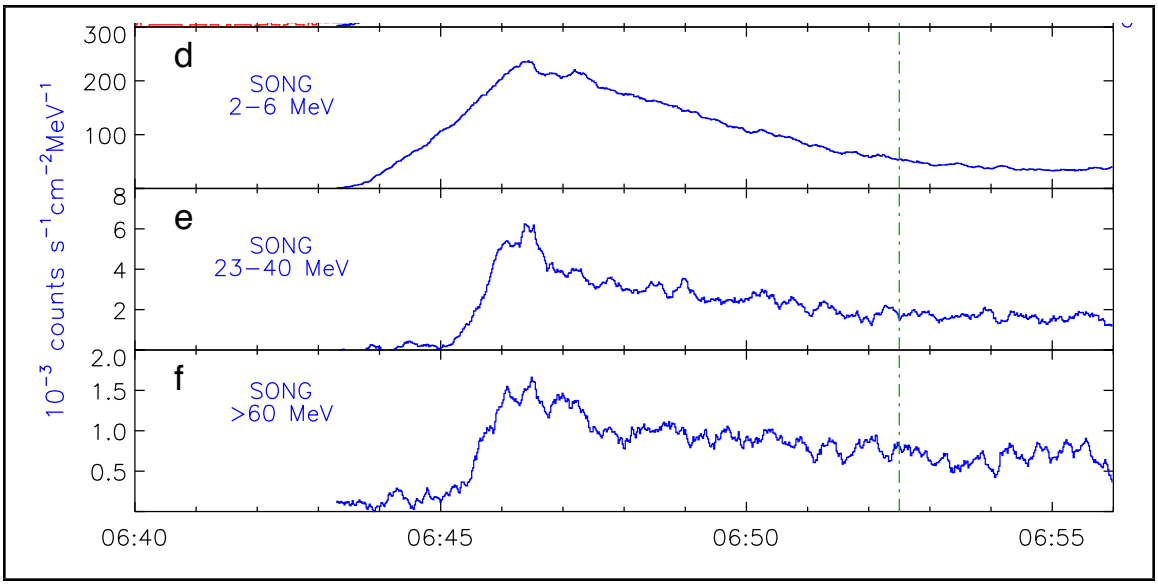

Figure 7.8: CORONAS-F/SONG gamma ray profiles during the 2005 January 20 event (UT). (Grechnev et al., 2008)

However, we have shown that the path length is closer to 1.2 AU (corresponding to a ~2-minute delay at 1 AU) resulting in a ~4-minute discrepancy between the rising edges of the high-energy gamma rays and the relativistic protons (0637:10 ST and 0641:30 ST respectively).

In the interest of argument we assume that the GLE protons were accelerated by the flare and stored in coronal loops. The high-energy gamma-ray emission is then a product of >300 MeV ions reaching the footpoints of the coronal loops and interacting with photospheric material (Ryan and Lee, 1991). The delay would result from the GLE protons diffusing through the low corona for ~4 minutes before escaping along open field lines. This diffusion should then yield a prolonged and less intense GLE profile than the high-energy gamma-ray profile (Ryan, 2000). However, the peak observed in Milagro has a sharp spike-like structure with a rise-time of 80 s, it has no prolonged falling edge, and is of comparable width to that of the high-energy gamma rays. Therefore, even if the

high-energy gamma-ray emission is due to ~ 300 MeV flare ions trapped in coronal loops, it is still not associated with the GLE protons.

7.2.3 Proton Spectra

From Figure 7.9 it is clear that the Mt. Washington NM count rate does not have the same GLE profile as that of Milagro or Climax early in the 2005 January 20 event. The sample rates for the Mt. Washington and Durham NMs are 5 minutes, and thus were unable to resolve the fast-evolving initial phase. In addition, the Mt. Washington count rate from 0650-0655 UT was only mildly elevated from later stages of the GLE, whereas stations with favorable viewing directions were strongly elevated. Based on these observations we conclude that the Mt. Washington and Durham NMs were on the outskirts of the anisotropic beam which produced the initial spike in intensity seen by some ground-level stations. After the initial phase, however, the Mt. Washington and Durham profiles model the isotropic extended phase seen by many ground-level stations. Therefore, the NH NMs are included in the χ^2 spectral analysis outlined in section 6.2.1 for time intervals beginning after 0656 UT, but are excluded from the analysis during the initial spike from 0615-0656 UT.

The profiles for Climax and Milagro during the 2005 January 20 GLE are nearly identical (Figure 7.9), indicating that they were sampling the same distribution of particles (close to the axis). The multiple data channels in Milagro provided enough data points to analyze the proton spectrum during the anisotropic phase from 0651-0656 UT.

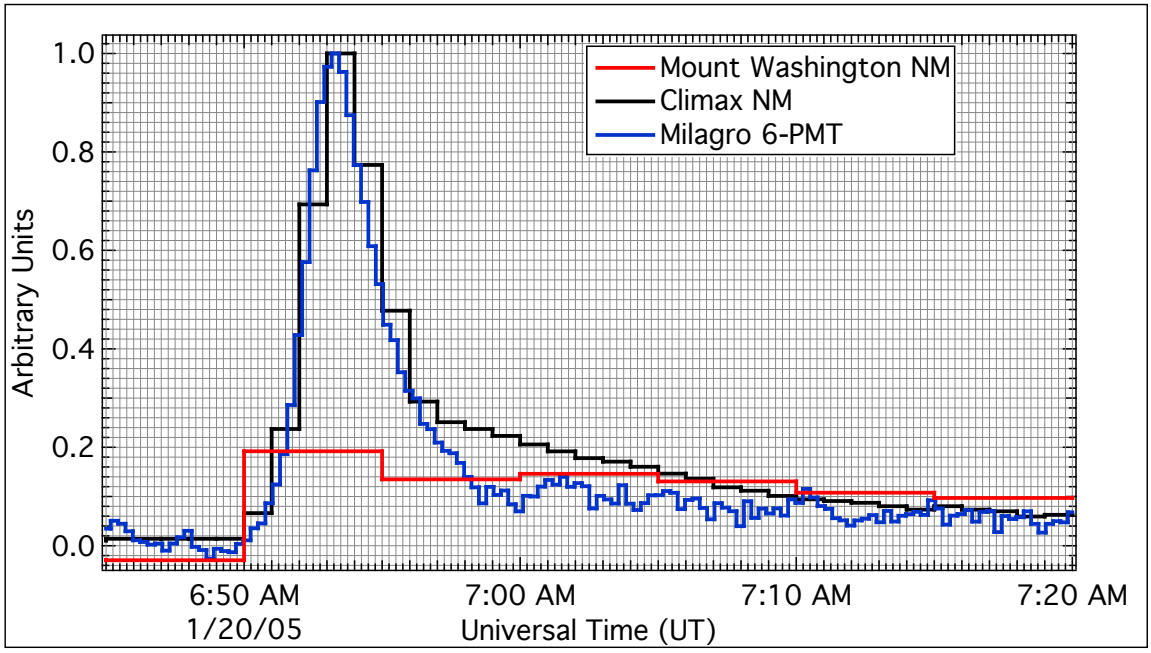

Figure 7.9: GLE profiles for the Milagro 6-PMT channel and the Mt. Washington and Climax neutron monitors. The strong anisotropy effects during early stages of the GLE (0651-0656 UT) cause the Mt. Washington and Durham neutron monitors to miss the spike-like peak in intensity seen in some ground-level stations, such as Milagro and Climax.

Results for the proton spectra are given in Figure 7.10, and in greater detail in Figures B.3-B.4. The evolution of the parameters from equation 6.7 are listed in Table 7.2. As was found in the 2001 April 15 GLE, the spectrum for every time interval during the 2005 January 20 GLE exhibits the exponential rollover form modeled by Ellison and Ramaty (1985).

The break energy during the initial spike between 0651-0656 UT is clearly elevated and set apart from any other period of the GLE (Figure 7.11). This, again, is similar to the 2001 April 15 GLE in which the most efficient particle acceleration occurred when the CME was lower in the corona. After 0656 UT the spectra soften dramatically (a softening of the spectra for a period of several minutes after the initial

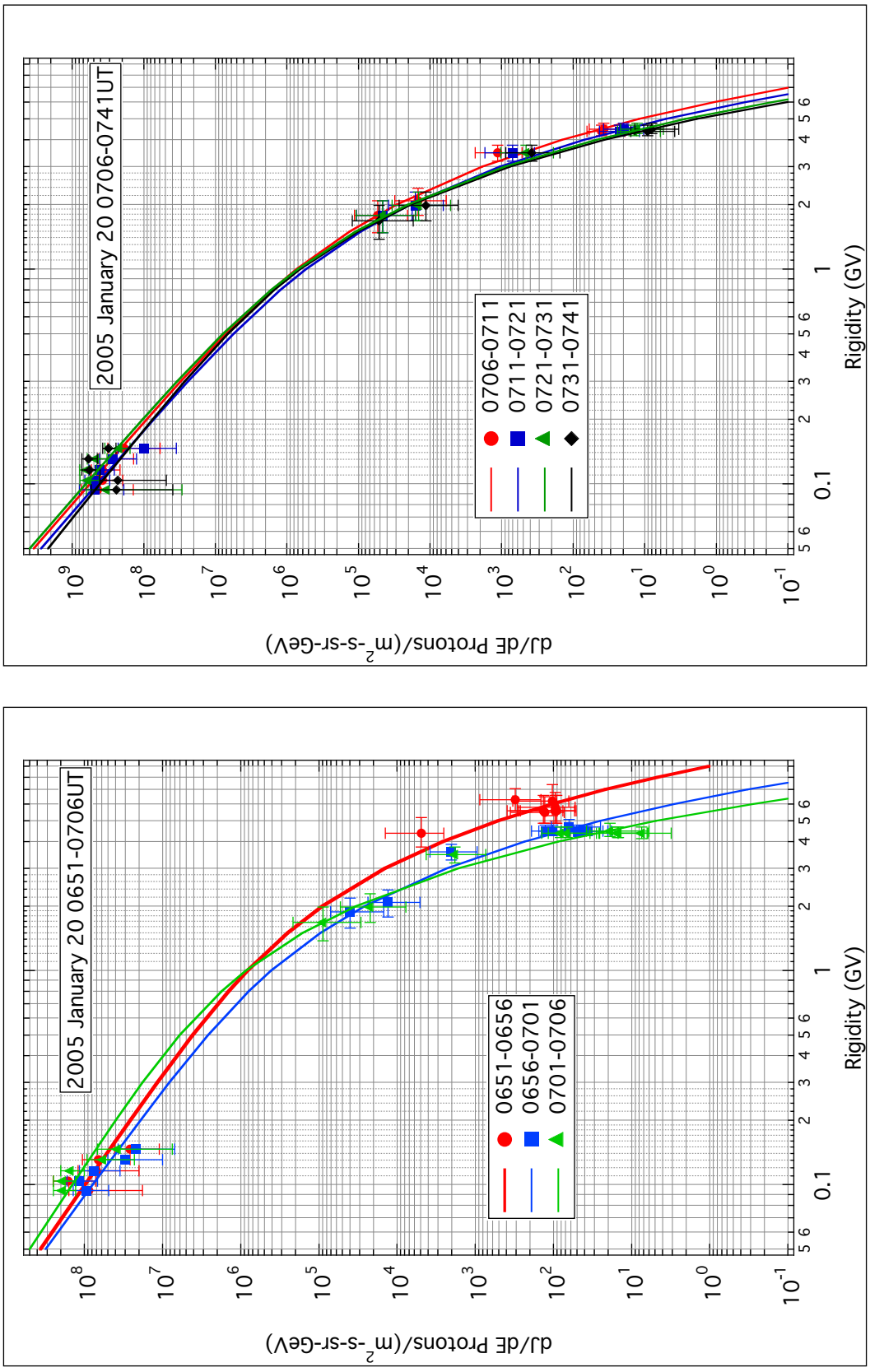

Figure 7.10: Time-resolved proton spectra during the 2005 January 20 GLE.

Time Interval (UT)	Flux, A ($\times 10^5$)	Spectral Index, γ	Break Energy, E_0 (GeV)
0651-0656	6.8 ± 2.5	1.1 ± 0.4	0.79 ± 0.13
0656-0701	9.6 ± 2.1	1.1 ± 0.2	0.48 ± 0.04
0701-0706	63 ± 15	0.8 ± 0.3	0.33 ± 0.06
0706-0711	17 ± 4.0	1.1 ± 0.2	0.41 ± 0.03
0711-0721	21 ± 5.7	1.1 ± 0.3	0.39 ± 0.06
0721-0731	26 ± 7.1	1.05 ± 0.4	0.35 ± 0.05
0731-0741	21 ± 6.4	1.15 ± 0.5	0.35 ± 0.05

Table 7.2: Evolution of the spectral parameters from equation 6.7 during the 2005 January 20 GLE. The hardest spectrum coincides with the initial spike in the Milagro GLE profile, and is evidence that efficient acceleration of protons to GeV energies occurred when the CME was low in the corona.

phase was also found by McCracken et al. (2008) and Bütikofer et al. (2009)) and seem to have reached an equilibrium state (Figure 7.10, top).

The spectra during the 2005 January 20 GLE seem to indicate two clear phases in the evolution of the CME-driven shock, an idea previously suggested by Evenson (1982) and Cane (1990). The timing results in section 7.2.2 show that a coronal shock accelerated particles through dense regions of solar atmosphere from 2.3-2.9 $R_\odot$, the hard spectrum during the earliest stages of the GLE indicate the particle acceleration was most efficient when the CME was blasting through these low coronal altitudes (high Mach number). After the GLE intensity peaked at 0653 UT (CME at ~3.7 $R_\odot$) it then declined rapidly and was accompanied by a softening spectrum. The softening of the spectra can be attributed to the CME-driven shock exiting the dense layers of the corona and reaching interplanetary space where it would transition to an interplanetary shock (low Mach number). Relativistic particles would then have access to multiple field lines, leading to the decreased anisotropy observed by Bombardieri et al. (2008).

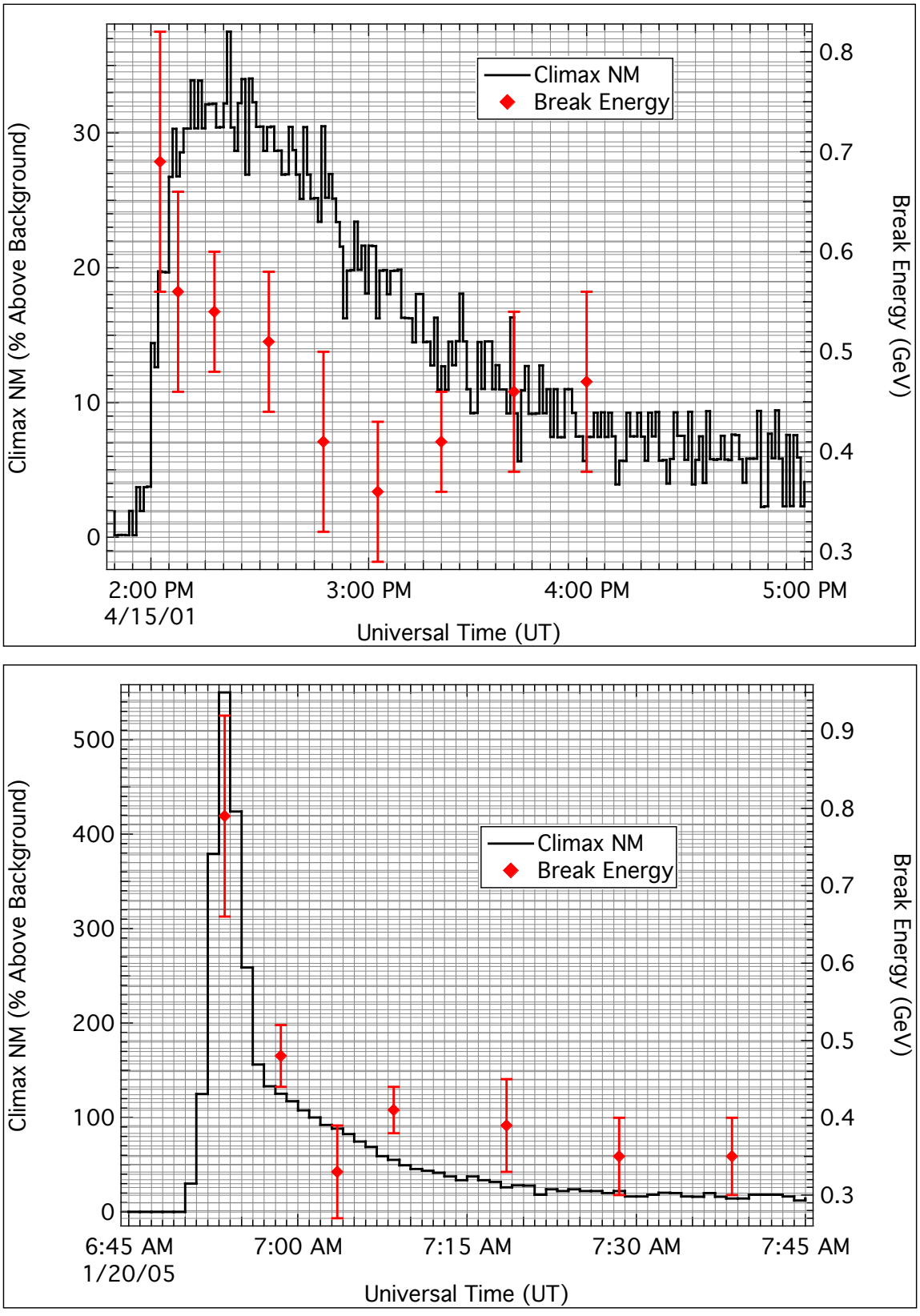

Figure 7.11: Evolution of the break energy during the 2001 April 15 and January 20 GLEs.

The transitions in the proton spectra (Figure 7.3), specifically the break energy (Figure 7.11, top), during the 2001 April 15 GLE are more gradual. Although the break energy is highest during the earliest stages of the GLE, one could argue that a fixed ~0.5 GeV break energy is consistent within the error bars. However, similar events in the past have also been hardest during their earliest stages, and the same behavior is clearly seen in the 2005 January 20 GLE. Given the similarities, it is fair to assume that the 2001 April 15 GLE acted in the same way. The extreme and rapid nature of the 2005 January 20 GLE may be the reason why the separate phases suggested by Evenson (1982) and Cane (1990) are discernible while not in classic GLE profiles such as the 2001 April 15 GLE.

We speculate that in the 2005 January 20 GLE the favorable magnetic connection, strong anisotropy, minimal scattering, and fast transit of the CME all conspire to reveal the initial spike in the GLE profile before the CME-driven coronal shock transitions to an interplanetary one. In the 2001 April 15 event, particle transport conditions and a slower CME transit through the corona cause the initial, coronal phase and extended, interplanetary phase to overlap, producing the classic GLE profile. Therefore, the fastest evolving GLEs may provide insight into the GLE process that is not directly observable in more ordinary events.

7.3 Discussion

Both the 2001 April 15 and 2005 January 20 events are associated with strong X-class flares and fast CMEs from the western solar limb, however the GLE profiles are much different. The 2001 April 15 event has a classic GLE profile similar to many well-connected events observed in the long history of NM observations (see section 3.2.2). On the other hand, the 2005 January 20 GLE has an extremely fast-evolving initial spike in intensity observed at some ground-level stations. Its prompt onset and deviation from the classic GLE profile have caused many to question if a CME-driven shock can duplicate the observations. We now discuss and interpret the results presented above in the context of other work.

The 2001 April 15 GLE onset and peak times are well removed from those of the associated flare. GLE onset occurred at 1346 ST, while flare onset in soft X-rays came at 1328 ST. The GLE peak lasted from 1357-1412 ST, but the flare peaked at 1341 ST, five minutes before the GLE onset. Similar to the results of Bieber et al. (1994), the timing of the GLE found in this analysis is better attributed to the associated CME. The CME liftoff occurred at 1324 ST and evidence of shock formation indicated by type II radio emission came at 1338:40 ST. The CME-driven shock then had more than 7 minutes to accelerate particles up to GeV energies before releasing them into interplanetary space. The CME height from shock formation to SPR time ranged from 2.5-3.3 $R_{\odot}$, in agreement with other CME heights at GLE onset found by Kahler (1994).

Characteristic	2001 April 15	2005 January 20
X-ray Flare Size	X14.4	X7.1
Source Location	S20°, W85°	N12°, W58°
CME Speed	1200 km/s	3242 km/s
Soft X-Ray Flare Peak (ST)	1341	0653
4-7 MeV Gamma-Ray Onset (ST)	1333	0635:40
>60 MeV Gamma-Ray Onset (ST)	N/A	0637:10
CME Onset (ST)	1324	0628
Type II Onset (ST)	1338:40	0635:40
Path Length (AU)	1.59 ± 0.01	1.2 ± 0.1
SPR time (ST)	1346	0639:30 ± :50
CME height at Type II Onset	2.5 $R_\odot$	>2.3 $R_\odot$
CME height at Injection	3.3 $R_\odot$	>2.9 $R_\odot$
CME height during GLE Peak	4.4-6.0 $R_\odot$	~3.7 $R_\odot$
Delay, SPR time - Type II Onset (min)	~7	~4
Preceding CMEs?	Yes	Yes

Table 7.3: Various characteristics and timing information on both the 2001 April 15 and 2005 January 20 events.

The proton spectra throughout the entire event are consistent with the spectral form derived by Ellison and Ramaty (1985) and attributed to a coronal shock origin. An analysis performed by Bombardieri et al. (2007) also found that the proton spectra at all stages of the 2001 April 15 GLE are best fitted to a shock acceleration spectral form.

The delays between the 2005 January 20 GLE and the associated flare are in the same order as those of 2001 April 15, but much shorter (Table 7.3). Flare onset in soft X-rays came at 0628 ST, and GLE onset occurred at 0639:30 ST. The Flare peaked at 0653 ST, and the GLE peaked at 0642 ST. The release delays between GLE protons and electromagnetic species are well established (Carmichael, 1962; Cliver et al., 1982), however, the delay for the 2005 January 20 event is the shortest ever recorded.

There is ample evidence for the existence of a CME-driven shock in the 2005 January 20 event such as type II radio emission (Gopalswamy et al., 2005; Aschwanden, 2010), charge states and abundance ratios (Desai et al., 2006; Labrador et al., 2005), and white light images (Gopalswamy et al., 2005). However, the short time delay and extreme intensity observed in some ground-level stations causes many to resurrect direct flare acceleration as the source of the highest-energy particles during the earliest stages of the GLE (*e.g.*, Simnett, 2006; Grechnev et al., 2008; McCracken et al., 2008; Mason et al., 2009). In addition to support for direct flare acceleration, skepticism has risen on wether or not a CME-driven shock could produce the observed GLE profile within the allotted time.

From the timing analysis described in section 7.2.2, the path length traversed by the relativistic protons at the time of the 2005 January 20 event was found to be 1.2 ± 0.1 AU. This gives a SPR time of 0639:30 ± :50 ST for the >4 GV protons, roughly 4 minutes after the onset of type II radio emission (Table 7.3). The CME height ranged from 2.3-2.9 $R_{\odot}$ from type II radio onset to SPR time, capable of driving a powerful shock through layers of dense solar atmosphere low in the corona before injecting the GeV protons into interplanetary space at ~2.9 $R_{\odot}$, consistent with the values for the 2001 April 15 event and in agreement with other CME heights at GLE onset (Kahler, 1994).

The active regions which eventually produced the X-class flares associated with the 2001 April 15 and 2005 January 20 GLEs also produced several large flares and CMEs in the days leading up to the events, as evidenced by Forbush decreases observed shortly after (see sections 5.1.2 and 5.2.2). When CMEs occur in rapid succession from

the same active region, some of the SEPs produced by one CME may become seed particles to the next CME (Mason et al., 1999; Kahler, 2001). A seed population swept up by a CME-driven shock can greatly reduce the time required to accelerate ions to GeV energies (see section 1.5.2). Although no in-situ measurements are available, it is reasonable to speculate that activity prior to the 2005 January 20 event within the same active region would result in a seed population extending up through a few MeV. A quick calculation using the model derived by Lee and Ryan (1986) shows that a 10 MeV proton can be accelerated by a coronal shock within ~5 minutes, on the same order as the observed delay in the 2005 January 20 event.

Intensities in some Spaceship Earth NMs during the initial phase of the 2005 January 20 GLE reached levels well in excess of 1,000%, while some registered no increase until after the initial phase ended. This indicates a *very* anisotropic and beam-like distribution of particles at GLE onset. The rise-to-maximum in Milagro channels (~80 s) is almost an order of magnitude faster than that of the 2001 April 15 GLE, which also was a well-connected event. The path length during the 2005 January 20 GLE (1.2 ± 0.1 AU) is close to the length of the nominal Parker spiral and significantly shorter than during the 2001 April 15 GLE (1.59 ± 0.01 AU), indicating there may have been minimal or no scattering during the relativistic protons' transit to Earth. These factors indicate that the rapid onset and extreme intensity of the 2005 January 20 GLE was caused by a very favorable magnetic connection and minimal upstream turbulence, and not from an additional or alternative acceleration mechanism.

We conclude that the accelerating source of the relativistic protons for the entire 2005 January 20 GLE is at a CME-driven shock for the following reasons:

1. Type II radio emission, indicating the presence of a CME-driven shock, began low in the corona when the CME height was ~2.3 $R_{\odot}$.
2. The path length derived by three independent analyses was 1.2 ± 0.1 AU, corresponding to a SPR time of 0639:30 ± :50 ST when the CME height was ~2.9 $R_{\odot}$, in agreement with other CME heights at GLE onset observed by Kahler (1994).
3. Although the delay between SPR time and type II onset is the shortest ever recorded (~4 minutes), the time to accelerate protons to GeV energies (as modeled by Lee and Ryan (1986)) is of the same order.
4. The extreme CME speed at low solar altitudes (greater particle density) combined with seed particles remnant from prior activity from the same active region could speed up the acceleration process.
5. The rapid onset and high intensity of the initial GLE spike observed in some ground-level stations is due to a beam-like distribution of particles and a favorable magnetic connection with little scattering.
6. The proton spectra for the duration of the GLE are consistent with shock acceleration, similar to the 2001 April 15 GLE which is widely recognized as having a coronal shock origin.
7. Finally, a flare-based model can not explain the ~4-minute delay between the high-energy gamma-ray emission and the onset of the GLE protons.

Shea and Smart (1996) noticed that occasionally a limited number of ground-level stations would exhibit a short-lived precursor spike prior to the onset of a more conventional GLE resolved at many more locations. The 2005 January 20 event is the latest, and perhaps best example, of these features. Others examples include the 1989 October 22 (Figure 7.12), 1960 May 4 (McCracken, 1962b), and 1978 May 7 GLEs (Figures 3.5, 3.6). An additional feature that all these GLEs share is an anisotropic pitch-angle distribution during early stages followed by a rapid decrease in the anisotropy. These events have led to theories of two separate acceleration mechanisms (Shea and Smart, 1998; McCracken and Moraal, 2007; Moraal et al., 2007; McCracken et al., 2008).

McCracken et al. (2008) concluded that the accelerating source of the precursor spike of the 2005 January 20 GLE was the flare itself based on the time profiles of ground-level stations and the CORONAS-F/SONG >60 MeV gamma rays. Under the assumption that the high-energy gamma rays and the relativistic protons were released from the same point at the same time, the delays of the observed onset times yield a 1.76 AU path length. McCracken et al. also concluded that a CME-driven shock forming at ~0642 ST accelerated the relativistic particles after the initial spike and for the remainder of the event. However, we have shown that the path length is much closer to 1.2 AU, and the resulting delay between the releases of the high-energy gamma rays and relativistic protons is difficult to attribute to a flare origin (see section 7.2.2). In addition, the type II radio onset occurs at 0635:40 ST and thus shock formation commenced well before 0642 ST.

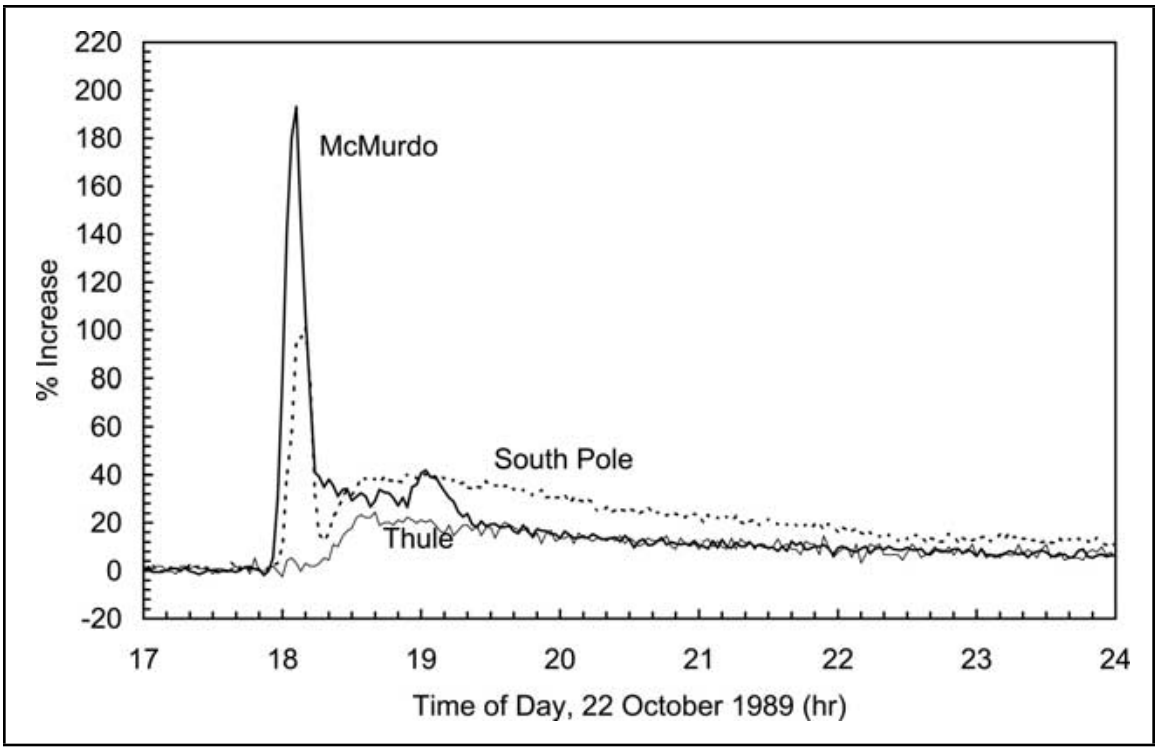

Figure 7.12: GLE profiles for the 1989 October 22 event in the McMurdo, South Pole and Thule neutron monitors (Shea and Smart, 1996; McCracken et al., 2008). The precursor spike resembles that of the 2005 January 20 GLE and was seen in only a few stations. Most neutron monitors observed a profile similar to the Thule station.

It is difficult to model the acceleration of the highest-energy particles directly from the flare site, however, we have no evidence that firmly disproves direct flare acceleration. It is also difficult to explain fast evolving GLEs, such as 2005 January 20, with two-theory models. On the other hand, shock acceleration not only models slowly-evolving classic GLE profiles (2001 April 15) very well, but we have also shown that for the 2005 January 20 GLE (the fastest evolving GLE ever observed) the rapid onset and proton spectra are consistent with shock acceleration. Occam's razor would dictate that these facts suggest that shock acceleration theory should be seen as the leading candidate to explain the origin of the highest-energy particles produced in solar processes.

7.4 Conclusions

Measurements of the 2001 April 15 and 2005 January 20 GLEs with the Milagro water Čerenkov detector and multiple NMs were used to analyze the proton spectra throughout the evolution of each event. The multiple data channels in Milagro enabled a self-consistent analysis of the proton spectra during the initial phase of the 2005 January 20 GLE despite the large anisotropy effects. The spectral results for all phases of each event are consistent with a coronal shock origin. The spectra were hardest during the rising edge of the 2001 April 15 GLE and the precursor spike of the 2005 January 20 GLE, indicating that the most efficient acceleration of the GeV protons occurred when the CMEs were at low solar altitudes ($<3\ R_{\odot}$). The onset of the type II radio emission for both events occurred after CME launch and prior to GLE onset, evidence that shock formation commenced low in the corona with sufficient time to accelerate protons to GeV energies. This agrees with recent modeling of GeV shock acceleration (Lee, 2005; Zank et al., 2000) that requires setting up the shock close to the Sun and retaining the particles for acceleration before they are released into interplanetary space.

The rapid evolution and high intensity of the 2005 January 20 GLE has generated both great interest and great debate within the field, causing many to resurrect direct flare acceleration as the source of the highest-energy particles during the initial phase of the GLE. However, we have shown that this extreme behavior is consistent with the same shock acceleration model explaining classic GLE profiles, *e.g.*, 2001 April 15, but on a faster timescale and not requiring a different process, *i.e.*, direct solar-flare acceleration.

Appendix A

Simulation Plots

Preliminary simulations for Milagro and the Milagro prototype, Milagrito, established that the detector was sensitive to shower cores up to 10 km radially. Simulating Milagro's sensitivity to solar cosmic rays required an extrapolation procedure to obtain the specific yield functions for the higher multiplicity channels near the cutoff rigidity, described in section 4.5.3.

This section contains the simulation results for isotropic and anisotropic (zenith) pitch-angle distributions for Milagro's scaler channels which were used to analyze the 2001 April 15 and 2005 January 20 GLEs. Milagro's specific yield functions are also compared to those of neutron monitors used in the analysis.

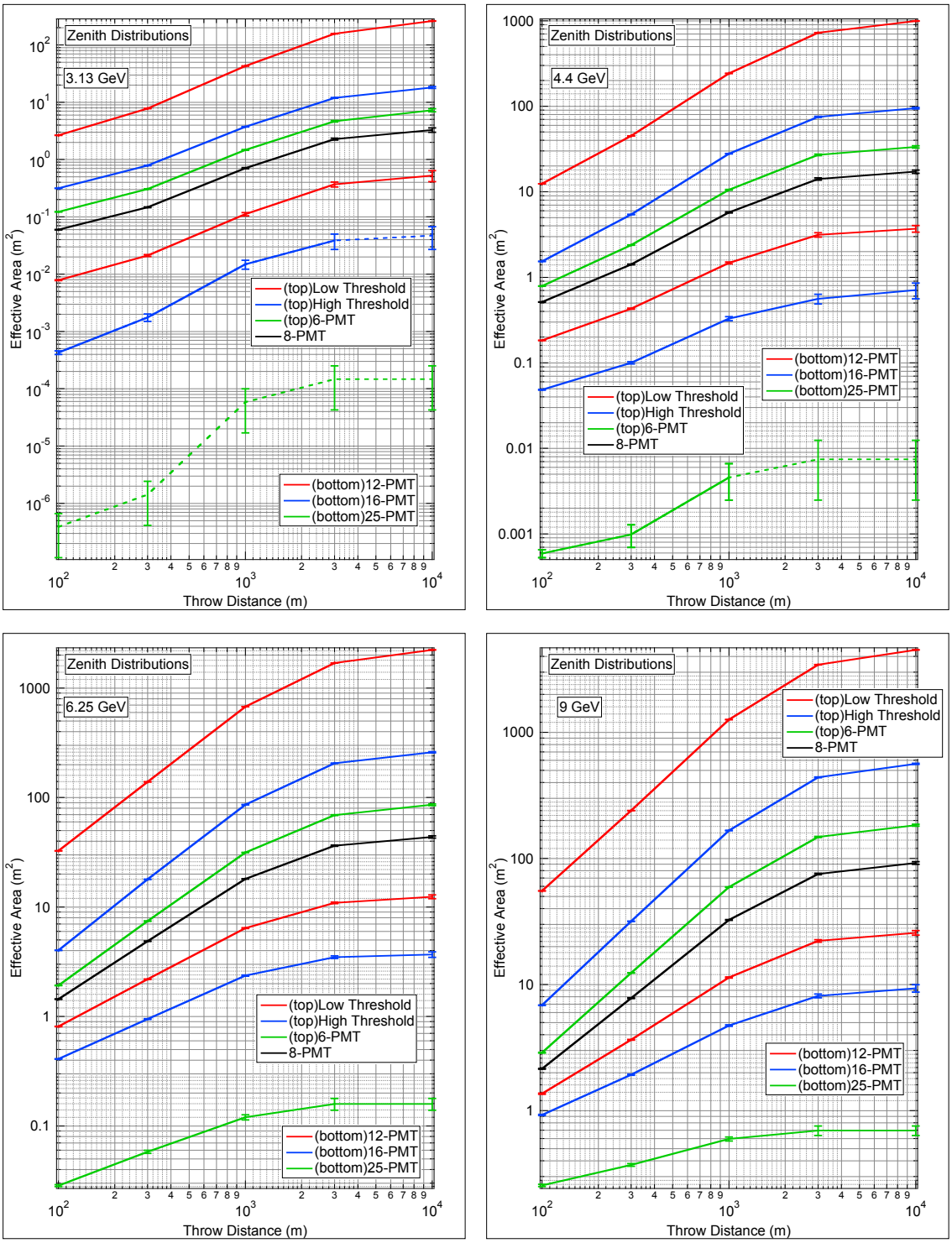

Figure A.1: Simulated proton effective area vs. throw distance for a zenith pitch-angle distribution from 3.13-9 GeV (dashed lines represent extrapolated values).

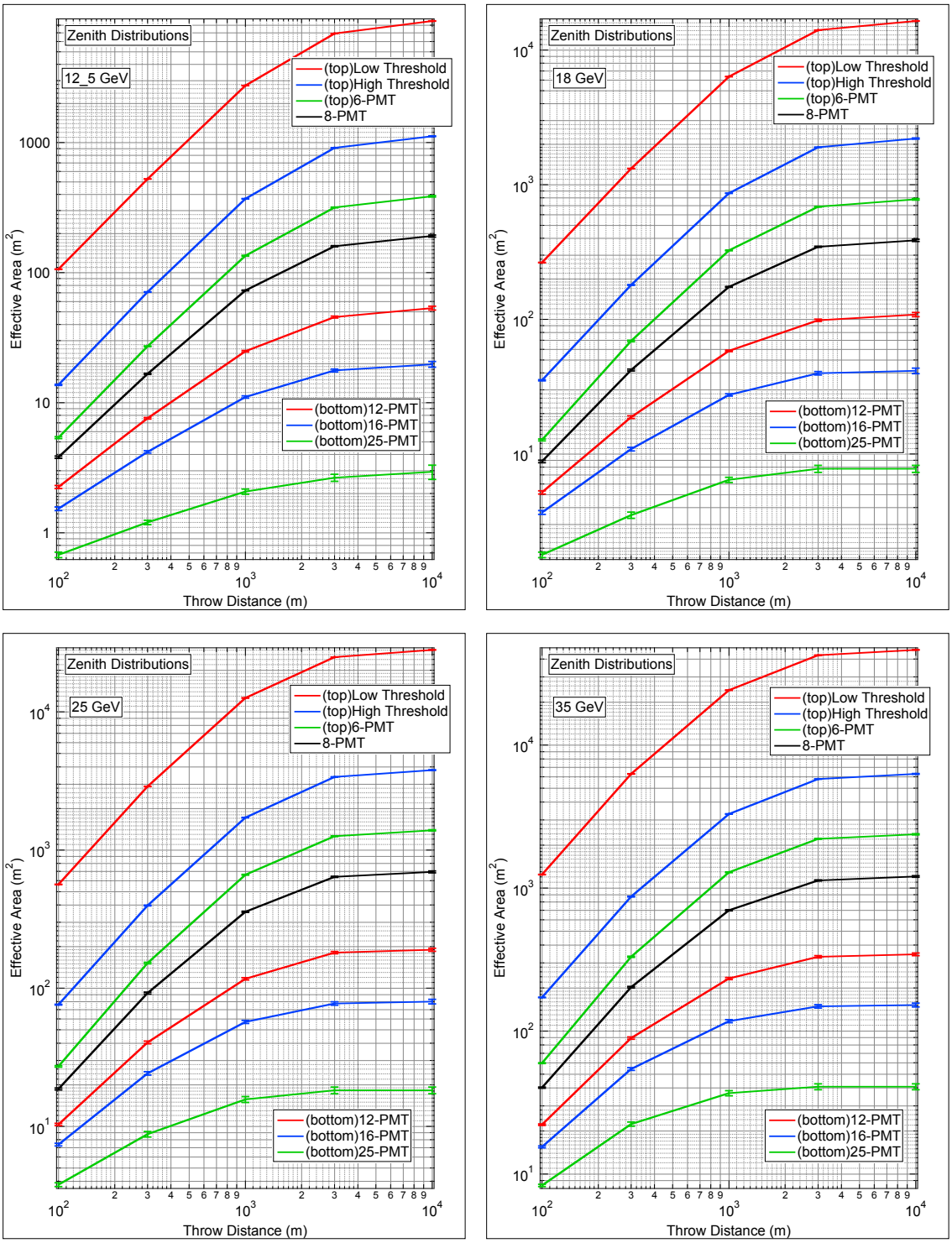

Figure A.2: Simulated proton effective area vs. throw distance for a zenith pitch-angle distribution from 12.5-35 GeV.

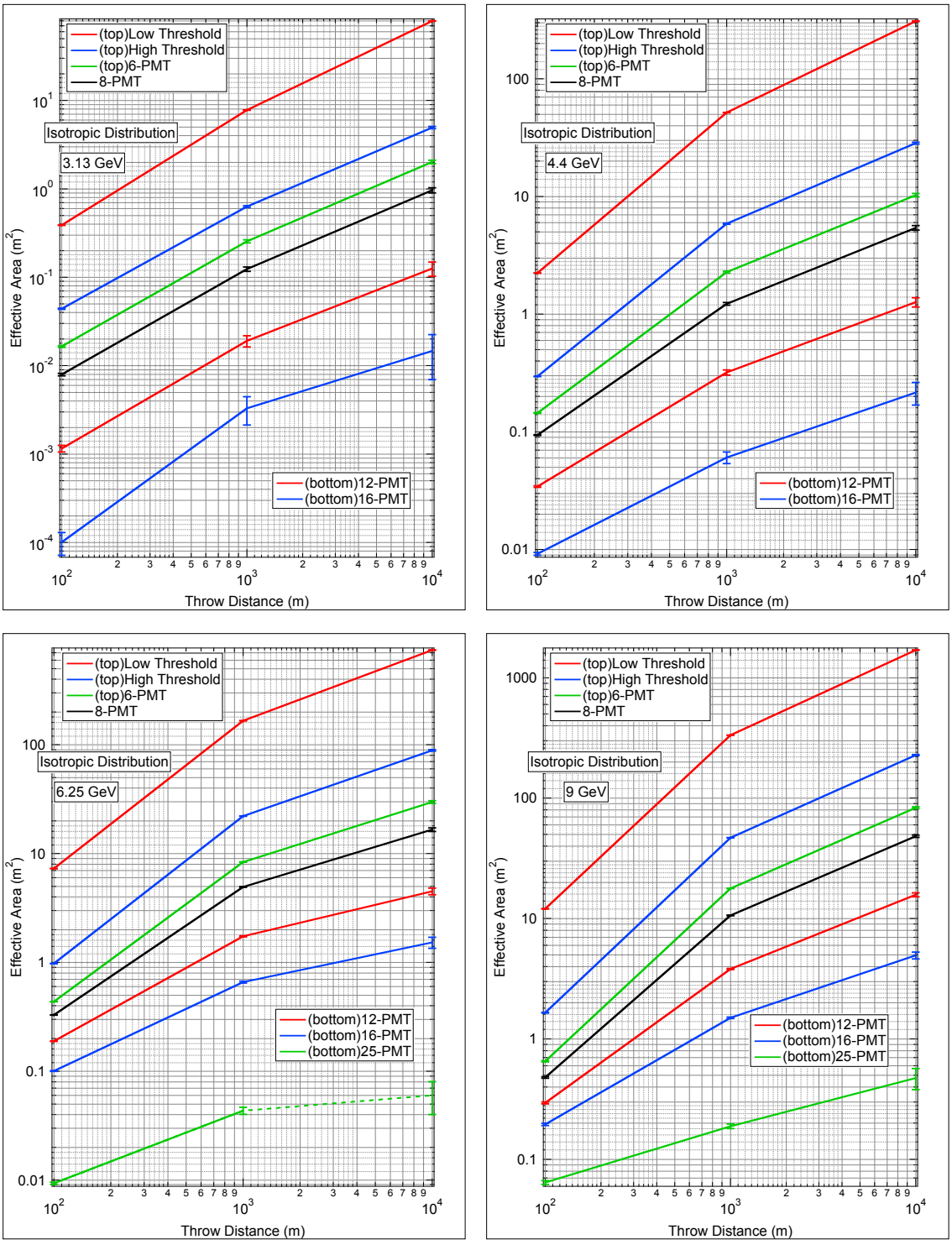

Figure A.3: Simulated proton effective area vs. throw distance for an isotropic pitch-angle distribution from 3.13-9 GeV (dashed lines represent extrapolated values).

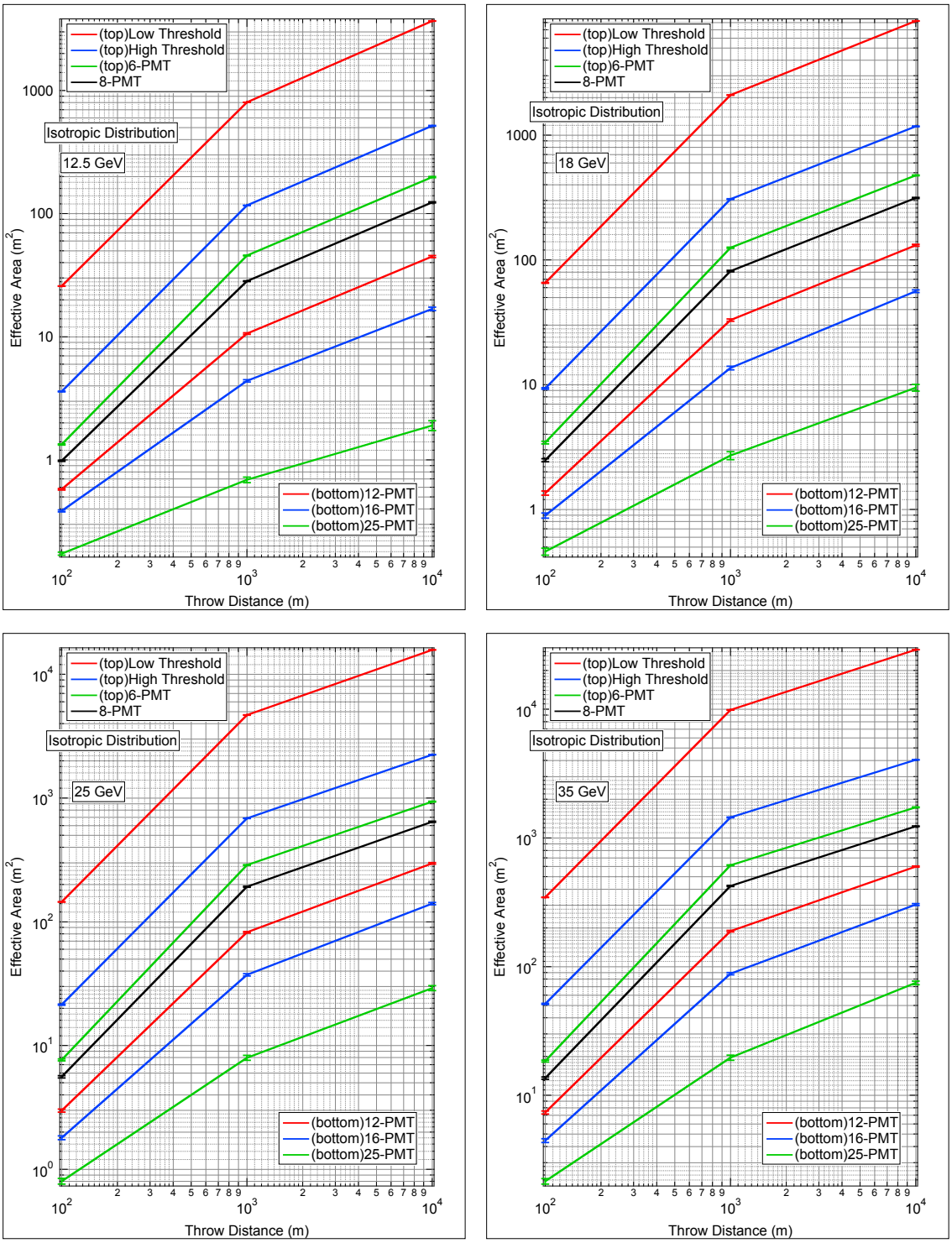

Figure A.4: Simulated proton effective area vs. throw distance for an isotropic pitch-angle distribution from 12.5-35 GeV.

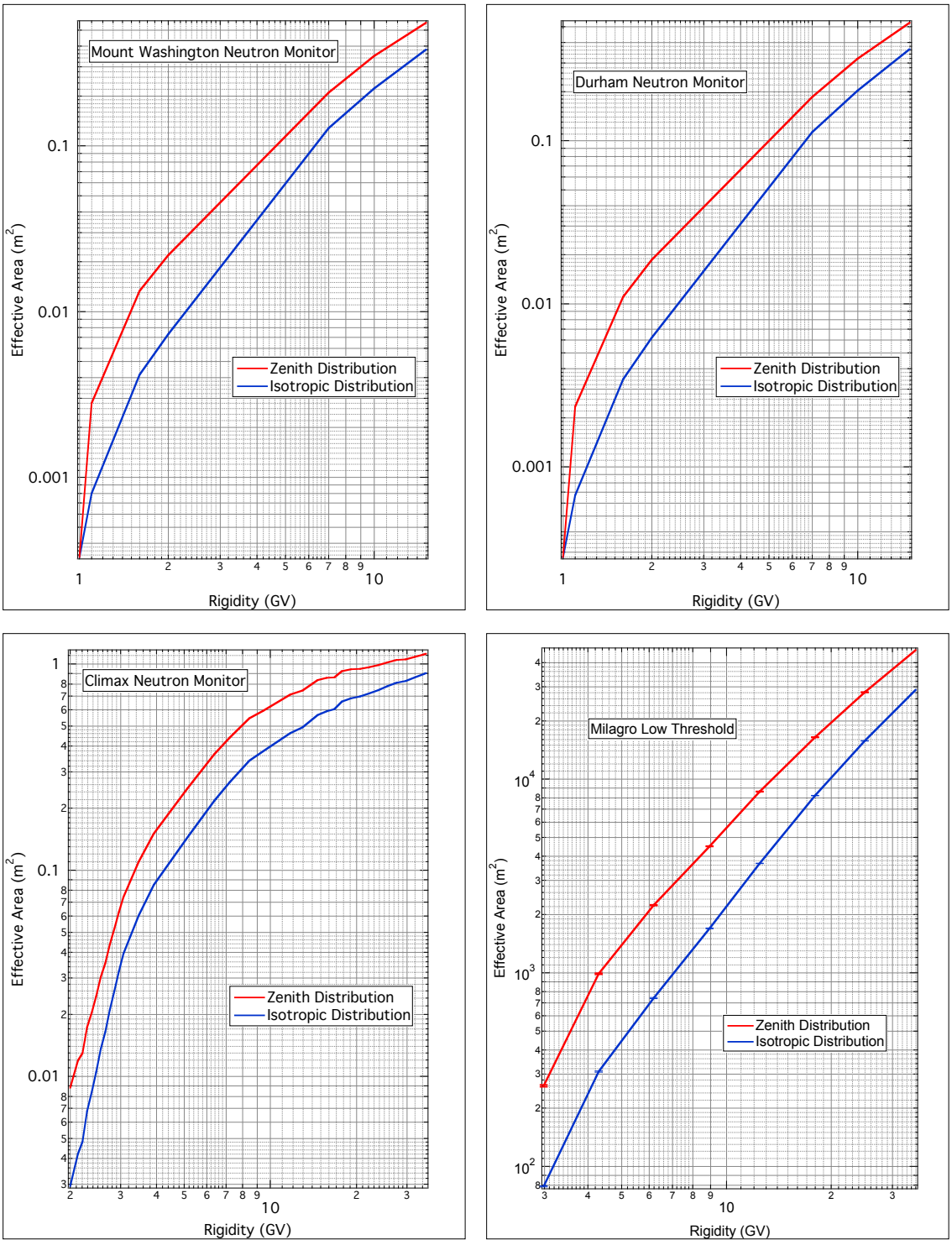

Figure A.5: Isotropic vs. zenith proton specific yield functions for Mt. Washington, Durham, and Climax neutron monitors (Mt. Washington and Durham out to 15 GV), as well as the Milagro low threshold channel.

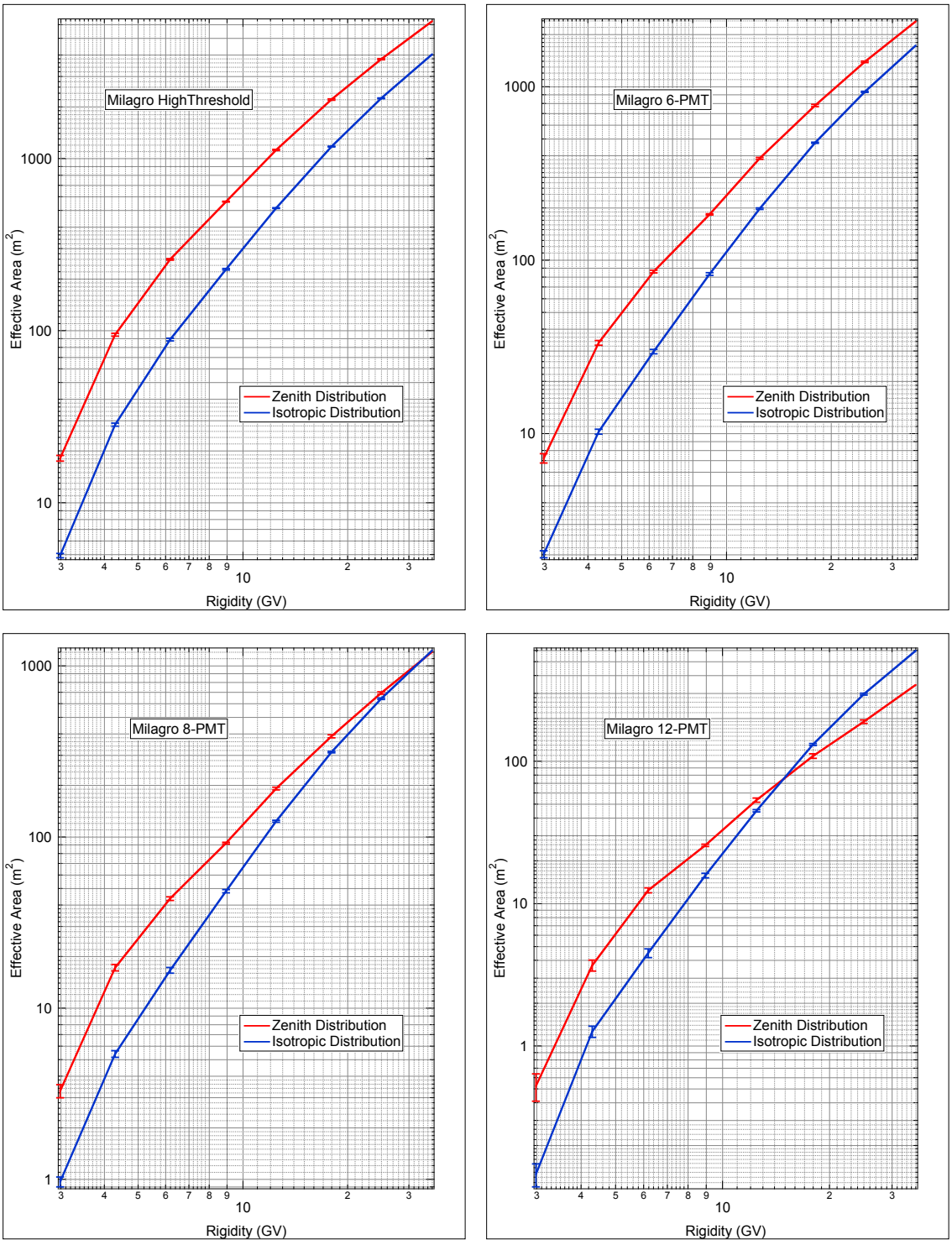

Figure A.6: Isotropic vs. zenith proton specific yield functions for Milagro high threshold, 6-PMT, 8-PMT, and 12-PMT channels.

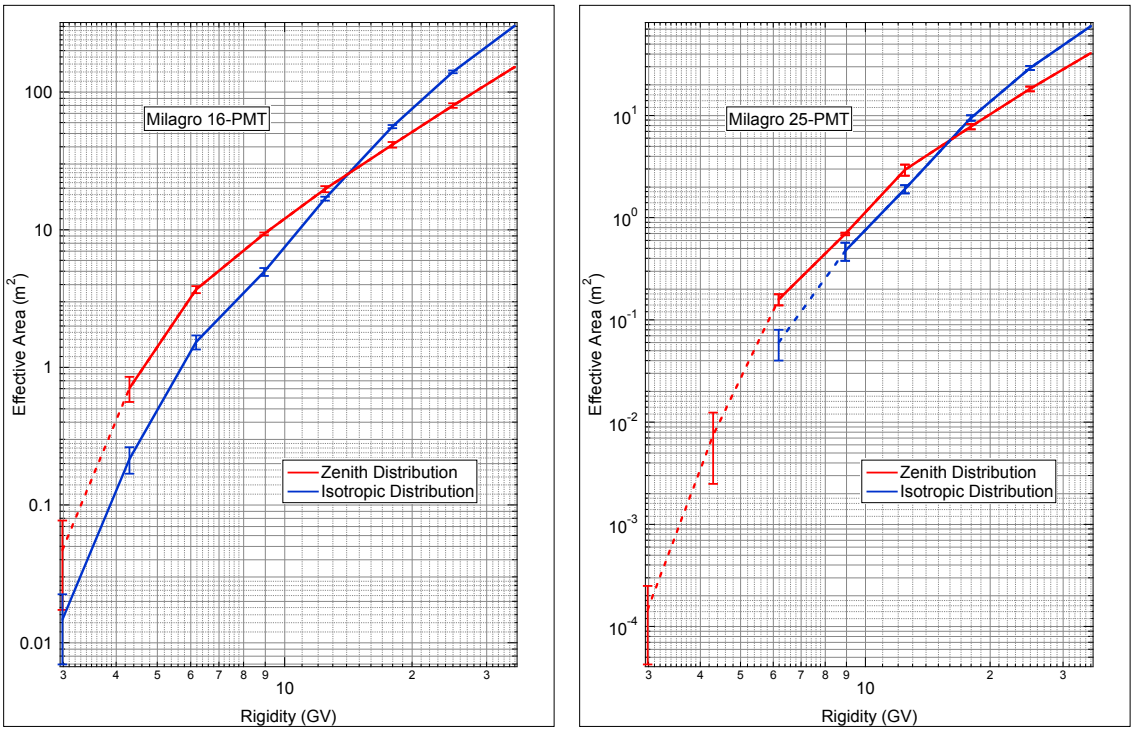

Figure A.7: Isotropic vs. zenith proton specific yield functions for Milagro 16-PMT and 25-PMT channels (dashed lines represent extrapolated values).

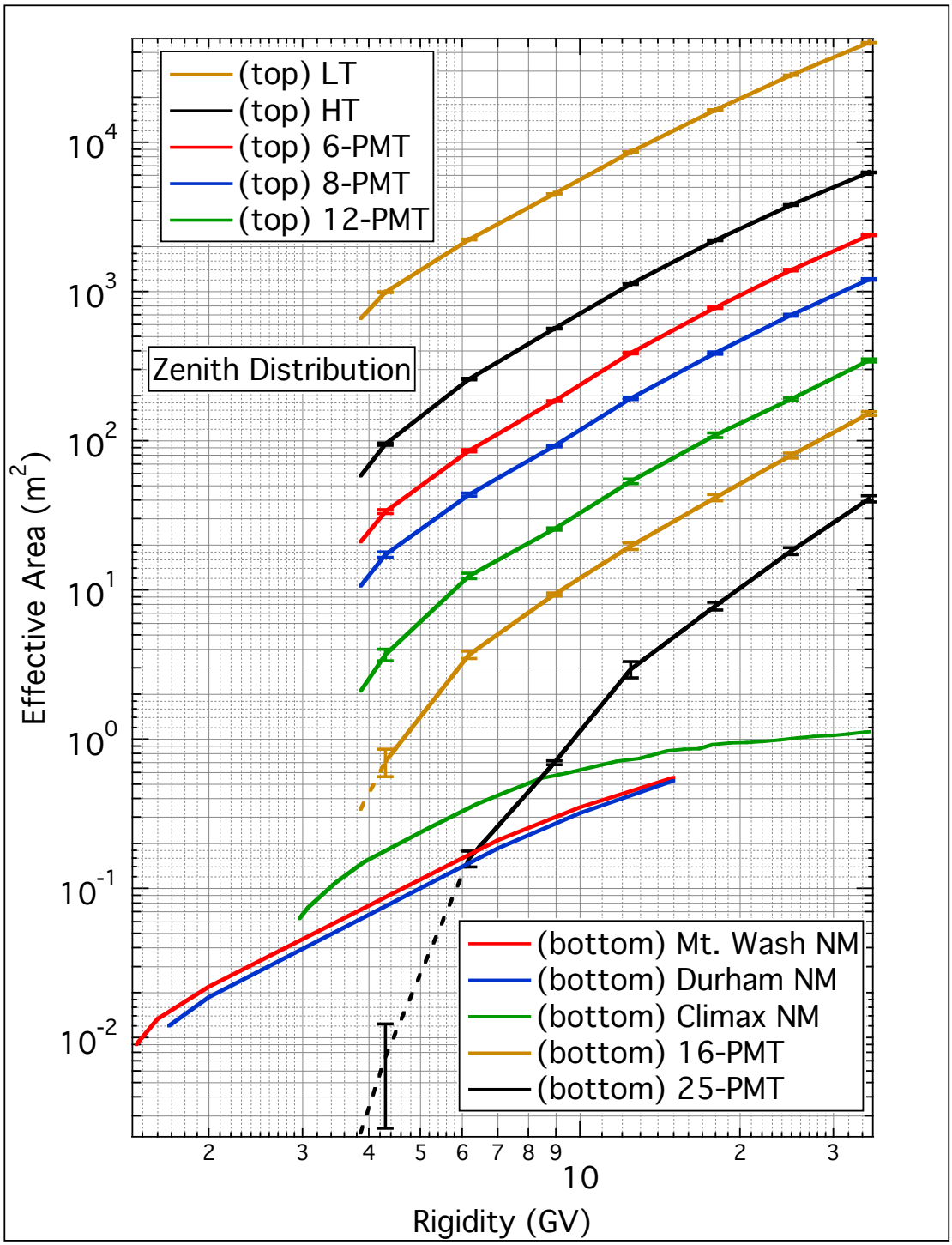

Figure A.8: Zenith proton specific yield functions for Climax, Mt. Washington, and Durham neutron monitors, as well as all available Milagro channels (dashed lines represent extrapolated values).

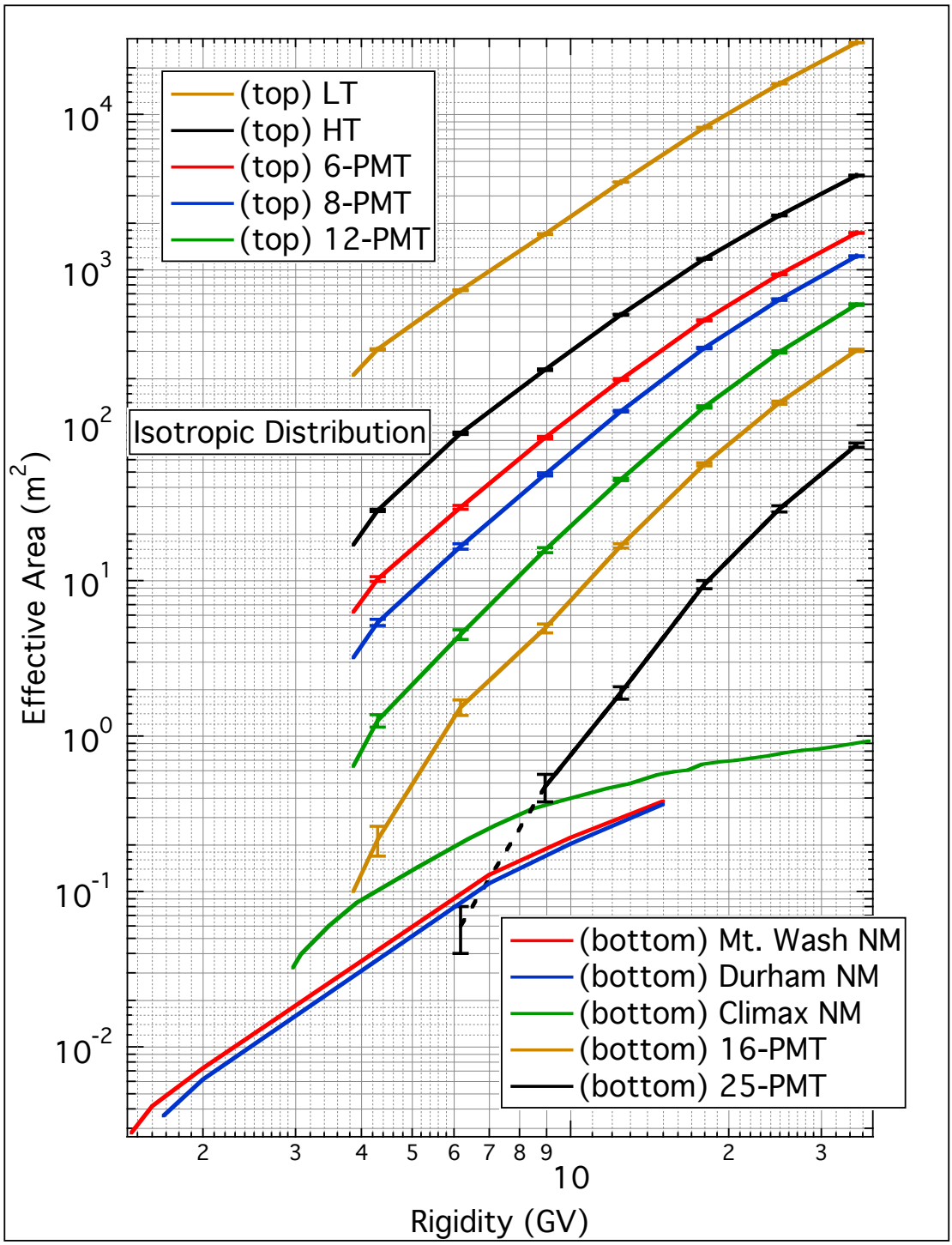

Figure A.9: Isotropic proton specific yield functions for Climax, Mt. Washington, and Durham neutron monitors, as well as all available Milagro channels (dashed lines represent extrapolated values).

Appendix B

Time-Resolved Spectra

Measurements of the proton spectra during both the 2001 April 15 and 2005 January 20 GLEs were derived from the analysis procedure outlined in chapter 6. Ground-level count rates were taken from the Mt. Washington, Durham, and Climax neutron monitors (see Table 3.2 for station characteristics), and all available Milagro scaler channels. Spacecraft data were taken from IMP-8 (courtesy of Dr. C. Lopate, private communication) for the 2001 April 15 event, and from SOHO/ERNE (courtesy of Dr. E. Valtonen, private communication) for the 2005 January 20 event.

Milagro multiplicity channels experienced instrumental difficulties at the time of the 2001 April 15 event, therefore, in addition to the neutron monitors listed above, only the low and high threshold channels in Milagro were used in the analysis. Based on the pitch-angle distribution results described in section 7.1.1, spectral measurements were performed using specific yield functions modeled by an isotropic pitch-angle distribution for time intervals from 1400 - 1425 UT, and an anisotropic pitch-angle distribution for time intervals after 1425 UT.

Many ground-based stations were unable to resolve the intense, initial phase of the 2005 January 20 GLE due to the anisotropic pitch-angle distribution (see section 7.2.1). As a result, the Mt. Washington and Durham neutron monitors were omitted from

the spectral analysis performed from 0651-0656 UT. However, the favorable viewing direction of Milagro during this anisotropic phase, produced signals in multiplicity channels up to 25-PMT. Proton spectra were measured using Milagro scalers channels up to 25-PMT until 0656 UT, up to 16-PMT until 0706 UT, and up to the high threshold channel from then on. Based on the pitch-angle distribution results described in section 7.2.1, spectral measurements were performed using specific yield functions modeled by an isotropic pitch-angle distribution for time intervals from 0651 - 0656 UT, and an anisotropic pitch-angle distribution for time intervals after 0656 UT.

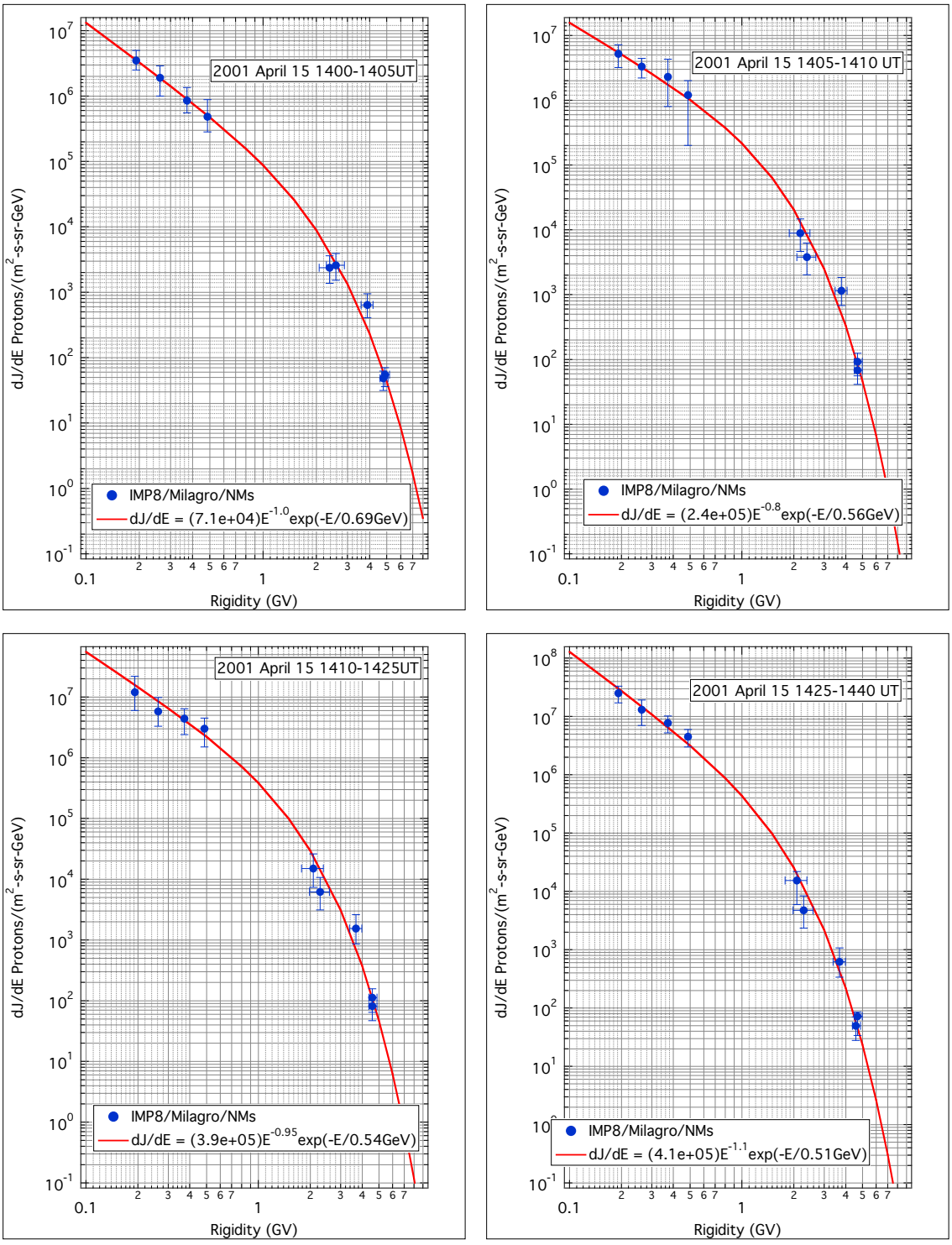

Figure B.1: Proton spectra for multiple time intervals in the 2001 April 15 GLE. The results were obtained from the analysis procedure described in chapter 5 using data from ground-level detectors and IMP-8 spacecraft data.

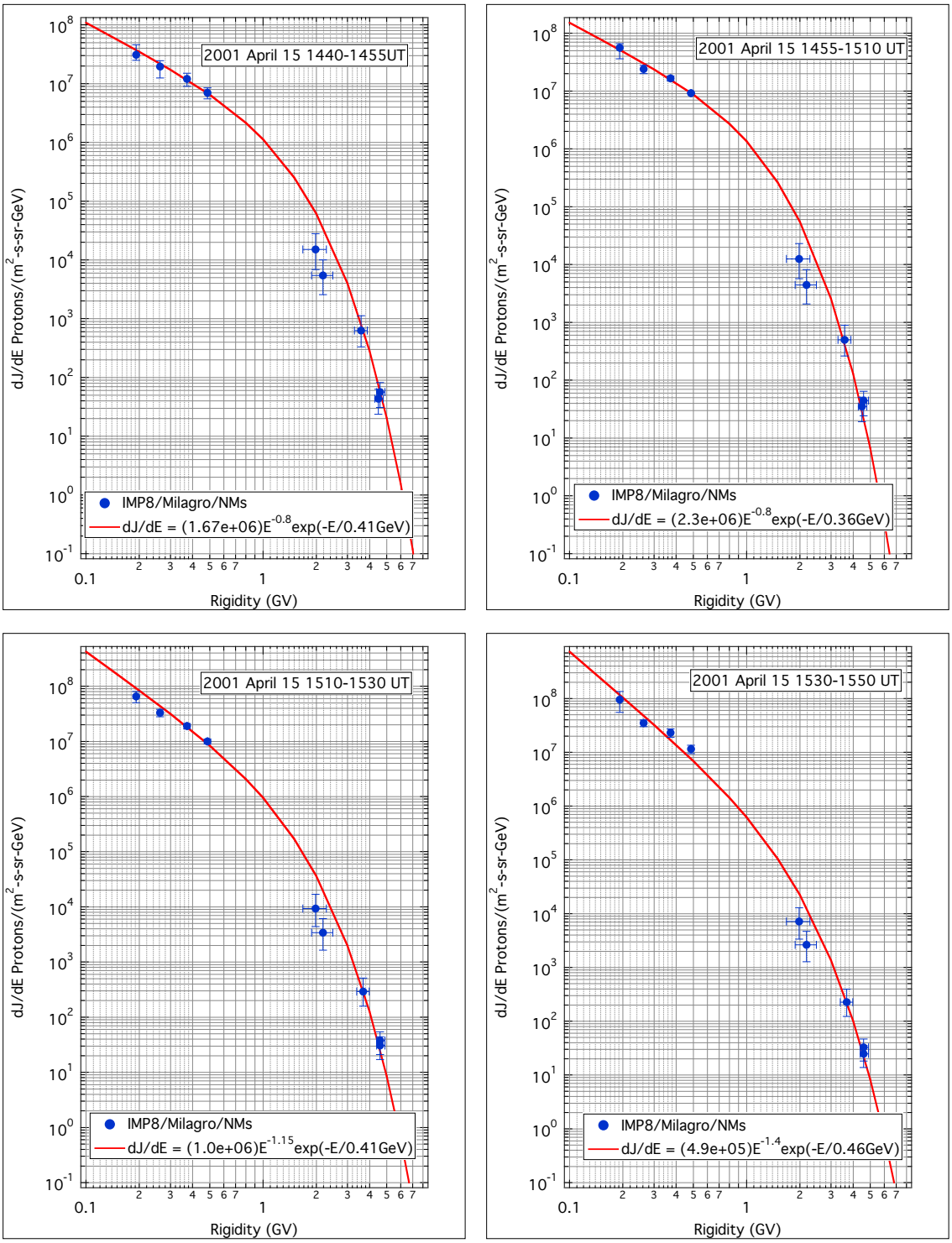

Figure B.2: Proton spectra for multiple time intervals in the 2001 April 15 GLE. The results were obtained from the analysis procedure described in chapter 5 using data from ground-level detectors and IMP-8 spacecraft data.

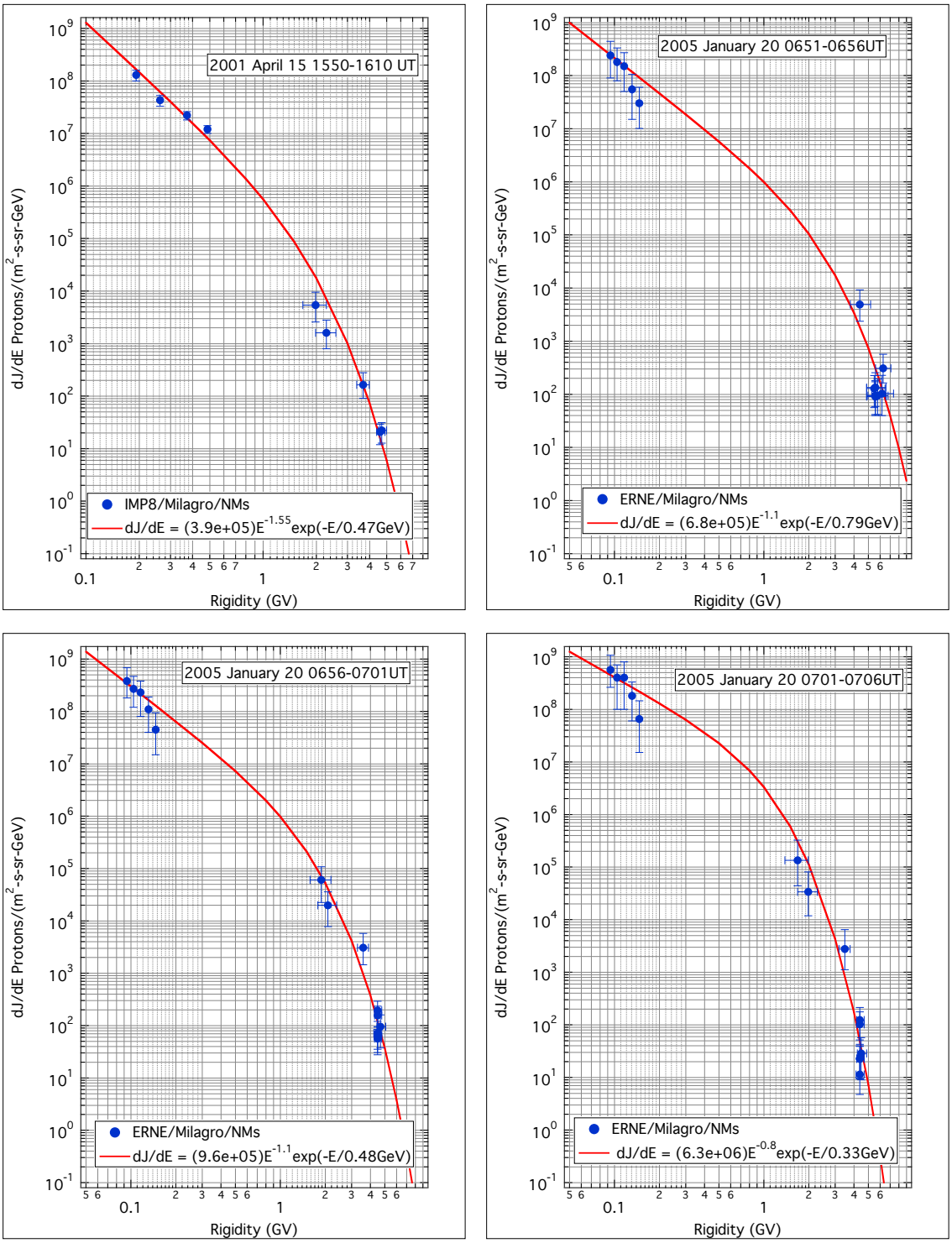

Figure B.3: Proton spectra for the final time interval of the 2001 April 15 GLE, and early stages of the 2005 January 20 GLE. The results were obtained from the analysis procedure described in chapter 5 using data from ground-level detectors and spacecraft data from IMP-8 (2001 April 15) and SOHO/ERNE (2005 January 20).

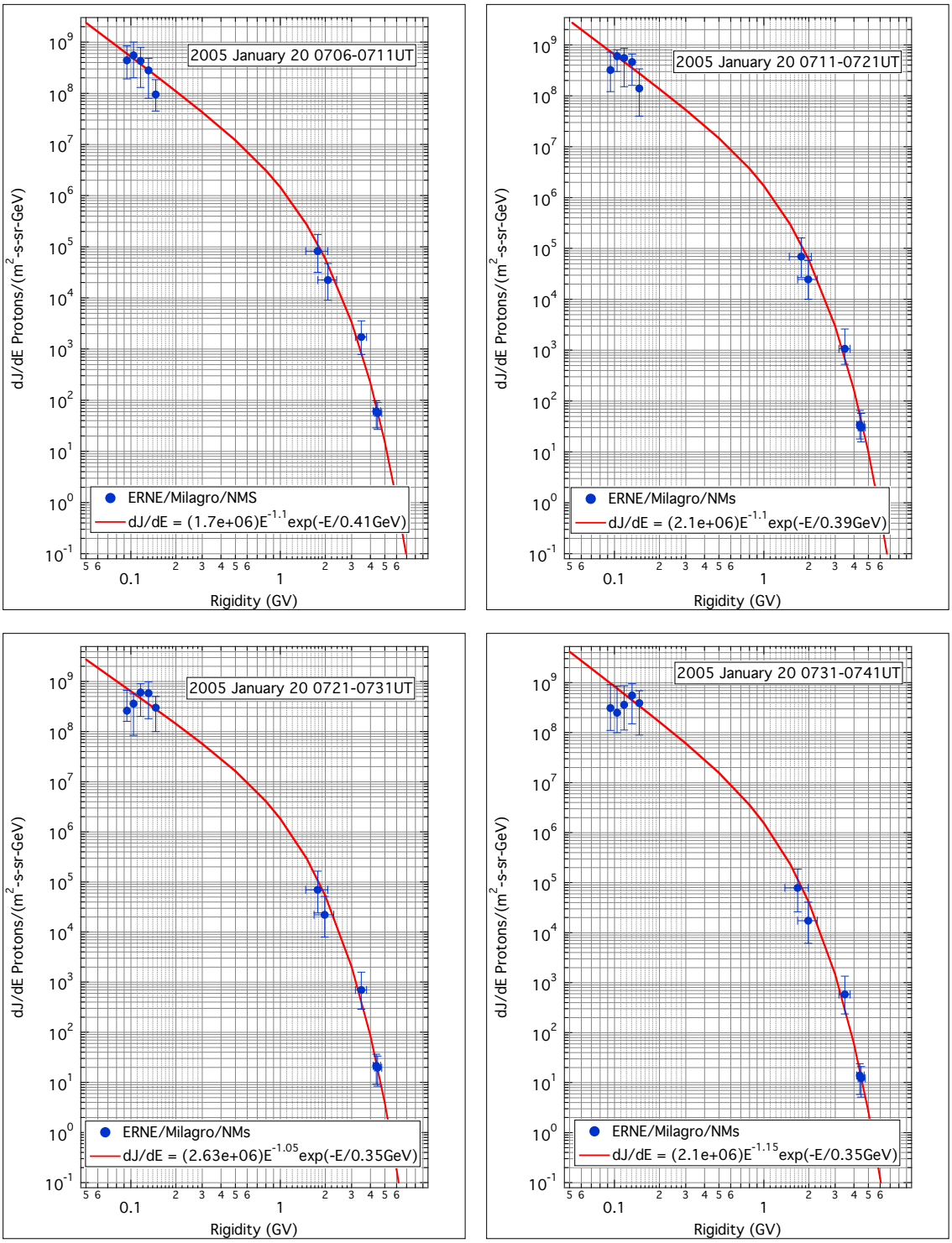

Figure B.4: Proton spectra for multiple time intervals of the 2005 January 20 GLE. The results were obtained from the analysis procedure described in chapter 5 using data from ground-level detectors and SOHO/ERNE spacecraft data.

References

Abdo, A. A. et al. (2007), The Large-Scale Cosmic-Ray Anisotropy as Observed with Milagro, *Astrophys. J.*, **698**, 2121.

Abdo, A. A. (2007a), Discovery of Localized TeV Gamma-Ray Sources and Diffuse TeV Gamma-Ray Emission from the Galactic Plane with Milagro using a New Background Rejection Technique - Ph.D. Thesis, *Michigan State Univ*.

Abdo, A. A., et al. (2007b), TeV Gamma-Ray Sources from a Survey of the Galactic Plane with Milagro, *Astrophys. J.*, **664**, L91.

Abdo, A. A., et al. (2008), A Measurement of the Spatial Distribution of Diffuse TeV Gamma Ray Emission from the Galactic Plane with Milagro, *Astrophys. J.*, **688**, 1078.

Achterberg, A., and Norman, C. A. (1980), Particle acceleration by shock waves in solar flares, *Astron. Astrophys.*, **89**, 353.

Agostinelli, S., et al. (2003), GEANT4 - A Simulation Toolkit, *Nucl. Instrum. Methods Phys. Res. A*, **506**, 250.

Allekotte, I. et al. (2008), The Surface Detector System of the Pierre Auger Observatory, *Nucl. Instrum. Methods Phys. Res.*, **586**, 409.

Aschwanden, M. J. (2010), GeV Particle Acceleration in Solar Flares and Ground Level Enhancement Events, *Subm. to Space Sci. Rev.,* arXiv:1005.0029.

Atkins, R., et al. (2000), Milagrito, a TeV Air-Shower Array, *Nucl. Instrum. Methods Phys. Res. A*, **449**, 478.

Atkins, R., et al. (2003), Observation of TeV Gamma Rays from the Crab Nebula with Milagro using a New Background Rejection Technique, *Astrophys. J.,* **595**, 803.

Auger, P., Ehrenfest, P., Maze, R., Daudin, J., Robley, and Freon, A. (1939) Extensive Cosmic-Ray Showers, *Rev. Mod. Phys.*, **11**, 288.

Battersby, S. (2005), Superflares Could Kill Unprotected Astronauts, *New Scientist*.

Beach, L., and Forbush, S. E. (1961), Cosmic-Ray Results, *Carnegie Inst. Wash. Publ.*, **21**, 175.

Beach, L., and Forbush, S. E. (1969), Cosmic-Ray Results, *Carnegie Inst. Wash. Publ.*, **22**, 175.

Bieber. J. W., and Evenson, P. (1991), Determination of Energy Spectra for the Large Solar Particle Events of 1989, *Proc. 22nd Int. Cosmic Ray Conf.*, **3**, 129.

Bieber, J. W., and Evenson, P. (1995), Spaceship Earth - An Optimized Network of Neutron Monitors, *Proc. 24th Int. Cosmic Ray Conf.*, **4**, 1316.

Bieber, J. W., Evenson, P., Droge, W., Pyle, R., Ruffolo, D., Rujiwarodom, M., Tooprakai, P., and Khumlumlert, T. (2004), Spaceship Earth Observations of the Easter 2001 Solar Particle Event, *Astrophys. J.,* **601**, L103.

Biermann, L. (1953), Physical Processes in Comet Tails and their Relation to Solar Activity, *Mém. Soc. Roy. Sci Liège*, **13**, 291.

Bigelow, F. H. (1890), Further Study of the Solar Corona, *New Haven*.

Bird, D. J. et al. (1994), The Cosmic-Ray Energy Spectrum Observed by the Fly's Eye, *Astrophys. J.*, **424**, 491.

Bird, D. J. et al. (1995), Detection of a Cosmic Ray with Measured Energy Well Beyond the Expected Spectral Cutoff due to Cosmic Microwave Radiation, *Astrophys. J.*, **441**, 144.

Birkeland, K. R. (1908, 1913), The Norwegian Aurora Polaris Expedition 1902-1913, *Christiana, Norway, H. Aschehoug & Co*., **1 & 2**.

Bombardieri, D. J., Michael, K. J., Duldig, M. L., and Humble, J. E. (2007), Relativistic Proton Production During the 2001 April 15 Solar Event, *Astrophys. J.*, **665**, 813.

Bombardieri, D. J., Duldig, M. L., Humble, J. E., and Michael, K. J. (2008), An Improved Model for Relativistic Solar Proton Acceleration Applied to the 2005 January 20 and Earlier Events, *Astrophys. J.*, **682**, 1315.

Bradt, H. L., and Peters, B. (1948), Investigation of the Primary Cosmic Radiation with Nuclear Photographic Emulsions, *Phys. Rev.*, **74**, 1828.

Bütikofer, R., Flückiger, E. O., Desorgher, L., Moser, M. R., Pirard, B. (2000), The Solar Cosmic Ray Ground-Level Enhancements on 20 January 2005 and 13 December 2006, *Adv. Space Res.*, **43**, 499.

Cane, H. V., McGuire, R. E., and von Rosenvinge, T. T. (1986), Two Classes of Solar Energetic Particle Events Associated with Impulsive and Long-Duration Soft X-Ray Flares, *Astrophys. J.,* **301**, 448.

Cane, H. V., Sheeley, N. R. Jr., and Howard, R. A. (1987), Energetic Interplanetary Shocks, Radio Emission, and Coronal Mass Ejections, *J. Geophys. Res.*, **92**, 9869.

Cane, H. V., von Rosenvinge, T. T., and McGuire, R. E. (1990), Energetic Particle Observations at the Helios 1 Spacecraft of Shocks Associated with Coronal Mass Ejections, *J. Geophys. Res.*, **95**, 6575.

Carmichael, H. (1962), High-Energy Solar-Particle Events, *Space Sci. Rev.*, **1**, 28.

Carmichael, H. (1968), *Cosmic Rays (Instruments), Annals of the IQSY*, **1**, 178.

Chapman, S. (1919), An Outline of a Theory of Magnetic Storms, *Proc. Roy. Soc. Ser. A*, **95**, 61.

Chapman, S., and Ferraro, V. C. A. (1931a), A New Theory of Magnetic Storms, Part I - The Initial Phase, *Terr. Mag. Atmos. Elect.* **36**, 77.

Chapman, S., and Ferraro, V. C. A. (1931b), A New Theory of Magnetic Storms, Part I - The Initial Phase (continued), *Terr. Mag. Atmos. Elect.* **36**, 171.

Chapman, S., and Ferraro, V. C. A. (1932), A New Theory of Magnetic Storms, Part I - The Initial Phase (continued), *Terr. Mag. Atmos. Elect.* **37**, 147.

Chapman, S., and Ferraro, V. C. A. (1933), A New Theory of Magnetic Storms, Part II - The Main Phase, *Terr. Mag. Atmos. Elect.* **38**, 79.

Chapman, S. (1950), Corpuscular Influences upon the Upper Atmosphere, *J. Geophys. Res.*, **55**, 361.

Chapman, S. (1957), Notes on the Solar Corona and the Terrestrial Ionosphere, *Smithsonian Contr. Astrophys.*, **2**, 1.

Chupp, E. L., Ryan, J. M. (2009), High Energy Neutron and Pion-Decay Gamma-Ray Emissions from Solar Flares, *Res. Astron. Astrophys.*, **9**, 11.

Clay, J. (1927), *Proc. Roy. Acad. Amsterdam*. **30**, 1115.

Cliver, E. W., Kahler, S. W., Shea, M. A., Smart, D. F. (1982), Injection Onsets of 2 GeV Protons, 1 MeV Electrons, and 100 KeV Electrons in Solar Cosmic Ray Flares, *Astrophys. J.*, **260**, 362.

Cranmer, S. R., Ballegooijen, A. A., and Edgar, R. J. (2007), Self-Consistent Coronal Heating and Solar Wind Acceleration from Anisotropic Magnetohydrodynamic Turbulence, *Astrophys. J. Suppl. Ser.*. **171**, 520.

Debrunner, H., and Lockwood, J. A. (1980), The Spatial Anisotropy, Rigidity Spectrum, and Propagation Characteristics of the Relativistic Solar Particles During the Event on May 7, 1978, *J. Geophys. Res.*, **85**, 6853.

Debrunner, H., Flückiger, E., Lockwood, J. A., and McGuire, R. E. (1984), Comparison of the Solar Cosmic Ray Events on May 7, 1978, and November 22, 1977, *J. Geophys. Res.*, **89**, 769.

Decker, R. B., and Vlahos, L. (1986a), Modeling of Ion Acceleration Through Drift and Diffusion at Interplanetary Shocks, *J. Geophys. Res.*, **91**, 13349.

Decker, R. B., and Vlahos, L. (1986b), Numerical Studies of Particle Acceleration at Turbulent, Oblique Shocks with an Application to Prompt Ion Acceleration During Solar Flares, Astrophys. *J.*, **306**, 710.

Demoulin, P., and Vial, J. C. (1992), Structural Characteristics of Eruptive Prominences, *Solar Phys.*, **141**, 289.

Desai, M. I., Mason, G. M., Gold, R. E., Krimigis, S. M., Cohen, C. M. S., Mewaldt, R. A., Mazur, J. E., and Dwyer, J. R. (2006), Heavy-Ion Elemental Abundances in Large Solar Energetic Particle Events and Their Implications for the Seed Population, *Astrophys. J.*, **649**, 470.

Deslandres, H. (1894), Mémoires et Observations. Recherches Photographiques sur les Flammes de L'atmosphère Solaire, *Bulletin Astronomique*, **11**, 55.

Desorgher, L. (2006), PLANETOCOSMICS Software User Manual, http://cosray.unibe.ch/laurent/planetocosmics.

Ellison, D. C., and Ramaty, R. (1985), Shock Acceleration of Electrons and Ions in Solar Flares, *Astrophys. J.*, **298**, 400.

Evenson, P., Meyer, P., and Yanagita, S. (1982), Solar Flare Shocks in Interplanetary Space and Solar Flare Particle Events, *J. Geophys. Res.*, **87**, 625.

Falcone, A. (2001), Observation and Study of GeV Solar Energetic Particles using the Milagrito Extensive Air Shower Detector - Ph.D. Thesis, *Univ. of New Hampshire*.

Feldman, W. C., Asbridge, J. R., Bame, S. J., Fenimore, E. E., and Gosling, J. T. (1981), The Solar Origins of Solar Wind Interstream Flows - Near-Equatorial Coronal Streamers, *J. Geophys. Res.,* **86**, 5408.

Firor, J. (1954), Cosmic Radiation Intensity-Time Variations and Their Origin. IV. Increases Associated with Solar Flares, *Phys. Rev.*, **94**, 1017.

Fitzgerald, G. F. (1892), Sunspots and Magnetic Storms, *The Electrician*, **30**, 48.

Forbes, T. G. (2000), Reconnection Theory in Three Dimensions, *Adv. Space Res.*, **26**, 549.

Forbush, S. E. (1937), On the Effects in Cosmic-Ray Intensity Observed During the Recent Magnetic Storm, *Phys. Rev. Lett.*, **51**, 1108.

Forbush, S. E. (1946), Three Unusual Cosmic-Ray Increases Possibly Due to Charged Particles from the Sun, *Phys. Rev.*, **70** 771.

Forbush, S. E., Gill, P. S., and Vallarta, M. S. (1949), On the Mechanism of Sudden Increases of Cosmic Radiation Associated with Solar Flares, *Rev. Mod. Phys.*, **21**, 44.

Forbush, S. E. (1956), Large Increase of Cosmic-Ray Intensity Following Solar Flare on February 23, 1956, *J. Geophys. Res.*, **61**, 155.

Gaisser, T. K., and Hillas, A. M. (1977), *Proceedings of the 15th International Cosmic Ray Conference*, **8**, 353.

Gary, D. E., Dulk, G. A., House, L. L., Illing, R., Sawyer, C., Wagner, W. J., McLean, D. J., and Hildner, E. (1984), Type II Bursts Shock Waves, and Coronal Transients - The Event of 1980 June 29, 0233 UT, *Astron. Astrophys.*, **134**, 222.

Gergely, T. E., Kundu, M., Erskine, F. T., Sawyer, C., Wagner, W. J., Illing, R., House, L. L., McCabe, M. K., Stewart, R. T., Nelson, G. J., Koomen, M. J., Michels, D., Howard, R., and Sheeley, N. (1984), Radio and Visible-Light Observations of a Coronal Arcade Transient, *Solar Phys.*, **90**, 161.

Gleeson, L. J., and Axford, W. I. (1967), Cosmic-Rays in the Interplanetary Medium, *Astrophys. J.,* **149**, L115.

Gloeckler, G., Fisk, L. A., Hefti, S., Schwadron, N. A., Zurbuchen, T. H., Ipavich, F. M., Geiss, J., Bochsler, P., and Wimmer-Schweingruber, R. F. (1999), Unusual Composition of the Solar Wind in the 2-3 May 1998 CME Observed with SWICS on ACE, *Geophys. Res. Lett.*, **26**, 157.

Gold, T. (1955), Discussion of Shock Waves and Rarefied Gases, Gas Dynamics of Cosmic Clouds, 103.

Gopalswamy, N., Yashiro, S., Kaiser, M. L., and Howard , R. A. (2003), Coronal Mass Ejection Interaction and Particle Acceleration During the 2001 April 14-15 Events, *Adv. Space Res.*, **32**, 2613.

Gopalswamy, N., Xie, H., Yashiro, S., and Usokin, I. (2005), Coronal Mass Ejections and Ground-Level Enhancements, *Proc. 29th Int. Cosmic Ray Conf.*, **1**, 169.

Gosling, J. T., Asbridge, J. R., Bame, S. J., Hundhausen, A. J., and Strong, I. B. (1968), Satellite Observations of Interplanetary Shock Waves, *J. Geophys. Res.*, **73**, 43.

Gosling, J. T., Hildner, E., MacQueen, R. M., Munro, R. H., Poland, A. I., and Ross, C. L. (1974), Mass Ejections from the Sun: A View from Skylab, *J. Geophys. Res.*, **79**, 4581.

Gosling, J. T., Hildner, E., MacQueen, R. M., Munro, R. H., Poland, A. I., and Ross, C. L. (1976), The Speeds of Coronal Mass Ejection Events, *Sol. Phys.*, **48**, 389.

Gosling, J. T. (1993), The Solar Flare Myth, *J. Geophys. Res.*, **98**, 18937.

Grechnev, V. V., Kurt, V. G., Chertok, I. M., Uralov, A. M., Nakajima, H., Altyntsev, A. T., Belov, A. V., Yushkov, B. Yu., Kuznetsov, S. N., Kashapova, L. K., Meshalkina, N. S., and Prestage, N. P. (2008), An Extreme Solar Event of 20 January 2005: Properties of the Flare and the Origin of Energetic Particles, *Solar Phys.*, **252**, 149.

Greisen, K. (1966), End to the Cosmic-Ray Spectrum?, *Phys. Rev. Lett.*, **16**, 748.

Haino, S., et al. (2004), Measurements of Primary and Atmospheric Cosmic-Ray Spectra with the BESS-TeV Spectrometer, arXiv:astro-ph/0403704v1.

Hale, G. E. (1908), On the Probable Existence of a Magnetic Field in Sun-Spots, *Astrophys. J.*, **28**, 315.

Hale, G. E. (1931), The Spectrohelioscope and its Work Part III. Solar eruptions and their Apparent Terrestrial Effects, *Astrophys. J.*, **73**, 379.

Hatton, C. J., and Carmichael, H. (1964), Experimental Investigation of the NM-64 Neutron Monitor, *Can. J. Phys.*, **42**, 2443.

Heck, D. (2010), http://www-ik.fzk.de/corsika/.

Heristchi, Dj., and Trottet, G. (1971), Upper Cutoff in the Spectrum of Solar Particles, *Phys. Rev Lett.*, **26**, 197.

Heristchi, Dj., and Trottet, G. (1975), Determination of the Upper Cutoff of the 1-2 September 1971 Proton Event from Satellite Measurements, *Solar Phys.*, **41**, 459.

Heristchi, Dj., Trottet, G., and Perez-Peraza, J. (1976), Upper cutoff of high energy solar protons, *Solar Phys.*, **49**, 151.

Hess, V. F. (1912), *Phys. Z.,* **13**, 1084.

Hinton, J. A. (1998), Ph.D. Thesis, *University of Leeds*.

Holder, J. et al. (2006), The First VERITAS Telescope, *Astropart. Phys.*, **25**, 391.

Hsieh, K. C., and Simpson, J. A. (1970), Galactic ^{3}He above 10 MeV per Nucleon and the Solar Contributions of Hydrogen and Helium, *Astrophys. J.,* **162**, L191.

Hughes, E. B. (1961), Ph.D. Thesis, *University of Leeds*.

Hughes, E. B., and Marsden, P. L. (1966), Response of a Standard IGY Neutron Monitor, *J. Geophys. Res.*, **71**, 1435.

Isenberg, P. A., and Jokipii, J. R. (1979), Gradient and Curvature Drifts in Magnetic Fields with Arbitrary Spatial Variation, *Astrophys. J.*, **234**, 746.

Johnson, T. H. (1933), The Azimuthal Asymmetry of the Cosmic Radiation, *Phys. Rev.* **43**, 834.

Jokipii, J. R. (1987), Rate of Energy Gain and Maximum Energy in Diffusive Shock Acceleration, *Astrophys. J.*, **313**, 842.

Kahler, S. W., Hildner, E., and Van Hollebeke, M. A. I. (1978), Prompt Solar Proton Events and Coronal Mass Ejections, *Solar Phys.*, **57**, 429.

Kahler, S. W., Sheeley, N. R. Jr., Howard, R. A., Michels, D. J., Koomen, M. J., McGuire, R. E., and von Rosenvinge, T. T. (1984), Associations Between Coronal Mass Ejections and Solar Energetic Proton Events, *J. Geophys. Res.*, **89**, 9683.

Kahler, S. W., Cliver, E. W., Cane, H. V., McGuire, R. E., Stone, R. G., and Sheeley, N. R. Jr. (1986), Solar Filament Eruptions and Energetic Particle Events, *Astrophys. J.,* **302**, 504.

Kahler, S. W., Cliver, E. W., Cane, H. V., McGuire, R. E., Reames, D. V., Sheeley, N. R. Jr., and Howard, R. A. (1987), Solar Energetic Proton Events and Coronal Mass Ejections Near Solar Minimum, *Proc. 20th Int. Cosmic Ray Conf.*, **3**, 121.

Kahler, S. W. (1994), Injection Profiles of Solar Energetic Particles as Functions of Coronal Mass Ejection Heights, *Astrophys. J.*, **428**, 837.

Kahler, S. W. (2001), The Correlation Between Solar Energetic Particle Intensities and Speeds of Coronal Mass Ejections: Effects of Ambient Particle Intensities and Energy Spectra, *J. Geophys. Res.*, **106**, 20947.

Kallenrode, M.-B. (2003), Current Views on Impulsive and Gradual Solar Energetic Particle Events, *J. Phys. G: Nucl. Part. Phys.*, **29**, 965.

Kuznetsov, S. N., Kurt, V. G., Yushkov, B. Yu., Kudela, K., Glakin, V. I., and Myagkova, I. N. (2008), CORONAS-F Satellite Data on the Delay Between the Proton Acceleration on the Sun and their Detection at 1 AU, *Proc. 30th Int. Cosmic Ray Conf.*, **1**, 121.

Labrador, A. W., Leske, R. A., Mewaldt, R. A., Stone, E. C., and von Rosenvinge, T. T. (2005), High Energy Ionic Charge State Composition in the October/November 2003 and January 20, 2005 SEP Events, *Proc. 29th Int. Cosmic Ray Conf.*, **1**, 99.

Lange, I., Forbush, S. E. (1948), Cosmic-Ray Results, *Carnegie Inst. Wash. Publ.*, **130**, 175.

Lange, I., Forbush, S. E. (1957), Cosmic-Ray Results, *Carnegie Inst. Wash. Publ.*, **20**, 175.

Lee, M. A., and Fisk, L. A. (1982), Shock Acceleration of Energetic Particles in the Heliosphere, *Space Sc. Rev.*, **32**, 205.

Lee, M. A., and Ryan, J. M. (1986), Time-Dependent Coronal Shock Acceleration of Energetic Solar Flare Particles, *Astrophys. J.,* **303**, 829.

Lee, M. A. (2005), Coupled Hydrodynamic Wave Excitation and Ion Acceleration at an Evolving Coronal/Interplanetary Shock, *Astrophys. J. Suppl. Ser.,* **158**, 38.

Linsley, J. (1983), Spectra, Anisotropies and Composition of Cosmic Rays above 1000 GeV, *Proc. of the 18th International Cosmic Ray Conference*, **12**, 135.

Lindsay, G. M., Luhmann, J. G., Russell, C. T., and Gosling, J. T. (1999), Relationships Between Coronal Mass Ejection Speeds from Coronagraph Images and Interplanetary Characteristics of Associated Interplanetary Coronal Mass Ejections, *J. Geophys. Res.*, **104**, 12515.

Lockwood, J. A. and Debrunner, H. (1999), Solar Flare Particle Measurements with Neutron Monitors, *Space Sci. Rev.*, **88**, 483.

Lockwood, J. A., Debrunner, H., Flückiger, E. O., and Ryan, J. M. (2002), Solar Proton Rigidity Spectra from 1 to 10 GV of Selected Flare Events Since 1960, *Solar Phys.*, **208**, 113.

Longair, M. S. (1992), High Energy Astrophysics - 2nd Ed., *Cambridge Univ. Press*.

Luhn, A., Klecker, B., Hovestadt, D., Gloeckler, G., Ipavich, F. M., Scholer, M., Fan, C. Y. and Fisk, L. A. (1984), Ionic Charge States of N, Ne, Mg, SI and S in Solar Energetic Particle Events, *Adv. Space Res.,* **4**, 161.

Luhn, A., Klecker, B., Hovestadt, D., and Möbius, E. (1987), The mean ionic charge of silicon in He-3-rich solar flares, *Astrophys. J.,* **317**, 951.

Lüst, R., and Simpson, J. A. (1957), Initial Stages in the Propagation of Cosmic Rays Produced by Solar Flares, *Phys. Rev.*, **108**, 1563.

Maia, D. J. F., Gama, R., Mercier, C., Pick, M., Kerdraon, A., and Karlicky, M. (2007), The Radio-Coronal Mass Ejection Event on 2001 April 15, *Astrophys. J.*, **660**, 874.

Mason, G. M., Gloeckler, G., and Hovestadt, D. (1984), Temporal Variations of Nucleonic Abundances in Solar Flare Energetic Particle Events. II - Evidence for Large-Scale Shock Acceleration, *Astrophys. J.,* **280**, 902.

Mason, G. M., Mazur, J. E., Dwyer, J. R. (1999), ^{3}He Enhancements in Large Solar Energetic Particle Events, *Astrophys. J.*, **525**, L113.

Mason, S., Klein, K.-L., Bütikofer, R., Flückiger, E., Kurt, V., Yushkov, B., and Krucker, S. (2009), Acceleration of Relativistic Protons During the 20 January 2005 Flare and CME, *Solar Phys.*, **257**, 305.

McCracken, K. G., and Palmeira, R. A. R. (1960), Comparison of Solar Cosmic Rays Injection Including July, 17, 1959, and May 4, 1960, *J. Geophys. Res.*, **65**, 2673.

McCracken, K. G., Rao, U. R., and Shea, M. A. (1962), The Trajectories of Cosmic Rays in a High Degree Simulation of the Geomagnetic Field, *MIT Tech. Rep.,* **77,** NYO-2670.

McCracken, K. G. (1962a), The Cosmic-Ray Flare Effect: 1. Some New Methods of Analysis, *J. Geophys. Res.*, **67**, 423.

McCracken, K. G. (1962b), The Cosmic-Ray Flare Effect: 2. The Flare Effects of May 4, November 12, and November 15, 1960, *J. Geophys. Res.*, **67**, 435.

McCracken, K. G., Rao, U. R., Fowler, B. C., Shea, M. A., and Smart, D. F. (1965), Cosmic Rays Tables (Asymptotic Directions, Variational Coefficients and Cutoff Rigidities), *IQSY Instruction Manual,* **10**.

McCracken, K. G., Rao, U. R., Fowler, B. C., Shea, M. A., and Smart, D. F. (1968), Cosmic Rays Tables (Asymptotic Directions, etc.), *Annals of the IQSY Instruction Manual,* **1**, 198.

McCracken, K. G., and Moraal, H. (2007), Two Acceleration Mechanisms for the 20 January 2005 Ground Level Enhancement, *Proc. 30th Int. Cosmic Ray Conf.,* **1**, 269.

McCracken, K. G., Moraal, H., and Stoker, P. H. (2008), Investigation of the Multiple-Component Structure of the 20 January 2005 Cosmic Ray Ground Level Enhancement, *J. Geophys. Res.,* **113**, A12101.

McCullough, J. F., et al. (1999), Status of the Milagro Gamma Ray Observatory, arXiv:astro-ph/9906383v1.

Meyer, P., Parker, E. N., and Simpson, J. A. (1956), Solar Cosmic Rays of February, 1956 and Their Propagation through Interplanetary Space, *Phys. Rev.*, **104**, 768.

Meyer, J.-P. (1985), The Baseline Composition of Solar Energetic Particles, *Astrophys. J. Suppl. Ser.,* **57**, 151.

Mitalas, R., and Sills, K. R. (1992), On the Photon Diffusion Time Scale for the Sun, Astro*phys. J.,* **401**, 759.

Moraal, H., McCracken, K. G., and Stoker, P. H. (2007), Analysis of the 20 January 2005 Ground-Level Enhancement, *Proc. of the 30th International Cosmic Ray Conference*, **1**, 265.

Moraal, H., Belov, A., and Clem, J. M. (2000), Design and Co-Ordination of Multi-Station International Neutron Monitor Networks, *Space Sci. Rev.*, **93**, 285.

Munakata, K., Bieber, J. W., Kuwabara, T., Hattori, T., Inoue, K., Yasue, S., Kato, C., Fujii, Z., Fujimoto, K., Duldig, M. L., Humble, J. E., Trivedi, N. B., Gonzalez, W. D., Silva, M. R., Tsuruta, B. T., and Schuch, N. J. (2001), A Prototype Muon Detector Network Covering a Full Range of Cosmic Ray Pitch Angles, *Proc. 27th Int. Cosmic Ray Conf.*, **9**, 3494.

Newton, H.W. (1940), Early Visual Observations of Bright Chromospheric Eruptions on the Sun's Disk, *J. Brit. Astron. Soc.* **50**, 273.

Newton, H.W. (1943), Solar Flares and Magnetic Storms, *Mon. Not. Roy. Astron. Soc.* **103**, 244.

Pallavicini, R., Serio, S., and Vaiana, G. S. (1977), A Survey of Soft X-Ray Limb Flare Images - The Relation Between Their Structure in the Corona and other Physical Parameters, *Astrophys. J.*, **216**, 108.

Parker, E. N. (1957), Acceleration of Cosmic Rays in Solar Flares, *Phys. Rev.*, **107**, 830.

Parker, E. N. (1958), Dynamics of the Interplanetary Gas and Magnetic Fields, *Astrophys. J.*, **128**, 664.

Pierre Auger Collaboration (2010a), The Pierre Auger Observatory and its Fluorescence Detector, submitted to *Nucl. Instrum. Methods Phys. Res.*, **A**, arXiv:0907.4282v1

Pierre Auger Collaboration (2010b), Measurement of the Energy Spectrum of Cosmic Rays Above 10^{18} eV using the Pierre Auger Observatory, *Phys. Lett. B.*, **685**, 239.

Reames, D. V. (1999), Particle Acceleration at the Sun and in the Heliosphere, *Space Sci. Rev.*, **90**, 413.

Reames, D. V. (2009), Solar Energetic Particle Release Times in Historic Ground-Level Events, *Astrophys. J.*, **706**, 844.

Rossi, B. (1964), Cosmic Rays, *McGraw Hill*.

Ryan, J. M., Lee, M. A., (1991), On the Transport and Acceleration of Solar Flare Particles in a Coronal Loop, *Astrophys. J.*, **368**, 316.

Ryan, J. M. (2000), Long-Duration Solar Gamma-Ray Flares, *Space Sc. Rev.*, **93**, 581.

Schwenn, R. (1983), Direct Correlations Between Coronal Transients and Interplanetary Disturbances, *Space Sci. Rev.*, **34**, 85.

Shea, M. A., Smart, D. F., McCracken, K. G. (1965), A Study of Vertical Cutoff Rigidities using Sixth Degree Simulations of the Geomagnetic Field, *J. Geophys. Res.*, **70** 4117.

Shea, M. A., and Smart, D. F. (1970), On the Application of Trajectory-Derived Cutoff Rigidities to Cosmic-Ray Intensity Variations, *Proc. of the 11th International Cosmic Ray Conference*, **29**, 533.

Shea, M. A., and Smart, D. F. (1990), The Influence of the Changing Geomagnetic Field on Cosmic Ray Measurements, *J. Geomagn. Geoelectr.*, **42**, 1107.

Shea, M. A., and Smart, D. F. (1996), Unusual Intensity-Time Profiles of Ground-Level Solar Proton Events, *High Energy Solar Phys.*, **374**, 131.

Shea, M. A., and Smart, D. F. (1996), Relativistic Solar Proton Events - Evidence for a Dual-State Injection Scenario, *Adv. in Solar Connection with Transient Interplanetary Phenomena*, **374**, 467.

Sheeley, N.R. Jr., Bohlin, J. D., Brueckner, G. E., Purcell, J. D., Scherrer, V. E., Tousey, R., Smith, J. B. Jr., Speich, D. M., Tandberg-Hanssen, E., Wilson, R. M., De Loach, A. C., Hoover, R. B., and McGuire, J. P. (1975), Coronal Changes Associated with a Disappearing Filament, *Solar Phys.*, **45**, 377.

Sheeley, N. R. Jr., Howard, R. A., Koomen, M. J., Michels, D. J., Schwenn, R., Muhlhauser, K.-H., and Rosenbauer, H. (1985), Coronal Mass Ejections and Interplanetary Shocks, *J. Geophys. Res.*, **90**, 163.

Simnett, G. M. (2006), The Timing of Relativistic Proton Acceleration in the 20 January 2005 Flare, *Astron. and Astrophys.*, **445**, 715.

Simpson, J. A. (1948), The Latitude Dependance of Neutron Densities in the Atmosphere as a Function of Altitude, *Phys. Rev.*, **73**, 1389.

Simpson, J. A. (1951), Neutron s Produced in the Atmosphere by the Cosmic Radiations, *Phys. Rev.*, **83**, 1175.

Simpson, J. A. (1953), Flying Atomic “Piles” , *University of Chicago Magazine* **45**, 5.

Simpson, J. A., and Uretz, R. B. (1953), Cosmic-Ray Neutron Production in Elements as a Function of Latitude and Altitude, *Phys. Rev.*, **90**, 44.

Simpson, J. A., Fonger, W., and Treiman, S. B. (1953), Cosmic Radiation Intensity-Time Variations and Their Origin. I. Neutron Intensity Variation Method and Meteorological Factors, *Phys. Rev.*, **90**, 934.

Simpson, J. A. (2000), The Cosmic Ray Nucleonic Component: The Invention and Scientific Uses of the Neutron Monitor - (Keynote Lecture), *Space Sci. Rev.*, **93**, 11.

Smart, D. F., and Shea, M. A. (1990), Probable Pitch Angle Distribution and Spectra of the 23 February 1956 Solar Cosmic Ray Event, *Proc. 21st Int. Cosmic Ray Conf.*, **5**, 257.

Smart, D. F., Shea, M. A., and Flückiger, E. O. (2000), Magnetospheric Models and Trajectory Computations, *Space Sci. Rev.*, **93**, 305.

Smart, D. F., and Shea, M. A. (2009), Fifty Years of Progress in Geomagnetic Cutoff Rigidity Determinations, *Adv. Space Res.*, **44**, 1107.

Steljes, J. F., and Carmichael, H. (1961), Solar Geophysical Data, Part B, CRPL-F 204.

Stewart, R. T., Dulk, G. A., Sheridan, K. V., House, L. L., Wagner, W. J., Sawyer, C., and Illing, R. (1982), Visible Light Observations of a Dense Plasmoid Associated with a Moving Type IV Solar Burst, *Astron. Astrophys.*, **116**, 217.

Stone, E. C., Cummings, A. C., McDonald, F. B., Heikkila, B. C., Lal, N., and Webber, W. R. (2005), Voyager 1 Explores the Termination Shock Region and the Heliosheath Beyond, *Science*, **309**, 2017.

Tousey, R. (1973), The Solar Corona, *Adv. Space Res.*, **13** 713.

Treat, J. E., and Greisen, K. (1948), Penetrating Particles in Extensive Air Showers *Phys. Rev.,* **74**, 414.

Tylka, A. J., Boberg, P. R., Adams, J. H. Jr., Beahm, L. P., Dietrich, W. F., and Kleis, T. (1995), The Mean Ionic Charge State of Solar Energetic Fe Ions Above 200 MeV per Nucleon, *Astrophys. J.* **444**, L109.

Tylka, A. J., Boberg, P. R., Cohen, C. M. S., Dietrich, W. F., Maclennan, C. G., Mason, G. M., Ng, C. K., and Reames, D. V. (2002), Flare- and Shock-Accelerated Particles in the Solar Events of 2001 April 14 and 15, *Astrophys. J.*, **581**, L119.

Uralov, A. M., Grechnev, V. V., Hudson, and H. S., (2005), Initial Localization and Kinematic Characteristics of the Structural Components of a Coronal Mass Ejection, *J. of Geophys. Res.*, **110**, A05104.

Webb, D. F., Cliver, E. W., Crooker, N. U., Cyr, O. C. St., and Thompson, B. J. (2000), Relationship of Halo Coronal Mass Ejections, Magnetic Clouds, and Magnetic Storms, *J. Geophys. Res.*, **105**, 7491.

Weekes, T. C. (2003), Very High Energy Gamma-Ray Astronomy, *Taylor and Francis*.

Weekes, T. C. et al. (1989), Observation of TeV Gamma Rays from the Crab Nebula using the Atmospheric Čerenkov Imaging Technique, *Astrophys. J.*, 342, 379.

Zank, G. P., Rice, W. K. M., and Wu, C. C. (2000), Particle Acceleration and Coronal Mass Ejection Driven Shocks: A Theoretical Model, *J. Geophys. Res.,* **105**, 25079.

Zatsepin, G. T., and Kuzmin, V. A. (1966), Upper Limit of the Spectrum of Cosmic Rays, *JEPT Lett.*, **4**, 78.

Zirakashvili, V. N., Ptuskin, V. S., and Rogovaya, S. I. (2007), Maximum Energy of Cosmic Rays Accelerated in Supernova Remnants, *Bulletin of the Russian Academy of Sciences*, **71**, 464.